MODELING, SIMULATION AND IMPLEMENTATION OF PRIMARY MIRROR CONTROL SYSTEM FOR THE PROTOTYPE SEGMENTED MIRROR TELESCOPE

A Thesis

Submitted for the Degree of

Doctor of Philosophy (Technology)

Submitted by

DESHMUKH PRASANNA GAJANAN

Department of Applied Optics & Photonics

University College of Technology

University of Calcutta

February 2019

I would like to dedicate this thesis to my loving parents

List of Publications

I. Papers in Refereed Journals:

1. Deshmukh, Prasanna Gajanan, Amaresh Mandal, Padmakar Singh Parihar, Dayananda Nayak, Deepta Sundar Mishra. "Design, development, and validation of a segment support actuator for the prototype segmented mirror telescope." Journal of Astronomical Telescopes, Instruments, and Systems. 2018 Feb; 4(1): 014005. doi: 10.1117/1.JATIS.4.1.014005.[1]

2. Deshmukh, Prasanna Gajanan, Padmakar Parihar, Deepta Sundar Mishra, and P. K. Mahesh. "Dynamic Loading Assembly for Testing Actuators of Segmented Mirror Telescope." Journal of Astronomical Instrumentation. 2017 Sep; 6(03): 1750006. doi: 10.1142/S2251171717500064.[2]

II. Papers in Proceedings:

1. Deshmukh Prasanna, Deepta Sundar Mishra, and Padmakar Parihar. "Primary mirror active control system simulation of Prototype Segmented Mirror Telescope." In Control Conference (ICC), 2017 Indian, pp. 364-371. IEEE, 2017. doi: 10.1109/INDIANCC.2017.7846502.[3]

---

[1] Presented in Chapter 2 and 3
[2] Presented in Chapter 4
[3] Presented in Chapter 6

2. Deshmukh Prasanna, Padmakar Parihar, Deepta S. Mishra, Ajin Prakash, and P. M. M. Kemkar. "A soft actuator for prototype segmented mirror telescope." In SPIE Astronomical Telescopes+ Instrumentation, pp. 991207-991207. International Society for Optics and Photonics, 2016. doi:10.1117/12.2231172.[4]

3. Deshmukh Prasanna and Padmakar Parihar. "Precision controller for segmented mirror telescope actuator: Control and tuning." In Control Conference (ICC), 2016 Indian, pp. 245-252. IEEE, 2016. doi: 10.1109/INDIANCC.2016.7441135.[5]

4. Parihar Padmakar, Deshmukh Prasanna, et al. "Prototype segmented mirror telescope: a pathfinder of India's Large Optical-NIR telescope project." In Ground-based and Airborne Telescopes VII. Vol. 10700. International Society for Optics and Photonics, 2018. doi: 10.1117/12.2313079.[6]

III. Presentations:

1. Poster presentation on 'Wind disturbance effect on PSMT Segment Support Actuator - Modeling and Controls', at the meeting of Astronomical Society of India (ASI-2017), March 06 - 10, 2017, Jaipur, India.

2. Poster presentation on 'A Programmable System on Chip (PSoC) based Controller for the PSMT Segment Support Actuators', at the Meeting of Astronomical Society of India (ASI-2017), March 06 - 10, 2017, Jaipur, India.

---

[4] Presented in Chapter 2
[5] Presented in Chapter 3
[6] Presented in Chapter 2

3. Oral presentation on 'Primary Mirror Active Control System Simulation of Prototype Segmented Mirror Telescope', at IEEE 2nd Indian Control Conference, Jan 2017, IIT Guwahati, India.

4. Oral presentation on 'A Soft Actuator for Prototype Segmented Mirror Telescope', at SPIE Astronomical Telescopes & Instrumentation 2016 Conference, June 2016, Edinburg, United Kingdom.

5. Oral presentation on 'Simulator for Primary Mirror Control System of Segmented Mirror Telescope', at the Meeting of Astronomical Society of India (ASI-2016), May 2016, University of Kashmir, India.

6. Oral presentation on 'Precision Controller for Segmented Mirror Telescope Actuator: Control and Tuning', at IEEE Indian Control Conference, Jan 2016, IIT Hyderabad, India.

7. Oral presentation on 'Performance testing of Thirty Meter Telescope Actuator', at TMT Science and Instrumentation Workshop 2015, 11-13 June 2015, IIST-ISRO, Thiruvananthapuram, India.

8. Poster presentation on 'Dynamic loading assembly for performance testing of Segmented Mirror Telescope Actuators', at Meeting of Astronomical Society of India (ASI-2015), Feb 2015, NCRA Pune, India.

9. Oral presentation on 'Development of Primary Mirror Control System for Segmented mirror telescopes', at India-South Africa Flagship Meeting, Sept 2014, IIA Bangalore, and at TMT Science Workshop 2014, Nov 2014, ARIES, Nainital, India.

10. Oral presentation on 'Control and Tuning of Segmented Mirror Telescope Actuator', at Meeting of Astronomical Society of India (ASI-2014), March 2014, IISER Mohali.

Abstract

The next generation large astronomical telescopes are primarily made of segmented mirrors and construction of such a telescope is a big challenge. It require enormous amount of works to conceptualize various sub-systems, design, analysis, planning and execution. It also demands to prototype various critical subsystems like actuators, edge sensors, segment support, drive and control system, etc. To build a 10m class Segmented Mirror Telescope in India, several activities have been initiated at the Indian Institute of Astrophysics. As a first step towards realizing bigger telescope, development of a Prototype Segmented Mirror Telescope (PSMT) has been proposed. Design and development of the few critical subsystems linked with the control of segmented primary mirror of the PSMT are part of this Ph.D. thesis.

The focus of the thesis is primary mirror control system, which comprises local and global control systems. The first task undertaken was, design and development of a soft actuator based on a voice coil motor. Before realizing it, detailed modeling and simulation have been conducted to make sure that the concept is feasible. Then after a prototype actuator was built. A customized precision controller has also been developed to control the actuator in closed loop mode. Varieties of experimentation show that indeed the prototype actuator meets most of stringent requirements. Further to check the performance under dynamically varying disturbances such as wind force, novel test equipment named Dynamic Loading Assembly has been developed. Through the tests conducted with DLA we ensured that the actuator is capable to reject wind induced disturbances.

To understand working of global control system of the PSMT and any other segmented mirror telescopes, we have developed a simulation tool called as the codeSMT. Creating the control matrix for any telescope made of many segment rings is cumbersome task. We have proposed a new numbering technique which is generic and can be used for any size SMT's. As a case study, the codeSMT is successfully tested in the PSMT active control simulation and error multiplier analysis. Finally, an integrated local and global control system of the PSMT has been designed, implemented and tested in the laboratory.

x

Contents

List of Figures

List of Tables

List of Acronyms

AO   –   Adaptive Optics

APS   –   Alignment and Phasing System

DLA   –   Dynamic Loading Assembly

ELT   –   Extremely Large Telescopes

EELT   –   European Extremely Large Telescopes

FLOPS   –   Floating-Point Operations Per Sec

GTC   –   Gran Telescopio Canarias

GC   –   Global Controller

GLC   –   Global Loop Controller

IIA   –   Indian Institute of Astrophysics

ITCC   –   India TMT Coordination Centre

LC   –   Local Controller

M1   –   Primary Mirror

M1CS   –   Primary Mirror Control System

NLOT   –   National Large Optical Telescope

NCS   –   Networked Control System

OWL   –   Overwhelmingly Large Telescope

PSD   –   Power Spectral Density

PSF   –   Point Spread Function

PSMT   –   Prototype Segmented Mirror Telescope

PSMA   –   PSMT Actuator

PTT   –   Piston Tip Tilt

SALT   –   Southern African Large Telescope

SID   –   System Identification

SMT   –   Segmented Mirror Telescope

SVD   –   Singular Value Decomposition

TMT   –   Thirty Meter Telescope

VCM   –   Voice Coil Motor

VCMT   –   Voice Coil Motor Testbed

Chapter 1   Introduction

1.1   Large Astronomical Telescopes

Astronomy is a scientific discipline mainly based on observations, as most of the experiments are not practical or impossible by nature. The invention of the first refracting telescope in the 16th century, and its improvement and use by Galileo to observe the sky, unlocked the potential of such instruments to push the limits of the observation of objects in the skies, by collecting more light than what the naked eye is capable of, and by magnifying the image. The technological and mathematical developments to improve the refracting telescope led Isaac Newton to the construction of the first reflecting telescope, based on the use of a parabolic reflecting mirror instead of a lens. The reflecting telescope exhibits some advantages with respect to the refracting one, in particular they don't have chromatic aberrations.

The primary mirror of an astronomical telescope has to be made larger to achieve higher angular resolution and better sensitivity. The brightness of the faintest objet that a particular telescope can observe is limited by the effective area of its primary mirror. Furthermore, the diameter of primary mirror, also affects the resolution and contrast of the images formed by the telescope in ideal conditions. Consequently, improving the performance of the telescopes has called for a constant increase of diameter along history. Figure 1-1 shows the evolution of the telescope aperture diameter of optical and infrared telescopes over last four centuries.
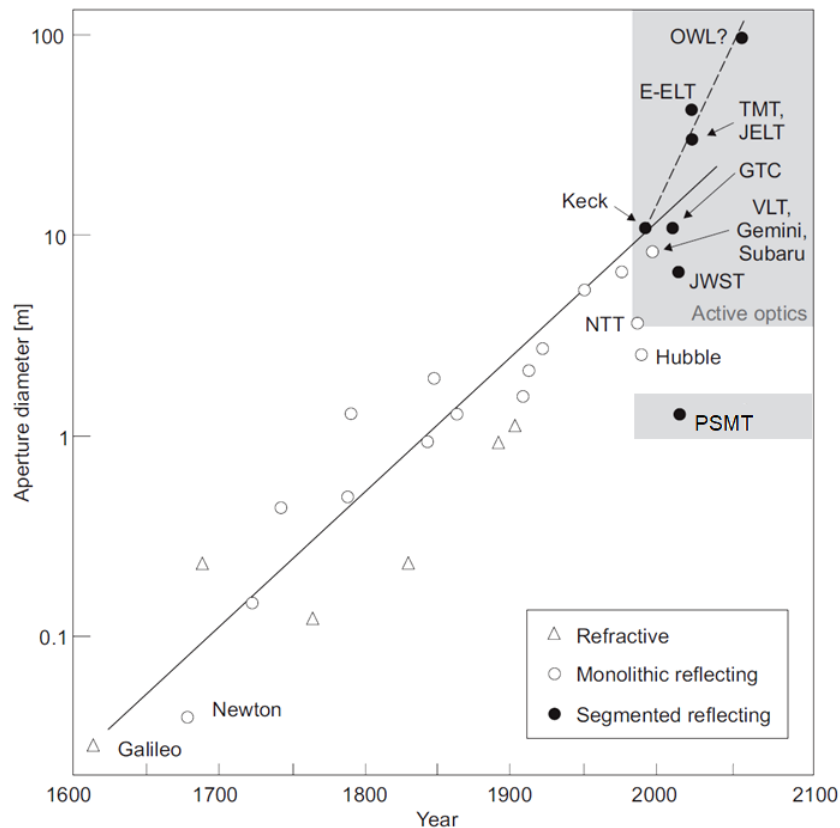
Figure 1-1 Evolution of telescope aperture diameter over time [adapted from (Bastaits Renaud 2010) and (Bely 2006)].

Clearly larger telescopes have increased light gathering power and there has always been a push to build larger and larger telescopes. The general trend in the development of the optical telescope has been on doubling of the aperture diameter about every 40 years (Bely 2006). About a dozen 8-10m telescopes are already in operation and the next generation Extremely Large Telescopes (ELTs) i.e. Giant Magellan Telescope (GMT), Thirty Meter Telescope (TMT) and European Extremely Large Telescope (E-ELT) are being constructed. These telescopes will change the way we view the universe and open new avenues of scientific exploration and discoveries. The massive segmented primary mirror of these telescopes will allow us to perform groundbreaking science, scoping out extrasolar planets, shining light on other galaxies, and improving our understanding of the fundamental laws of physics. In the coming decades they will help to answer few pressing scientific questions listed below (Redd 2018):

1. Planets: the discovery and characterization of planets and protoplanetary systems around other stars. They will let us observe the atmospheres of planets inside and outside our own solar system. They will also be capable of directly imaging larger planets and potentially characterizing their atmospheres.

2. Galaxies: to look back in time at the most distant galaxies, so we can understand their formation and evolution. They will also be able to peer into the details of distant galaxies to count their stars. Currently, astronomers can only resolve individual stars in our own galaxy and its nearest neighbours.

3. Dark matter: to make direct measurements of the expanding Universe. This could tell us more about dark matter and how it is distributed.

4. Dark Energy: Upcoming telescopes will attempt, for the first time, to constrain dark energy by directly observing the global dynamics of the universe. Such measurement will truly offer an independent and unique approach to the exploration of the expansion history of our universe.

Perhaps the most exciting questions these Extremely Large Telescopes will help us to answer are the ones we haven't yet thought to ask, and the serendipitous discoveries that will take us by surprise.

Building a giant telescope from a single monolithic mirror poses many difficulties (Nelson, Mast and Chanan 2013). The weight of a large monolithic mirror of size 8m or above can exceed several tons. Such a massive structure is hard to cast and incredibly difficult to support. The accidental risk factors of mirror breakage during coating, transportation, installation are exceedingly high. Besides, the standalone facilities for figuring, polishing, coating and testing of the large mirror are incredibly complicated and expensive to build and maintain. These difficulties typically grow rapidly with the increasing mirror size and make building of large monolithic mirrors highly impractical.

Figure 1-2 An artist's rendering of Extremely Large Telescope under construction. The Thirty Meter Telescope, TMT (left) and the European Extremely Large Telescope EELT (right). (Source: www.tmt.org, www.eso.org).

An obvious solution to these and other problems is to construct the primary mirror from the smaller segments, rather than building a single large monolithic mirror. Segmented mirror technology offers a viable and much simpler alternative to a large single monolithic primary mirror. Considering the problems related to the mass or thickness of the mirror, the gravitational deflection suffered by an optical mirror increases as D^4. This means that a monolithic mirror must have N times the thickness of a segmented mirror consisting of N equal segments covering the same area. For example, the 36 segments of the Keck Telescope are 7.5 cm thick, for which an equivalent monolith would be 2.7m thick. Although many critical problems are greatly reduced by building the primary from small segments, there are a number of issues, concerns, and technological difficulties arise due to segmentation (Nelson, Mast and Chanan 2013), which must be understood and dealt with before one can confidently proceed with building a large telescope having a segmented primary mirror. The various issues and complications associated with segments can generally be grouped into four categories:

1. Many fold increase in the number of parts and hence proportionally increase in the complexity.

2. Segments are difficult to polish because they are off-axis sections of the parent figure of revolution and are therefore not locally axisymmetric.

3. Segments require both active position control and optical alignment. Optical alignment places the mirror segments in the proper relative positions with respect to one another to within optical tolerances whereas active position control keeps these relative positions fixed.

4. Segment edges and the associated intersegment gaps add to both diffraction and thermal background effects.

1.2 Segmented Mirror Telescopes

Historically, in 1932, Horn d'Arturo in Italy built a 1.5m mirror out of 61 hexagonal segments, which was only used vertically and was not actively controlled (D'Arturo Horn 1955). Much later, in 1970s, Pierre Connes in France built a 4.6m segmented-mirror telescope for infrared astronomy (Chevillard 1977). It was fully steerable and actively controlled telescope, but the image quality wasn't good, and the telescope did not come into operation. A variation on the theme of a segmented-mirror telescope was the Multiple Mirror Telescope (MMT) (Beckers 1982); it consisted of six 1.8m telescopes in a common mount. The MMT was a multiple mirror rather than a true segmented mirror telescope and now no longer exist in its original multiple mirror configuration.

In late 1970s the Keck Observatory began as a conceptual design study for a 10-m segmented mirror telescope (Nelson, Mast and Faber 1985). Keck project formally begun in 1984, and its full science operations began in 1993. The telescope was quite successful, and as a result, a second Keck telescope was built in 1996. The second telescope was built at 75m from the first to allow the two Keck telescopes to be used for interferometry as well as for individual observations. Each of the Keck has its own suite of scientific instruments and is equipped with an adaptive optics system. The success of the Keck telescopes led to the Gran Telescopio Canarias, (GTC) (Espinosa 1998), a 10-m telescope similar to Keck on La Palma in the Canary Islands. The Keck design has a hyperbolic primary mirror which leads to the

requirement of polishing the off-axis mirror segments. However, telescopes with a spherical primary mirror can also be designed with identical segments. But such telescopes have to contend with a large spherical aberration. An example of spherical primary mirror telescope design is the Hobby-Eberly Telescope (HET) (Barnes T. G. 2000), and the Southern African Large Telescope (SALT) (Gerhard and Buckley 2004) completed in 1997 and 2005 respectively. Following the success and challenges faced in building and operating these 8 to 10m class segmented mirror telescopes, astronomers are now heading towards the 20 to 40m class telescopes.

All the upcoming Extremly Large Telescopes such as Giant Magellan Telescope (GMT), Thirty Meter Telescope (TMT) and European Extremely Large Telescope (E-ELT) will have a segmented primary. Extremely large segmented mirrors intended to be used in these mega telescopes bring new challenges to the telescope design and control problem. In order to achieve very high spatial resolution as well as sensitivity equivalent to a single monolithic mirror, all the mirror segments must be precisely positioned. Once mirror segments are aligned and phased by making use of an Alignment and Phasing System (APS), any subsequent deformations in the shape of the Primary Mirror (M1) due to gravity, thermal changes, and wind-induced disturbances are taken care of by the Primary Mirror Control System (M1CS). The M1CS performs this task with the help of three position actuators combined with six edge sensors per segment working at few nanometre scales. Three actuators per segment provide the essential tip, tilt, and piston to the segment. All the actuators receive a command from the global control loop and generate the required displacement for maintaining the position of mirror segments against the external disturbances. The performance of the segmented mirror telescope very much depends on the performance of the actuators combined with the edge sensors.

Table 1-1 Comparison of different components and parameters of existing and upcoming SMTs.

Segmented Mirror Telescope	Telescope Size (m)	Segment size (m) [*]	No. of Segments [†]	Actuators (per segment) & Type	Edge Sensor (per segment)	Segment Weight (Kg) [‡]	M1CS Controller Technology	Year of Completion
Keck I & II	10	1.8	36	3, (Hard actuator)	6, Capacitive	400	Customized hardware	1993, 1996
HET	9.2	1.15	91	3, (Hard actuator)	6, Capacitive	100	Distributed controller	1997
SALT	9.2	1.15	91	3, (Hard actuator)	6, Capacitive / Inductive	100	VME SBC	2005
GTC	10.4	1.9	36	3, (Hydraulic, Hard) ; 6, (Moment)	6, Capacitive	470	CAN bus	2007
LAMOST	4.9, 3.6	1.1	37 + 24	3	--	--	DSP56F807, CAN	2008
JWST	6.5	1.3	18	7, (Hard) (Hexapod)	NA	20	BALL Aerospace (Cryogenic electronic)	est. 2020
LOT	12m	1.44	84	3	6	--	--	est. 2025
GMT	24.5	8.4	7, Circular	165 Pneumatic (Hard)	2, Interferom-etric	16, 200	--	est. 2024
TMT	30	1.44	492	3, (Soft)	6, Capacitive	200	TI C2000 (ARM+DSP) MCU	est. 2027
EELT	39	1.45	798	3, (Soft)	6, Inductive	245	NI PXI-FPGA	est. 2025
PSMT	1.5	0.6m	7	3, (Soft)	6, Inductive	45	PSoC 5lp, CAN bus	est. 2020
NLOT	10	1.44	61	3, (Soft)	6, Capacitive / Inductive	200	--	est. 2025 +

[*] Segment size measured corner to corner in case of hexagonal mirror.
[†] Segment are hexagonal in shape, except for GMT which has circular segments.
[‡] Segment weight with its support structure.

1.3 Control System in SMT

The segmentation of the primary mirror enables us to construct large telescopes but on the other hand, brings an increased level of control challenges. A typical SMT equipped with Adaptive Optics (AO) has several control loops working at different temporal and spatial frequencies are responsible for the final image quality. The architecture of different loops of SMT depends on the amplitude and the frequency range of different disturbances acting on it. Major disturbances include: (a) the gravitational deformation of the telescope, (b) the thermal expansion of the telescope structure, (c) the wind-induced deformation of the telescope, and (iv) the wavefront deformation due to atmospheric turbulence. (Angeli, Cho and Whorton 2003).

The relatively slower main axis loop (telescope mount control) ensures that the telescope is pointing toward the field of interest in the sky. Typically it involves two axes of rotation namely altitude and azimuth, both running in the closed loop tracking mode at predefined track rates. The fact that the primary mirror is segmented demands all the segments to be co-aligned and co-phased initially to act as a single mirror surface and further needs to be maintained in the presence of the different disturbance. The initial alignment is typically done using an Alignment and Phasing System (APS) and once done this loop is disconnected for few weeks until realignment of entire M1 is necessary. The role of maintaining the mirror shape is done by the global control system which continuously monitors the edge sensor readings (two edge sensors per inter-segment edge) and commands the actuators below each segment (three actuators per segment) to correct for any deviation of edge sensor readings compared to the reference. Further, relatively faster loop at the individual actuators (local controllers) makes sure that incoming set points from the global controller are maintained continuously by the actuator. This local closed loop controller is necessary to maintain the position of actuators to the desired set point, in the presence of wind & vibration disturbances.

Since the wavefront reaches the telescope after passing through the Earth's atmosphere, the wavefront is deformed due to the atmospheric turbulence. If left uncorrected, the effective image quality obtained is called the seeing limited performance. Whereas the corrected image quality obtained is called as the diffraction limited performance. A system called as Adaptive Optics (AO) is incorporated in the large telescope which corrects for image blurring aberrations induced by the wavefront propagating through Earth's atmosphere.
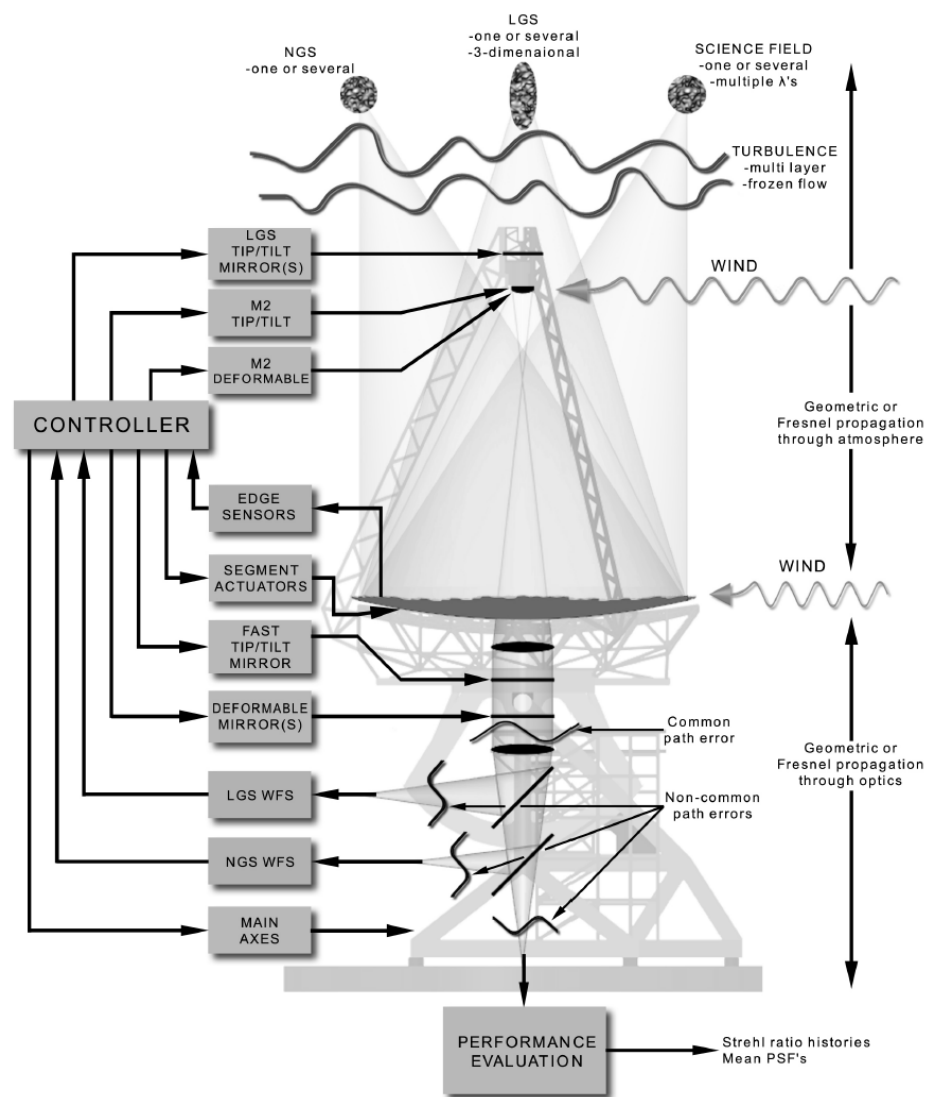
Figure 1-3 Control loops around the primary mirror responsible for the operation of the large Segmented Mirror Telescope. Different sensors and actuators working at different temporal and spatial frequencies influence to the final image quality. (Graphics adopted from (Angeli, Cho and Whorton 2003)).

As seen in Figure 1-3, AO can have two major groups of actuators: the deformable secondary mirror and the higher-order deformable mirrors. The corrections done by the deformable secondary mirror (including tip/tilt mirror) is capable of low order wavefront corrections. The high order deformable mirror down in the optical path can handle any residual optical path difference and misalignment due to control system as long as the correction amplitude is small enough and within its range of travel. The detailed description and operation of the AO system are beyond the scope of this thesis.

1.4   Primary Mirror Control System

The Primary Mirror Control System (M1CS) is responsible for making all the mirror segments behave like a monolithic mirror. The M1CS maintains the mirror shape in the presence of slow disturbances attributable to changing temperature, telescope elevation angle (gravity vector), as well as dynamic disturbances from wind and vibration sources. M1CS typically runs at 1Hz bandwidth. Different components of M1CS include Actuators, Edge sensors, Local controllers, and the Global Controller. The M1CS Network is also a major component, which is responsible for the communication between the Global controller and local controllers. The primary mirror position control system (Cohen, Mast and Nelson. 1994) uses a two-step process: 1) Initially, the desired readings of the edge sensors are determined by external optical means called alignment and phasing system. 2) Then, after the mirror is stabilized against gravity and thermal effects by moving the actuators to maintain the sensor readings at their desired values.

A schematic view of Primary Mirror Control System components is given in the Figure 1-4. Edge sensor continuously monitors relative intersegment displacements and send it to the global controller. The global controller uses a predetermined control matrix to compute required actuator displacements to correct the shape of the disturbed primary mirror. The newly computed actuator position (setPoint) commands are sent over the network by the global controller to the actuator local controllers and local controllers follow these setPoint commands.
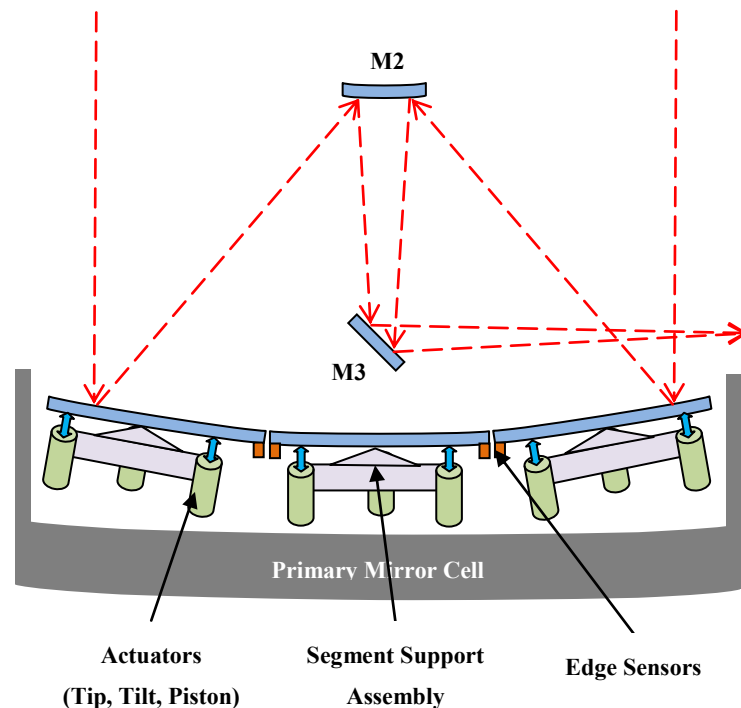
Figure 1-4. A schematic view of Primary Mirror Control System components – Actuators, Edge Sensors, and the segment support assembly. The Edge sensors measure any relative displacement of mirror segments, and actuators correct it to maintain the shape of M1 at a global scale (Deshmukh, Parihar and Mishra, et al. 2016).

1.5   National Large Optical Telescope (NLOT) project

During 1980s, the largest optical telescope in India was 2.34m Vainu Bappu Telescope and the gap between the optical telescopes used by Indian astronomers compared to that available elsewhere in the world was not much (about two times). Subsequently world moved to 8-10 size telescopes, whereas, Indian astronomers have to depend on 2 m class telescopes in all these years. Now when giant telescope of 20-40m size are going to be reality, then most of Indian astronomers will have access to currently largest telescope of 3.6m Devesthal Optical Telescope at Nainital, Uttrakahnd. It's true that being partner to the TMT project, Indian astronomical community will have access to one of the world best and largest telescope, however, there would be huge gap between 3.6m and 30m. The gap can be filled by either

buying nights in some of existing 8-10m size telescopes or having Indian own telescope of this size.
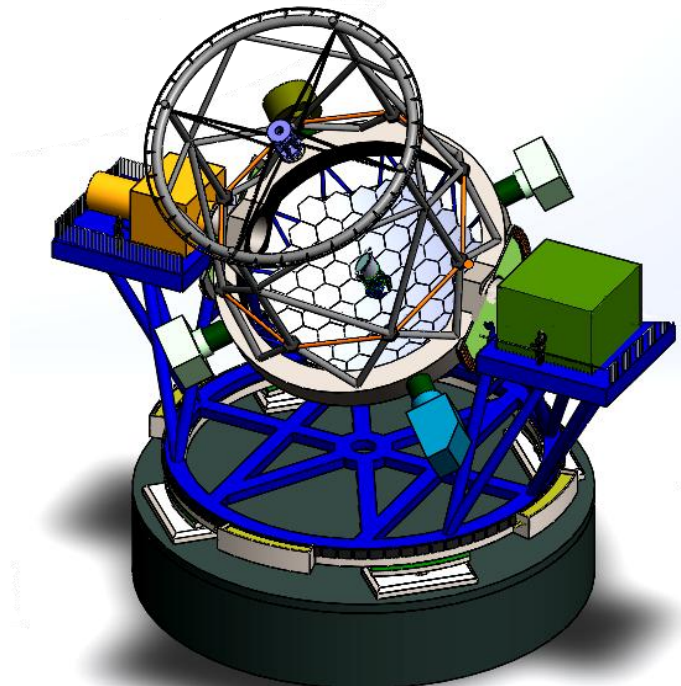
Figure 1-5. A conceptual view of the National Large Optical Telescope (NLOT). NLOT will be is a segment telescope with a primary mirror of 10m in diameter.

In year 2007 a group of astronomers from IIA, initiated a project to install a modern, state-of-the-art 8-10m class telescope working in optical and NIR regions in India. However, setting up 8-10 meter size telescope requires huge amount of investment and the manpower, therefore, a thorough understanding and characterization of the intended sites are necessary. So it was decided to undertake, a detailed site survey program to characterize the Hanle site where current 2m telescope is installed as well few more potential sites within few km from it. Initially this project was named Indian Large Optical Telescope (ILOT) project, which later renamed to National Large Optical Telescope (NLOT) project. At the same time, India proposed to join the 30m TMT project, with an aim to give an impetus to Indian astronomers to be able to participate in forefront research areas. After joining TMT project in 2010 and stream lining TMT related works for a couple of years, the focus was again brought back to NLOT from 2015 and a new working group was formed to prepare a detailed project report for NLOT as well as to carry out a pilot study on

segmented mirror telescope technology. A large telescope based on segmented mirror telescope cannot be simply acquired from any commercial telescope manufacture and it is usually a joint work of scientific research institution and large number of private industries. With an objective to develop the technology required to build a large segmented mirror telescope, several R&D activities have been initiated at Indian Institute of Astrophysics (IIA), Bangalore India. The key technologies which need to be addressed are linked with handling mirror segments. More specifically to have mastery in the control of the segmented primary mirror, so that one will not be going through same problematic phase experienced by several groups who have developed large segmented mirror telescopes like HET (Palunas 2006) and SALT (Gajjar 2006). Therefore, before embarking on such a large and expensive segmented mirror telescope project, it was decided to understand complexities of the segmented mirror technology by laboratory experimentation as well as by making a full-fledged prototype telescope of nearly 1.5m aperture Prototype Segmented Mirror Telescope (PSMT).

1.6 Prototype Segmented Mirror Telescope (PSMT) project

The PSMT will have all kind of subsystems which one can expect in any large telescope made of segmented mirrors. In order to reduce the cost of the prototype various measures have been undertaken and one of them is to make use of spherical optics rather than aspheroid parabola/hyperbola. The proposed prototype telescope will use seven hexagonal mirrors, which will be supported by simple mirror support assembly and driven by indigenously developed voice coil based actuators. We also plan to make use of in-house developed inexpensive inductive edge sensor, which can precisely sense inter-segment relative displacement. The telescope mount is suppose to be Alt-Az and secondary will be supported by trusses made of steel. The primary axes like elevation, azimuth and field de-rotator will be driven by direct drive motors. Though the main objective of this telescope is to understand and demonstrate the segmented mirror technology, however, we have designed the telescope in such way

that it can also be used to few dedicated science cases. The telescope is planned to be installed at Hanle, Ladakh, India which is a potential site for the countries large telescope project. The entire development activities are divided into two phases. In the first phase a seven segments laboratory test bed will be developed. Whereas, in the second phase the full-fledged telescope will be realized. Design and development of various subsystems required for the PSMT telescope is already in progress (Parihar 2018). This prototyping effort is one step toward realizing a large telescope in India.

Figure 1-6. A conceptual view of the Prototype Segmented Mirror Telescope (PSMT). PSMT is a seven segment telescope with a primary mirror of 1.5m in diameter.

1.6.1 PSMT for the Technology Demonstration

Few primary objectives behind developing PSMT for the technology demonstration are outlined below:

1. The performance of segmented primary mirror will only match to an equivalent monolithic primary mirror when all mirror segments are aligned

and phased using a customized alignment and phasing system (APS). Phasing the mirror segment with a few tens of nm accuracy is a challenge and PSMT would be truly a test for the APS. Once primary mirror segments are aligned by making use APS and precision actuators, then keeping them aligned over long span of time (about a month) with help of edge sensor, actuator and mirror control is most critical task. One need to ensure that alignment stay during change of gravity and any other environmental parameters such as temperature and humidity.

2. Another objective behind developing the PSMT is to understand effect of wind and other disturbances on primary mirror control.

3. The effort is being made to indigenously develop edge sensor, actuator, a complex segment support, etc. The PSMT will serve as a best test bed for all these critical components.

1.6.2 PSMT for the Science Observations

The effective diameter of the PSMT is about 1.5m, which makes PSMT a decent size telescope. A telescope of this size can be very effectively used in photometric and spectroscopic monitoring program, provided it delivers a good image quality. In narrow field mode PSMT is designed to provide sub-arc second image quality over about an arc-minutes FoV, which can be best suited for photometric study of individual variables and transient point source. Narrow field can also facilitate spectroscopic monitoring using fiber fed mid/high resolution spectrograph. In wide field mode, image quality is expected to match the local seeing and provide 10 arc-minute FoV, best suited for photometric monitoring program.

Instead of making the PSMT as a general observing, facility, it will be used for very few specific science cases.

1.7   Scope of the Thesis

The broad objective of this thesis work is to develop a technology required to control a primary mirror of the segmented mirror telescope. Primarily the focus is on the development of Local and Global control systems for the PSMT primary mirror. The project has evolved through various stages and below we provide a brief description of the tasks carried out within the scope of this thesis. The local control system of the SMT consists of an Actuator and local control electronics, which receives set-points from the global controller. Whereas, the global control system is responsible for maintaining the shape of the primary mirror in the presence of different disturbances.

1.7.1 Local Control System

Every mirror segment of the primary mirror needs to be precisely aligned so that, altogether they will act as a single large mirror. Mirror segments are supported by three actuators which allow to tip, tilt, and piston to the individual mirror segment. The actuators used in SMT's are of very high precision (few nanometres) linear actuators with a large stroke. They should also have the ability to suppress broad frequency range disturbances arising due to wind and structure vibrations. For the PSMT, we explored various possibilities including buying off-the-shelf components, however, finally we decided to develop our soft actuator, which is not only lesser in cost but also simple in manufacturing. This actuator design led to the indigenous development of subcomponents named Voice Coil Motor (VCM) and Disc Flexures. We have also developed a customized controller and drive electronics for the PSMT actuator. Further to test the performance of the actuator in the presence of dynamical disturbances (due to wind and gravity), a novel test instrument named Dynamic Loading Assembly (DLA) was developed. The PSMT actuator has gone through a rigorous performance test and found to meet most of the design requirements.

1.7.2 Global Control System

Once the mirror segments of the primary mirror get aligned and phased (correction for inter-segment piston error) then after it is a responsibility of the primary mirror control to maintain the shape of the primary mirror over the weeks and months. The edge sensors detect any changes in the mirror segment position due to varying gravity and/or temperature and subsequently get corrected by the actuators with the help of a global controller. The global controller which forms an outermost closed loop works at a relatively slower rate. To explore the Primary Mirror Control System in more detail way, we have developed a software tool called as the codeSMT. The codeSMT is fairly generic in the sense that it can be used for any size telescope made of one or more rings as well having a different sensor-actuator geometrical configuration. The tool is also capable of carrying out error analysis, more specifically it allows to study the effect of sensor noise on various modes of the primary mirror. Another notable feature of this analysis tool is that it can incorporate the dynamic behaviour of the actuators in the presence of wind disturbances, which helps to evaluate telescope performance. Finally, we have implemented the global controller developed for the PSMT in the real hardware and tested its functioning.
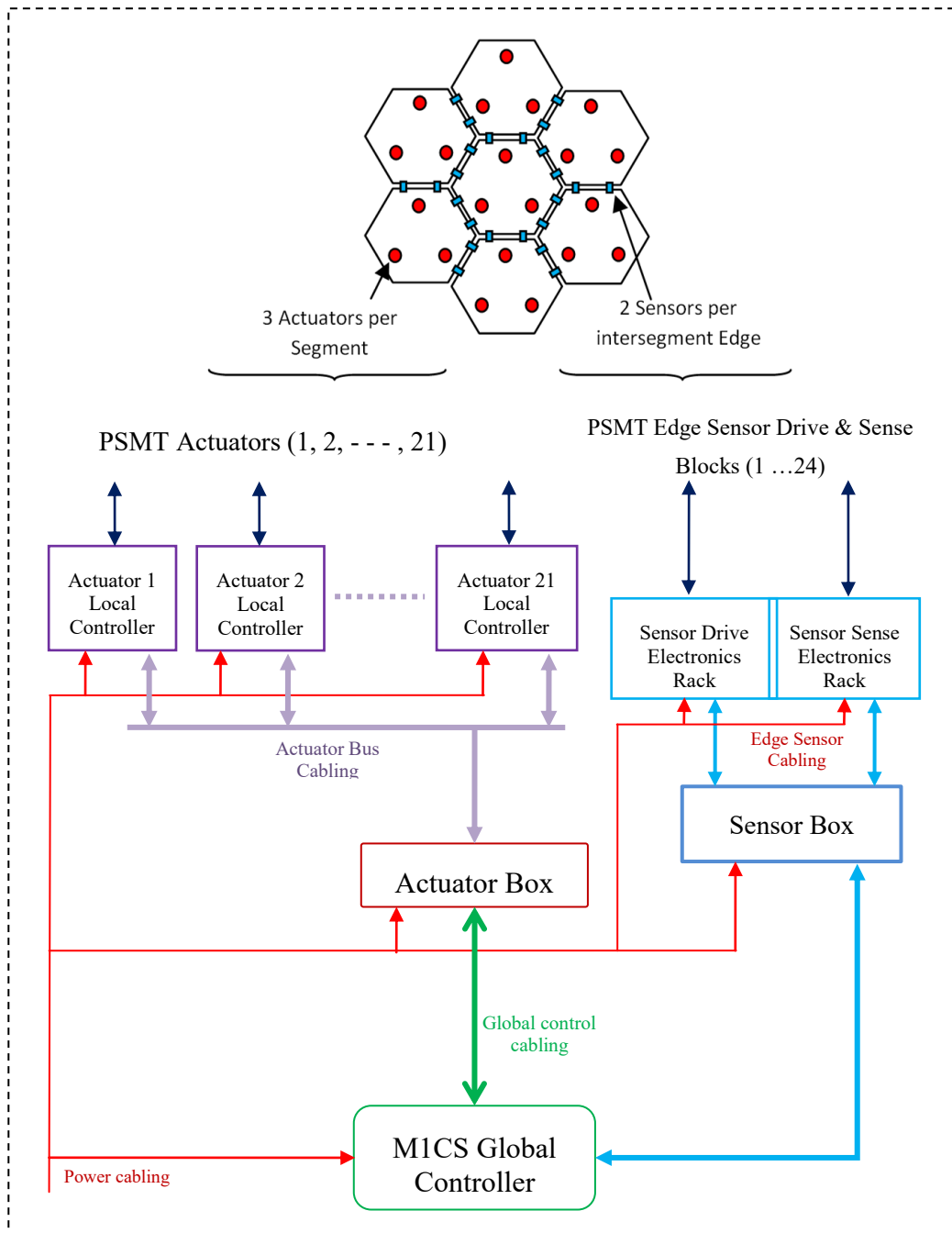
Figure 1-7. The Primary Mirror Control System concept design for the Prototype Segmented Mirror Telescope (PSMT).

1.8 The Contributions to Technology

The major contributions of this thesis are enlisted below. Each of the following points is described in details in the subsequent sections of this thesis.

i. A novel design of a soft actuator for the PSMT. This led to two innovative technology developments namely VCM and Disc Flexures which are successfully implemented in a prototype soft actuator. This also helped in reducing the overall cost of the actuator.

ii. First of its kind Dynamic Loading Assembly - DLA for dynamics testing of SMT actuators.

iii. Accurate wind model for the IAO Hanle site and it is used in the active control simulation of the PSMT.

iv. First of its kind SMT simulator tool (the codeSMT) with few integrated modeling capabilities. (Since this tool is generic, it can be used for most of the existing and upcoming SMTs).

v. Implementation of the entire local and global control system for the PSMT. (M1CS Networked Control System Testbed that includes prototype actuator, local and global controllers with the necessary software and hardware).

Figure 1-8. The India TMT Coordination Center (ITCC) Laboratory at IIA, Bangalore where this thesis research work was carried out.

1.9   Outline of the Thesis

The Chapter 1 provides a brief introduction of the segmented mirror telescopes, as well as importance and complexities associated with various control loops linked to the primary mirror.

The segment support actuator developed for the Prototype Segmented mirror telescope is presented in Chapter 2. Whereas, the effort made to develop a customized actuator controller which forms local controller loop is presented in the Chapter 3. The PSMT Actuator and Controller developed are tested for its performance. Some of the performance related test results linked with PSMT actuator is also given in the Chapter 3. Further to conduct tests under dynamically varying disturbances like wind and vibration, a novel device called the Dynamic Loading Assembly has been developed and its design, development and validation results are presented in Chapter 4. The performance test of the DLA itself and dynamic tests of PSMT actuator, conducted using DLA are also presented in the Chapter 4.

Chapter 5 provides details of mathematics and algorithm required for the global controller used in the SMT's. . The chapter also describes our effort to create a generic M1CS simulation tool called as the codeSMT. Further, two test case studies conducted using the codeSMT are presented in Chapter 6. This includes the Active Control Simulation of the PSMT in Section 6.1 and the Error Multiplier study of PSMT in Section 6.2. Finally, in the Chapter 7, the hardware implementation of M1CS for PSMT is presented along with elaborate description of different modes of operations and the algorithm used.

The last Chapter 8 of the thesis is conclusions and future works. The addiitoal relevent material have been given in the apendix.

Chapter 2   Actuator for PSMT

2.1 Introduction

The actuators used in the Segmented Mirror Telescope are responsible for providing the tip, tilt, and piston to the individual mirror segments. Such actuators can be classified into two broad categories: hard/rigid actuator and the soft actuator. The actuators used in existing segmented mirror telescope such as W. M. Keck Observatory (Keck) (Meng, et al. 1990), Southern African Large Telescope (SALT) (Swiegers and Hitesh 2004), Gran Telescopio Canarias (GTC) (Lefort and Castro 2008), Large Sky Area Multi-Object Fibre Spectroscopic Telescope (LAMOST) (Xu, Xu and Jin 2003), and Hobby–Eberly Telescope (HET) (Krabbendam, et al. 1998) , are hard/rigid actuators and have extremely high axial stiffness. One of the main drawbacks of a hard actuator is, it supports very low control bandwidth, which results in poor active dynamic interactions between the actuator and the mirror segment and hence cannot suppress high frequency disturbances induced by wind and other structural vibrations. Whereas, the soft actuators proposed for upcoming SMTs like the Thirty Meter Telescope (TMT) (Lorell, Aubrun, et al. 2006), (J. Nelson 2005) and the European Extremely Large Telescope (E-ELT) (Jiménez, et al. 2010) uses a Voice Coil Motor (VCM) that gives high bandwidth actuation. The soft-actuator is fairly straightforward to implement, relatively inexpensive, lightweight and compact. It has very few moving parts, capable of producing large forces, can provide large mechanical range, and does not require lubrication.
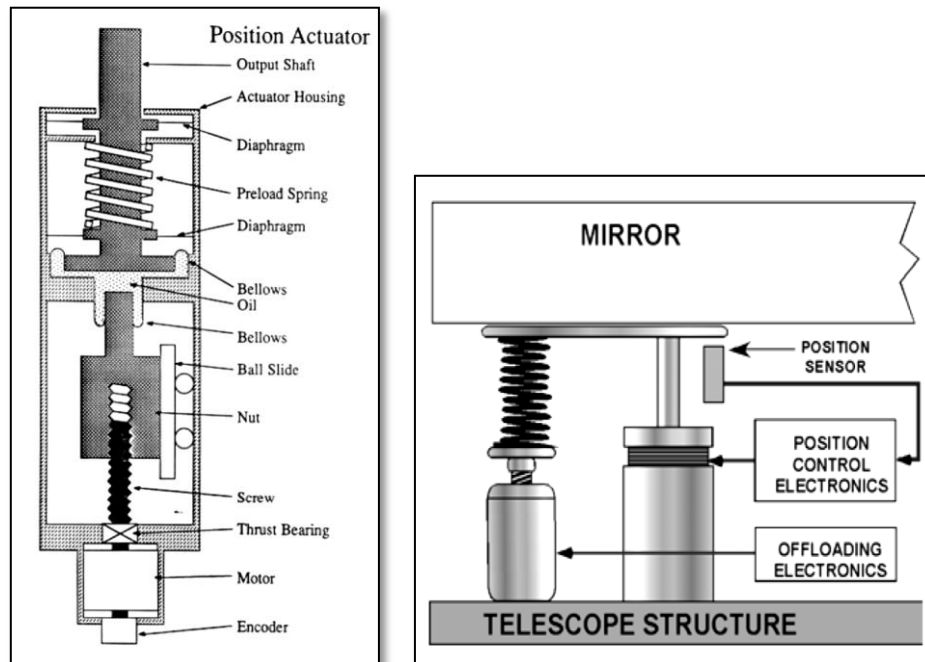
Figure 2-1. Schematic of Hard actuator of the KECK (left) and Soft actuator of the TMT (right). (Graphics adopted from (D. G. MacMartin 2003) and (Lorell, Aubrun, et al. 2006)).

Among upcoming SMTs, the TMT actuator (Lorell, Aubrun, et al. 2006) is an off-axis mechanism with VCM as its prime mover and an offloader for taking care of static loads. The VCM and stepper motor based offloading mechanism are linked to the actuator output shaft through the lever arm, hence providing amplification in the force as well as in displacement. In the TMT actuator, for effective rejection of high-frequency disturbances, a passive eddy current based damper which uses two powerful magnets and a copper plate have been incorporated. The local control loop runs at a very faster rate uses a very high-resolution optical encoder directly coupled with the output shaft of the actuator. The E-ELT actuator (Jiménez, et al. 2010) on the other hand is an on-axis, direct acting actuator with a two-stage control scheme - course and fine. The fine stage is moved with the help of VCM, and a high-resolution encoder whereas course stage is similar to the offloader in TMT actuator but uses the brushless DC motor and relatively low-resolution encoder. Both TMT and E-ELT actuators use flexural elements for vibration isolation and reducing the wear and tear due to friction. One of the major differences between these two actuators is the

absence of passive damper in the E-ELT actuator. For the PSMT, likewise, any other existing SMT's we had a choice of using commercially available rigid actuators, however, we decided to go with soft segment actuator, primarily to reduce the cost as well as to explore high bandwidth disturbance rejection capability of the soft actuator in the real telescope. Since the size of our mirror segment is only 60cm, so we cannot use the TMT actuator, which is being produced in India. Therefore we decided to come up with our own soft actuator which uses the same design philosophy like TMT and E-ELT but very different in implementation. The key features of the PSMT actuator are it uses VCM, gravity offloading through spring and lead screw, on axis mechanism, compact, and lightweight, low cost, and ease of operation.

2.2 PSMT Actuator Requirements

A detailed actuator design requirement has been generated by considering the operational requirement of the telescope combined with the outcome of optomechanical design and analysis works. Table 2-1 provides a summary of design requirements considered for PSMT actuator. The challenging part of the design is that it should act as a precision force as well as position actuator. For small telescope structure like ours, structural deformation due to gravity and temperature is expected to be negligible, and hence actuator primarily works as a force actuator. Whereas during alignment and phasing, the accurate position of mirror segments with few tens of nanometer accuracy is required, and that time it should act like a nanopositioner. It is essential for an actuator to dissipate lower power to avoid effects on the telescopic seeing, and hence the offloading mechanism is required in case of the soft actuator. For PSMT, we have considered baseline offloader to be a discrete offloading mechanism (see Figure 2-10). The damping in the actuator is provided through the voltage driven VCM, whereas the passive damping option is kept as an option for the future.

Table 2-1 The PSMT actuator design requirement table.

Requirement		Value	Unit
Stroke		±1.5	mm
Positioning Accuracy		25	nm
Command rate		100	Hz
Track Rate	(position)	350	nm/sec
	(force)	7	mN/sec
Tracking Error		<25	nm
Continuous Tracking Time		>3600	Sec
Slew Rate	(position)	77.5	μm/sec
	(force)	1.55	N/sec
Dynamic Force	(continuous)	23	N
	(wind)	0.5	N
Axial Stiffness		20, 000	N/m
Avg. Power		1.5	Watt
Dimensions		12 x 35	cm x cm
Axial Load		140	N
Inertial Load		14	Kg
Lifetime		10	Years
Weight		< 6	Kg

2.3 Modeling and Simulation

In the design phase, we have developed a simple Spring-Mass-Damper based model of PSMT actuator. The basic block diagram can be seen in Figure 2-2, where a mass is resting on a sufficiently high stiffness spring, and the VCM is exerting a parallel force on the mass. The position of the actuator is determined by the position sensor, whereas the actuator force is decided by current flowing through the VCM. We have derived the first principle based VCM model and then combined it with the spring-mass model to get the final actuator transfer function. Since VCM can be controlled by either voltage mode or current mode, therefore, we explored both modes and found a voltage-driven-without-damper mode to be suitable (this mode also provides some amount of damping due to the back emf (Eq. 2.10) produced in the

VCM). The Voltage/Current driven with damper mode of operations are also feasible, but with the additional complexity of the damping mechanism (we may consider this option in the next phase of prototyping). Therefore, the present baseline design of the actuator is the voltage driven VCM without a damper.
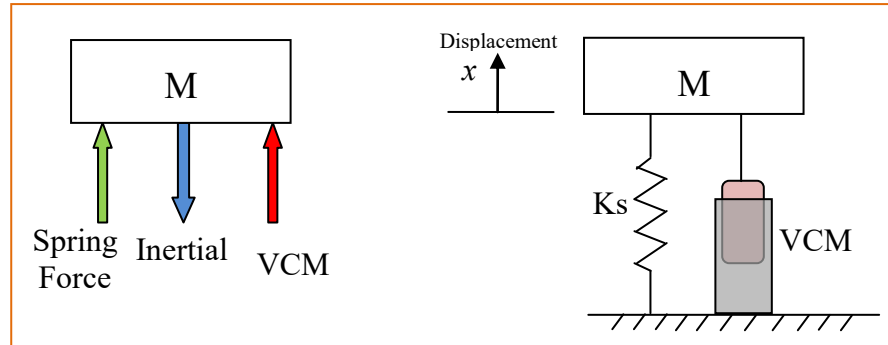
Figure 2-2. Spring mass model of PSMT actuator. The 'x' is the output displacement of the actuator. Spring and VCM are connected to the mass M on the one side and the rigid base on another side.

Since the actuator is a linear device, therefore it has a single degree of freedom i.e. displacement, which is indicated by the symbol 'x' (Note that the lateral degree of freedom is not a part of this modeling procedure, and is restricted by using the disc flexure in the actuator. Details of the disc flexure are in the Section 2.4.3). The VCM force is indicated by Fv whereas spring constant is denoted as Ks. Other parameters used in this analysis along with their values are given in the Table 2-2.

Table 2-2 Design parameter table for modeling of PSMT Actuator

Parameter	Description	Values	Unit
M	Total Moving Mass per Actuator [Mirror + Segment Support Assembly (SSA) + Act. moving mass + Sensor]	12 (with margin = 14)	Kg
	Mirror mass (1)	21	Kg
	SSA mass (1)	15	Kg
	Edge sensors mass (12)	2	Kg
	Act. moving mass (3)	2	Kg
	Extra margin	2	Kg
K_s	Spring constant	20	N/mm
K_v	Force constant of VCM	13	N/A

K_b	Back emf constant	13	V sec/m
R	Resistance of voice coil	3.25	ohm
L	Inductance of voice coil	5.27	mH
$d \times h$	Diameter x Height	7.7 x 6	cm

Let, the input to the actuator system is the force from VCM, i.e., F_v which is a function of time $F_v(t)$, and the output displacement x is a function of time $x(t)$. We consider x being positive in an upward direction. Also, here the input force in the upward direction is assisted by the compressed spring and is opposed by the inertial force due to mass M.

Therefore,

Spring force: $F_s = K_s\, x$ Equation 2-1

Inertial force: $F_i = M\, \ddot{x}$ Equation 2-2

VCM force : $\quad F_v = K_v\, i$ Equation 2-3

where,
F_v = force exerted by the vcm on mass; F_i = inertial force;
M = mirror mass + actuator components mass; K_s = spring constant;
x = displacement of mass M due to force F; K_v = voice coil constant ;
$i = VCM\,current$

According to the principle of equilibrium of forces, the sum of all the forces on the body must be equal to zero.

$\therefore\ F_v - F_s - F_i = 0$ Equation 2-4

In time domain : $\qquad F_v(t) = F_i(t) + F_s(t)$ Equation 2-5

In frequency domain : $F_v(s) = Ms^2 x + K_s x$ Equation 2-6

$\therefore\ x(s) = \dfrac{F_v(1/M)}{s^2 + (K_s/M)}$ Equation 2-7

Using Equation (2.3) in Equation (2.7):

$$x(s) = \frac{K_v \, i(s) \, (1/M)}{s^2 + (K_s / M)}$$

$$\therefore \quad \frac{x(s)}{i(s)} = \frac{K_v \, (1/M)}{s^2 + (K_s / M)} \qquad\qquad\qquad \text{Equation 2-8}$$

Applying Kirchhoffs Voltage Law (KVL) to the electrical equivalent circuit of VCM and taking Laplace transformation we get:

$$E(s) = (R + Ls)i(s) + E_b \qquad\qquad\qquad \text{Equation 2-9}$$

Where,

$$E_b = \text{backemf} = K_b \, s \, x(s) \qquad\qquad\qquad \text{Equation 2-10}$$

$E(s) =$ voltage applied to vcm

$K_b =$ back emf constant

$R =$ resistance of VCM

$L =$ inductance of VCM

Electrical equivalent circuit of VCM
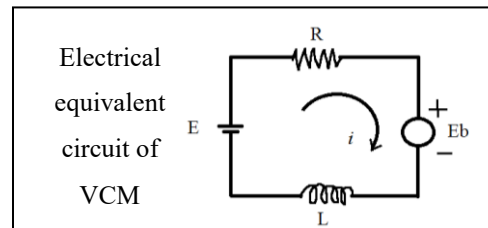
Using Equation (2.3), (2.6) & (2.10) in (2.9):

$$E(s) = (R + Ls)\left(\frac{Ms^2 + K_s}{K_v}\right)x(s) + K_b \, s \, x(s) \qquad\qquad \text{Equation 2-11}$$

If we consider the displacement of mass M as output and voltage applied to VCM as input, then the transfer function of the system can be written as (from Equation 2.11):

$$\frac{x(s)}{E(s)} = \frac{K_v}{LM\,s^3 + RM\,s^2 + (LK_s + K_b K_v)s + RK_s} \qquad \ldots m/V \qquad \text{Equation 2-12}$$

This is the transfer function of our actuator when its VCM is driven by voltage input $E(s)$ which results in the displacement $x(s)$. The unit of this transfer function is

m/V. In order to get the transfer function in the units of *m/m,* we need to multiply with the mapping constant (force to displacement) to the numerator of Equation 2.12.

The transfer function of the PSMT actuator using the parameters from Table 2-2 in Equation 2.12:

$$\therefore \frac{x(s)}{E(s)} = \frac{13}{0.07385s^3 + 45.5s^2 + 274.5\,s + 65000} \qquad \dots m/V \qquad \text{Equation 2-13}$$

Using Equation 2.13, we evaluated the open loop and the closed loop time and frequency responses in MATLAB. Following are the results obtained. For the closed loop response, the PID gains are obtained by two methods- based on robustness criteria and based on Matlab PID auto-tuning toolbox. For robustness (K. J. Åström 2002), the reasonable values of the phase margin $\phi_m = 30^\circ - 60^\circ$ and of the gain margin $g_m = 2 - 5$. The Stability and robustness to the process uncertainties can be expressed in terms of the loop transfer function given by:

$$L_{TF} = P \times C; \qquad where, P = plant, C = controller \qquad \text{Equation 2-14}$$

The phase margin is obtained from the lowest frequency where the loop transfer function L_{TF} has unit magnitude. The comparison of open loop and closed loop characteristics along with closed loop parameters are listed in Table 2-3:
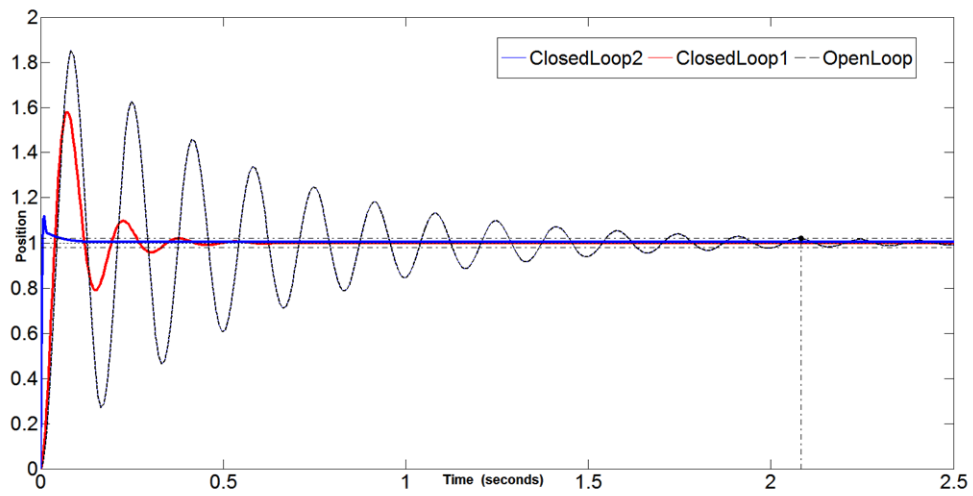
Figure 2-3. Open-loop and closed-loop step response of the PSMT actuator model. In open loop, the response is underdamped and slower, whereas it gets faster in the closed loop mode.

(a)

(b)
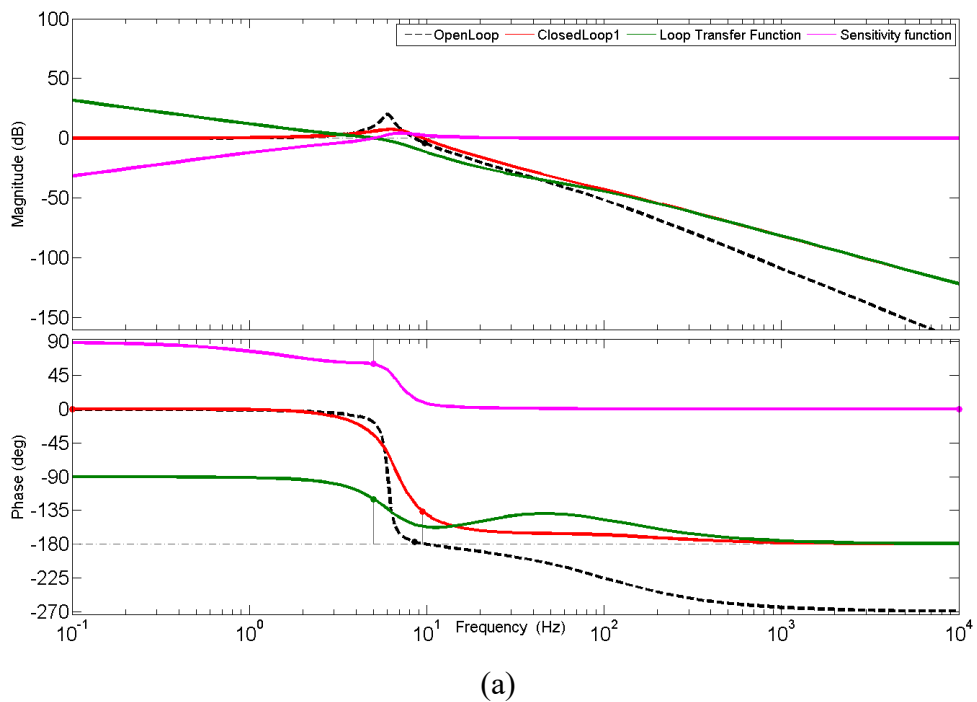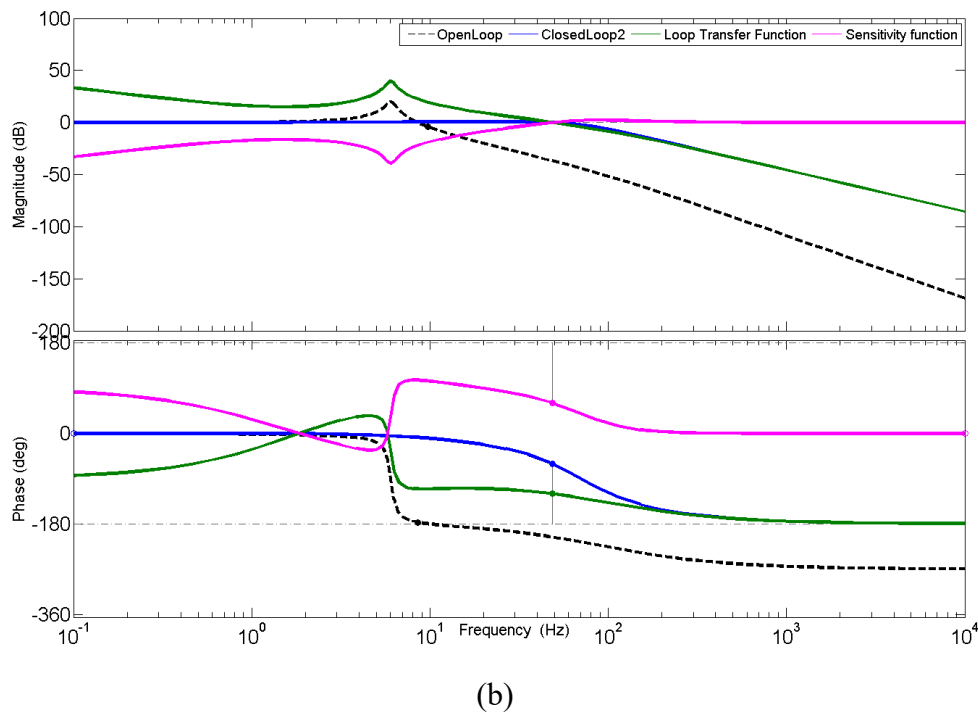
Figure 2-4. The frequency plot of open loop and closed loop response of PSMT actuator model. Plots also consist of the loop transfer function and the sensitivity functions. The top (a) and bottom (b) plots correspond to the two different closed loop responses.

Table 2-3. Comparison of open loop and closed loop characteristics.

Parameter	Open loop	Closed loop-1 (Robustness criteria)	Closed loop-2 (Matlab auto-tuning)
Kp	-	0.593	5.17
Ki	-	24.30	28.51
Kd	-	0.004	0.234
Rise Time (sec)	0.029	0.026	0.004
Settling Time	2.083	0.330	0.058
Overshoot	85.34	58.08	12.03
Peak Time	0.083	0.073	0.009
Phase Margin	--	60deg @ 5Hz	60deg @ 48.7Hz

It can be seen that closed loop-1 is more robust than the closed loop-2, whereas both the control gains give a stable performance. Controller-2 has a better sensitivity performance over the broader frequency range, but with the drawback of resonant mode

excitation as seen in Figure 2-4. The controller-2 response is also better in terms of rise time, settling time and peak overshoot characteristics. This indicates that the PSMT actuator in the closed loop can give a stable response and is controllable when used with a properly tuned controller. Further, we have also developed the dynamic model of the Actuator based on the first principle approach and represented it as a state space model. This enabled us to develop a MIMO model of the actuator, so as to include the Wind disturbance force as one of the inputs along with the position/voltage command to the actuator. The details of the dynamic model are not within the scope of this Chapter and are presented later in Section 6.1.2.1 of Chapter 6.

2.4 Mechanical Design

The details of the mechanical design of the PSMT actuator are presented in this section. A 3D model, as well as one of the vertical cross-section of the actuator, is shown in Figure 2-5. The base part of the VCM which includes a magnet and an iron body rests on the offloading stage driven by a stepper motor coupled to the lead screw. The top part of the VCM, which includes coil, is directly coupled to the output shaft of the actuator through the spacers. The main helical spring whose one end sits on the offloader base also gets connected with the top part of the VCM. This arrangement provides a configuration where the main spring (driven by offloader) and the VCM both exert parallel forces on the actuator shaft. In one of the scenario when VCM coil is not at all energized at that time entire load of the mirror segment is born by off-loader. However, during actual operation, about 90 percent load is taken care of by off-loader, only about 10% is handled by the VCM and this way the power dissipation is minimized. Since the main spring has got very little lateral stiffness, therefore, to maintain the alignment of the VCM as well as to prevent any damage, a twin Disk Flexures Spring (DFS) have been incorporated into the upper part of the VCM and actuator output shaft. The DFS also support the spacers to isolate them from the rigid body of the actuator making it a soft actuator. Three mechanical hard stops placed on a plane at 120 degrees apart, prevent actuator moving out of the safe range of travel ($\pm$1.5mm). The hard stops also prevent any accidental overshoots, which can easily damage the disk flexure as well as the

VCM. A high-resolution optical position encoder from MicroE Systems has been installed at the output shaft, which gives the differential position of the actuator w.r.t. its rigid frame and is used to close the VCM position loop.
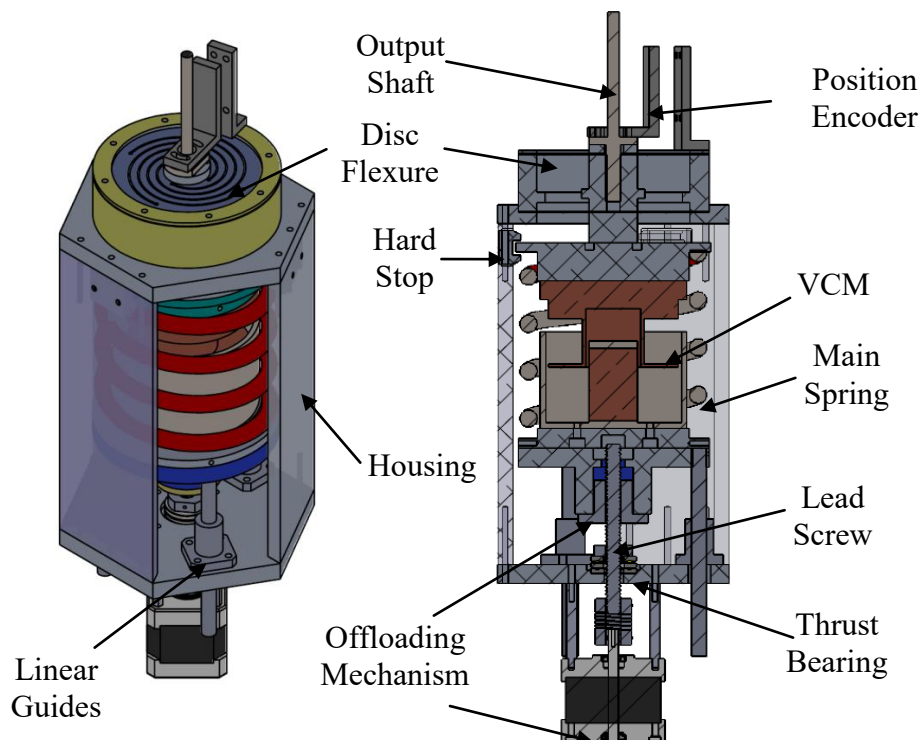
Figure 2-5. The PSMT actuator mechanical model and a cross-section view. The major components of this actuator are the VCM, the main spring, and the disc flexure spring.

The base of VCM and the main spring can be moved up / down by using an offload stage. This stage is supported by a linear guide mechanism to restrict the lateral displacement/rotation. It also helps in minimizing the static load taken by the VCM and transfers it to the main spring. The Offloader loop is activated based on the current flowing through the VCM or based on user command and minimizes the overall power consumption.

Following is the brief description of the major components developed and used in the actuator.

2.4.1 The Voice Coil Motor (VCM)

Since there is no domestic manufacturer of precision VCM, therefore to minimize the cost of PSMT actuator, we decided to design and develop the VCM needed to drive the actuator. In-house designed and developed VCM is shown in Figure 2-6. As a first step, the design and analysis of VCM were carried out using our analytical formulation and FEA tools (Meeker 2013) available to model electromagnetic devices. The magnet used here is of NdFeB grade N42 and with the cylindrical shape of dimension 25x38mm. The VCM outer diameter is 77mm, and the height is 90mm during operation. The outer stator is made of Mild Steel material, and the coil is made of 0.8mm Copper wire. The maximum design stroke of this VCM is 20mm, and maximum continuous force is 30N, whereas requirement is 2.5 mm and 23N respectively.
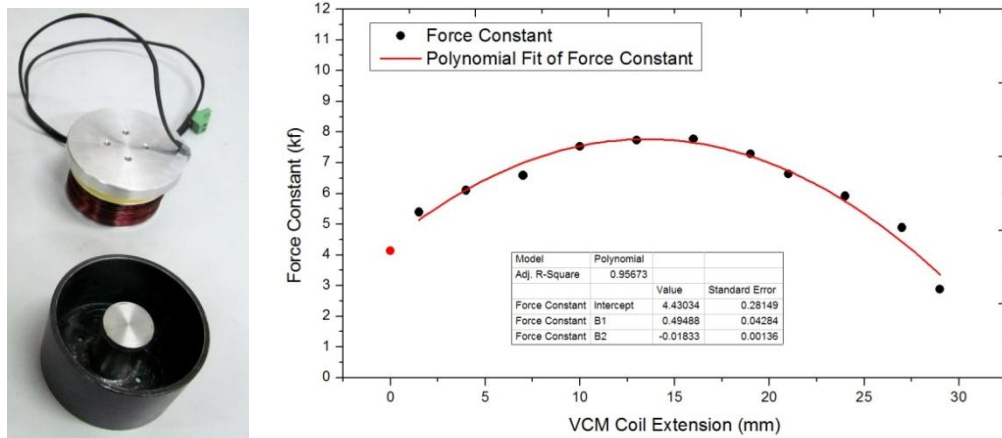
Figure 2-6. The VCM designed for the PSMT actuator and its calibration result. The force constant obtained from the calibration test is 6.9N/A at mid-range.

The VCM is calibrated on a custom built VCM test-bed (Figure 2-7) which comprises a translation stage equipped with a load cell. The VCM coil is displaced wrt its stator and the VCM Extension Vs. force is recorded at a constant input current of one ampere. The force constant obtained for the prototype VCM from the calibration test is 6.9N/A at mid-range.
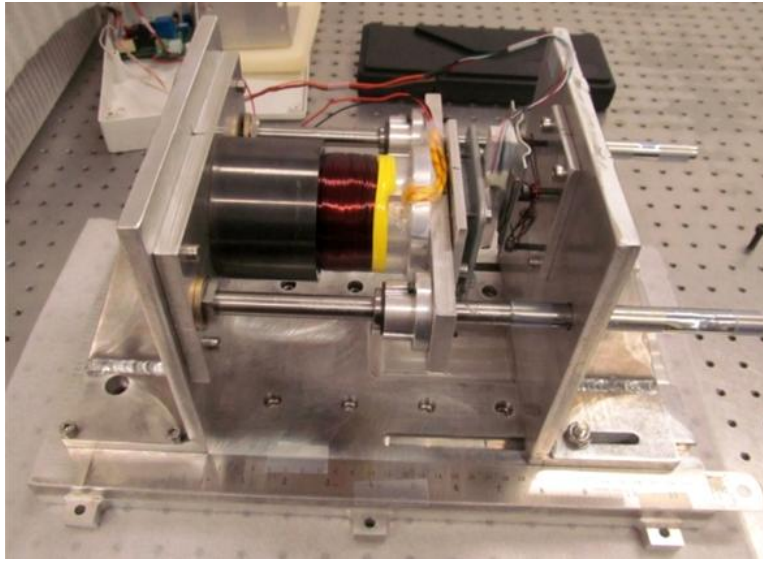
Figure 2-7. The prototype VCM and its calibration testbed designed and developed at IIA Bangalore.

2.4.2 Main Spring

The main spring takes the maximum load on the actuator. This spring along with the disc flexure is responsible for isolating the rigid frame of the actuator from its output shaft. The stiffness of this spring is around 22.6N/mm. The free length of spring is 100mm with 2 active turns and flat ends. This is also a custom design part with the material of spring steel and a wire diameter of 9mm.
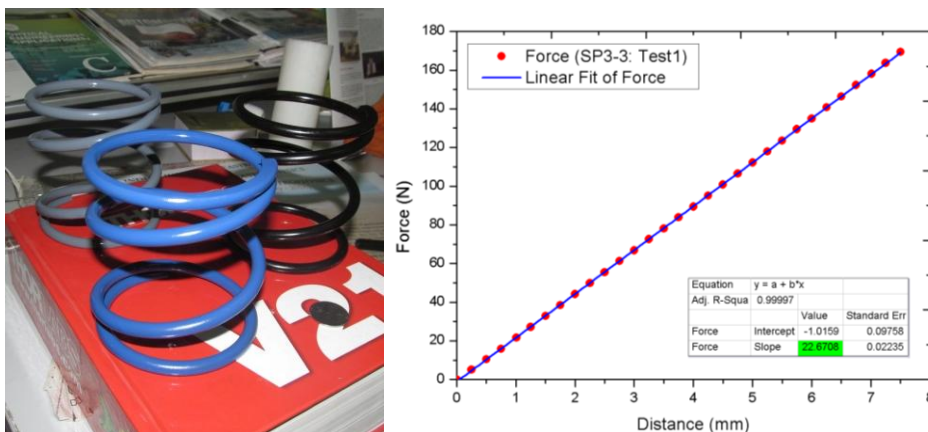
Figure 2-8. Fabricated main spring and calibration result. The stiffness obtained from the calibration test is 22.6N/mm and is linear over a wide range.

2.4.3 The Disc Flexure

The DFS support the output shaft of the actuator to isolate it from the rigid body of the actuator making it a soft actuator. The DFS designed for PSMT actuator is a Stainless Steel disc of 500um with four spiral cuts of 1mm width and specially designed with circular ends. This disc flexure has the axial stiffness of approximately 0.48 N/mm. The safe range of operation is around ±3.5 mm, whereas for the PSMT actuator we need a maximum range of ±1.5mm. The combination of two such discs separated by a spacer is used in the PSMT actuator. Before manufacturing, the disk flexure is design and modeled using FEM analysis tool available in Autodesk Inventor software.
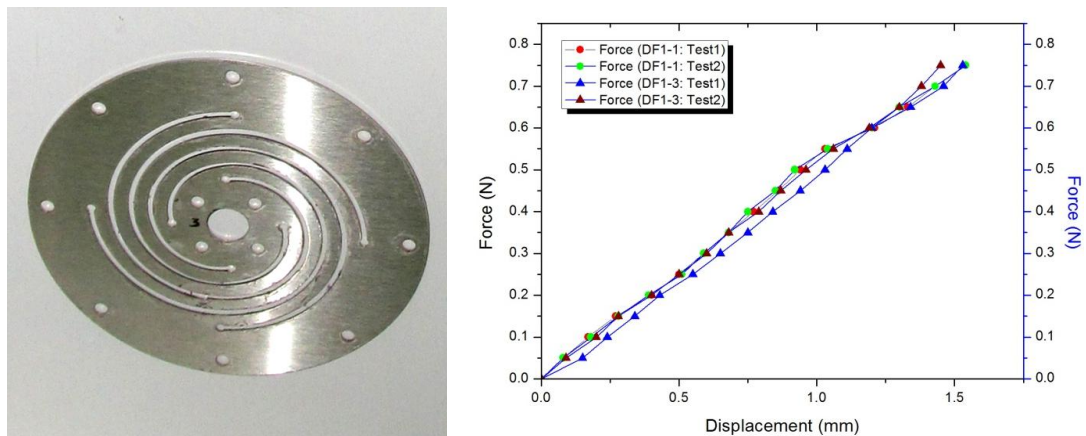
Figure 2-9. The Disc Flexure Spring fabricated for PSMT actuator and its calibration result. The average stiffness obtained from the calibration tests is 0.48N/mm.

2.4.4 The Offloader

The offloader used in PSMT actuator is a lead screw mechanism driven by a stepper motor. The cross-section view of the offloader is shown in Figure 2-10. The 8mm lead screw and a spring-loaded nut are connected to the stepper motor shaft through a flex coupler. The linear guides restrict the lateral displacement. A thrust bearing is also incorporated to transfer the load to the actuator body. Hence, the axial

load on the stepper motor is minimal. The offloader is designed to provide the displacement greater than 10mm and with the axial load capacity more than 140N

Lead screw & Nut

Thrust Bearing

Coupler

Stepper Motor
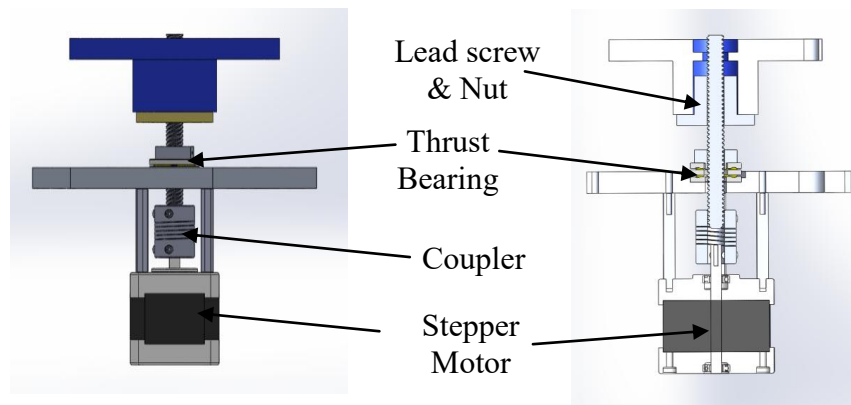
Figure 2-10. The offloader assembly and a cross section of the assembly.

2.5   Summary and Conclusion

The Prototype Segmented Mirror Telescope requires 21 actuators to control the shape of its primary mirror. In this project, we have developed the segment support actuator for the PSMT. First, we developed a parametric model of the actuator followed by conceptual mechanical design, fine-tuned to meet the requirements. The prototype actuator was fabricated, and then it went through the detailed testing and validation phase. The proposed actuators have its prime mover as a Voice Coil Motor (VCM) which takes care of the dynamic load on the actuator and generates required force to correct for disturbances. The Voice Coil Motor (VCM) is surrounded by a single spring of large diameter and large stiffness. A linear position encoder at the output shaft gives the absolute position of the actuator with respect to the rigid frame. The VCM combined with high-resolution linear position encoder provides very accurate positioning ability. The output shaft of the actuator is isolated from its rigid frame with the help of a Disc Flexure Spring (DFS), made of very thin metallic discs. This actuator also consists of an offloading mechanism which in turn offloads the static load on the VCM to reduce the overall power consumption. In our design,

almost all components required for the actuator are custom designed and built. However, we have put our best efforts to minimize the production cost and made it affordable for the PSMT, which is a relatively low budget project.

The development of Actuator led to the indigenous development of VCM and DFS. The design, fabrication, and calibration of VCM and DFS were done at ITCC Laboratory of IIA, Bangalore. The VCM and DSF are designed using numerical simulation and FEM analysis technique. Detailed control analysis has also been carried out to understand the performance of the actuator in different conditions, i.e., open loop, closed loop, with and without external disturbance, etc. Based on the results obtained from simulation and parametric sensitivity analysis, stable design parameters are obtained and used in the mechanical design. The actuator is designed to provide the output stroke of +/- 1.5mm and the track rate of >350nm/s (7mN/s) with tracking accuracy requirement better than 25nm. In addition to these, it is also expected to have high reliability and long life. This soft actuator is a compact, lightweight and very low-cost solution in comparison to TMT and EELT actuators, for the relatively small and low budget project like the PSMT. The main limitation of the PSMT actuator is high power consumption due to the on-axis mechanism in comparison to the off-axis counterpart. Also due to the on-axis mechanism, it needs larger VCM with high force constant.

Functionality and performance tests of this actuator are carried out using the actuator test station and the closed loop controller. The controller implemented is based on the incremental PID algorithm, in which PID gains are obtained from the relay tuning method. Actuator test results satisfy the PSMT actuator requirements. Details of the controller design and test results are presented in Chapter 3. The disturbance rejection tests are also conducted with the help of Dynamic Loading Assembly (DLA), which is capable of emulating the wind disturbance on SMT actuators. Details of DLA and disturbance rejection tests are presented in Chapter 4 of this thesis.

Chapter 3   Actuator Controller and Test Results

To control the PSMT soft actuator in a closed loop and to perform few other actuator calibration/testing related tasks, we have developed a precision actuator controller and the driver. The controller is implemented on a Programmable System on Chip (PSoC) 5LP based hardware. The controller is successfully implemented and tested with the prototype actuator developed for PSMT at IIA, Bangalore and results are satisfactory.

Here our primary focus is on the implementation of precision controller at actuator level, whereas in the actual implementation to SMT system level there may be an additional concern associated with Control Structure Interaction (CSI) as described in (MacMynowski, Thompson and Sirota. 2008) and (Dimmler, et al. 2008) which arises due to the structural coupling between segments mounted on a flexible mirror cell. The CSI limits the achievable local loop bandwidth. Since PSMT is a relatively small telescope compared to TMT and E-ELT, the CSI is not a significant concern for the PSMT. So the CSI related details are not within the scope of this work, the specific control algorithms developed here may need to be slightly modified in the actual application for large SMTs.

The controller is presented in the Section 3.1, the control system design and tuning related details are presented in Section 3.2. Finally, Section 3.3 presents the results obtained in the laboratory experiments.

3.1 Controller Hardware

The electronics of local actuator controller has been developed around PSoC (Programmable System on Chip) hardware. The PSoC 5LP CY8CKIT-059 board is chosen because of its versatility, low cost, and ease of design. It supports the design of both analog and digital component on a single chip along with ARM Cortex M3 processor. The local control system of each actuator uses the PID algorithm to maintain its position to the desired setpoint which is provided by the global controller via CAN network. For the best performance, the PID gains are determined experimentally using relay tuning method. The block diagram of the controller and customized driver electronics board that runs the control algorithm to operate a voice coil motor, offload stepper motors as well as acquires position feedback from the optical encoder is shown in Figure 3-1.

Since the PSoC controller itself cannot provide the required drive current to the motors, intermediate drive electronics is used to serve the purpose. The voice coil driver consists of a 16 bit Digital to Analog converter (PCM56), followed by a linear power amplifier based on OPA549T. The offloader is driven by a DRV8825 Stepper Motor Driver. A quadrature decoder module is implemented inside the PSoC controller chip to decode the position signal from the actuator encoder. The current sensor (LEM HX 03-P/SP2) is used to measure the current flowing through the VCM of the actuator.
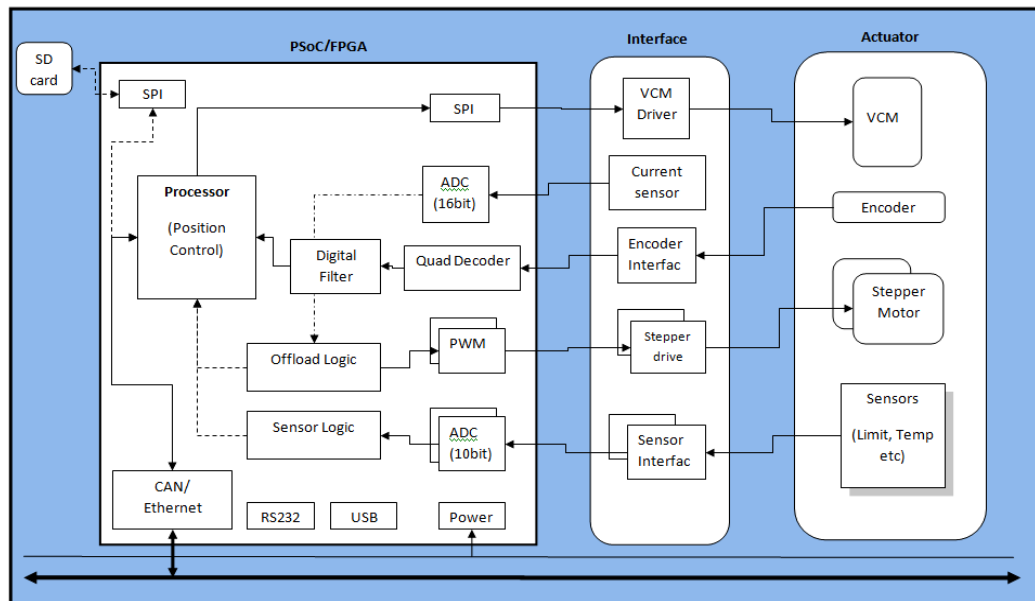
Figure 3-1. Block diagram of the actuator controller along with different interfaces and actuator peripherals.

After several experimentations with the drive electronics and PCB, the final drive board was designed. The drive board along with the PSoC controller is shown in Figure 3-2.
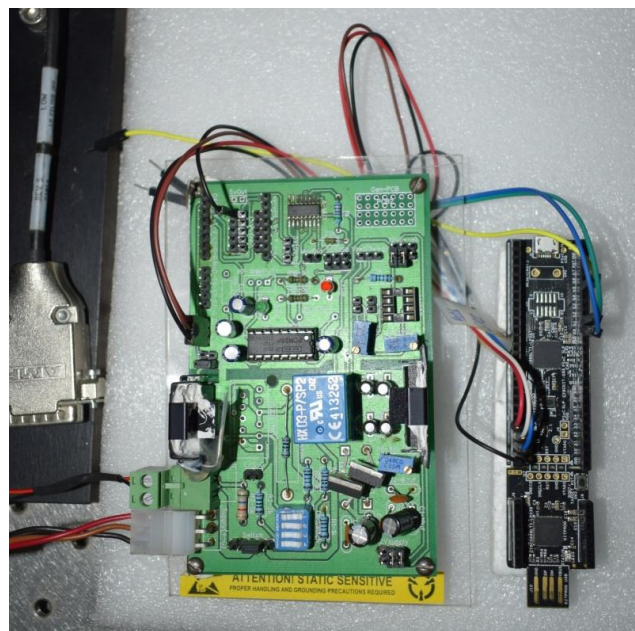
Figure 3-2. The controller electronics for the PSMT Actuator. Control electronics consist of a drive board and a PSoC 5LP controller.

During the laboratory testing, commands are given through computers serial port and acquired data is displayed on serial plotting tool on the PC. Data logging is done on the PC for further analysis. This actuator controller is also capable of receiving commands from the global control network and sending back data to the network monitor node computer using CAN interface. In the actual PSMT telescope, such 21 local controllers will be connected to a global controller network. Further details of the global controller and network are presented in Chapter 7.

3.2 The design of Control System for the Actuator

The Controller mainly consists of a PID position controller, an offloader controller, a position Quadrature decoder and a network interface. The VCM provides the dynamic force requirements of the actuator in the closed loop with a position sensor. The actuator output shaft position is continuously sensed for any deviation from the set position and is corrected by sending new drive signal based on the closed-loop control law. During the testing phase, the position sensor data is sampled at 400Hz, and the control command is sent to the actuator at 200Hz. The control law used here is based on a simple incremental PID control algorithm. Suitable PID equation (Equation 3-1) is derived for implementing this algorithm in its digital form.

The offloader handles the static load primarily coming from the variable gravitational force due to change in telescope pointing. The offloading system is a simple on/off logic based on the current flowing in the VCM. When the current through the VCM exceeds the threshold (or commanded by the user), stepper motor driver moves the motor in the appropriate direction for a very short time to minimize the static current through the VCM. This loop is very slow and typically operates once or twice in an hour (preferably between two science observations). Precaution is taken to avoid limit cycle oscillation by implementing dead band logic and is implemented as parallel hardware logic on PSoC's digital logic blocks.

The control algorithms and loops, written as an application program in the controller are given in the form of a flowchart in (Appendix A). Synchronization

among the different controller tasks and modules is achieved by using timers and interrupts. The timer generates an interrupt at regular interval of 2.5msec, 5msec and 1sec and CPU serves the interrupt request. The 2.5msec interrupt has the highest priority, and 1sec interrupt has the lowest. Each interrupt has its interrupt service routine (ISR) functions, and care is taken such that the time required to serve each ISR is less than its period. The experimental timing and priority validation of the ISR operation is shown in Figure 3-3.
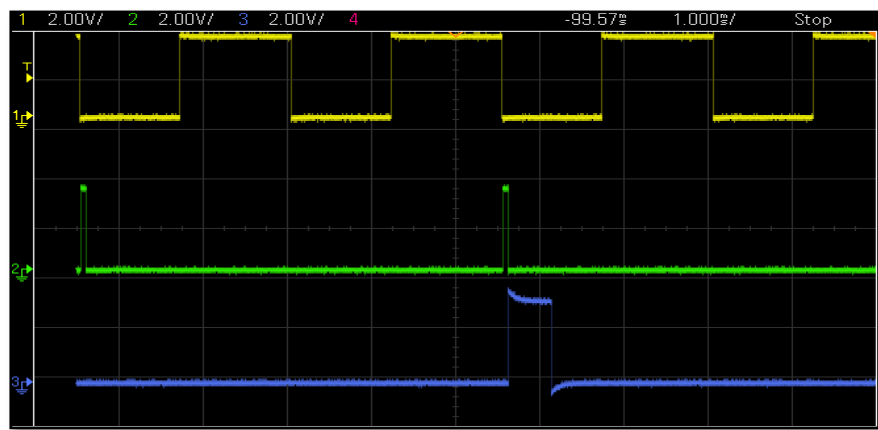
Figure 3-3 Experimental verification of individual ISR timings, priorities and execution time on a digital oscilloscope. Top plot corresponds to 2.5msec, central plot to 5msec and bottom plot to 1sec ISR.

Using the combination of different PSoC hardware modules and algorithms running at timed ISRs are responsible for the successful operation of this controller. The overall functionality of the controller can be seen in terms of few primary loops such as position loop, tuning loop, offloading loop, etc.
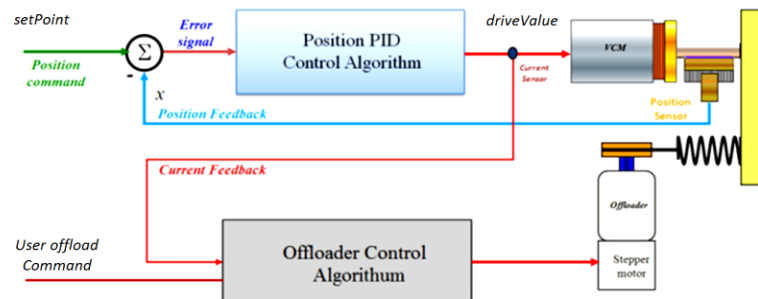
Figure 3-4 Schematic of Position and offloading control loop.

The schematic of position and offloading control loops implemented in our controller and similar to (Lorell, Aubrun, et al. 2003) is shown in Figure 3-4.

Following is the brief description of these loops and the related experimental results are presented in Section 3.3.

3.2.1 The Position Loop

In the position loop, the task is to maintain the actuator position with the commanded set point in the closed loop of operation. The controller receives setPoint from the global controller, and it converts this (using PID law) into a corresponding driveValue and sends it to a digital-to-analog converter (DAC) connected to VCM power amplifier via SPI interface. The controller reads the position encoder data stored in a Quadrature decoder buffer, and then the position error value is computed by comparing the present position with the setpoint position.

Following is the equation of incremental PID position algorithm (Haugen 2010) used in the controllers PID block.

$$u(n) = u(n-1) + K_P \left[e(n) - e(n-1) \right] + K_I \, Ts \, e(n)$$

$$+ \frac{K_D}{T_S} \left[e(n) - 2e(n-1) + e(n-2) \right] \qquad \text{Equation 3-1}$$

where,

$u(n)$ is drive signal; $e(n)$ is positione error; T_S is sampling period; K_P, K_I, K_D are PID gains.

The error value and the already stored Proportional (K_P), Integral (K_I) and Derivative (K_D) gains in the controller are used by the PID block to generate the new drive value (and send to the DAC again). This operation of position loop repeats at the 200Hz rate. The optimal values of K_P, K_I, and K_D are decided by the tuning procedure. The above operation is for the closed loop mode, whereas as in open loop mode actuator bypasses the PID block and computes the drive value directly from the input set point and sends it to the DAC.

3.2.2 The Tuning Loop

Tuning is done to determine the optimum PID gains of the closed loop actuator controller. Even though all the actuators in SMT will have similar gains and may not require tuning for every unit, our aim here is to find that best set of gain values. This tuning loop runs on request by the user. Tuning block is implemented in parallel with the PID block and runs for a specific amount of time. We did experimenting with different techniques and chosen the relay tuning method for our controller. It is to be noted that the controller implementation described here is different from that of Matlab based control simulation described in Section 2.3.

Relay tuning (Khalore 2012) is a PID tuning method, and this is non-destructive compared to the conventional methods of tuning (Åström and Tore 1995). This method can work with a very small input of oscillation and hence suitable for segmented mirror telescope actuators. Relay controller is programmed to switch automatically (by closing the loop) every time plant output crosses the predefined upper and lower threshold value. During tuning, we shift the control of actuator from PID controller to relay tuning which will put the actuator in sustained oscillation within few cycles.
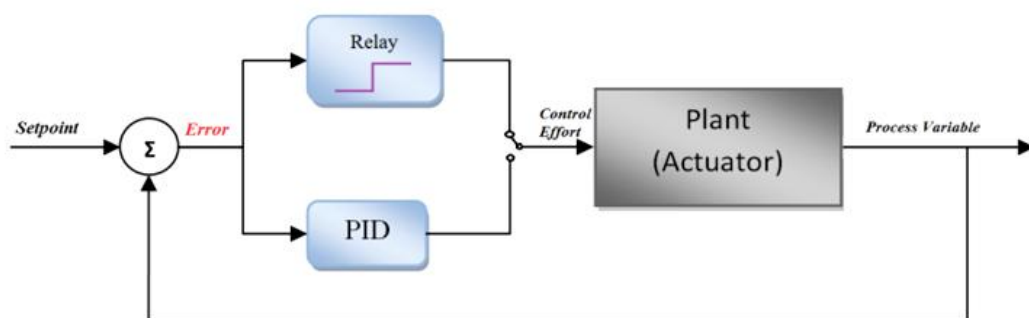
Figure 3-5   Schematic of relay tuning of PID controller. The relay controller works in parallel with the position controller.

We capture the input relay and the actuator output response and calculate the parameters called: ultimate gain (Pu) and ultimate period (Tu) which gives the PID

gains using empirical rule by Ziegler and Nichols (Tomas 2004) (Tomas 2004) (Tomas 2004) (Tomas 2004) (Tomas 2004) (Tomas 2004) as given in Table 3-1.

Table 3-1. The Ziegler and Nichols empirical rule to obtain PID gains.

	K_P	K_I	K_D
PI	0.4 PU	1.8 PU / TU	
PID	0.58 PU	2 PU / TU	PU TU /8

3.2.3 The Offloader Loop

The Purpose of offloader is to reduce the current through VCM by transferring load on VCM to the main spring. The block diagram of the offloader loop is shown in Figure 3-4. The offloader logic is hardware implemented on the PSoC chip and runs in parallel to the main position loop. The offloading can be activated in two modes, automatic or manual mode. In automatic mode, the input to the offloader block is from the current sensor connected in series with the VCM drive. The offloader logic continuously reads the value of current flowing through VCM and compares it with the dead band hysteresis logic shown in Figure 3-6. Subsequently, it generates the required trigger for activating the offloader stepper motor. The polarity of current flow in the VCM is used to decide whether offloader motor should move in the upward or downward direction. In the manual mode, offloader can be activated or deactivated by the user command from the global controller.

The parallel hardware implementation of the automated offloader logic on PSoC controller is given in further details in Appendix A.
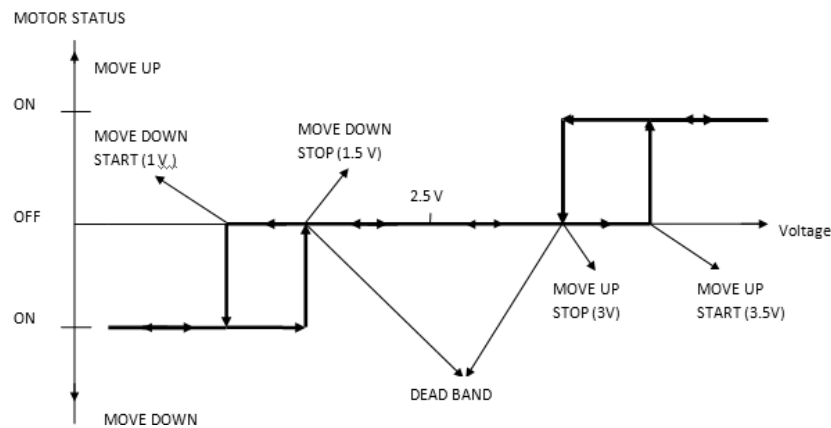
Figure 3-6 The offloader hysteresis logic diagram to avoid limit cycle oscillation.

3.3 The Test Results

The PSMT prototype actuator has gone through functionality as well as performance tests using the PSoC based actuator controller. The actuator is mounted on a test stand in a vertical direction, and the output shaft is loaded using a moderate stiffness load spring. The actual parameters of the prototype actuator on the present test setup are as follow:

K_S=22670 (N/m); M=1.035 (Kg); L=0.00188 (H); R=2.62 (Ω);
K_b=6.9 (Vsec/m); K_v=6.9 (N/A); K_{DFS}=992 (N/m); K_{LS}=2380 (N/m).
where,
K_{DFS} is a disc flexure stiffness, & K_{LS} is a load spring stiffness.
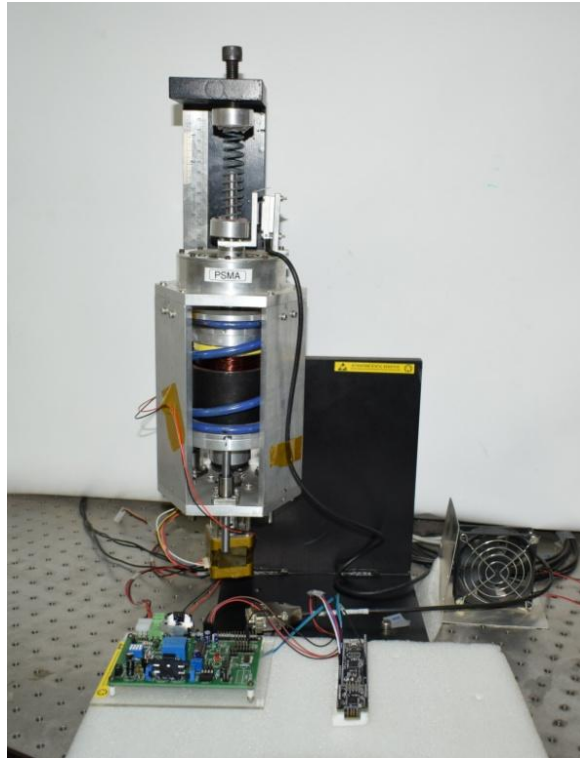
Figure 3-7. PSMT actuator test setup at IIA Bangalore. Test setup includes the prototype PSMT actuator along with the actuator mount, a drive board, and a controller board.

Following are different experimental test results obtained during tests conducted in August-December 2016.

3.3.1 Input-output mapping

This test is to obtain the relation between the output position and the input drive command to the actuator. The mapping relation obtained is implemented in the actuator controller to evaluate the appropriate drive signal to be given to the actuator to achieve the required position. This relation also gives us the DC gain of our system. To obtain the mapping relation, we supplied different known voltages to the actuator in open loop mode, and corresponding output positions are measured. The following plot shows this mapping relation, which is mostly linear with the mapping slope of 148.8 μm/V. In the controller, we have implemented mapping as a linear relation, and any residual mapping error due to linear approximation will be taken care by closed loop operation.
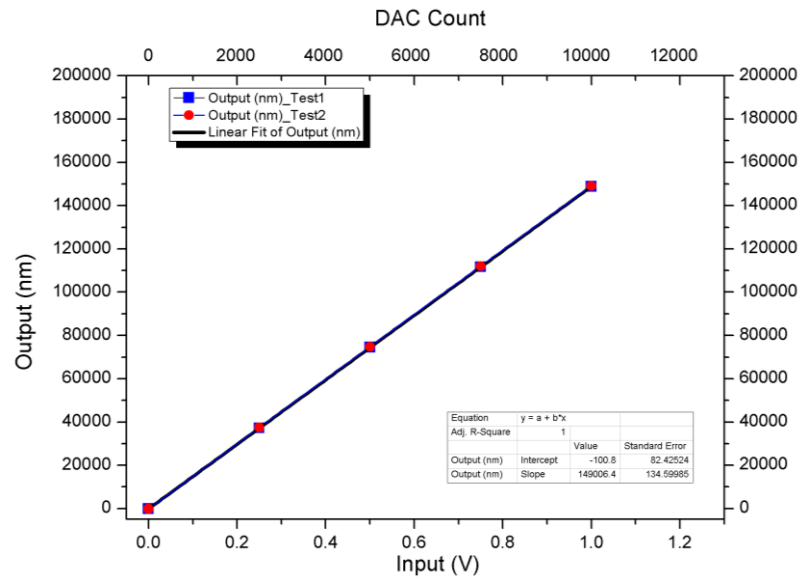
Figure 3-8 The mapping relation plot of input voltage given to the drive board (DAC count) and the output position of the actuator.

3.3.2 Open Loop Response

In this test, we studied the open loop response of the actuator. A constant step input of 3μm was given to the actuator controller, and the corresponding output was recorded in the open loop mode. As seen, the position gets deviated over a period of time due to the low stiffness of a soft actuator in open loop mode. Also, the step response of the system is underdamped.
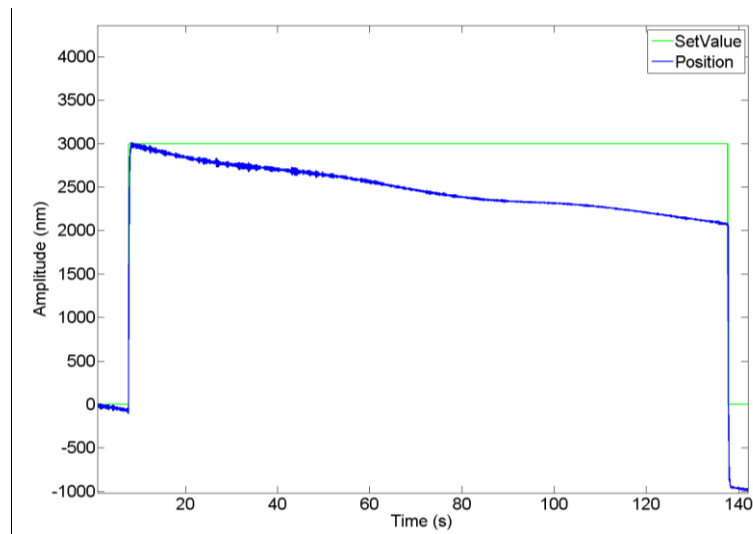
Figure 3-9 The open loop step and steady-state response of PSMT Actuator.

Further, we conducted the tracking test of the actuator in open loop mode with the track rate 350nm/s. The difference between the command track position and the actual position can be seen in Figure 3-10, and it builds up over a period of time. This is the major problem in tracking a soft actuator in open loop mode, so we need the closed loop operation for precise tracking.
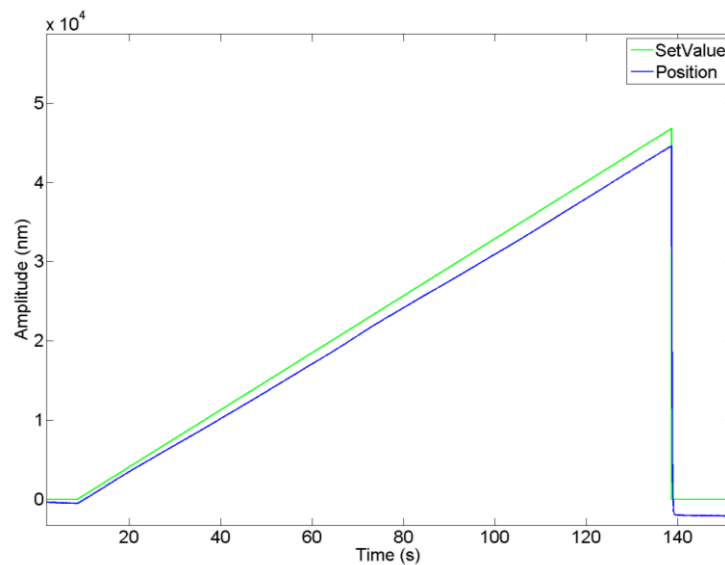
Figure 3-10 Open Loop tracking performance of PSMT actuator. Track rate of around 350nm/sec is achieved easily without any transients but with position deviation.

3.3.3 Controller tuning

For the closed-loop control, the PI control scheme has been used in the actuator controller. To achieve the best performance, the first task is to tune the PI controller and derive its optimum gain values. Since every mechanical system is unique and has slightly different dynamics, we have chosen the Relay tuning method, which is an experimental method of controller tuning (Deshmukh and Parihar 2016). The relay response is used to calculate the ultimate period (Tu), ultimate gain (Pu) and the PI gains as given in Table 3-2.
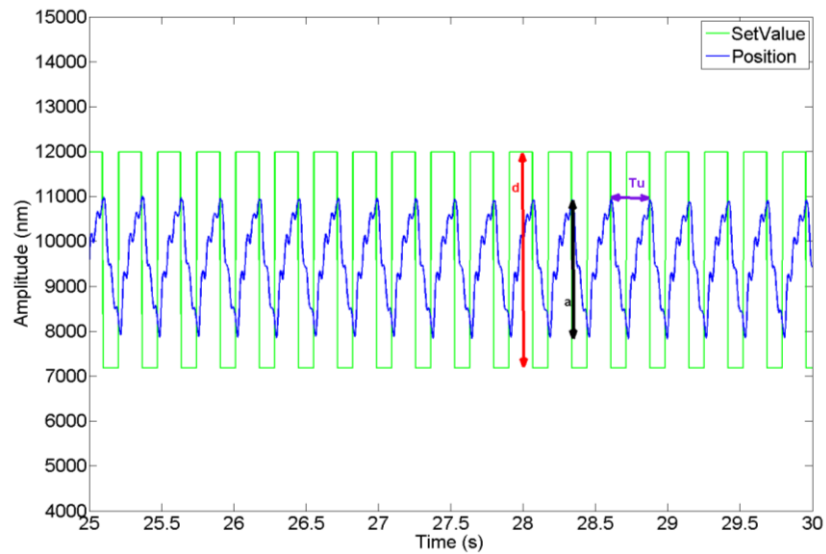
Figure 3-11 A relay response of the PSMT actuator. Sustained oscillations were achieved quickly, and we obtained the parameters from this response.

As seen from the output response in Figure 3-11, we observe that the maximum peak to peak amplitude is 2637 nm (2198 Encoder Count), whereas the input relay has peak-to-peak oscillation amplitude of 4800nm (4000 Encoder Count). Also, the period of oscillation of the output response is around 294ms.

Table 3-2 The optimum PID gains obtained by using the Relay based tuning method.

Parameters:			
Relay amplitude:	D	= 4000*1.2	= 4800nm
Output Peak-peak Amplitude:	a	= 2198*1.2	= 2637nm
Ultimate period:	Tu	= 0.294 sec	
Ultimate Gain:	Pu	= (4*D)/(pi*a)	= 1.158
PI gains (Modified Eq):	Kp	=0.4*PU	**= 0.46**
	Ki	= 1.8*Pu/Tu	**= 7.08**

3.3.4 Closed loop Response

In this test, we evaluated the closed loop performance of the system using the PI gains obtained from the relay tuning method (see Table 3-2). The tests conducted were step response, steady-state response, and the track rate performance. The open loop step

response of this actuator is underdamped as seen before, whereas the closed loop response is critically damped (1 damped oscillation) as seen in Figure 3-12. The critically damped response is the optimal response we can expect from the system, and it stabilizes the system faster than any other type of stable system (overdamped/underdamped). Furthermore, the small overshoot, in the beginning, can be avoided by implementing a set point filter (Hägglund 2012) in the closed loop controller to smoothen out sudden step input changes to the controller. In the closed loop steady state response, the actuator position is maintained around the set point of 3µm with the RMS steady state error of 5.73nm.
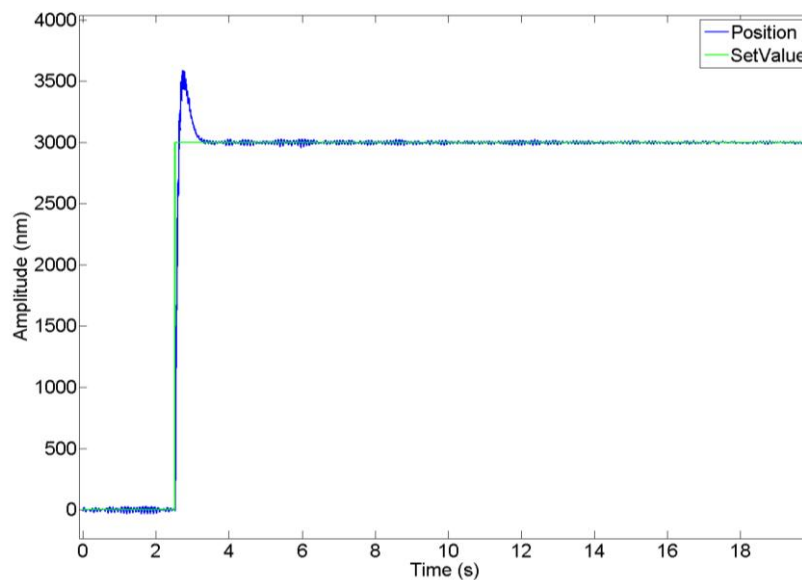
Figure 3-12. The closed loop step response of the actuator. The position is maintained around the given set point of 3um.
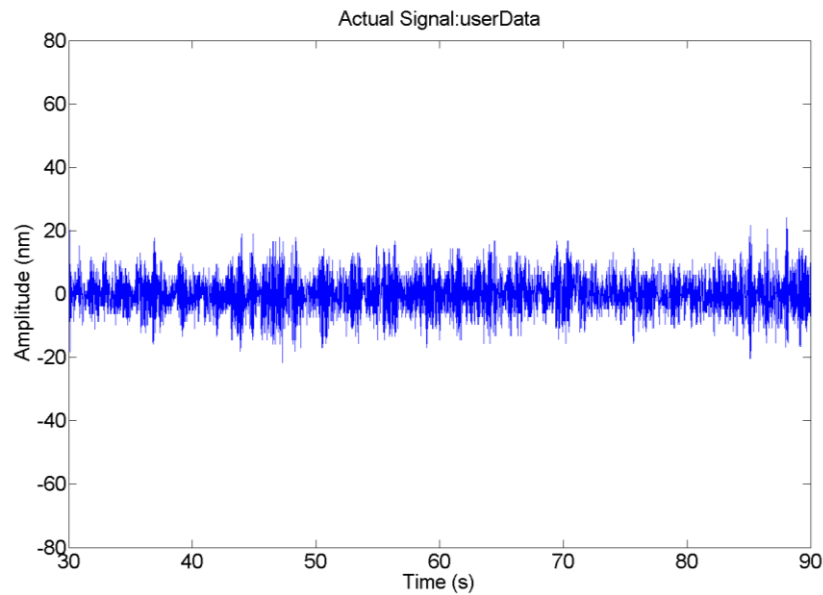
Figure 3-13 The closed loop steady-state response of the actuator in a closed loop. The obtained steady-state error is 5.73 nm RMS.

For the prototype actuator under test, one of the design requirement is Position track rate $\geq$ 350 nm/sec with RMS tracking Error $\leq$ 25nm Table 2-1. These requirements ensure that the actuator will maintain the alignment of the mirror segment, under changing gravity loads when the telescope is tracking. In this experiment, we changed the position reference (setPoint) of the actuator closed loop with the known slope (350nm/sec) and monitored the tracking performance. As seen below Figure 3-14, the tracking was achieved very smoothly; the set point (Red) and the actual position (Blue) follow each other very closely. The tracking error is shown in Figure 3-15 and position is maintained with the RMS tracking error of 10.15 nm.
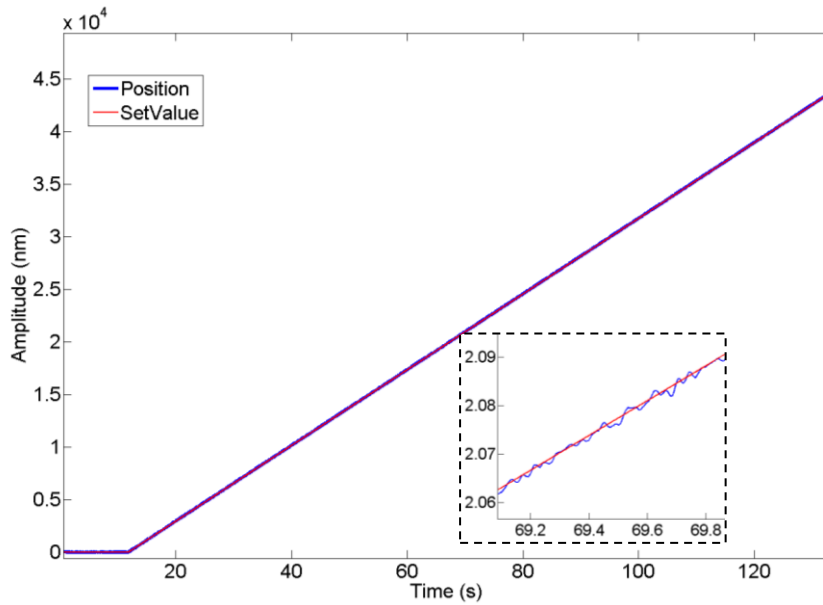
Figure 3-14 The tracking rate response with 350nm/sec track input. The output closely follows the input without any transients. The close-up view of track rate response is shown in the right corner.
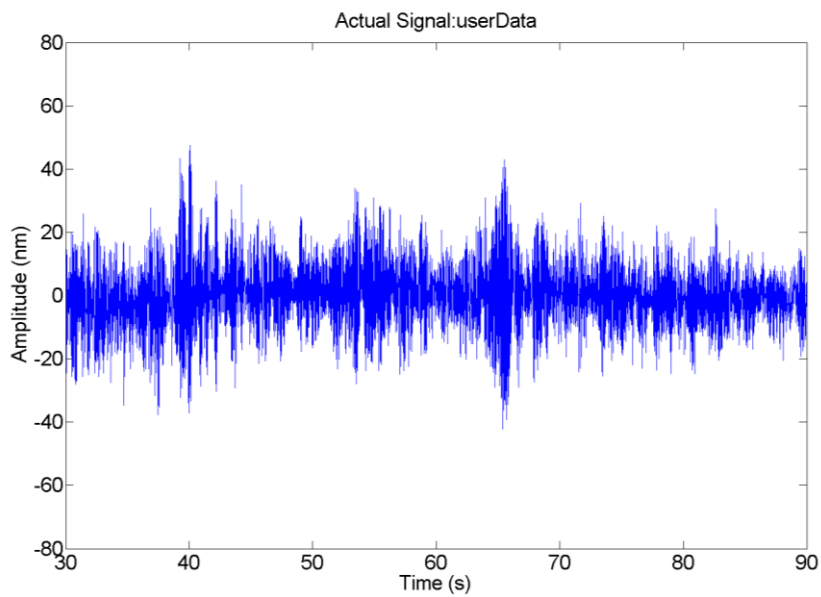
Figure 3-15 The closed-loop tracking error of the actuator obtained by subtracting the track rate input from the actual position. The tracking is achieved with the RMS error of 10.15nm which is compliant with the PSMT actuator requirement of 25nm.

3.3.5 Offloading Tests

The open loop and closed loop offloading tests are conducted with the PSMT actuator. In the open loop mode Figure 3-16, offloader displaces the actuator position smoothly without any transients.
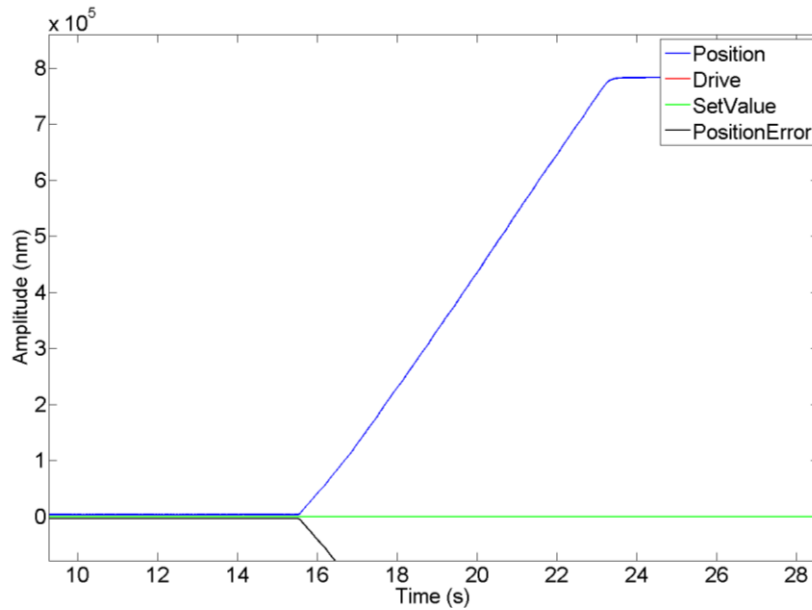
Figure 3-16 The offloading response with the actuator in open loop mode. The offloader is driven continuously and as seen actuator position is displaced very smoothly without any transients.

In the closed loop Figure 3-17, the actuator position loop is kept in the closed loop mode, and the offloader is moved continuously at 500nm/sec rate. The actuator maintains its position near the set point with the position error below 40nm during offloading, and 5.8nm after the completion of offloading. The VCM current reduction is observed as seen in Figure 3-17.
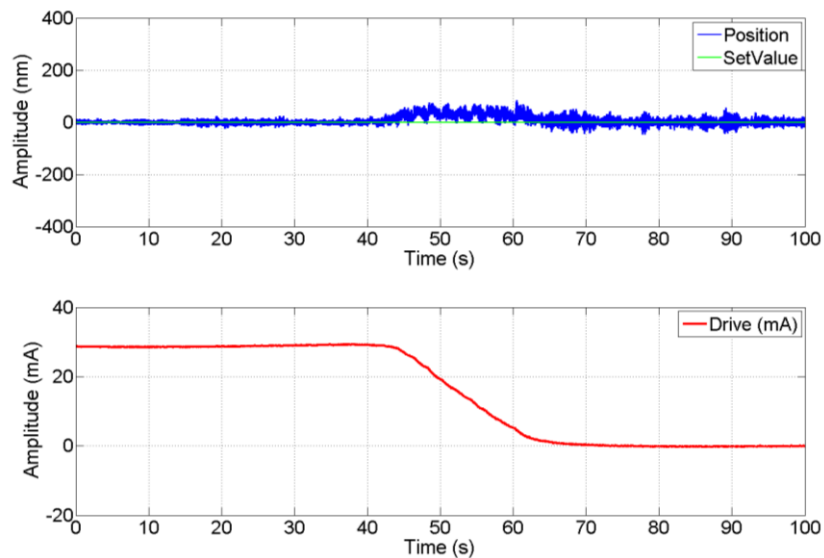
Figure 3-17 The offloading response at 500nm/sec rate with the actuator in closed loop mode. As seen actuator position is maintained around the set point without any transients. The position error while offloading is below 40 nm, and after completion of offloading it is 5.83nm.

3.4 Summary and Conclusion

In this chapter, we presented our work on the implementation of the precision control system for segment support actuator of the PSMT. The precision controller is developed and implemented on a Programmable System on Chip (PSoC 5Lp) board along with the customized drive electronics. The closed-loop proportional-integral (PI) controller is implemented for the position loop using the feedback from a linear optical encoder. For any servo system, it's essential to determine the gain accurately, and there are different method proposed in the literature (Åström and Tore 1995) to get optimal values of the PID gain. For the current work, we have implemented Relay based tuning, and the obtained PID gains are used for further experiments.

The actuator controller connects to the main bus from the global controller to receive the reference position command and is typically updated at 1Hz. It reads the local position sensor of the actuator at the fastest rate (500 Hz - 1 KHz) and filters the noise if any. This position information is used by local closed loop (PID) controller to maintain the position of the actuator to the commanded position. This position loop

runs at 200Hz command rate. Dedicated drive electronics is used to drive the high power VCM to generate the required force. Local controller also has a current sensor to measure the current through VCM, which is used to trigger the Offloader mechanism. This, in turn, saves the static power consumption of actuator. The local controller is capable of executing controller tuning algorithms to get the suitable PID gains as well as system identification routines to get the actuator system model. Different modes of operation (open loop, closed loop, calibration, tuning, APS, etc.) are implemented in the Local controller firmware and is operated/selected from the global controller.

Using this controller we conducted several experiments to test the performance of the prototype soft actuator, such as steady-state response, tracking error test, offloading response, and disturbance rejection, etc. The closed-loop step response is achieved with SS error of 5.73 nm RMS. Closed loop track response is achieved with tracking error of 10.15 nm RMS. Closed loop Offloading is achieved at the rate of 500nm/sec and with the position maintained below 40nm. And once offloading is complete, the SS position is maintained with RMS of 5.83nm. This is within the requirement of PSMT actuator.

In the near future, we intend to carry out few advanced tests like lifetime and survivability (to understand the vibration and earthquake effect). The life testing of a few crucial components will be useful to understand the component reliability. However, these tests will require suitable test facilities created in the lab. Based on all these test results, the present prototype actuator will be improved, and finally, 21 such actuators will be fabricated and used in the PSMT

Further, we have conducted tests related to disturbance rejection with the help of Dynamic Loading Assembly (DLA) which is capable of emulating the wind disturbance on SMT actuators. This setup is used to study the performance of actuator and controller, under dynamic loading conditions in a realistic way. The details of DLA and test results are presented in Chapter 4.

Chapter 4   Dynamic testing of the PSMT Actuator

Upcoming large telescopes are based on segmented mirror telescope (SMT) technology which uses small hexagonal mirror segments placed side by side to form a large monolithic surface. The segments alignment needs to be maintained against external disturbances like wind, gravity, structural vibration and temperature. This is achieved by using three position actuators per segment working at few-nanometer scale range along with a local closed loop controller. The actuator along with a controller is required to meet very stringent performance requirements, such as track rates up to 300 nm/sec (90mN/sec) with tracking errors less than 5 nm, dynamical forces of up to $\pm$ 40 N, ability to reject disturbances introduced by the wind as well as by mechanical vibration generated in the mirror cell, etc.

Actuators being developed for upcoming segmented mirror telescopes are required to go through various performance tests against dynamic disturbances. An example of a test setup designed for dynamic testing of actuators in the literature is the WEB (Wind Evaluation Breadboard) (T. Viera, et al. 2008) developed for E-ELT telescope, which is a seven segment telescope with all the control subsystems of a complete segmented mirror telescope. Though such an experiment can be the best possible attempt to understand the wind effect on SMT actuators, however, such experiments are extraordinarily costly and designed to serve several other objectives. Another example of dynamic testing of the actuator can be found in (Witvoet, et al. 2015), is an indirect method of dynamic testing in which actuator developed for E-

ELT is subjected to the dynamic wind disturbances by artificially adding the force disturbance signal to the voice coil force of actuator itself.

We have attempted to develop a device which facilitates us to conduct actuator performance tests like tracking, slewing, wind rejection, etc. in a more direct and realistic manner in the laboratory itself. The multi-purpose Dynamic Loading Assembly has been primarily designed and developed to test the soft actuator developed at Indian Institute of Astrophysics, Bangalore for the Prototype Segmented Mirror Telescope (PSMT). However, it can also be used to test other soft actuators with little or no modifications. It has static and dynamic loading capability up to 250N and 18N respectively, with a bandwidth sufficient to generate wind disturbances. DLA is a novel device, which is not only simple in operation but also cost-effective. Well before using the DLA for meaningful testing of the actuator, the DLA itself has gone through various tests and improvement phases. We have successfully demonstrated that DLA can be used to check the extreme performance of SMT actuator, which is expected to track the position/force with a few nanometer accuracies.

In the following sections, we describe requirements for the DLA, functionality, as well as the effort made toward design and simulation aspects of it. Further, we have explained the mechanical aspects of DLA and the customized control electronics developed for it. Finally, we have presented experimental results obtained from the DLA alone as well as testing with the prototype actuator.

4.1   Dynamic Loading Assembly (DLA)

The primary objective of DLA is: a) to develop a laboratory test-bed to simulate wind-induced dynamic loads on the SMT actuators, b) to evaluate the performance of Actuator and Controller for dynamic loading conditions. The design requirement of the DLA is primarily driven by different kind of tests we are supposed to undertake on the actuators. We have followed the standard procedure of instrument development and gone through the phases like; modeling and analysis, the design of

mechanical unit as well as controller, fabrication & assembling, calibration, and testing, etc. These crucial phases of the development have been described in the sub-sections below:

4.1.1 DLA system requirements

The DLA interfaced with the test actuator should be able to generate disturbance force in the frequency range in which wind is a dominant contributor (<10Hz). When the telescope moves in elevation, then the axial force due to gravity changes systematically, and the actuator should be able to track the force. Due to thermal changes, when telescope mirror cell undergoes through predictable distortion that time the actuator has to track the position. The DLA should be able to simulate these two different tracking requirements. To understand the effect of inertial loading on the actuator, DLA should have easily configurable counterweights. The counterweight used in DLA acts as a static load due to segment mass on the actuator and is fixed during the DLA operation. It should be designed in such a way that it will have minimal force losses due to friction/stiction. It should be able to generate different types of user-defined disturbances in an extremely smooth and controlled manner. To mimic the wind, it should either use the real wind data and generate wind force disturbances or make use of wind model. Some of the important DLA design parameters are listed in Table 4-1 below.

Table 4-1 DLA Design Requirements and actual design parameters.

Parameter	Requirement	Fabricated
Static Loading	35 to 840 N	50 to 250N
Dynamic Loading @3 m/s wind	+/- 2 N	> +/- 2N
Continues Loading (in case of quasi-static offloading)	40N	36N (for VCM used in the design. It can provide >40N but for short duration)
First natural frequency mode	Above 10Hz	Around 25Hz @ 75N static load
Near Instantaneous Force disturbance	5N	9N
Max Drive current	2A	3A

4.1.2 DLA modeling and simulation

Before realizing the DLA, a simple lump mass model was created, and analysis was carried out. Firstly from this exercise, we ensured that the DLA concept is indeed feasible and we can generate the required dynamic disturbances. Additionally, it helps to choose/design right kind of components for the DLA so that device can meet the design requirements as given in the previous section.
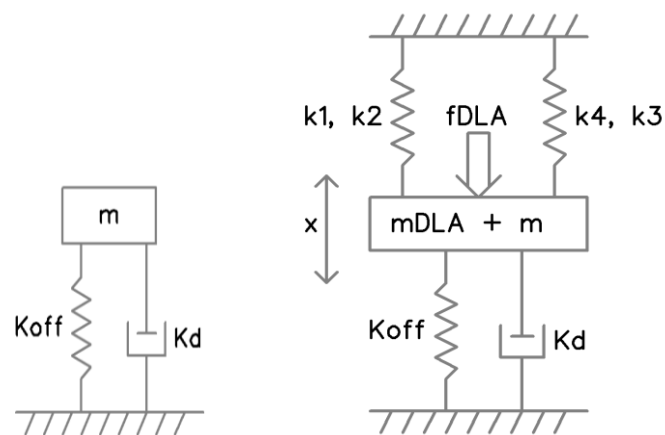
Figure 4-1. (Left) Simple spring, mass, and damper based actuator model. (Right) The equivalent of the DLA along with the actuator.

As seen in Figure 4-1, the mass *m* is the moving mass of the actuator, and the *mDLA* is the static load representing mirror mass. The DLA side support springs k_{1-4} are used to provide the support and isolation between the top rigid frame and the moving mass at the actuator output. The effective stiffness of k_{1-4} is chosen to be less than 10% of the actuator main spring stiffness so as to reduce its effect on overall dynamics. Primarily from modeling, we could optimize the mass of the device as well as able to design springs required. Subsequently, the transfer function of the device was derived, and dynamic behavior has been studied. The details of the model and simulation can be found in Appendix B.

4.1.3 Mechanical design

Based on modeling and simulation, once parameter selection of core components required for DLA was decided then after with the aid of CAD design software, conceptual as well as detailed mechanical design works were undertaken. Subsequently, components were manufactured and assembled in IIA mechanical workshop. The 3D model of DLA and PSMT actuator along with realized system is shown in Figure 4-2. The heart of the DLA is a Voice Coil Motor (VCM) from H2W which can act like force and/or linear positioning device. The stator part of the VCM is firmly mounted on a rigid base plate which itself is fixed with strong steel structure (fixed frame). The coil (bobbin) part of the VCM which moves vertically when it electrically energies, is guided by two linear bearing that makes it always aligned with respect to the stator. The four side springs provide mechanical isolation between the actuator shaft and the fixed frame. Few circular counter-weights can be used to introduce the static load that mimics the actual mirror mass which needs to be handled by the actuator. The design is modular in such a way that the static loading can be varied with the help of inserting/removing counter-weights. In the present design of DLA, the range of static loads which can be inserted on the actuator is 5.3Kg to 25.5Kg (52N to 250N). There is also a provision to either move the whole DLA assembly or the actuator under test, up and down. This feature enables us to use the same DLA to test actuators of different dimensions (e.g., TMT, E-ELT, and PSMT) with minimal effort. Presently we have two prototypes SMT actuators developed for the PSMT and TMT project at our disposal. DLA have static and dynamic loading capability up to 250N and 18N respectively, with the bandwidth greater than 10 Hz.
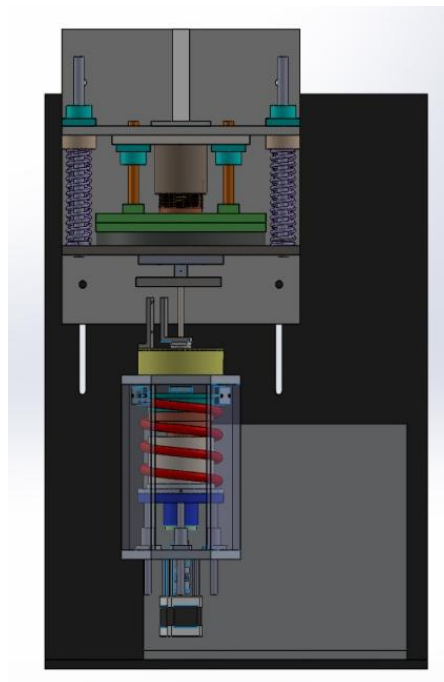
(a)
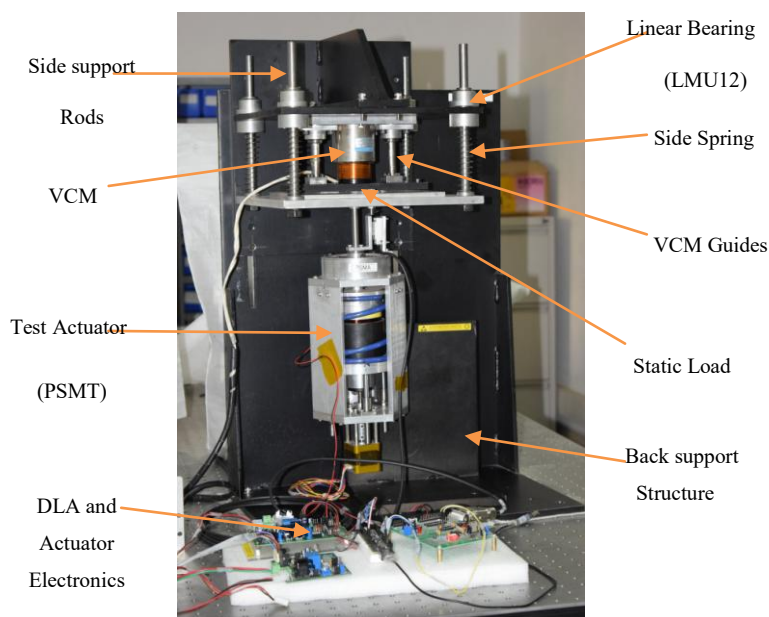
(b)

Figure 4-2. The CAD model of DLA along with PSMT Actuator (a) and realized DLA (b). The driver electronics and the controller developed to control DLA are also shown.

The DLA is designed in such a way that there is a minimal loss of force due to the side spring. Also, care is taken to reduce the effect of friction due to bearings as well as bushings. All the blocks above the actuator up to the DLA VCM coil are

clamped together to provide support and avoid backlash effect due to loose interfaces. The design of spring is such that the effective frequency of oscillation of structure is above the bandwidth of wind input. To measure the force exerted by DLA, a load cell is inserted between the base plate of DLA and actuator shaft.

4.1.4 Functioning of the DLA system

The functional block diagram of the DLA system is shown in Figure 4-3. It consists of a LabView based GUI running on the host computer and communicating bi-directionally with NI DAQ card. It sends commands to the NI DAQ system, receives various signals and displays it in real time, as well as keep logs of the events. The user-defined waveform is also digitally created in the LabView. Whereas, DAQ convert the digital signal received from the LabView into analog and feed it to the high power VCM Amplifier through interface board. Finally, VCM driven by the power amplifier, generate a force profile which follows the input signal. Mainly for the purpose of monitoring, we have also incorporated a few sensors such as load cell, a current sensor, limit switch, etc. The sensors are connected to DAQ through interface board, which digitizes their outputs and provide to LabView GUI. In addition to hard limit switches, which prevent the device from over-run, there are also soft limits incorporated in the GUI so that device can be operated in the safe domain. There is a separate Actuator Controller (see (Deshmukh and Parihar 2016) for details) which can drive the actuator in an open loop or closed loop. The linear position encoder installed in the actuator provides position information with few nanometer accuracies. The output of the encoder is used to judge the performance of the DLA as well as actuator under test.
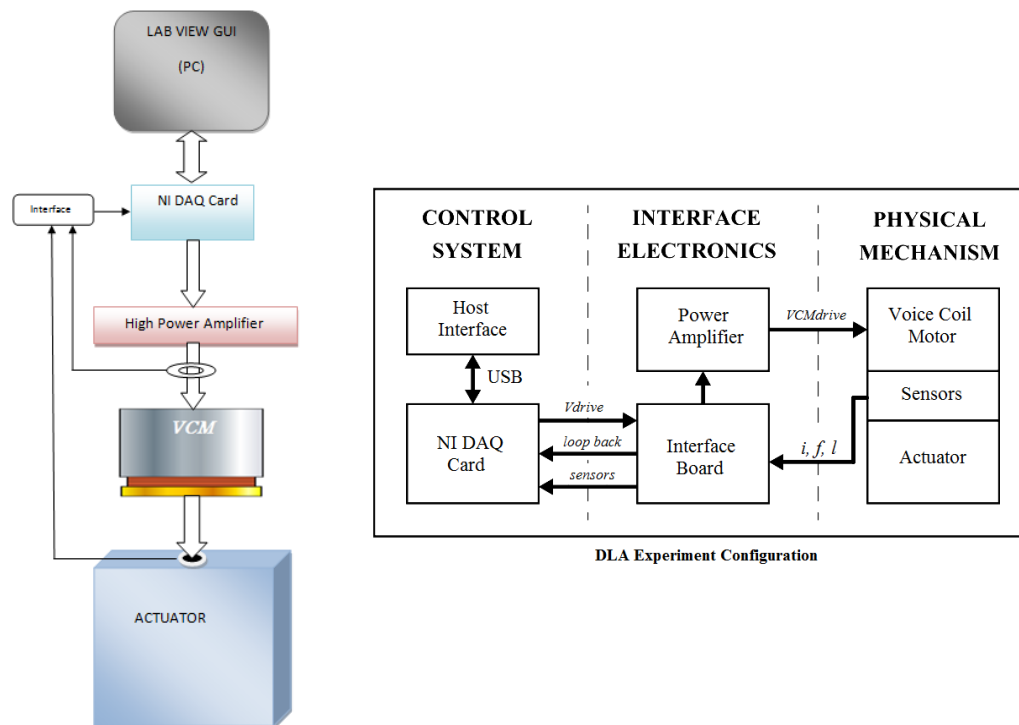
Figure 4-3. (Left) DLA Functional block diagram and (right) the interface diagram.

Different inputs, outputs and interfaces of DLA as shown in Figure 4-3 are enlisted below.

System Inputs: It includes the waveforms corresponding to actual wind data along with the different standard reference waveform such as sine, triangular, square, ramp waveforms.

System Outputs: It includes the Position encoder, a force sensor, a current sensor, limit switches.

Internal Interfaces: It includes the interfaces between NI LabView to DAQ, DAQ to the power amplifier, and the onboard tracks of VCM drive board.

External Interfaces: It includes the interfaces to the Current sensor, a force sensor, limit switches, power amplifier to VCM, VCM to Actuator.

4.2 DLA Control Electronics

A current drive based hardware scheme, which comprises an improved Howland current pump (Feucht 2014) is adopted so that it can drive the VCM in variable loading condition. This hardware scheme is designed to supply the precise value of coil current, and the input voltage can be varied so that the required current is passed through VCM which is proportional to the value of gain *Gm* (transconductance gain). The output impedance of the current pump configuration is a critical figure of merit and is adjusted so as to supply the required fixed value of current to the fluctuating nature of loads. The advantage of using Howland current pump is that it supports both sourcing and sinking of current, i.e., defines the direction of the current flow through the load, and hence the bi-directional operation of VCM is possible. The power amplifier selected for DLA OPA549 a linear power amplifier which can support maximum output current up to 10A. The schematic of the improved Howland current pump amplifier is shown in Figure 4-4.
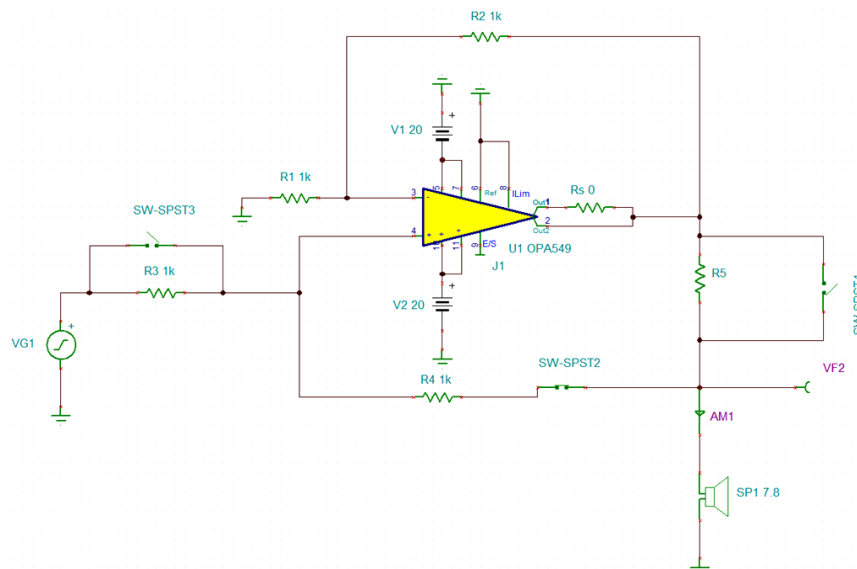
(a)
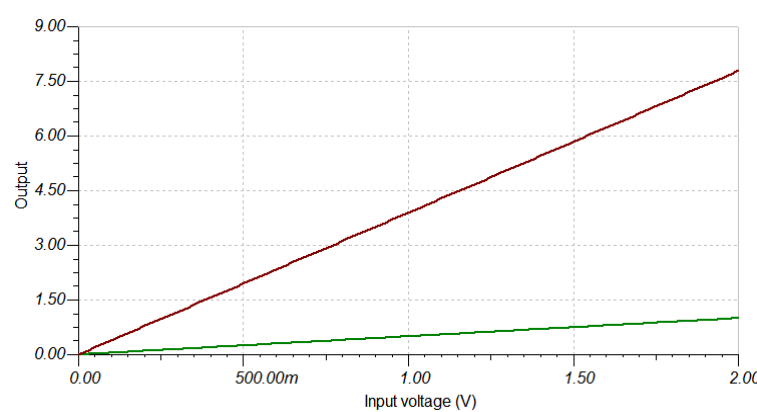
(b)

Figure 4-4. (a) Schematic of the Howland current pump using TINA-TI simulator (Current mode). And (b) the simulation result for Current Mode Response (Red= Output Load Voltage, Green= Output Current).

Table 4-2 Requirements to be satisfied by the DLA drive electronics

Sr. No.	Parameter (Unit)	Value
1	Coil current (A)	2
2	Output voltage (V)	15
3	Load impedance(Ω)	7.8
4	Total power rating (W)	32
5	Control input range (V)	+/-10

In Table 4-2, we provide the requirement considered while designing the Howland current pump which is a transconductance amplifier. Whereas, the above requirement is mainly derived from the maximum force which the DLA is expected to generate as well as some of the parameters of the VCM. The VCM used is H2W NCC15-24-050-1R (H2W 2010) which has the coil resistance of 7.8 Ω, the inductance of 5.8 mH (both at 20 degrees C) and the max power rating of 32 watts. Also, the force constant of the VCM is 18.38 N/A. The supply potential of the power amplifier is kept at +/-12V, 2A (+/-32V, 5A for high current operation). From the comparison of the simulation and experimental results of Howland current pump shows that the trans-conductance value very closely matches (0.507 against simulated 0.499). Whereas, that of Voltage gain value found to be slightly different (1.93 against simulated 2.00).
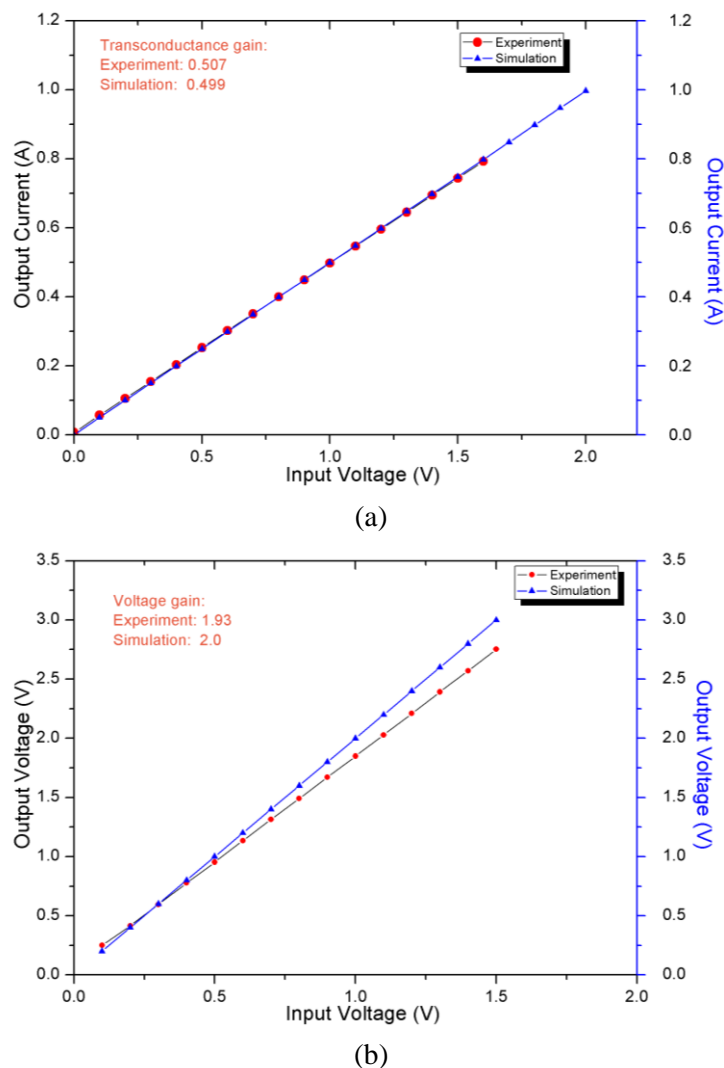
Figure 4-5. Results (a) Current mode response and (b) Voltage mode response (Simulation vs. Experiment).

In addition to Howland current pump, the drive board has also got provision for interfaces with few sensors as shown in Figure 4-6. Different sensors used are, 1) Force Sensor: 200N load cell fitted just above the actuator shaft. 2) Current sensor: the sensor used is HX 03-P/SP2 with +/- 3A measurement capacity. 3) Limit Switches: Hall Effect based A1102EUA-T limit switches are used for safety purpose. Since this drive electronics is supposed to drive high power VCM, therefore while designing the PCB, care has been taken so that it can support the high current. The drive board developed for DLA is capable of operating in either the Current or Voltage mode and this mode selection can be done using the switches (SW-SPST1, 2 & 3) provided on the board. However, since voltage mode introduces some amount of

damping in the dynamic systems, which result in a smoothened response, therefore, we have selected the current mode operation for further experimentation.
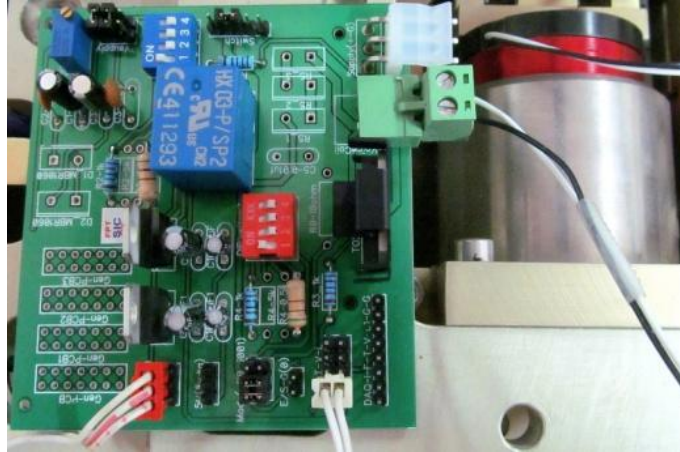
Figure 4-6. Fabricated drive PCB for the DLA. This board consists of a high power linear amplifier to drive DLA VCM. It also includes a current sensor along with an interface to force sensor and limit switches.

4.3   Experimental Results

The results of different experiments conducted with DLA as well as the prototype actuator are presented in this section. The tests conducted are primarily focused on verifying the functionality of DLA as well as evaluating the performance of the actuators. During testing, the whole setup is placed on a vibration isolation table, so that device will be free from external influences.

All together we have conducted five different tests. Three of them are to evaluate the performance of the dynamic loading assembly itself. Whereas, the other two tests are linked with the prototype actuator. To execute these tests, we also made the necessary change in the standard LabView code. Experimental data was logged and analyzed off-line.
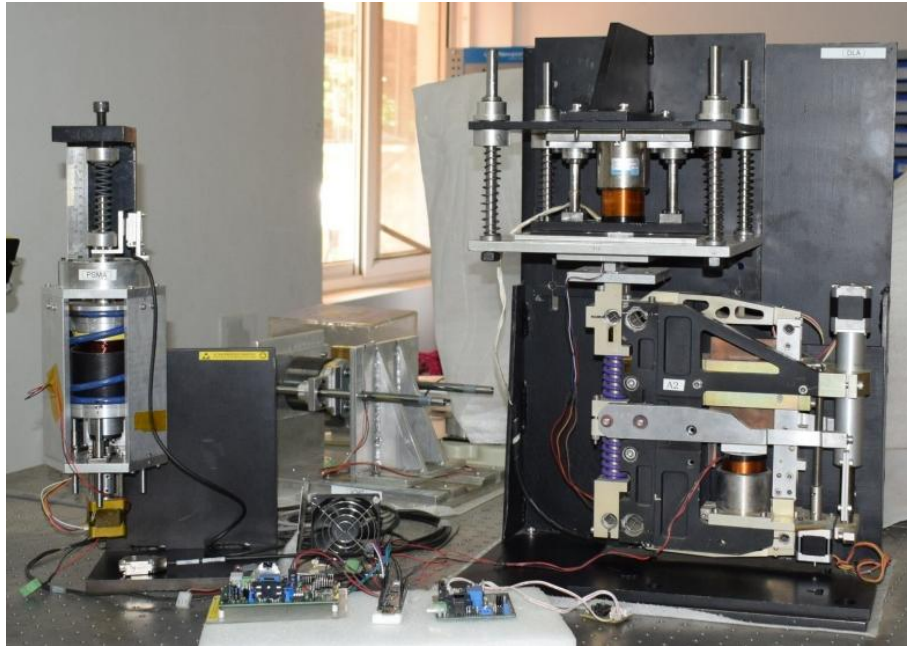
Figure 4-7. Dynamic Loading Assembly at the ITCC laboratory of IIA Bangalore, with the PSMT & TMT prototype actuators.

4.3.1 Frequency response of the DLA

This test is to confirm the functionality of DLA to generate dynamic wind disturbances having frequency content up to 10Hz. To study this, we generated known sine wave using DLA and observed its effect on the actuator in terms of corresponding Encoder displacement. While doing this experiment we kept input amplitude to be constant (0.3A, 5.5N), however, input signal frequency is varied from 1 to 15 Hz as seen in Figure 4-8. We observed that the response for fixed sinusoidal current input gets reflected as a sinusoidal output. Since we have operated DLA in current mode, therefore the current flowing through the VCM can be found constant over the whole frequency sweep. However, the output amplitude of DLA recorded using optical encoder get attenuated as frequency increases, which can be primarily considered the effect of passive built-in eddy current based damper incorporated in the latest TMT actuator system. As seen in Figure 4-9, the amplitude at 15 Hz is about 25% smaller than the amplitude at the lowest frequency (1 Hz) used. For this test setup, the first resonance frequency is observed around 20Hz (experimental), whereas

from modeling it was expected at 23.7 Hz (modeling). This small deviation can be attributed to some unaccounted parameters/dynamics of the system. Below 15 Hz the response of DLA is as expected, and it can be very well used to generate wind spectra precisely. We found that the dominant frequency in the output response is the same as the input signal. It ensures that we would be able to generate any signal of our interest using DLA.
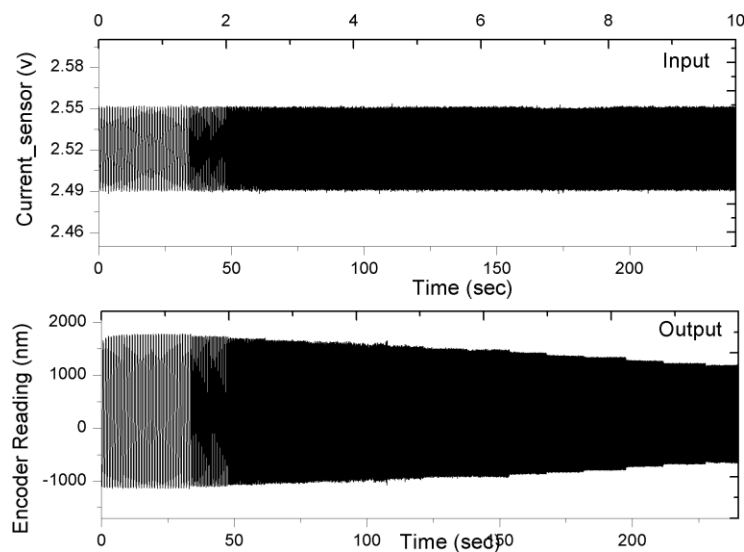
Figure 4-8. Input current to the DLA & output encoder response (1 to 15Hz). As seen with the increase in frequency the output response is getting attenuated which can be attributed to the finite damping in the DLA & actuator system.
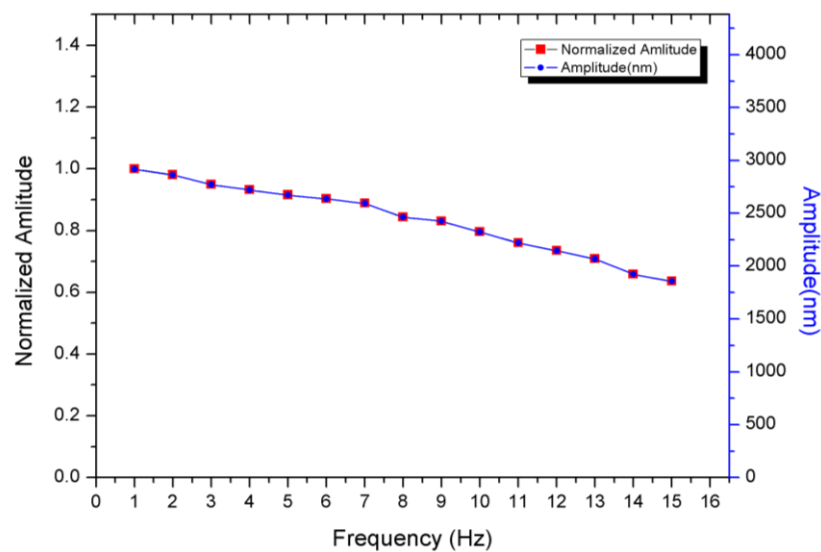
Figure 4-9. Normalized frequency transfer function response. Normalization is w.r.t the output amplitude at the lowest frequency. The response above shows that there is no natural frequency mode below 15Hz this validates that DLA will be able to generate wind disturbance corresponding to the inputs less than 10Hz without any problem. The damped natural frequency mode is observed around 20Hz for this system.

4.3.2 Maximum dynamic loading capability

In this test, the maximum dynamic loading capability of the DLA is explored. The requirement is to generate time-varying force on the actuator with a peak value of 2N (this is the maximum force exerted on the actuators supporting 1.4 m mirror @ 4m/s wind). We generated a sine wave using DLA and observed the output response in terms of corresponding encoder displacement. During this test, input frequency was kept constant at 1Hz whereas, the amplitude is changed from 0.1 to 0.7A, which correspond to an equivalent force of 2 - 12N. We observed the nearly linear response of DLA for dynamic disturbances of different amplitude with a slope of 10.51 um/A. The requirement of DLA to generate maximum dynamic load (>2N) on the actuator is satisfied.
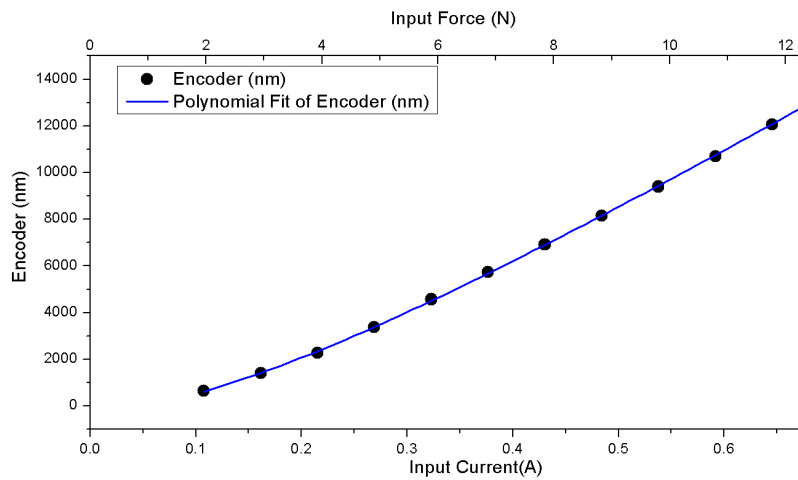
Figure 4-10. Response with the varying amplitude of dynamic input to DLA. The relation is nearly linear and with the slope of 10.51 um/A. The requirement of DLA to generate maximum dynamic load (>2N) on the actuator is satisfied.

4.3.3 Continuous loading capability of the DLA

The soft actuator designed for PSMT as well as giant telescopes have got off-loading mechanism, which is expected to take 90-95 % of the static load. It is the VCM which first takes care of any change in the static load while tracking or slewing. However, subsequently, the actuator controller either continuously or occasionally transfers this excess load to the off-loader. In the case when exchange of force is done occasionally, then the force buildup by unshared static load need to be borne by VCM. One of the important specifications for any soft actuator is the ability to withstand against continuous loading, without degrading the tracking performance. This test is to verify the continuous loading capability of DLA in which a ramp force needs to be generated up to maximum 40N. During this test, we generated a ramp input signal with slopes of 1.2N/s, and corresponding actuator displacement is observed. The test is performed in open loop mode, and encoder position, the force exerted by DLA as well as a current flowing through the VCM coil were recorded and plotted in Figure 4-11. One can observe a slight deviation of encoder curve when force is being retracted. The PSD analysis of encoder output data linked with detrended (removal of the smooth variation by fitting low order polynomial) ramp-up

part shows that there is no any jitter and/or additional disturbances found (see Figure 4-12.).
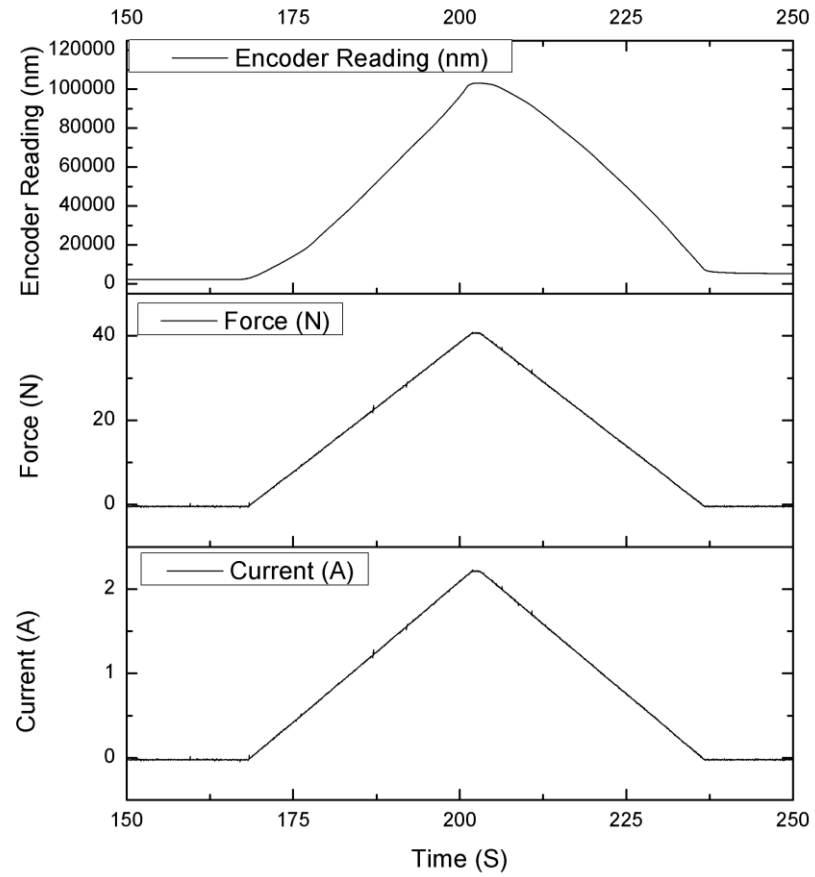
Figure 4-11. Force ramp response of DLA with maximum continuous force up to 40N (Test is conducted in open loop mode).
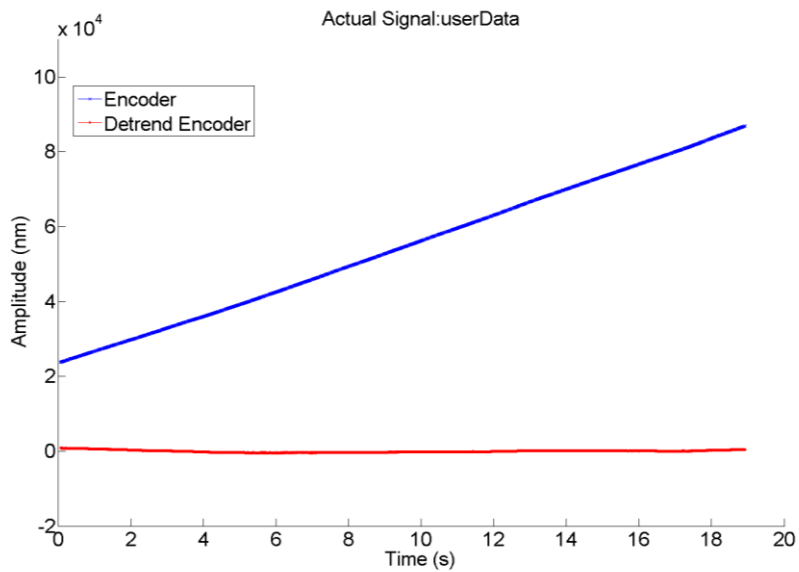
(a)
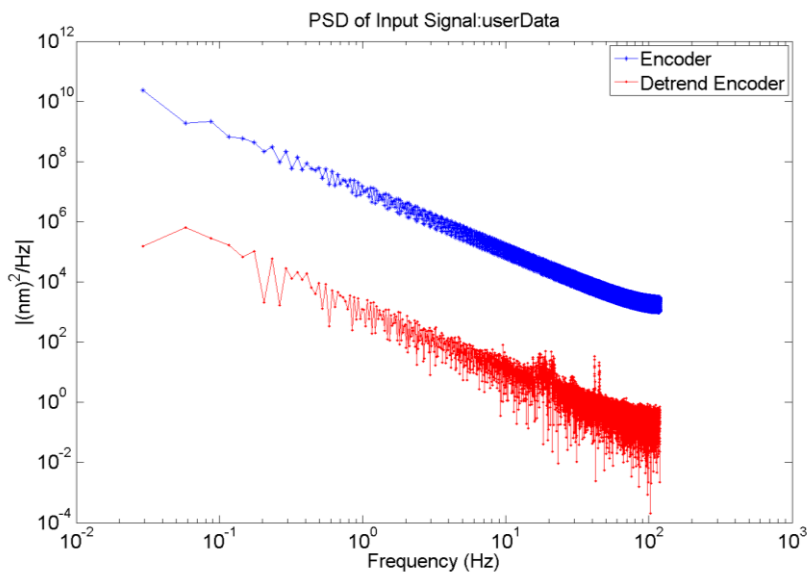
(b)

Figure 4-12. (a) Force ramp response of DLA along with its detrended (DC subtracted) version. (b) PSD plot of the same data. As can be seen, no further disturbances are observed in the PSD curves apart from some power at the natural frequency mode of the system at 20Hz.

4.3.4 Tracking the force (gravity)

For a small telescope in which mirror cell can be considered rigid, no structural deformation takes place at different telescope orientation, and hence actuator need not be tracking the position. However, while following the object when telescope moves in elevation, there would be a systematic change in axial load (modulated by *wcos(z)*, where *w* is the static mass of the mirror and *z* is zenith angle). In such case, the soft actuator will act as a force actuator and expected to compensate for the variable axial force in such a way that segment will remain aligned. This mode of operation of the actuator can be considered force tracking mode. Whereas, while turning in elevation, the mirror cell of the large telescope also get deformed and hence require to be corrected for both, variable force as well as position. We used DLA with two prototype soft actuators built for two different telescope projects – PSMT and TMT. While tracking the celestial objects (at 15deg/hr max), the PSMT and TMT actuators will require tracking the force at the rate of 7mN/sec and 90mN/sec respectively. In order to conduct this test, the DLA was commanded to generate triangular force profile. The actuator under test get subjected to this variable force and allowed to correct it in a closed loop operation. The external force exerted by DLA is compensated by the equal and opposite force generated by the actuator as shown in Figure 4-13 and Figure 4-14. While chasing the external force, the PSMT actuators could achieve RMS tracking error of 5.44nm. When a similar test was conducted with the TMT actuator, then we could achieve the RMS tracking performance of 3.18nm.
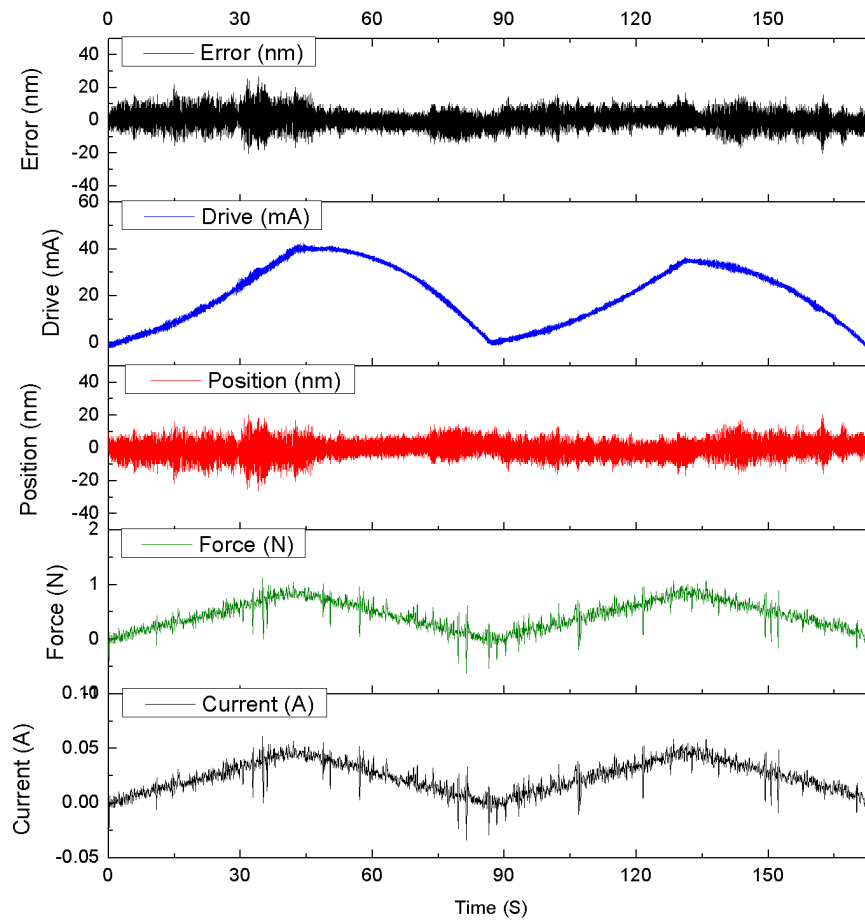
Figure 4-13. With PSMT Actuator, closed-loop force track rate of 22 mN/sec is achieved with the RMS tracking error of 5.44nmRMS. The external force disturbance is compensated with the help of additional drive signal.
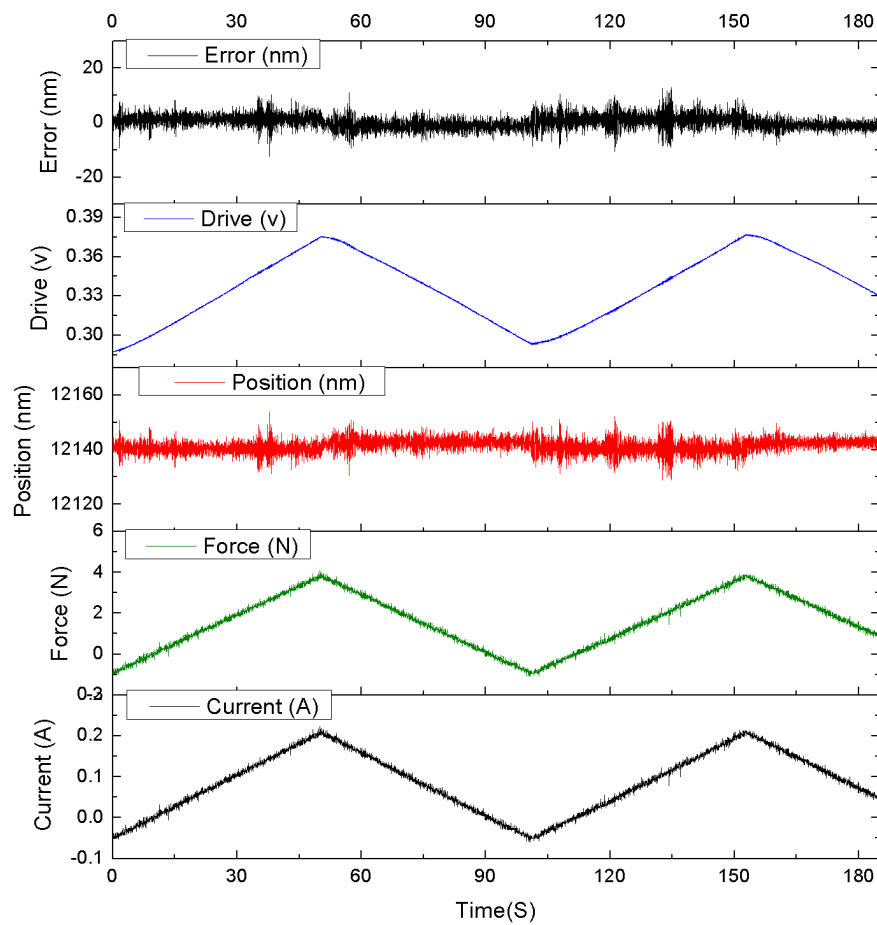
Figure 4-14. With TMT Actuator, closed-loop force track rate of 90mN/sec is achieved with the RMS tracking error of 3.18nmRMS. The external force disturbance is compensated with the help of additional drive signal.

4.3.5 Testing the wind disturbance rejection capability of the actuator

This is a last and crucial test to evaluate wind disturbance generation capability of DLA and ability to reject/suppress the wind effect by the actuator and the controller system. We used the actual wind data collected from Gemini South Telescope Wind Test Experiment (Observatory 2001) (Observatory 2001) (Cho, Stepp and S. Kim 2001) [Case: b09045oo.dat_windv5time (top of dome)]. The wind data is further processed using the Matlab-based tool developed by us which converts

Wind Speed data (m/s) to DLA Input Voltage (V). While doing the conversion, we have taken into account the size of the mirror, the drag coefficient as well as the expected mean speed at the site of interest (4m/sec in our case).
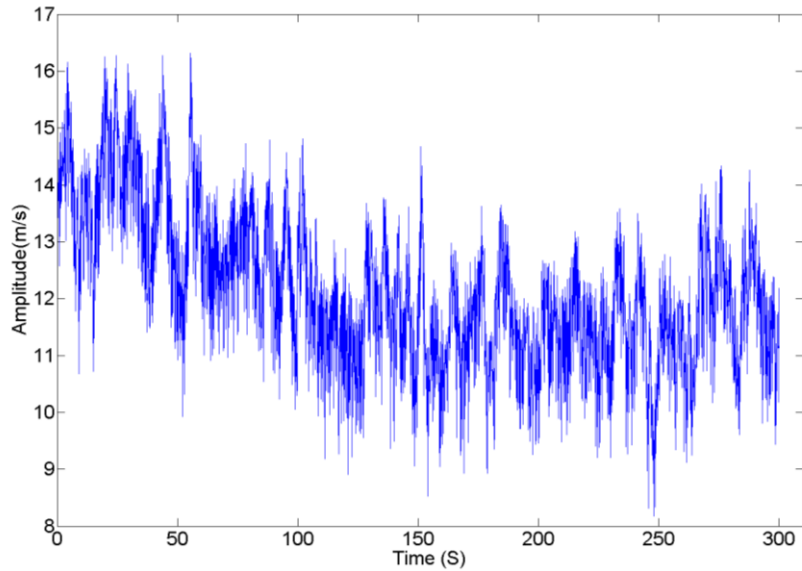
(a)
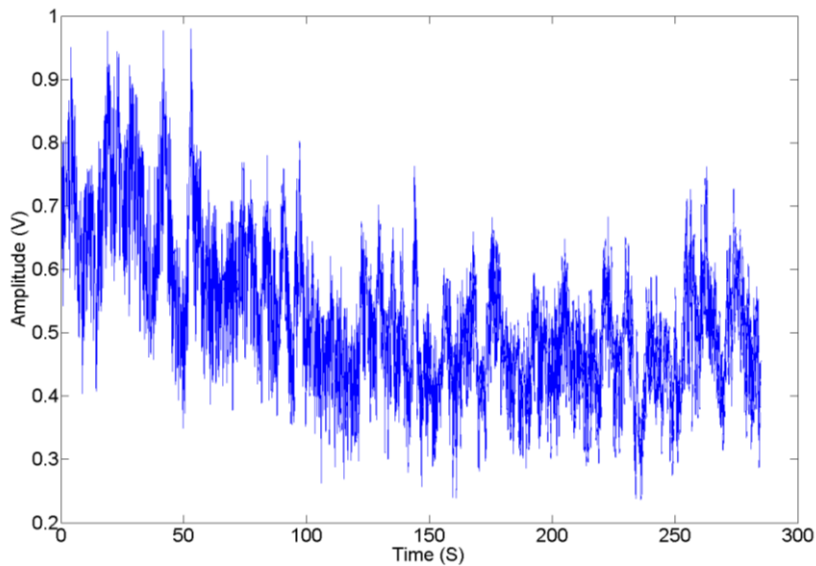
(b)

Figure 4-15. (a) Sample wind speed profile from Gemini South Telescope Wind Test Experiment [Data case: b09045oo.dat_windv5time (top of dome)]. (b) The input is given to the DLA to generate disturbance on the actuator. This profile corresponds to the voltage equivalence of the actual wind speed.

It can be seen that the wind does have a typical distribution and follows a spectral characteristic. It can be better characterized by von Karman model. The PSD plot along with the von Karman model fit of one of Gemini data set is shown in Figure 4-16.
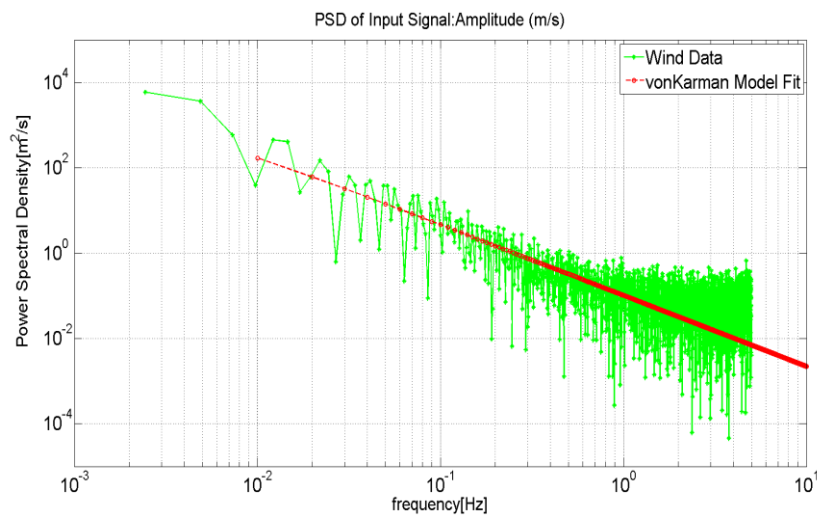
Figure 4-16. PSD of wind data [Data case: b09045oo.dat_windv5time (top of dome)]. The modeled von Karman spectrum is shown for comparison. The Force PSD on the primary mirror segments will be of the same nature.

To check the capability of the DLA that how well it can mimic the input wind profile as a force disturbance, we conducted an open loop test. In this test, one of the wind profile data is converted into the voltage profile and fed to DLA, while actuator controller was switched off. The output of the DLA is a disturbance, characterized in terms of encoder position. The input (wind) and output (encoder position) were compared, and a strong correlation (~80.4%) was found among them. In addition to this, we have also compared the PSD of the input and output, which is over-plotted in the Figure 4-18. As one can see from this figure, there is close agreement between these two PSD until 2.5 Hz. Since wind data itself is gathered at 5Hz sampling, therefore, we could not compare PSD beyond 2.5 Hz. However, a peak seen at around 20 Hz in output data is the first resonance frequency of the DLA system. This experiment ensures that the DLA is capable of simulating the wind disturbances on SMT actuator in the laboratory.
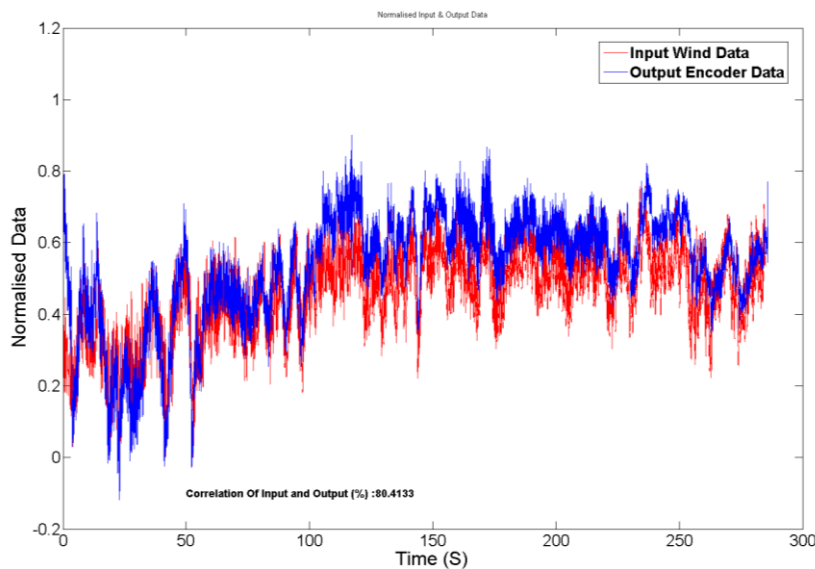
Figure 4-17. Comparison of input wind data and open loop output displacement (both normalized). Normalization is w.r.t the peak amplitudes. Correlation between these two signals is 80.4%.
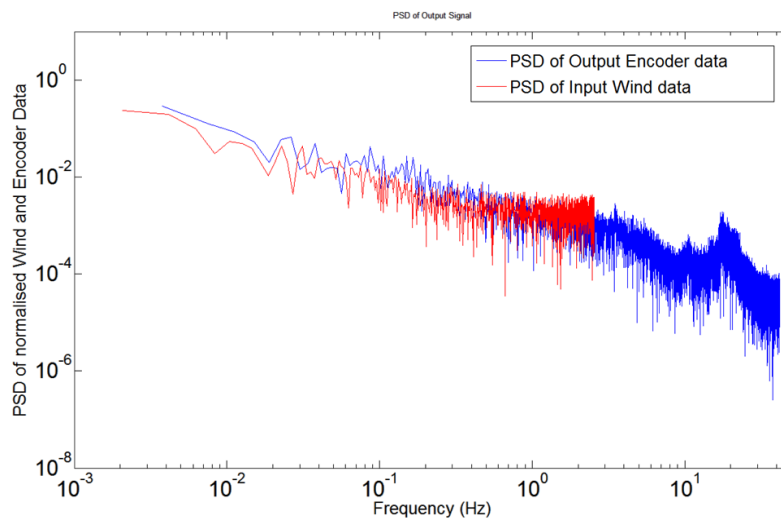
Figure 4-18. The PSD of the open loop response of the Actuator in comparison with the input wind disturbance data. The peak observed around 20Hz is due to the natural frequency mode of the system. As seen, the wind spectrum is recreated in the lower frequency regime which is the main frequency region of our interest.

Next, we switched ON the actuator controller and put it into open loop mode. The output of the encoder was monitored. As expected, in open loop mode the soft actuator was unable to correct the wind disturbances, and RMS error of about 61nm was seen. In addition to this, since soft actuator has got poor dynamic stiffness in the

low-frequency region, therefore, the whole actuator get displaced downward by 178 nm, which is the effect of DC part of the wind profile.

The last test was conducted to test the disturbance rejection ability of the actuator in a closed loop control mode. This time again the same wind disturbance was generated using DLA, however, allowed the actuator to correct it. This time RMS position error was found to be 4.7nm, which otherwise was 61nm in the open loop mode.
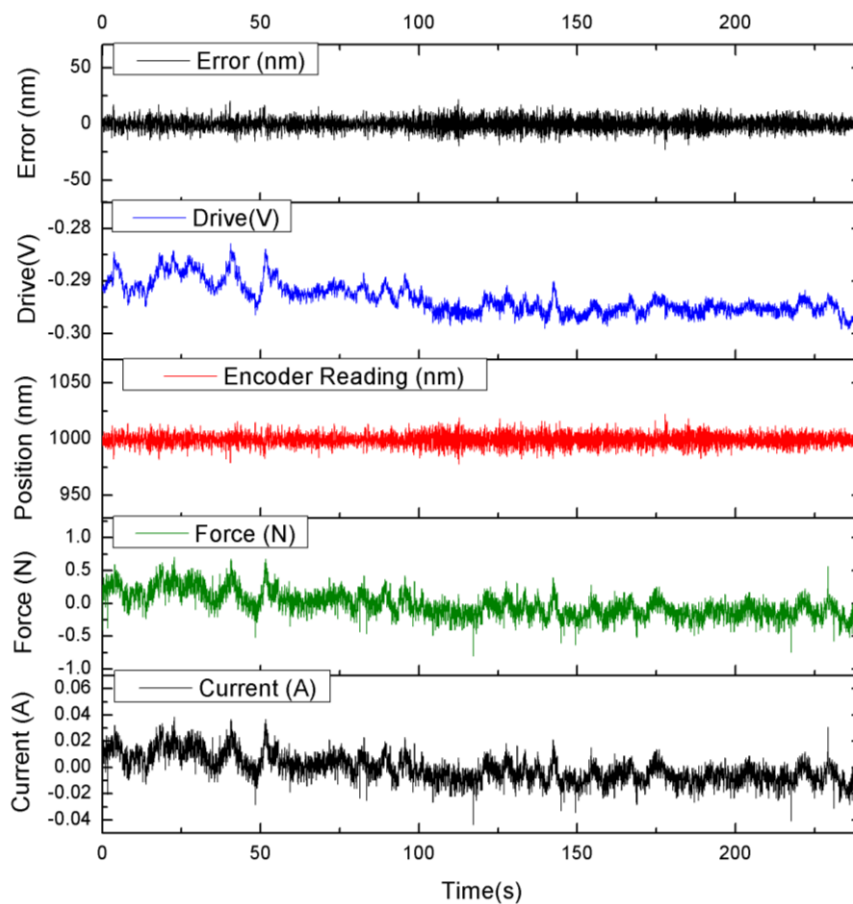
Figure 4-19. With TMT Actuator, the closed-loop response for input wind disturbance. The RMS Tracking Error of 4.7 nm is achieved. Due to the closed loop operation additional drive signal is consumed to overcome the disturbance force as seen above. In open loop mode, same wind disturbance deviates actuator position up to 61nm RMS.

Similarly, the closed loop test was conducted to evaluate the wind rejection capability of PSMT actuator. The RMS error was found to be 12.43nm, which otherwise was 303nm RMS in the open loop mode.
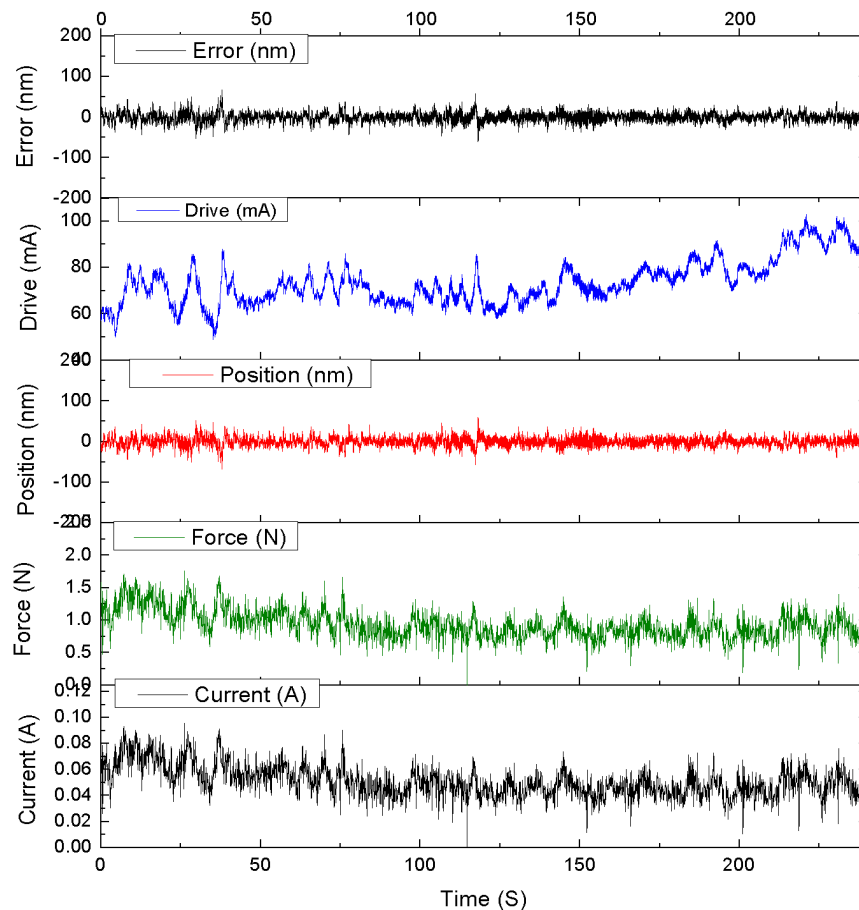
Figure 4-20. With PSMT Actuator, the closed-loop response for input wind disturbance. The RMS Tracking error of 12.43 nm is achieved. Due to the closed loop operation additional drive signal is consumed to overcome the disturbance force as seen above. In open loop, same wind disturbance deviates actuator position up to 303nm RMS.

4.4   Summary and Conclusion

The soft actuator appears to be a natural choice for the large segment mirror telescopes which aimed to perform reasonably well to the science programs requiring very high spatial resolution by the aid of extreme AO (Lorell, Aubrun, et al. 2006), (MacMynowski, Thompson and Shelton, et al. 2011). This primarily happens because they have got the ability to reject structural vibration which is nothing but high-frequency, low-amplitude disturbances. In addition to this, VCM based soft-actuator also promises high precision in a straightforward mechanical configuration and hence opens the avenue for development of low-cost actuator for any segmented mirror telescope such as PSMT. These soft-actuators need to go through various performance tests, which usually require complicated and expensive test setup (Jiménez, et al. 2010) (T. Viera, et al. 2008) (Witvoet, den Breeje, et al. 2014). In the present work, we have shown that a simple device like our DLA, which is also very cost-effective and easy to design and realize, can be used to evaluate most of the performance requirements of any SMT actuators.

We modeled, designed, manufactured and tested a dynamic loading assembly which can be used to simulate the wind-induced disturbances in the laboratory. Since the device is primarily developed to test the performance of soft actuators, therefore, the effort has been made first to identify different performance requirements of SMT actuators and then after the top level requirements for the DLA were generated. In the next step, the mechanical design of DLA was carried out, and its parameters were fine-tuned by using analytical modeling. The care was taken to keep structural modes out of wind spectral range ($< 10Hz$) and minimize the loss of force due to the device itself. Above two aspects, we could achieve by selecting appropriate springs as well as bearings. Additionally, voice coil motor (VCM) is used to generate dynamic disturbances, which provide high bandwidth and frictionless operation. We have also developed a dedicated control electronics for the DLA, which can also handle a couple of sensors used in the device. While designing the PCB, the care has been taken that it should withstand in high power mode during which the current flowing in the circuitry can be as large as 3A. The drive electronics has provision to select either

voltage or current mode of operation to drive VCM. The smoothing effect of back emf generated by the VCM can be avoided if we operate VCM in the current mode, which in turn generate more accurate wind force profile at higher frequencies. In the beginning, different tests were conducted to check the performance of DLA device itself. Once it was found that DLA can generate the required disturbances precisely then, we used it to test the performance of two different prototype actuators being developed for two different projects, namely PSMT and TMT. We could demonstrate that despite being soft actuators, the PSMT and TMT both actuators can effectively suppress the wind-induced disturbance with achieved RMS Tracking Error of 4.7 nm and 12.43 nm when operated in the closed loop.

After conducting verities of the tests over the period of about two years, we have identified a few limitations in the present DLA system, which may be taken into account when developing the next version of it. One of the limitations of the device is that it cannot generate force slew rates (say 15N/s), may require in testing actuator performance when the telescope is slewing from one object to other during the pointing. Another limitation is that DLA can introduce maximum static load up to 250N and is always subjected with 50N and above static load arising from fixed intermediate plates used to interface actuator with the DLA.

Chapter 5   Code SMT: A simulation tool for Primary Mirror Control System

In the Segmented Mirror Telescopes, once the mirror segments of the primary mirror get aligned and phased for the correction inter-segment piston error with the help of Alignment and Phasing System, then after it is the responsibility of primary mirror control to maintain its shape over the weeks and months. The edge sensors detect any changes in the mirror segment position due to varying gravity and/or temperature and subsequently get corrected by the actuators with the help of a global controller. The current chapter deals with our effort to develop a global controller for the M1CS as well as a simulation tool.

5.1   The Global Control System

The global controller is a very vital part of the primary mirror control system, also known as the global loop controller. The out of plane degrees of freedom (piston, tip, and tilt) of each segment in the Segmented Mirror Telescope (SMT) primary mirror is actively controlled using three actuators per segment and two edge sensors along each intersegment gap. The conversion of position information from sensor space to required displacement in actuator space is done using the global controller with the help of the interaction matrix. The global loop controller then sends commands to three actuators on each segment to maintain shape, as nearly as possible. All the segments get adjusted with their neighbors within a few nanometers. This loop operates at approximately 1 Hz.

The control of large segmented telescopes is a challenging one due to the complexity and high order of the system. The high order dynamics leads to high order controllers that require more memory and faster computations for implementation (Angeli, Cho and Whorton 2003). While this may not pose a severe problem for telescopes with a small number of segments (e.g., PSMT), as the number of segments increases the computational requirements will be enormous. It is essential to integrate the actuator and sensor system with M1CS global controller and investigate the performance and computational requirements of control design. In this work we have designed, simulated, and implemented an entire primary mirror control scheme for the Prototype Segmented Mirror Telescope and generalized it further into a software analysis tool called as the codeSMT, presented in Section 5.2. Further using the codeSMT tool we have conducted two major studies, one on active control simulation and other on error multiplier analysis for the PSMT, which we have presented later in the Chapter 6.

5.1.1 Mathematical formulation

The geometry of a typical SMT with seven segments and with hexagonal mirrors (similar to PSMT) is shown in Figure 5-1. The basic mathematical formulation used in the following sections has been derived from the pioneering works carried out by Jerry Nelson and his collaborators for the Keck and TMT telescopes (J. Nelson 2005), (MacMartin and Chanan. 2003), (Chanan, et al. 2004) and (MacMartin and Chanan 2004). Three actuators per segment are placed in a triangular geometry supports the mirror to provide tip, tilt, and piston. The numbering and location of actuators and sensors are also shown. Central mirror has 12 edge sensors at its periphery altogether, whereas outer ring mirrors have 6 edge sensors. Each edge sensor has one drive half and one sense half. Every side of the segment has one drive and one sense alternately. Sensors are placed such as to sense the intersegment height differences.
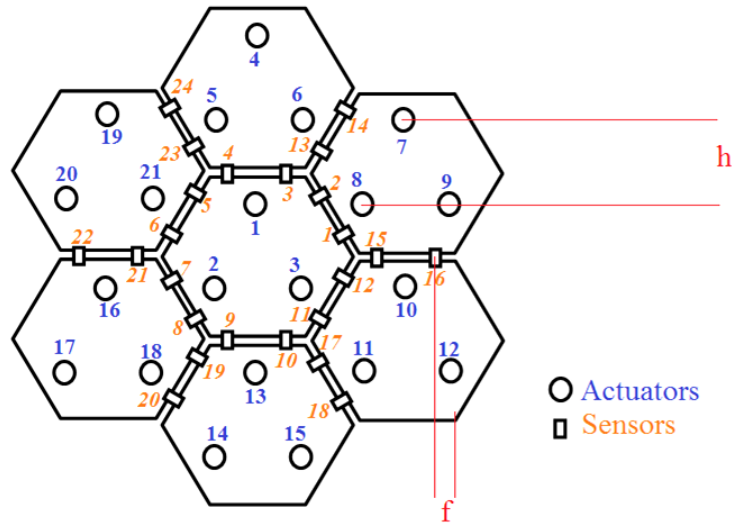
Figure 5-1 Numbering scheme of Actuators and Sensors on the seven segments of the PSMT.

It can be seen that (from Figure 5-1) every actuator can influence the maximum of 12 edge sensors (e.g., Actuator 1, 2, 3 have an influence on sensor 1 to 12 only.) Whereas every sensor has an influence on exactly 6 actuators. The numbering sequence of sensors and actuators as shown in Figure 5-1, does not have any particular significance unless and until we know which segment have which sensors and actuators associated with it. We have selected this numbering scheme to make it convenient to extend it to develop a simulation tool for a generic SMT parameters (see Section 5.2).
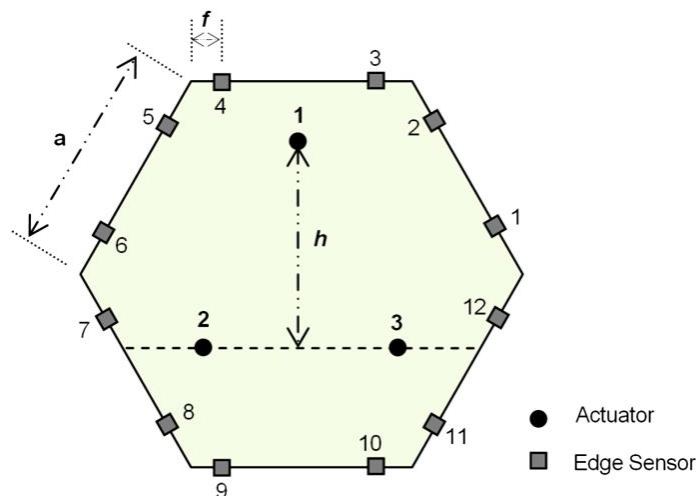
Figure 5-2 Location of sensors and actuators w.r.t segment.

Different segment parameters considered while mathematical formation are:

h = perpendicular distance from any actuator to line joining other two actuators of that segment (actuator triangle height).

f = distance of sensor half from the nearest segment edge.

a = side length of segment.

(x, y) = coordinates of segment center.

Following are the set of equations that gives the relation of edge sensors to the individual actuator displacement. The relations are obtained from the geometry in Figure 5-2 (similar to the one used in (Chanan, et al. 2004)), wherein the Actuator is displaced by ΔZ, and the corresponding displacement at every sensor is computed by the formula in Equation 5.1.

$$\Delta s = \Delta z\, \frac{r}{h}$$
<div align="right">Equation 5-1</div>

Where,

r = perpendicular distance from the sensor to the rotation axis, and the sign of r is positive if the sensor and actuator are on the same side of the rotation.

Δs = sensor height displacement

Δz = actuator height displacement

Therefore the equation of sensor readings due to the displacement of Actuator-1 are given as:

$$\Delta s_{1,1} = \Delta z_1 \left(\frac{1}{3} h + f \cos 30^\circ \right) / h, \qquad \Delta s_{7,1} = \Delta z_1 \left(\frac{1}{3} h - f \cos 30^\circ \right) / h,$$

$$\Delta s_{2,1} = \Delta z_1 \left(\frac{1}{3} h + (a-f) \cos 30^\circ \right) / h, \qquad \Delta s_{8,1} = \Delta z_1 \left(\frac{1}{3} h - (a-f) \cos 30^\circ \right) / h,$$

$$\Delta s_{3,1} = \Delta z_1 \left(\frac{1}{3} h + a \cos 30^\circ \right) / h, \qquad \Delta s_{9,1} = \Delta z_1 \left(\frac{1}{3} h - a \cos 30^\circ \right) / h,$$

$$\Delta s_{4,1} = \Delta z_1 \left(\frac{1}{3} h + a \cos 30^\circ \right) / h, \qquad \Delta s_{10,1} = \Delta z_1 \left(\frac{1}{3} h - a \cos 30^\circ \right) / h,$$

$$\Delta s_{5,1} = \Delta z_1 \left(\frac{1}{3} h + (a-f) \cos 30^\circ \right) / h, \qquad \Delta s_{11,1} = \Delta z_1 \left(\frac{1}{3} h - (a-f) \cos 30^\circ \right) / h,$$

$$\Delta s_{6,1} = \Delta z_1 \left(\frac{1}{3} h + f \cos 30^\circ \right) / h. \qquad \Delta s_{12,1} = \Delta z_1 \left(\frac{1}{3} h + f \cos 30^\circ \right) / h.$$

<div align="center">Equation 5-2</div>

Here,

for sensors 7 to 12, $\Delta s_{j,1}$ can also be obtained from $\Delta s_{j-6,1}$,

but with $\cos 30^\circ$ replaced by $(-\cos 30^\circ)$ & $\sin 30^\circ$ replaced $(-\sin 30^\circ)$.

From Equation 5.2

$$A_{j,1} = \pm \Delta s_{j,1} / \Delta z_1$$

In general;

$$\Delta s_j = \sum_i A_{j,i} \Delta z_i,$$

$$\Delta z_i = \sum_j A_{j,i}^{-1} \Delta s_j \qquad \text{Equation 5-3}$$

where,

$i = all\ actuators,\ j = all\ sensors.$

So for *i* actuators and *j* sensors in a given SMT we have;

$$s_j = A_{j,i} \times z_i \qquad \text{Equation 5-4}$$

Where, *z* is a vector containing all of the actuator lengths *(i),* and *s* is a vector of all of the sensor lengths *(j).* The interaction matrix *A(j* x *i)* is determined solely by geometry. The control Equation 5-4 directly gives the sensor values corresponding to the actuator lengths. The *A* matrix can be computed solely by knowing the geometry of SMT as presented in Section 5.1.2. But in practice, it is generated by finding the

relation of every actuator to every sensor (elements of the interaction matrix) experimentally on the actual telescope.

5.1.2 Interaction matrix (A)

The A matrix is called as active control matrix or interaction matrix which is primarily formulated from the geometrical distribution of edge sensors and actuators in a segmented mirror telescope. Individual elements in this matrix are nothing but the constants which relates every actuator to every sensor. The matrix A is a sparse matrix in which most of its elements are zero (see Figure 5-5), due to the reason that every actuator have an influence on at max 12 sensors and every sensor have an influence on exactly six actuators.

The relations to form the A matrix are as below (based on Equation 5.2 and given in (Chanan, et al. 2004)). Putting in the appropriate signs, trigonometric factors, and normalizations for all terms, we obtain the typical matrix elements.

$$A_{1,1} = -(\frac{1}{3}h + f\cos 30^\circ)/h - \eta\sin 30^\circ,$$

$$A_{2,1} = \left[\frac{1}{3}h + (a-f)\cos 30^\circ\right]/h - \eta\sin 30^\circ,$$

$$A_{3,1} = -(\frac{1}{3}h + a\cos 30^\circ)/h - \eta,$$

$$A_{4,1} = (\frac{1}{3}h + a\cos 30^\circ)/h - \eta,$$

$$A_{5,1} = -\left[\frac{1}{3}h + (a-f)\cos 30^\circ\right]/h - \eta\sin 30^\circ,$$

$$A_{6,1} = (\frac{1}{3}h + f\cos 30^\circ)/h - \eta\sin 30^\circ,$$

$$A_{7,1} = -(\frac{1}{3}h - f\cos 30^\circ)/h + \eta\sin 30^\circ,$$

$$A_{8,1} = \left[\frac{1}{3}h - (a-f)\cos 30^\circ\right]/h + \eta\sin 30^\circ,$$

$$A_{9,1} = -(\frac{1}{3}h - a\cos 30^\circ)/h + \eta,$$

$$A_{10,1} = (\frac{1}{3}h - a\cos 30^\circ)/h + \eta,$$

$$A_{11,1} = -\left[\frac{1}{3}h - (a-f)\cos 30^\circ\right]/h + \eta\sin 30^\circ,$$

$$A_{12,1} = (\frac{1}{3}h - f\cos 30^\circ)/h + \eta\sin 30^\circ,$$

Equation 5-5

The matrix elements $A_{j,1}$ with j=7 to 12 can be obtained from $A_{j-6,1}$ with $\cos 30^\circ$ replaced by $(-\cos 30^\circ)$ & η replaced by $-\eta$. (no change in $\sin 30^\circ$).

where,

$$\eta = \frac{l^2}{8h\delta}$$

$\eta =$ quantifies the relative sensitivity to rotation $($dihedral angle$)$ w.r.t shear,

$l =$ is the vertical height of the edge sensor, and

$\delta =$ is the sensor gap.

Equation 5-6
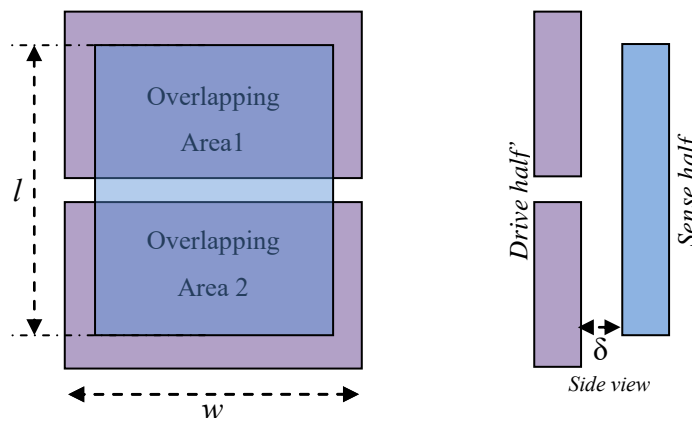
Figure 5-3 Geometry of the edge sensor.

The η quantifies the relative sensitivity to the rotation (dihedral angle) w.r.t shear. l is the vertical height of the edge sensor and δ is the sensor gap (see Figure 5-3). In our entire calculation for PSMT, we have taken η value to be 0.05 which is a conservative approach, whereas in reality it will be estimated experimentally on the telescope. Maintaining the proper sign conventions, entire control matrix A is filled in the same way in Equation 5-5.

The actuator changes that will maintain the desired sensor readings are calculated with the aid of the pseudo-inverse matrix elements $A^{-1}_{ji.}$ via,

$$\Delta z_i = \sum_j A^{-1}_{j,i} \Delta s_j$$

Equation 5-7

Where the symbol Δz_i refers to the difference between the actual and desired actuator values and similarly for the corresponding differences Δs_j in the sensor readings.

In the KECK telescope, the values of the ratios *f/a*, *g/a* and *h/a* are selected close to optimal in the sense of minimal noise multiplication, but they also reflect various practical considerations. That is the precise values of these ratios do not have a fundamental significance (Chanan, et al. 2004). The parameter *g* is the edge sensor position offset from the segment side and is applicable only for horizontal edge sensors that are used in the KECK telescope. The telescopes with vertical sensors like PSMT, TMT, E-ELT will have *g*=0.

In KECK telescope: *a*= 900mm, *f*= 173mm, *g*= 55mm, *h*= 706mm. Therefore the ratios, *f/a*=173/900= 0.192222; *g/a*=55/900= 0.061111; *h/a*=706/900= 0.784444. Using these ratios from KECK, we have estimated optimal values of parameters for different telescopes as listed in

Table 5-1.

Table 5-1 The interaction matrix parameters for different telescopes.

Telescope	a(mm)	f(mm)	g(mm)	h(mm)	l(mm)	gap(d)mm
KECK	900	173	55	706	--	--
SALT	577	110	0	452	--	--
CELT	500	96.1	0	400	20	--
TMT	720	138.3	0	564.7	44	2.5
PSMT	300	57.7	0	235.2	20	4
NLOT	720	138.3	0	564.7	44	2.5

The *A* matrix formed for the PSMT Telescope with parameters from Table 5-1 is shown below in graphical matrix form.

																			Actuator Number		
Sensor	1	2	3	4	5	6	7	8	9	10	11	12	13	14	15	16	17	18	19	20	21
1	-0.572	0.8238	-1.252	0	0	0	-0.532	1.3843	0.1477	0	0	0	0	0	0	0	0	0	0	0	0
2	1.1986	-0.718	0.519	0	0	0	-0.095	-1.491	0.5851	0	0	0	0	0	0	0	0	0	0	0	0
3	-1.491	0.5851	-0.095	-0.718	0.519	1.1986	0	0	0	0	0	0	0	0	0	0	0	0	0	0	0
4	1.3843	0.1477	-0.532	0.8238	-1.252	-0.572	0	0	0	0	0	0	0	0	0	0	0	0	0	0	0
5	-1.252	-0.572	0.8238	0	0	0	0	0	0	0	0	0	0	0	0	0	0	0	0.1477	-0.532	1.3843
6	0.519	1.1986	-0.718	0	0	0	0	0	0	0	0	0	0	0	0	0	0	0	0.5851	-0.095	-1.491
7	-0.095	-1.491	0.5851	0	0	0	0	0	0	0	0	0	0	0	0	1.1986	-0.718	0.519	0	0	0
8	-0.532	1.3843	0.1477	0	0	0	0	0	0	0	0	0	0	0	0	-0.572	0.8238	-1.252	0	0	0
9	0.8238	-1.252	-0.572	0	0	0	0	0	0	0	0	0	1.3843	0.1477	-0.532	0	0	0	0	0	0
10	-0.718	0.519	1.1986	0	0	0	0	0	0	0	0	0	-1.491	0.5851	-0.095	0	0	0	0	0	0
11	0.5851	-0.095	-1.491	0	0	0	0	0	0	0.519	1.1986	-0.718	0	0	0	0	0	0	0	0	0
12	0.1477	-0.532	1.3843	0	0	0	0	0	0	-1.252	-0.572	0.8238	0	0	0	0	0	0	0	0	0
13	0	0	0	0.5851	-0.095	-1.491	0.519	1.1986	-0.718	0	0	0	0	0	0	0	0	0	0	0	0
14	0	0	0	0.1477	-0.532	1.3843	-1.252	-0.572	0.8238	0	0	0	0	0	0	0	0	0	0	0	0
15	0	0	0	-0.532	1.3843	0.1477	0	0	0	0	0	0	0	0	0	0	0	0	-0.572	0.8238	-1.252
16	0	0	0	-0.095	-1.491	0.5851	0	0	0	0	0	0	0	0	0	0	0	0	1.1986	-0.718	0.519
17	0	0	0	0	0	0	0	0	0	0	0	0	0	0	0	-1.491	0.5851	-0.095	-0.718	0.519	1.1986
18	0	0	0	0	0	0	0	0	0	0	0	0	0	0	0	1.3843	0.1477	-0.532	0.8238	-1.252	-0.572
19	0	0	0	0	0	0	0	0	0	0	0	0	-1.252	-0.572	0.8238	0.1477	-0.532	1.3843	0	0	0
20	0	0	0	0	0	0	0	0	0	0	0	0	0.519	1.1986	-0.718	0.5851	-0.095	-1.491	0	0	0
21	0	0	0	0	0	0	0	0	0	-0.095	-1.491	0.5851	1.1986	-0.718	0.519	0	0	0	0	0	0
22	0	0	0	0	0	0	0	0	0	-0.532	1.3843	0.1477	-0.572	0.8238	-1.252	0	0	0	0	0	0
23	0	0	0	0	0	0	0.8238	-1.252	-0.572	1.3843	0.1477	-0.532	0	0	0	0	0	0	0	0	0
24	0	0	0	0	0	0	-0.718	0.519	1.1986	-1.491	0.5851	-0.095	0	0	0	0	0	0	0	0	0

Figure 5-4 Values of *A* matrix elements of the PSMT. It can be seen that central three (first three) actuators have an effect on 12 sensors and rest of the actuators affect 6 sensors.
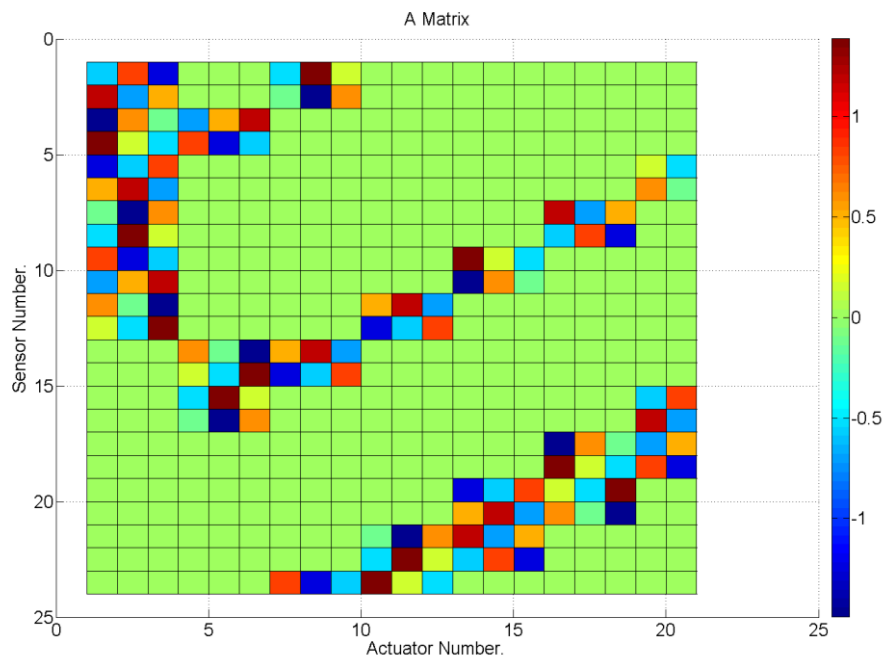
(a)
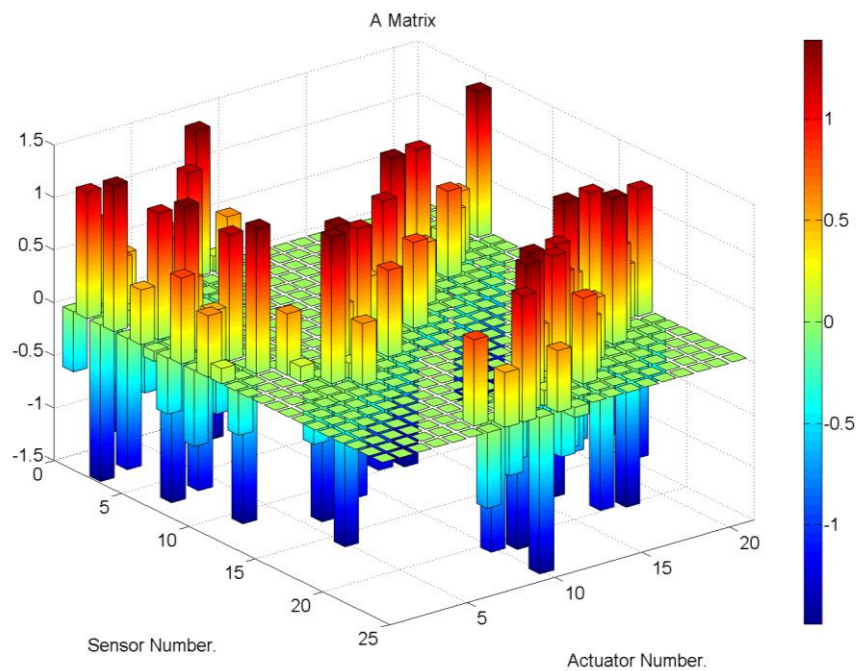
(b)

Figure 5-5 (a, b) Graphical representation of the control matrix (*A* matrix) of the PSMT.

5.1.3 Matrix Inversion and SVD

To correct the deformed mirror shape, we measure the edge sensor readings and use it with A^{-1} matrix (see Equation 5.7) to find desired actuator corrections. So we need to obtain the A^{-1} from the A matrix first. Matrix inversion is the process of finding the matrix A^{-1} that satisfies the equation $A^{-1} \times A = I$ (i.e., identity matrix) for a given invertible matrix A. Implementing the actual control requires solving the inverse problem, i.e., what (changes in the) sensor readings are required to produce the desired (changes in the) actuator lengths.

Since in general, every segment requires six edge sensors and three actuators, therefore, the number of actuators is always lesser than the number of sensors, and hence A is not a square matrix (overdetermined system). Therefore, the inverse of A matrix does not exist, for that matter, an exact solution does not exist. The least-squares solution can be constructed from the pseudo-inverse matrix, which does exist and can be constructed by straightforward means and which will still be denoted by

A^{-1}. The particularly useful technique for constructing the pseudo-inverse is the singular value decomposition (SVD) (Golub and Loan. 1996) and (Press, et al. 1989)) of the original control matrix.

In SVD, the ($j \times i$) matrix A (where $j \geq i$) can be written as the product of three matrices:

$$A_{j \times i} = U_{j \times j} W_{j \times i} V^T_{i \times i}$$

<div align="right">Equation 5-8</div>

Where,

U is $j \times j$ column orthogonal matrix, and its columns are Eigenvectors of AA^T,

W is $j \times i$ diagonal matrix whose diagonal elements w_i are positive or zero and is referred to as the singular values of the matrix A,

V is $i \times i$ orthonormal matrix, and its columns are Eigen vectors of $A^T A$. The symbol ^{T} denotes transpose.

The pseudo-inverse of A is then obtained as

$$A^{-1} = VW^{-1}U^T$$

<div align="right">Equation 5-9</div>

Here the W^{-1} is pseudoinverse of the matrix W, which is formed by replacing every non-zero diagonal entry by its reciprocal and transposing the resulting matrix. The jth diagonal element ($1/w_j$) of W^{-1} is replaced by 0 in the event that $w_j = 0$.
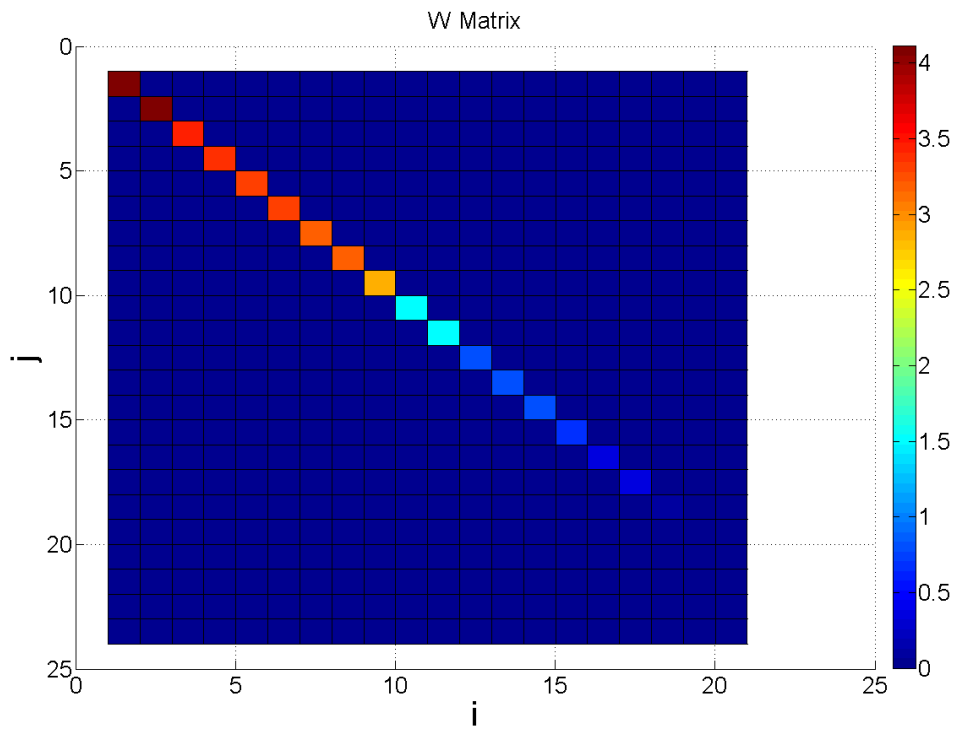
Figure 5-6 The graphical representation of the *W* matrix. Diagonal values of *W* are the singular values of matrix *A*.

The matrix *V* defines an essentially unique orthonormal basis set of modes of the system, such that any arbitrary configuration of the system can be expressed as a unique linear combination of these modes. In particular, V_{ij} gives the value of the ith actuator in the jth mode (Chanan, et al. 2004).
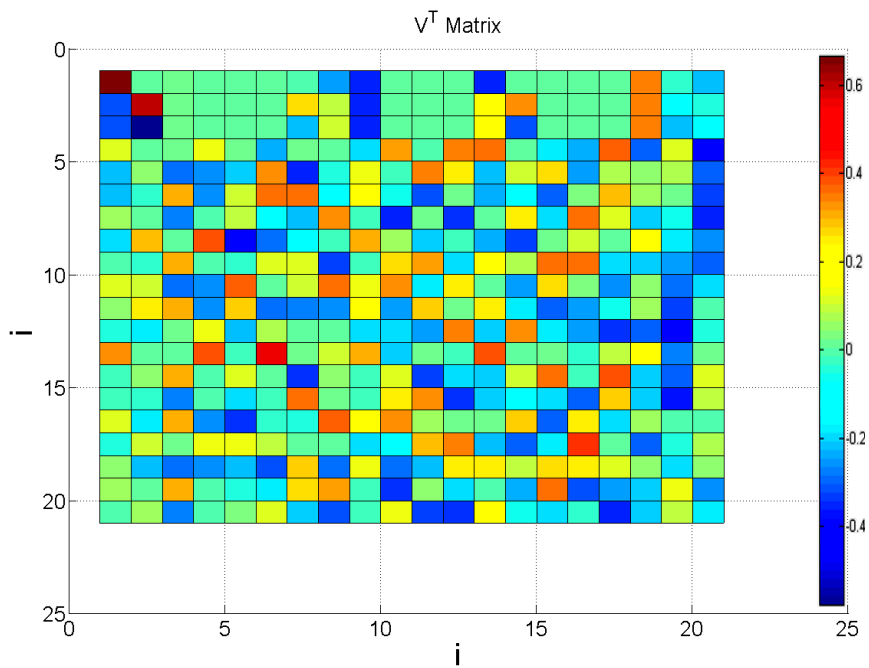
Figure 5-7 The graphical representation of the V^T matrix.
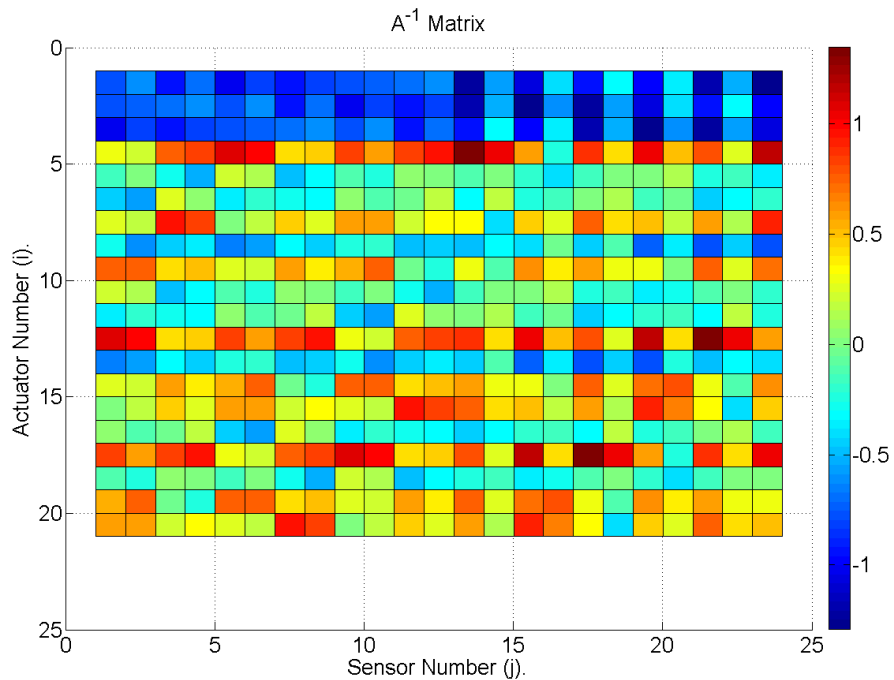
Figure 5-8 The graphical representation of A^{-1} matrix obtained using SVD.
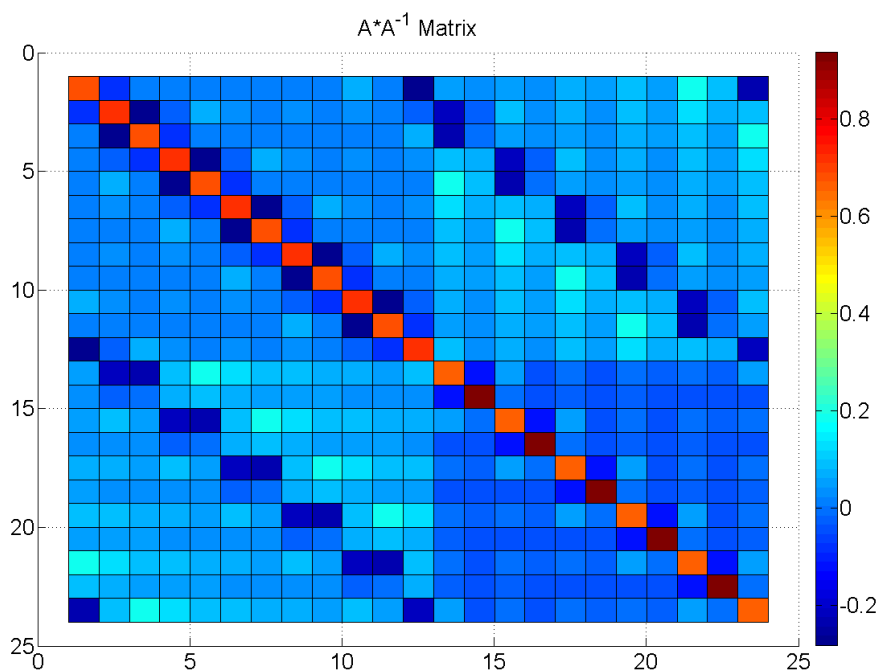
Figure 5-9 Product of A matrix and A^{-1} matrix ($A \times A^{-1}$).
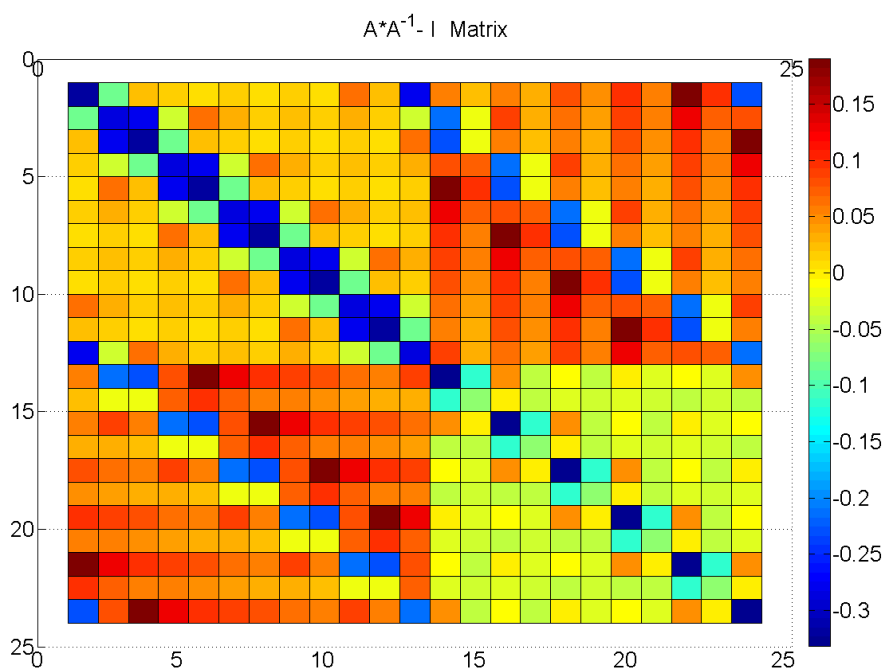
Figure 5-10 Residue calculation from the product of A and A^{-1} matrix ($A \times A^{-1} - I$).

As seen in Figure 5-10, very small but the finite residue is present due to the error in the pseudo-inversion process, which is unavoidable whereas its effect on the

global controller calculation error is negligible. The SVD is one of the widely used methods for constructing the pseudo-inverse. We obtained results from the SVD calculations and compared with other inversion techniques (see Appendix C) and the SVD method was found to be suitable and sufficient for our application.

5.2   The codeSMT tool

To explore the Primary Mirror Control System in a more detailed way, we have developed a generic software tool called as the codeSMT. The codeSMT is fairly generic in the sense that it can be used for a telescope of any size, made of one or more rings, and having diverse sensor-actuator geometrical configurations. The tool is also capable of carrying out error analysis; more specifically it allows studying the effect of sensor noise on various modes (un-corrected deformations) of the primary mirror. Another notable feature of this tool is that it can incorporate the dynamic behavior of the actuators in the presence of wind disturbances, which helps to evaluate the telescope performance.

5.2.1 Features of the codeSMT tool

The codeSMT is a generic design and simulation tool developed for conducting a variety of studies related to the Primary Mirror Control System of SMTs. This tool is equipped with different features such as formulating the SMT with various telescope parameters like mirror sizes, the number of segments, types of sensors and actuators, disturbances, control loops, etc. Also, it is capable of generating results in the form of mirror deformations, wavefront error, point spread function (PSF), error multiplier plots, parameter sensitivity plots, including text data outputs. A dedicated segment plotting tool is designed and integrated with codeSMT so as to visualize overall primary mirror shape as well as the shape of the primary mirror in different spatial modes (defocus, astigmatism, coma, spherical, etc.). The sensitivity of various parameters related to SMT primary mirror can be studied in

terms of its effect on the mirror shape and on the error multipliers which is an advantageous feature during the early design phase of the SMTs.

Main Features:	
Parameter sensitivity :	Segment size, a
	Actuator position, h
	Sensor position, f
	Sensor type
	Number of Rings, N
Input data of actuator/sensor	
Open /closed loop iterations	
Wind disturbance	
Noise and error analysis	
Telescope segment geometries	
3D segment plots	
Mode shapes plots	
PSF of the primary mirror	
Tip-Tilt of the primary mirror	
Image motion and evolution	
Link to ZEMAX	
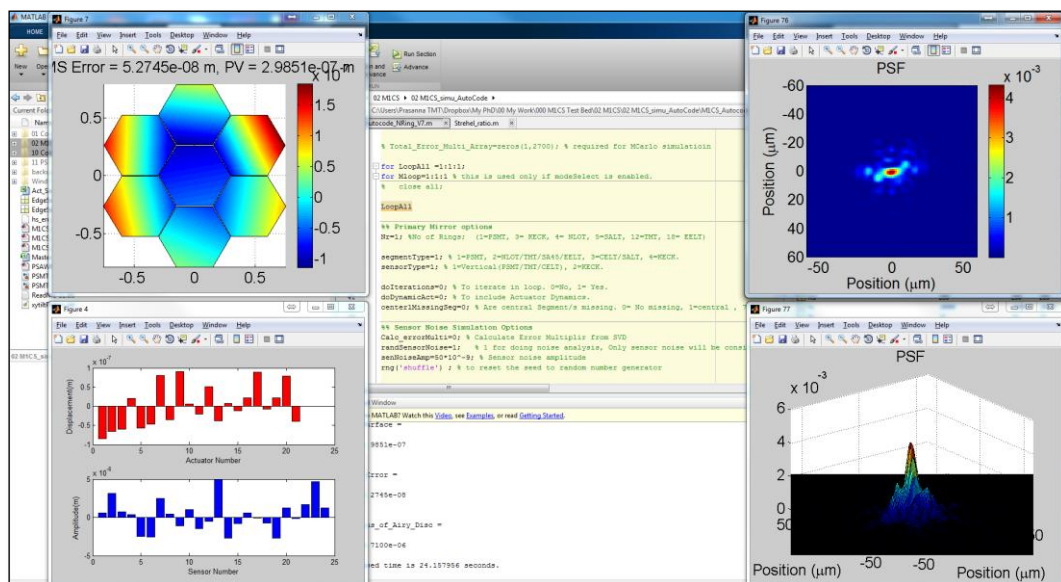
Figure 5-11 Screenshot of the codeSMT tool with sample outputs.

5.2.2 Design of the codeSMT tool

The main computation module in the codeSMT is to transform the edge sensor readings into the corresponding actuator corrections, so as to maintain the shape of the primary mirror w.r.t., its reference shape. The underlying mathematical formulation used in codeSMT is similar to that of explained in Section 5.1. The relation between sensors and actuators are represented by a control matrix called A matrix.

$$s = A \times z \ \text{ and } \ z = A^{-1}s \qquad\qquad \text{Equation 5-10}$$

Here, s is a vector holding position value of the all the edge sensors and z is another vector representing displacement values of all actuators. The control matrix A depends solely on the geometry of actuators and sensors placed in the mirror segment (see Figure 5-2). However, during real operation of any segmented mirror telescope, edge sensor values are the known quantity, and the displacement of actuators is required to be computed to bring back the shape of the mirror.

To do the calculation of converting the sensors readings to the actuator commands, we first need to formulate the actuator, sensor, and interaction matrices in proper order. This requires exact knowledge of, which segment is associated with which actuators and which actuators affect which sensors. Also, the order of actuator and sensor is significant. As seen in Figure 5-1 and Figure 5-12, one actuator can affect at max 12 edge sensors whereas one sensor has an influence on exactly 6 actuators. So for the scheme of the order and numbering of the segments, actuators, and sensors we did the rigorous literature review of several existing and upcoming SMTs. We realized that there is no standard/generic practice of the component numbering scheme and the influence matrix generation. Though the numbering sequence of sensors and actuators does not have any significance on calculations, having the exact knowledge of which sensors and actuators are associated with which segments and in the proper order of Sensor-Actuator relation is the necessity. It is also true that we could manually do the numbering and formulate the interaction matrix, but it becomes complicated to handle it manually for large telescopes with few hundred sensors and actuators. Also, there is no direct mathematical formula for the

relation between actuator number and the corresponding sensor numbers so as to automate the process.
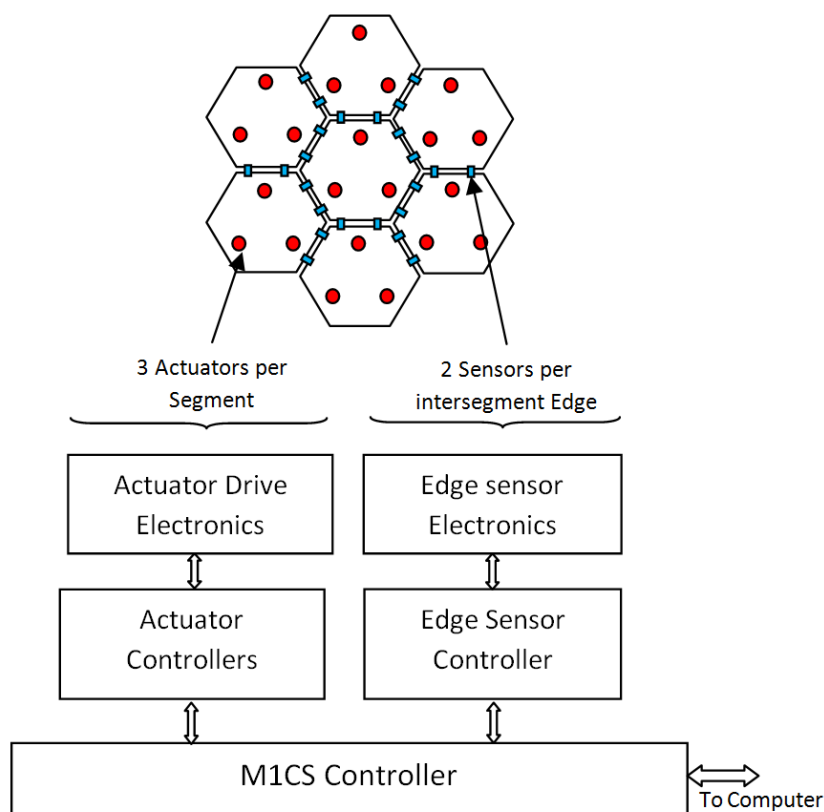
Figure 5-12. Schematic view of the PSMT M1 Control System (PSMT M1CS).

To solve this need of component numbering, we have introduced a new numbering scheme and also derived the interaction matrix database (for up to 12 ring telescopes) which can be easily used by the telescope designers, if they follow proposed numbering scheme. There is also a provision to alter this numbering scheme by the use of a mapping scheme provided with this tool. The database is generated by a semi-automated process using the segment data templates developed by us in the Microsoft Office Excel software.
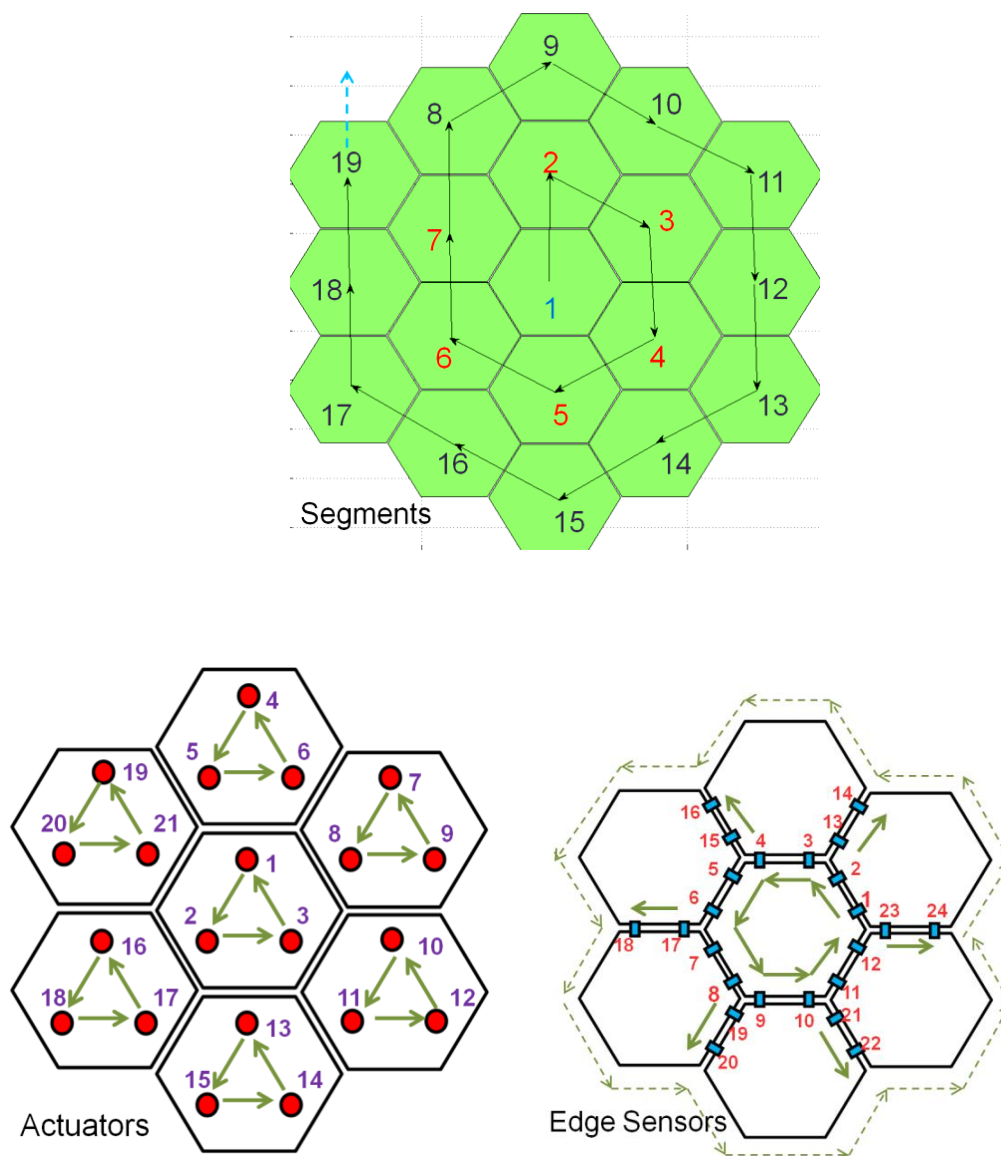
Figure 5-13. The segment, actuator, and sensor numbering scheme proposed for the codeSMT tool.

In Figure 5-13 the arrow indicates the direction of numbering. For the segments, it is in a clockwise direction, for actuators, it is in anticlockwise within the segment and clockwise in inter-segment. For the sensors, it is the anticlockwise direction for segment periphery ring, and in radially outward direction for intersegment gaps.
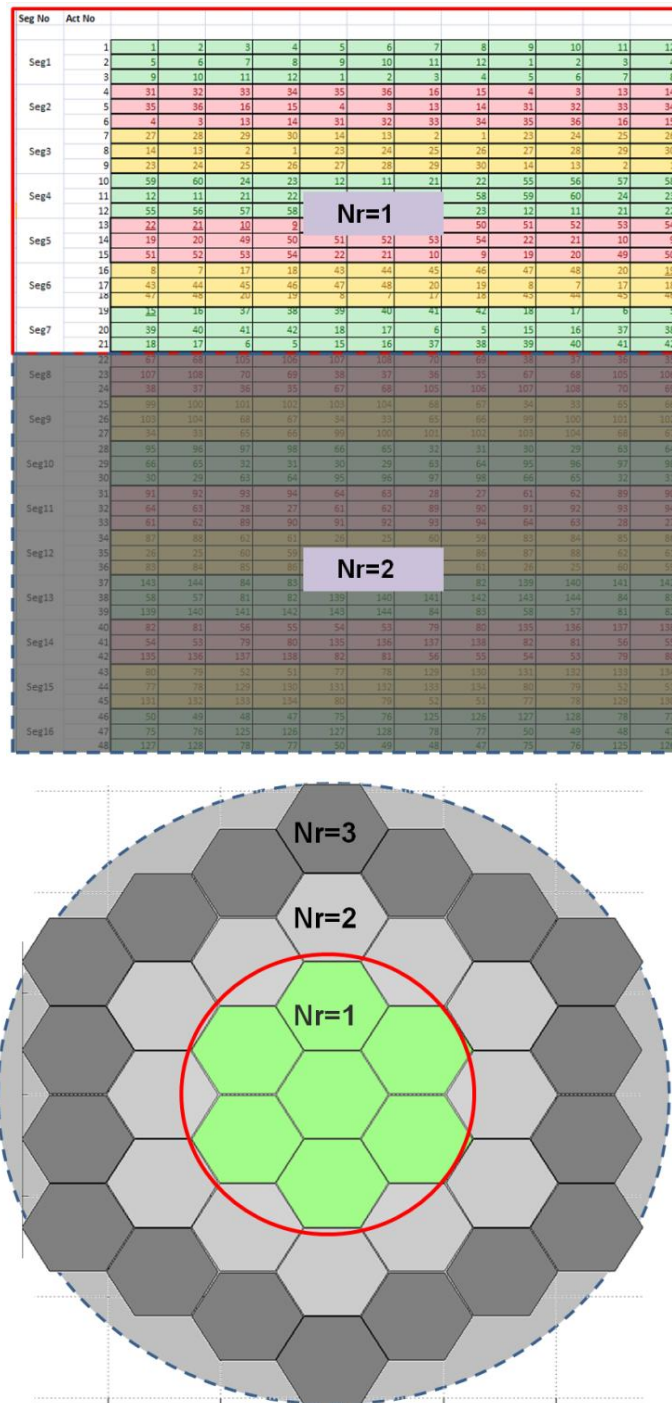
Figure 5-14. The codeSMT interaction matrix database (partial), ring numbering and masking scheme.

Presently we have developed the database of 12 rings telescope and is of the size of 1407x7 elements. The advantage of this approach is that this database needs to be developed only once and is reusable for formulating any SMT. Figure 5-14 shows the working of masking scheme used to get the database of required SMT from the

generic database. In this process, using the single database telescopes from 1 ring to 12 rings can be formulated by masking the redundant part of the database. In its simplest form, the global controller receives edge sensor values as input, and it generates actuator commands as output to maintain the primary mirror shape. Once these actuator commands are executed, the mirrors shape changes. To visualize this in real time, we have developed a plotting tool for the codeSMT as shown below. Different representative cases shown below are for PSMT, 4.5m telescope, NLOT, KECK, SALT and TMT.
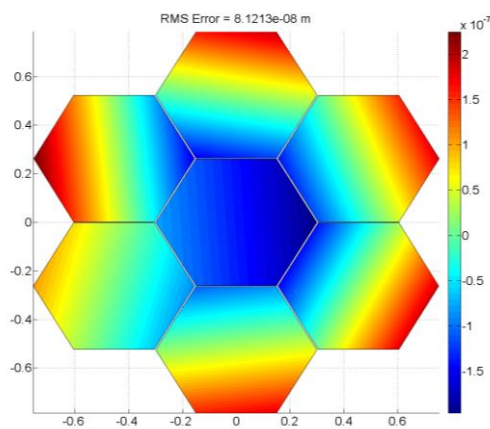
(a) PSMT
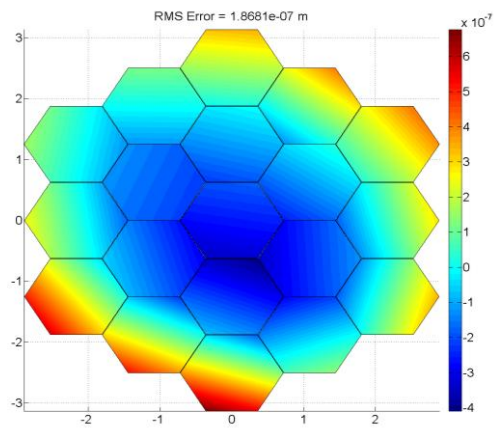
(b) 4.5m Telescope
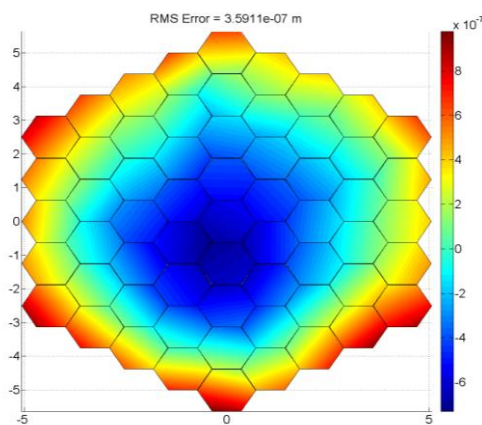
(c) NLOT

(d) Keck Telescope

(e) SALT   (f) TMT
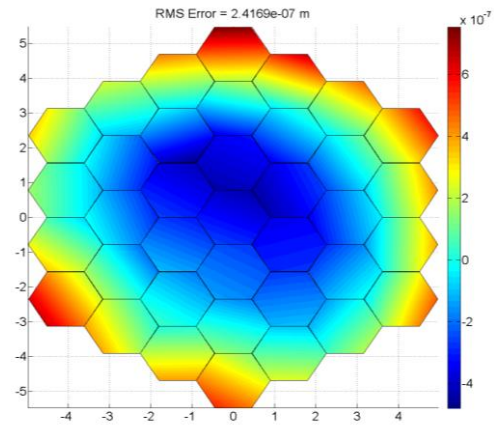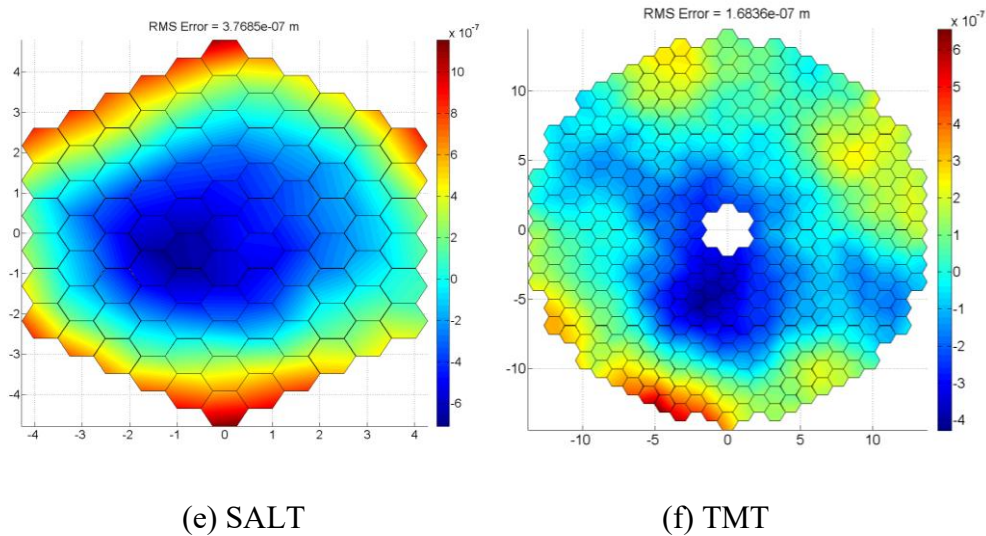
Figure 5-15. The primary mirror segment plotting tool developed for the codeSMT. Different telescopes (PSMT, 4.5m telescope, NLOT, KECK, SALT and TMT) primary mirrors are shown with a deformed mirror shape (axis values in units of meters).

Further, the very nature of Global controller formulation in terms of SVD based decomposition of interaction matrix allows us to visualize the mirror in the form of its individual Zernike mode shapes Figure 5-16. There are 3N-3 modes, where N is the number of segments. The term (-3) corresponds to first three unobservable modes – Tip, Tilt, and Piston.

The mirror surface can be measured in terms of RMS surface error obtained from RMS actuator positions. This surface deformation is in addition to the actual mirror shape of an ideal telescope under study. This further gives us the wavefront error, which is twice the surface error. The wavefront obtained from the deformed M1 is further utilized to compute the PSF of the overall telescope (see Figure 5-17).
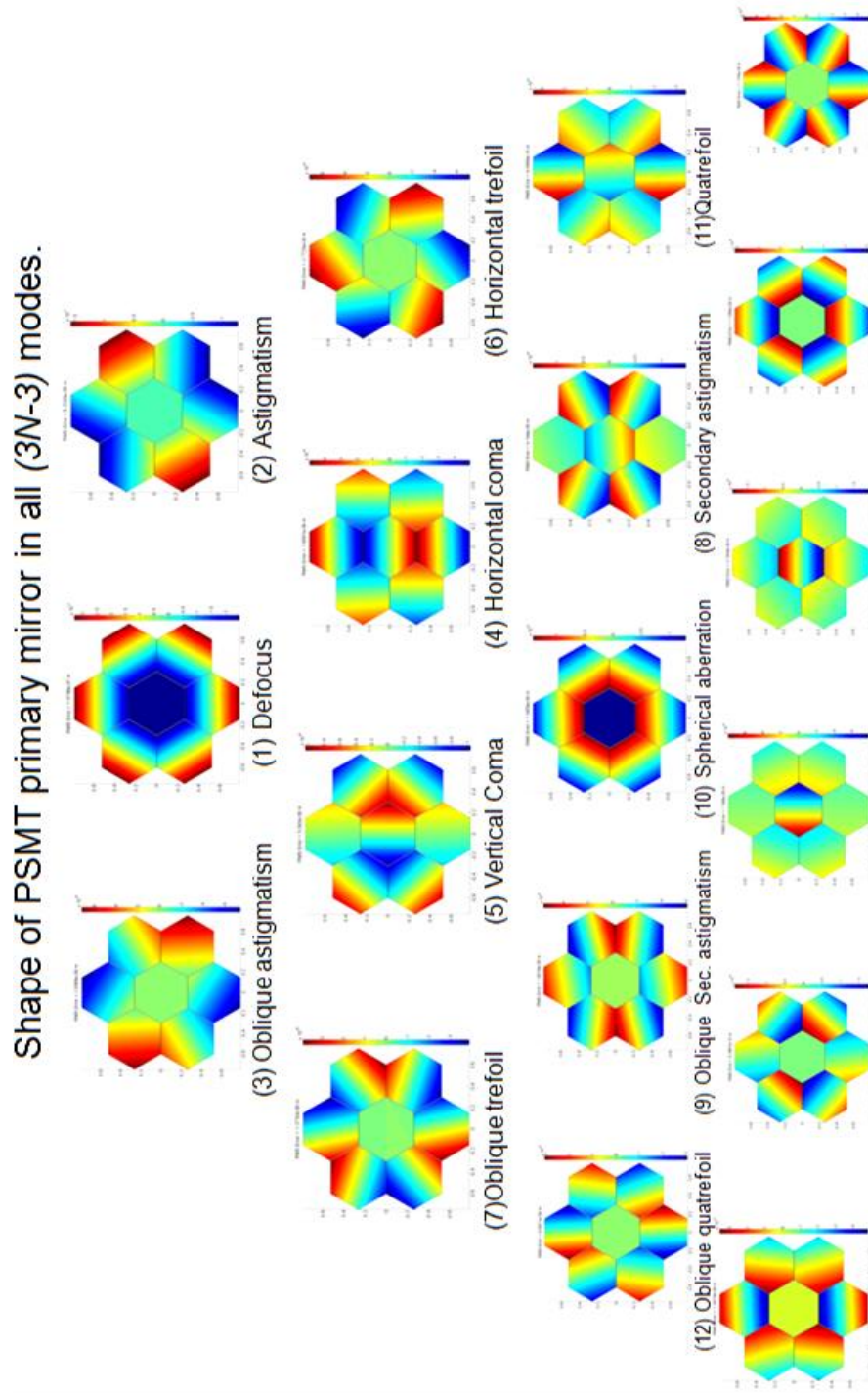
Figure 5-16 The mirror mode shape plots of a PSMT obtained from a typical deformed mirror. As seen shapes resemble with the Zernike mode shapes.

Following is the sample result obtained from the codeSMT tool for the PSMT case with a disturbed mirror shown with its PSF.
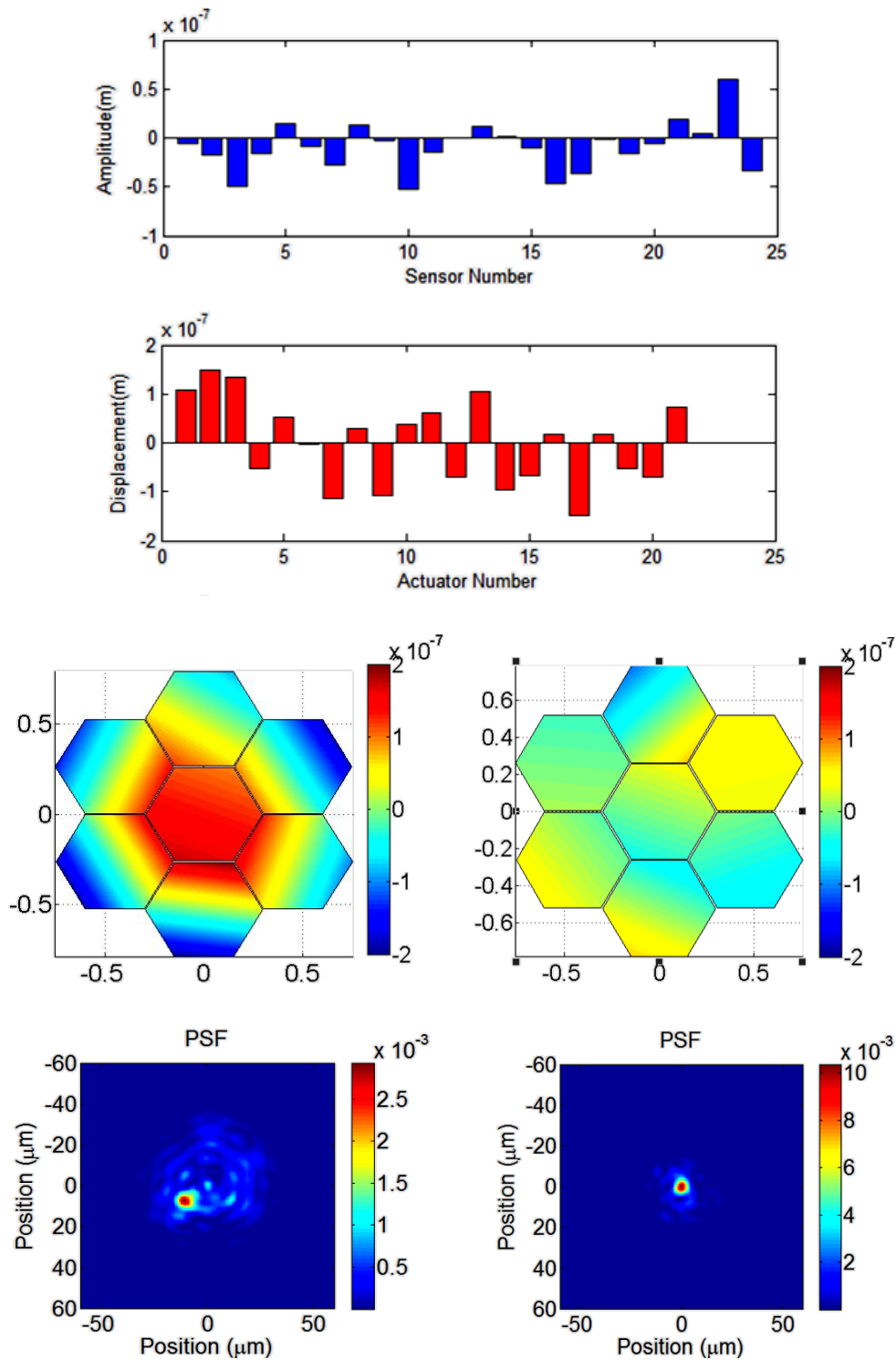
Figure 5-17 A typical PSMT case showing edge sensor data of a disturbed mirror and the actuator displacements evaluated to correct the mirror shape using the codeSMT tool.

In the above PSMT case, primary mirror surface deformation is 85.5nm RMS (generated using the random edge sensor data of 26.1nm RMS) gets corrected to 29.2nm RMS after the global controller correction. This process can be continued in codeSMT in OL or CL to see the evolution of telescope. But if there is no disturbance telescope will exponentially go to the ideal shape and PSF will be a perfect airy pattern due to the telescope aperture (1.5m for PSMT) along with the impression of hexagons.

5.3   Summary and Conclusion

There are very few operational SMTs, and only handfuls are planned in the coming decade. Any telescope design starts with a thorough simulation and performance analysis. At present, there are no generic simulation tools available for the Primary Mirror Control System of SMTs. It is because in general telescope designers opt for the customized models developed with the limited reconfigurability. So we decided to develop a generic design and simulation tool called the codeSMT for conducting a variety of studies related to M1CS of SMTs.

In this chapter, we introduced the basics of the Global control system and mathematical modeling of a generic SMT. The interaction matrix (A) which gives the relation between edge sensors and actuators was established. For this task segment, actuator, and sensor numbering scheme is very important, and we have introduced a new numbering scheme for the codeSMT tool. The matrix inverse (A^{-1}) was obtained by the Singular Value Decomposition based matrix inversion technique, where the pseudoinverse of A matrix is obtained (since A matrix is a nonsquare, i.e., overdetermined system). Further in this chapter, detailed design aspects of the codeSMT tool and its features are presented.

The codeSMT tool is equipped with different features such as formulating the SMT with various telescope parameters like mirror sizes, the number of segments, types of sensors and actuators, disturbances, control loops, etc. Also, it is capable of

generating results in the form of mirror deformations, wavefront error, point spread function, error multiplier plots, parameter sensitivity plots, including text data outputs. A dedicated segment plotting tool is designed and integrated with codeSMT so as to visualize overall primary mirror shape as well as the shape of the primary mirror in different spatial modes. The sensitivity of various parameters related to SMT primary mirror can be studied in terms of its effect on the mirror shape and on the error multipliers which is a handy feature during the early design phase of the SMTs. The codeSMT has been used to conduct two major studies, one on active control simulation and other on the error multiplier analysis of the PSMT, both are presented in Chapter 6.

Chapter 6   Case Studies using the codeSMT tool

Using the codeSMT tool described in Chapter 5, we conducted two major studies related to Error Analysis and Active Control Simulation (ACS) of the Prototype Segmented Mirror Telescope and is described in Section 6.1 and Section 6.2 respectively.

6.1   Case study I: PSMT Active Control Simulation

The codeSMT tool is capable of doing active control system simulations by incorporating a realistic actuator and disturbance models. In this work, we have conducted a study on parametric modeling and analysis of the active control system of the Prototype Segmented Mirror Telescope. By making use of actuator dynamic model developed by us, the actuator parameters are fine-tuned so that it can meet desired response and characteristics of a soft actuator to be used in the PSMT. This actuator model is a state space model of the soft actuator with Multiple-Input Multiple-Output (MIMO) capability to incorporate dynamic wind disturbances. Further, it was integrated with the feed forward PID controller, and gains were appropriately tuned to get the excellent wind rejection and to meet the performance requirements. As a next step, we introduced a dynamic wind disturbance model capable of continuously generating representative wind time series data, to mimic wind induced disturbances on the actuators via primary mirror segments. The Actuator and Edge sensors operate together in a relatively slower closed loop with the help of global controller utilizing SVD based algorithm which convert edge sensor

information to actuator commands. Here codeSMT plays a vital role as a global controller and for the visualization as described in Section 5.2. Finally, after integrating the actuator, controller and disturbance modules, we could develop an active control system model of the PSMT primary mirror, which is used for performance estimation in the normal condition as well as in the presence of wind disturbances. One of the significant advantages of our method is, it is fully parametric and can be used for the design and analysis of upcoming segmented mirror telescopes of different sizes and design parameters. Also, it can be easily integrated with the optical simulation software such as Zemax for further studies.

6.1.1 PSMT ACS Components

The active control system is the main part of the PSMT primary mirror which will ensure the positioning of mirror segments to make them act like a continuous surface. The major components of the active control system are Actuators, Edge sensors, Local Controllers and Global Controller. The actuators are used to position each of the seven segments in the piston, tip, and tilt: 21 actuators in total. In the case when mirror segment is supported by the rigid/hard actuator, it is thermal, gravity and wind-induced effects which basically changes the segments relative position and hence gets reflected as a change in the sensor reading. In such a case, actuator acts as a position actuator only. Whereas, if the segment is supported by the soft actuator then, in order to balance variable force due to changing gravity while the telescope is pointing/tracking, it should act like force actuator. Therefore, the soft actuator should have the ability to act like position as well a force actuator. The local controller at actuator is primarily responsible for executing the commands generated by the global controller as well as to maintain the position of the actuator to this commanded position in the presence of wind disturbance. It reads the local position sensor on actuator at the fastest rate (500 Hz - 1 KHz) and filters the noise if any. This position information is used by local closed loop controller (PID controller) to maintain the position of the actuator to the commanded position. This position loop runs at around 100Hz command rate. The actuator combined with the edge sensor very much dictates

the performance of the PSMT. The Edge sensors are considered to be the absolute reference in the primary mirror active control. It will be mounted on the back side of the segments, with two sensor halves on each inter-segment edge: 24 pairs in total. Edge sensor and its electronics continuously monitor relative intersegment displacements, evaluate the piston and gap information between segments and sends to the global controller. The global controller receives the Edge sensor readings and translates it into the required Actuator displacement typically at 1Hz bandwidth. The primary role of the global controller is to run the Primary Mirror Control System (M1CS) algorithm on real-time and maintain the mirror shape in the presence of disturbances.
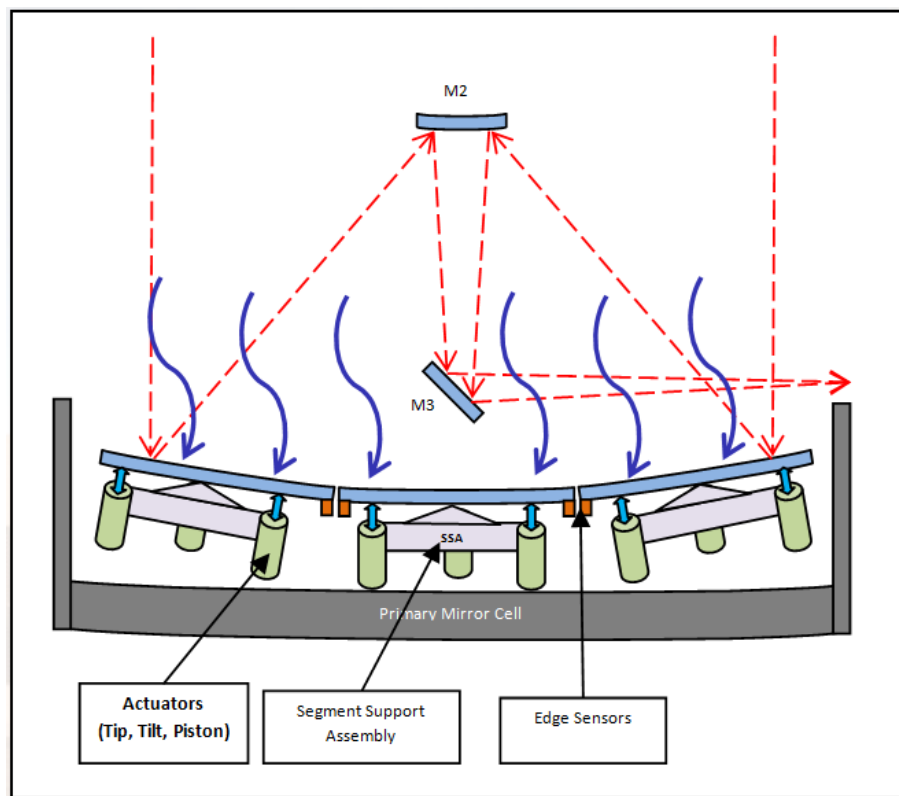
Figure 6-1. Schematic view of the PSMT ACS components along with wind disturbance on the primary mirror.

6.1.2 Modeling & Simulation

6.1.2.1   Actuator Dynamic Model

The PSMT actuator described in Chapter 2 has a Voice Coil Motor (VCM) as its prime mover. It is surrounded by a single spring of large diameter and large stiffness. The base of the VCM rests on the rigid offloading stage driven by a stepper motor whereas the top part of the VCM is directly supporting the output shaft of the actuator through spacers. The Disc Flexure Springs support the spacers to isolate them from the rigid body of the actuator making it soft actuator. Stops are used to limit the maximum displacement of the actuator to the required stroke. A position encoder at the output shaft gives the absolute position of the actuator with respect to the rigid frame.
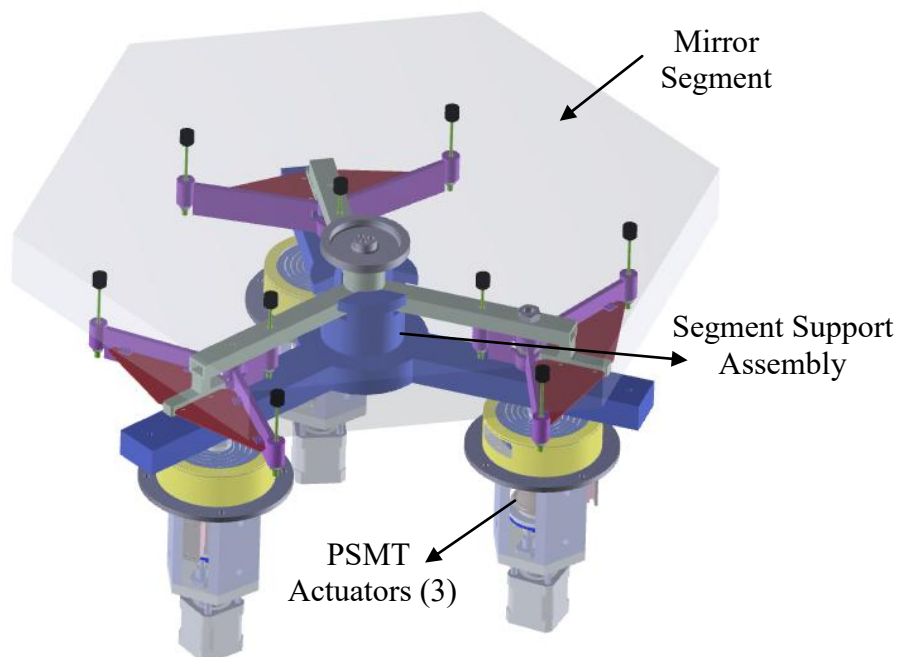
Figure 6-2. Concept design of PSMT Primary segment assembly with three prototype actuators.

This actuator is designed using the following design criteria:

Table 6-1 List of Actuator Parameters used in the simulation.

Parameter	Value	Unit
Actuator moving mass + Mirror mass	14	Kg
VCM Force Constant	13	N/A
VCM resistance	3.25	Ohm
VCM Inductance	5.27	mH
Back EMF constant	13	V.s/m
Effective Spring Constant	20000	N/m

For Actuator modeling purpose, we have used the first principle approach and represented it as a state space model. It enables us to develop a MIMO model of the actuator, so as to include the Wind disturbance force as one of the inputs along with the position/voltage command to the actuator. The state space helps to represent a physical system in a mathematical model as a set of input, output and state variables related by differential equations (Rowell 2002). Here the states are nothing but the dynamics of a system at a particular time. Following is a schematic of a spring-mass model of the PSMT actuator (Figure - 4) along with the disturbance force acting from the top. The rigid base assumption here is valid for PSMT which is relatively small size telescope, whereas for a larger telescope we may have to consider Control Structure Interaction (CSI) arising due to the flexible mirror cell (Preumont, R. Bastaits and Rodrigues 2009). Here the inputs to the plant are wind disturbance and the input voltage (VCM voltage) whereas the output is the position of the actuator shaft.
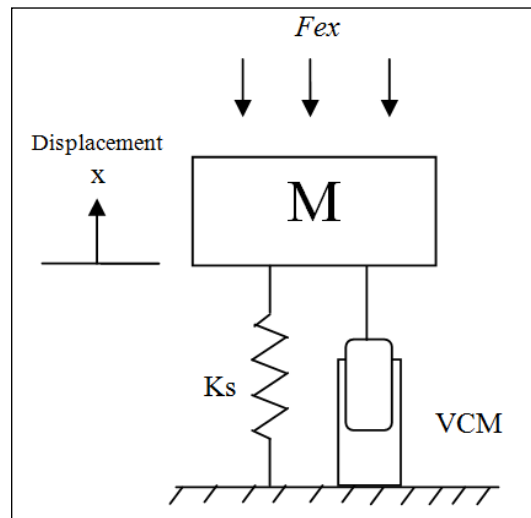
Figure 6-3. Spring Mass Model of the PSMT Actuator.

Let, F_{ex} be the external force or wind disturbance acting upon the mirror as shown in the figure in (N), F_{VCM} be the force exerted by the VCM on the mass M, K_S be the spring constant of the spring, M be total mass of mirror and actuator moving mass, and x be the resultant displacement of the mass (M) due to the two forces acting upon it.

Then, the force equilibrium equation is written as:

$$F_{vcm} - F_{ex} = M\frac{d^2x}{dt^2} + K_s x \qquad\qquad \text{Equation 6-1}$$

We have the force exerted by the VCM given as:

$$F_{vcm} = K_v i \qquad\qquad \text{Equation 6-2}$$

Where K_v is the force constant of the voice coil in N/amp, i is the current flowing through the VCM in the amps.

And, the VCM dynamics is given as:

$$E = Ri + L\frac{di}{dt} + e_b \qquad \text{Equation 6-3}$$

The (Equation 6.2) and (Equation 6.3) are the two fundamental relationships of a linear voice coil actuator (Baronti, et al. 2009).

Using equation (Equation 6.2) in (Equation 6.1):

$$i = \frac{F_{ex} + M\frac{d^2x}{dt^2} + K_s x}{K_v} \qquad \text{Equation 6-4}$$

Using equation (Equation 6.4) in (Equation 6.3) we get:

$$E = \frac{LM}{K_v}\frac{d^3x}{dt^3} + \frac{RMd^2x}{K_v dt^2} + (\frac{LK_s + K_b K_v}{K_v})\frac{dx}{dt}$$
$$+ \frac{RK_s}{K_v}x + \frac{L}{K_v}\frac{dF_{ex}}{dt} + \frac{RF_{ex}}{K_v} . \qquad \text{Equation 6-5}$$

Then the states can be assigned as

$$X_1 = x; \ \dot{X}_1 = s\,X(s) = X_2; \ \dot{X}_2 = s^2 X(s) = X_3 \qquad \text{Equation 6-6}$$

Where, $X_1, \dot{X}_1, \dot{X}_2 \ and \ \dot{X}_3$ represent the position, velocity, acceleration and jerk respectively.

Using equations (Equation 6.6) in (Equation 6.5) we get:

$$\dot{X}_3 = -\frac{K_v}{LM}\left(\frac{RM}{K_v}X_3 + (\frac{LK_s + K_b K_v}{K_v})X_2 + \frac{RK_s}{K_v}X_1 \right)$$
$$- \frac{R}{LM}F_{ex} - \frac{1}{M}\frac{dF_{ex}}{dt} + \frac{K_v}{LM}E . \qquad \text{Equation 6-7}$$

Here, out of different states - position, velocity and acceleration of the actuator shaft, our primary interest is to study the output position of the actuator with respect to the input voltage and input wind force. In a particular mirror segment, the position of such three actuators defines the effective tip, tilt, and piston of that segment. Details about evaluating mirror position are described in Section 6.1.2.3 of this Chapter.

Finally, the state space model can be written in matrix form as below:

$$\dot{X} = AX + BU$$
$$Y = CX + DU$$

Equation 6-8

Here, A is the state transition matrix which is in controllable canonical form, B is the input matrix, and C is the output matrix. Since we are interested in the actuator position so we take the output matrix as $C = [1\ 0\ 0]$.

$$\begin{bmatrix} \dot{X}_1 \\ \dot{X}_2 \\ \dot{X}_3 \end{bmatrix} = \begin{bmatrix} 0 & 1 & 0 \\ 0 & 0 & 1 \\ \dfrac{-RK_s}{LM} & -\dfrac{LK_s + K_b K_v}{LM} & -\dfrac{R}{L} \end{bmatrix} \begin{bmatrix} X_1 \\ X_2 \\ X_3 \end{bmatrix} + \begin{bmatrix} 0 & 0 & 0 \\ 0 & 0 & 0 \\ \dfrac{-R}{LM} & \dfrac{-1}{M} & \dfrac{K_v}{LM} \end{bmatrix} \begin{bmatrix} F_{ex} \\ \dot{F}_{ex} \\ E \end{bmatrix}$$

$$Y = \begin{bmatrix} 1 & 0 & 0 \end{bmatrix} \begin{bmatrix} X_1 \\ X_2 \\ X_3 \end{bmatrix}$$

Equation 6-9

Substituting the parameter values given in Table 6-1, we will get:

$$A = \begin{bmatrix} 0 & 1 & 0 \\ 0 & 0 & 1 \\ -880162.49 & -3716.9939 & -616.113 \end{bmatrix} \quad B = \begin{bmatrix} 0 & 0 & 0 \\ 0 & 0 & 0 \\ -44.008 & -0.071428 & 176.032 \end{bmatrix}$$

Equation 6-10

Following is the Simulink block created using the state, input, output matrix (Equation 6-10), which takes the input as voltage and wind force (also derivative of wind force) and gives the output position, as described before.
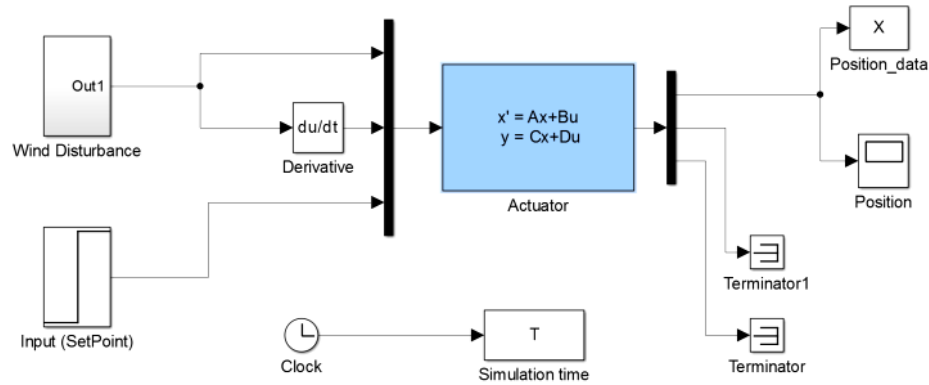
Figure 6-4. A Simulink based dynamic model of the actuator (with wind and voltage as input parameters and position as output).

→ Transfer function with respect to input (I/P) voltage and position output (O/P): (i.e., if *Fex*=0 then from (Equation 6.5):

$$\frac{X(s)}{E(s)} = \frac{K_v}{LMs^3 + RMs^2 + (LK_s + K_bK_v)s + RK_s} \qquad \text{Equation 6-11}$$

→ Transfer function with respect to the wind I/P and position O/P: (i.e., if *E*=0 then from (Equation 6.5):

$$\frac{X(s)}{F_{ex}(s)} = -\frac{Ls + R}{LMs^3 + RMs^2 + (LK_s + K_bK_v)s + RK_s} \qquad \text{Equation 6-12}$$

In equation (Equation 6.11) in (Equation 6.12) the inputs *E* is in the volts, the force *Fex* is in Newton, and output in the meter. As seen in the frequency response below (plotted using (Equation 6.11) in (Equation 6.12), with respect to both the inputs, the output is almost flat indicating that this actuator will respond to the inputs in the lower frequency and attenuates in the higher frequency region. Whereas in the context of wind most of the frequency content lies below 1Hz and falls rapidly until 10Hz and hence it is correctable using closed-loop control. A resonant mode is observed at 6.02 Hz mainly because of the spring-mass system.
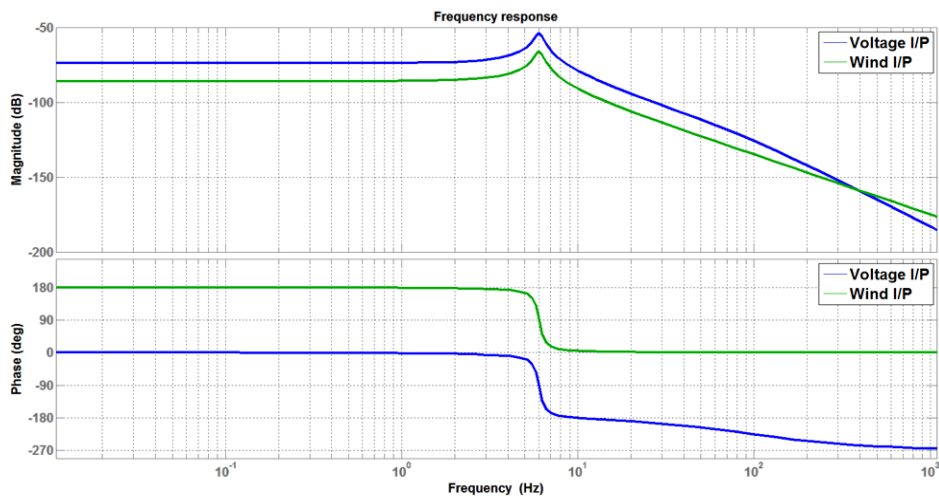
Figure 6-5. Frequency response plot (bode plot) with voltage input (wind input = zero) and wind input (voltage input =zero). In practical case wind energy is mostly below 10 Hz.

6.1.2.2   Local Control Model

As given below there are three major blocks in the local control system modeling - Actuator, closed loop Controller and Wind disturbance. We have used the state space model of Actuator as described above. The controller chosen here is a PID controller with a feed forward path. A soft actuator requires constant input to maintain its position (unlike rigid actuator), and a feed forward path provides it corresponding to the setpoint value (Figure 6-6). The controller tuning is done using Matlab auto-tuning toolbox (Gains: KP=5.23 (no unit); KI=28.51(1/second); KD=0.23 (second)).
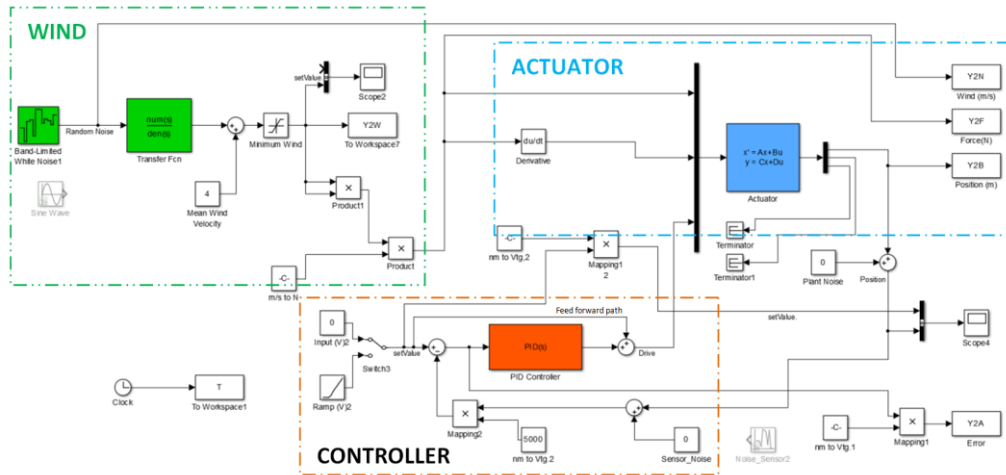
Figure 6-6. A Simulink block diagram showing a single Actuator model, closed-loop PID Controller, and Wind Filter Block. Such 3 Modules are combined to form a Segment model, and similar 21 such modules are combined (7 segments) to form the PSMT Model.

6.1.2.3 Single Segment Model

To represent a single segment model, three local control systems (Actuator + Controller + Wind) are combined. To reduce the complexity, we do not consider the dynamics due to the Segment support assembly itself (it is considered as a rigid system). The output positions of three actuators are used to compute the dynamic Tip, Tilt, and Piston of the mirror segment as described below.
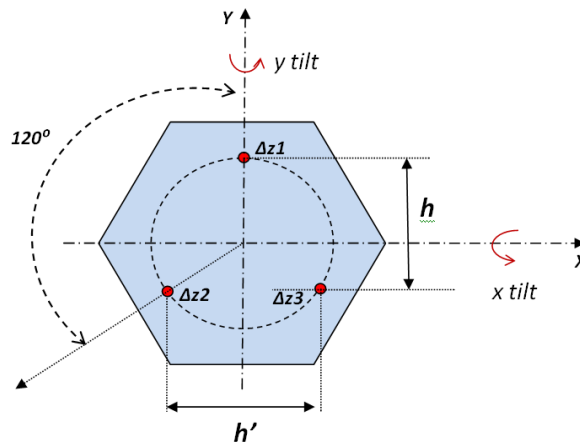
Figure 6-7. A mirror segment with three actuators spaced 120 degrees apart and separated by distance h'. (For PSMT, mirror side length = 300mm, h= 235.2 mm and h'=271.58mm).

Let $\Delta z_1, \Delta z_2, \Delta z_3$ are the linear displacements at the actuators of a given segment. Then the tip, tilt, and piston of the segment is given by the formula (Physik Instrumente (PI) 2009) below:

$$x\ tilt\ =\ \frac{2.\Delta z_1 - (\Delta z_2 + \Delta z_3)}{2.h}$$

$$y\ tilt\ =\ \frac{(\Delta z_2 - \Delta z_3)}{2.h'} \qquad \text{Equation 6-13}$$

$$piston = \frac{(\Delta z_1 + \Delta z_2 + \Delta z_3)}{3}$$

Similarly, we combine 7 segments (21 Actuators) to form a PSMT model in which a global controller is required to maintain the shape of the primary mirror.

6.1.2.4 Global Control Model

The primary mirror of PSMT is shown below with its mirror segments, actuators, and edge sensors. Here we used the same mathematical formulation presented in Section 5.1.1.
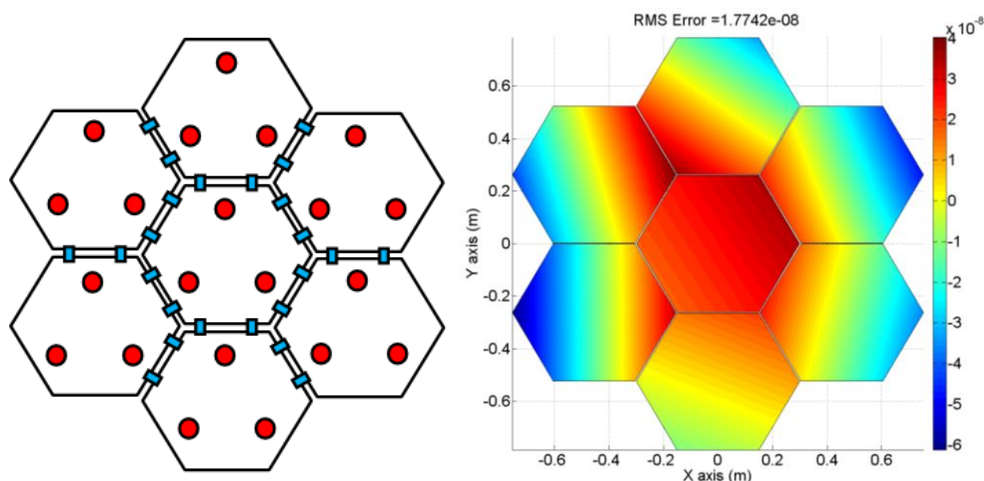
Figure 6-8. PSMT primary mirror with 7 hexagonal mirrors, 21 Actuators (circle) and 24 Edge sensors (squares). A typical case of the mirror deformation is shown in the right figure which is sensed by the Edge sensors and corrected by the Actuators.

When the telescope is in operation, all the information from the edge sensors is read continuously and is used to correct the mirror deformations if any, by

commanding all the actuators. This conversion from sensor readings to actuator commands is done by the global controller. For our simulation purpose, we have developed an Edge sensor simulator based on the geometrical relation (given in Equation 5.4) of actuators and edge sensors along with random noise associated with the Edge sensors.
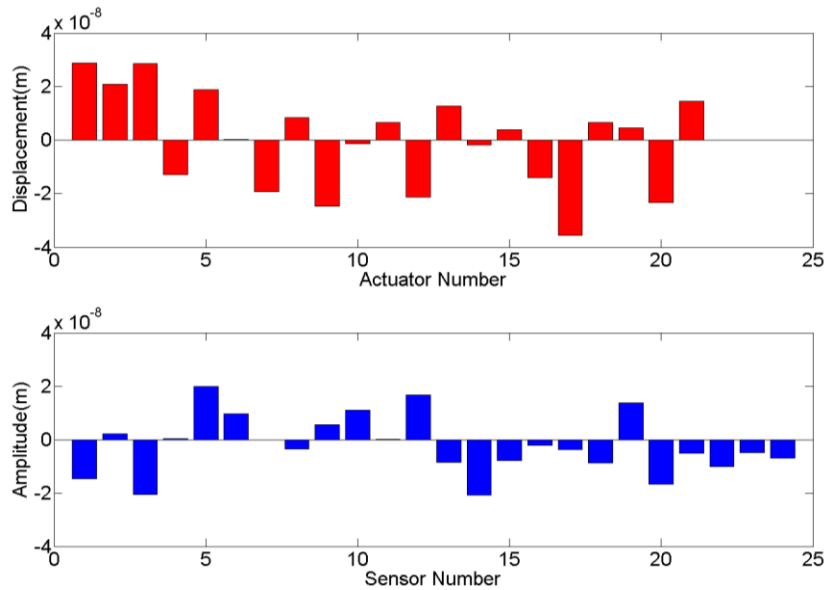
Figure 6-9. A typical case showing edge sensor data of a disturbed mirror (corresponding to the mirror shape in Figure 6-8) and the actuator displacements evaluated to correct the mirror shape using SVD method. (Here, surface deformation is 17.7nm RMS, corresponding to the random edge sensor noise of 11nm).

6.1.3 Wind Disturbance Model

In this section, we describe the method we have used to generate the dynamic wind data in the time domain. This data is used as an input in actuator dynamic model as described before. A Simulink block is designed to generate the representative wind data for the Indian Astronomical Observatory (IAO), Hanle site, which is a possible site for the PSMT. Here we use the concept given in (S. Jiang, et al. 2006) and (Andersen and Enmark 2011) which states that, if we pass a time domain random signal x(t) through a time-invariant filter with H(f) as its frequency response, the

resulting time domain signal y(t) has a Power Spectral Density given by the following equation:

$$S_y(f) = S_x(f)|H(f)|^2$$

<div align="right">Equation 6-14</div>

In the above equation, we have used the input signal x as the Random White Gaussian Noise (flat spectrum). The filter H(f) is designed based on the actual site wind data and is similar to the von Karman model spectrum as shown in Figure 6-10. The designed filter transfer function is:

$$H(s) = \frac{1.521s^3 - 0.3281s^2 - 0.0836s + 0.002921}{s^5 + 7.754s^4 + 4.669s^3 + 0.6155s^2 + 0.0195s + 0.0001544}$$

<div align="right">Equation 6-15</div>
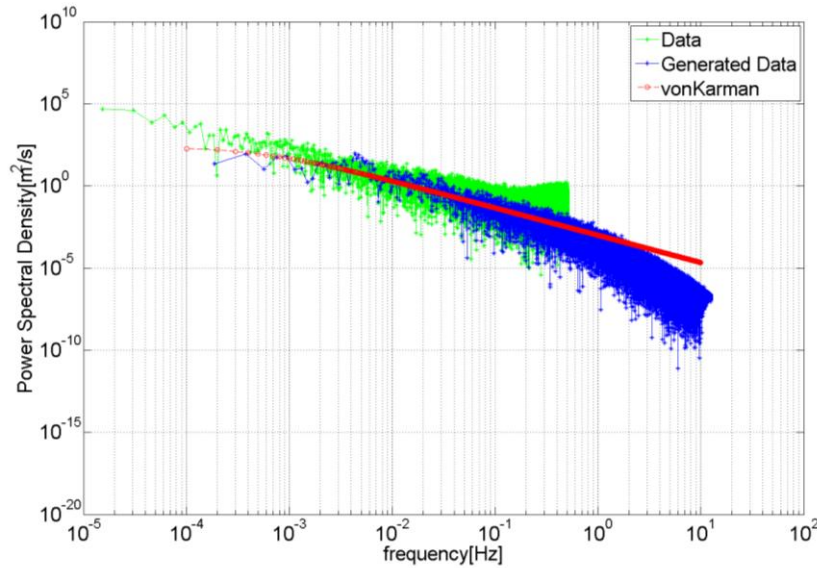
Figure 6-10. A PSD of wind data generated in comparison with the actual IAO, Hanle site wind data spectrum and modeled von Karman spectrum. A good match can be seen in the frequency region of interest (0.001 Hz to 1 Hz) with some deviation in the high-frequency region.

To convert the wind speed data generated in the time domain to its corresponding Force (Angeli, Upton, et al. 2004) on the PSMT actuator, we have used the following equation with relevant parameter values of the PSMT:

$$F = \frac{1}{2} \rho A_s C_d V^2$$

<div align="right">Equation 6-16</div>

where,

F = Wind force on PSMT mirror segment.

$\rho = 0.733 \ Kg / m^3$; (air density for IAO Hanle site)

$A_s = 0.234 \ m^2$; (Segment area)

$C_d = 1.75$; (based on the wind flow simulation over the PSMT mirror segments)

$V = 4.079 \ m / s$; (mean wind speed from wind data survey of IAO Hanle site)

Based on the above wind modeling study it is found that the dynamic force on the mirror segment of PSMT corresponding to the mean wind speed of 4.079 m/s is around 2.49N. This force is shared among three actuators and corrected actively by the local controllers.

6.1.4 Simulation Results

In the simulation the mean wind speed of 4m/s is used for modeling purpose with a frequency spectrum corresponding to von Karman spectrum, and it equals to 2.49N of force on each PSMT segment.
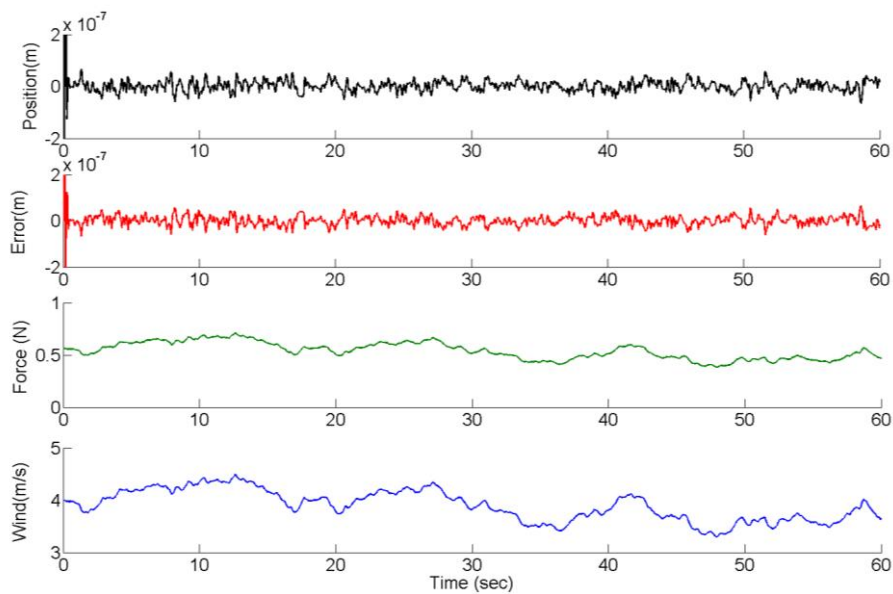
Figure 6-11. A result of time domain simulation of actuator closed loop operation in the presence of wind disturbance.

The plot in Figure 6-11 shows - Wind speed, Force, Position, and Position error of the actuator. In the closed-loop simulation, good wind disturbance rejection

was achieved with a strong relationship with an integral gain. The overall performance is satisfactory with the closed loop tracking error of 20.3nm RMS. (Controller gains: Kp=5.23(no unit), Ki=200(1/second), Kd=0.23(second)).
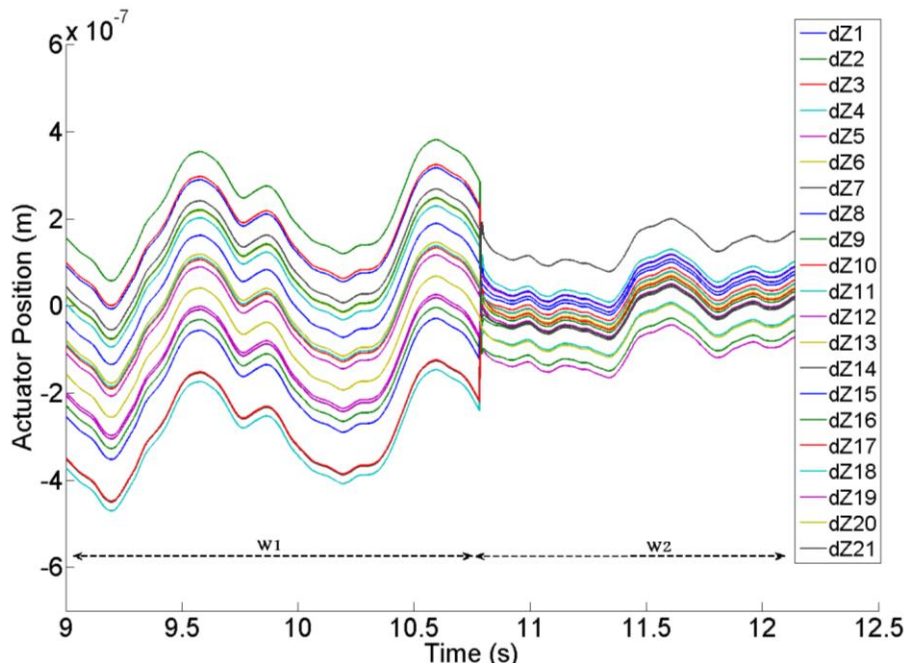
(a)
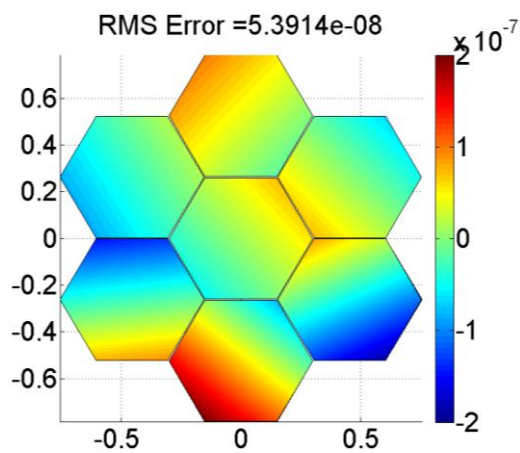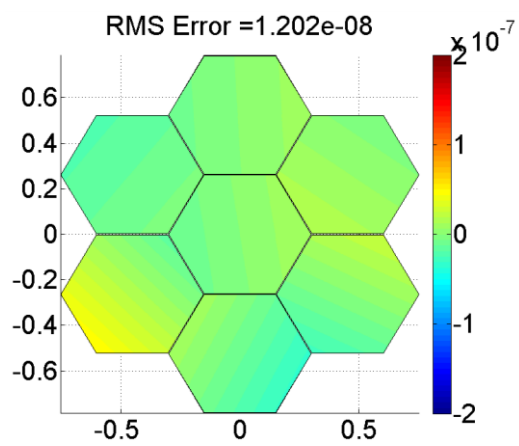
(b)   (c)

Figure 6-12. The active control of a primary mirror where all 21 actuators are taking action based on the commands given by the global controller.

The Figure 6-12 shows one of the instants of the active control of a primary mirror where all 21 actuators are taking actions based on the commands given by the global controller. The global controller is doing computation as described previously and trying to maintain the shape of the mirror. (a) The time domain plot of the disturbed mirror and later corrected by the global controller (here, dZ1 to dZ21 are the actuator displacements), (b) The disturbed mirror state in W1 window with 53.9 nm RMS, and (c) the corrected mirror state in the W2 window with 12nm RMS. All this is happening in the presence of continuous wind disturbance on the mirror surface and closed loop controller rejecting it.

Such simulation studies are very helpful to understand the active control system behavior of the upcoming SMTs under design as these models are scalable. That's why such simulation leads to better design parameter selection reducing the risk of failures and cost of building Next Generation Telescopes. In the future, we plan to incorporate the Telescope Mount control model in the present active control model. Also, we plan to develop an interface to the optical analysis software for direct performance estimation of PSMT. This will enable us to study the correlation between wind disturbance and image motion of the telescope in real time.

6.2   Case study II: PSMT Error Multiplier Analysis

For SMTs if there is any noise at the Edge sensors that will be treated by the actuators as the information and actuator will respond to it in terms of corrections. This leads to the deformation of mirror surface because of unwanted correction. To see how much the mirror gets deformed due to noisy sensors we can compute the overall error multipliers as defined in (Chanan, et al. 2004) and (MacMartin and Chanan 2004). So the error multiplier is a number that gives an estimate of how much mirror surface will get disturbed due to the noisy edge sensors and also compelling means of design optimization of M1CS components.

The codeSMT tool is useful for evaluating the overall error multiplier of a given telescope configuration. It offers two ways to estimate this error multiplier value – Analytically by using Interaction matrix and Numerically using the Monte Carlo numerical simulation. The error analysis study using both the methods was conducted for the PSMT and is presented in Section 6.2.1 and Section 6.2.2 respectively. This is the very first time in the literature anyone has estimated the error multiplier numerically whereas the concept was mentioned earlier in (Chanan, et al. 2004). The Monte Carlo simulation for 10 million iterations was conducted for the PSMT telescope configuration, and results were found to be accurate to 4th decimal places as compared to analytical estimates. Further, we did a sensitivity analysis of each of the PSMT baseline parameters with error multiplier and results obtained are presented later in Section 6.2.3 of this Chapter.

6.2.1 Error Multiplier from Singular Value Decomposition

In the codeSMT tool, the interaction matrix A is an essential part of M1CS control. In actual we need A^{-1} rather than A, so we use SVD based inversion technique to get pseudo-inverse of A matrix. We need to take pseudo-inverse due t the reason that A is a non-square matrix. The very nature of matrix inverting method of SVD gives us an opportunity to see the mirror into its spatial modes.

In SVD, the $(j \times i)$ matrix A (where $j \geq i$) can be written as the product of three matrices:

$$A_{j \times i} = U_{j \times j} W_{j \times i} V^T_{i \times i}$$

<div align="right">Equation 6-17</div>

Where,

U is a $j \times j$ column orthogonal matrix, and its columns are Eigenvectors of AA^T,

W is a $j \times i$ diagonal matrix whose diagonal elements w_i are positive or zero and is referred to as the singular values of the matrix A,

V is a $i \times i$ orthonormal matrix and its columns are Eigen vectors of $A^T A$. The symbol ^{T} denotes transpose.

The decomposed matrix W is a diagonal matrix and elements (σ_i) are singular values (Eigenvalues) of A matrix. So, as per (Chanan, et al. 2004), the analytical value of Individual Error Multiplier is given by:

$$\alpha_i = \frac{1}{\sigma_i \sqrt{Nact}}$$

<div align="right">Equation 6-18</div>

where,

α = error multiplier

σ_i = singular values of A matrix corresponding to i^{th} mode.

$Nact$ = Total number of actuators

Also, the Total Error Multiplier is given by

$$\alpha = \sqrt{\frac{1}{N_{act}} \sum_{i=1}^{N_{act}} \left[\sigma_i^{-2} \right]}$$

<div align="right">Equation 6-19</div>

Table 6-2 PSMT parameters used for error multiplier analysis.

Parameters		Nominal value
a	segment side length	0.30 m
eta	dihedral angle sensitivity	0.0531
f	sensor distance	0.057 m
h	actuator triangle height	0.235 m
l	sensor vertical length	0.02 m
del	sensor gap	0.004 m
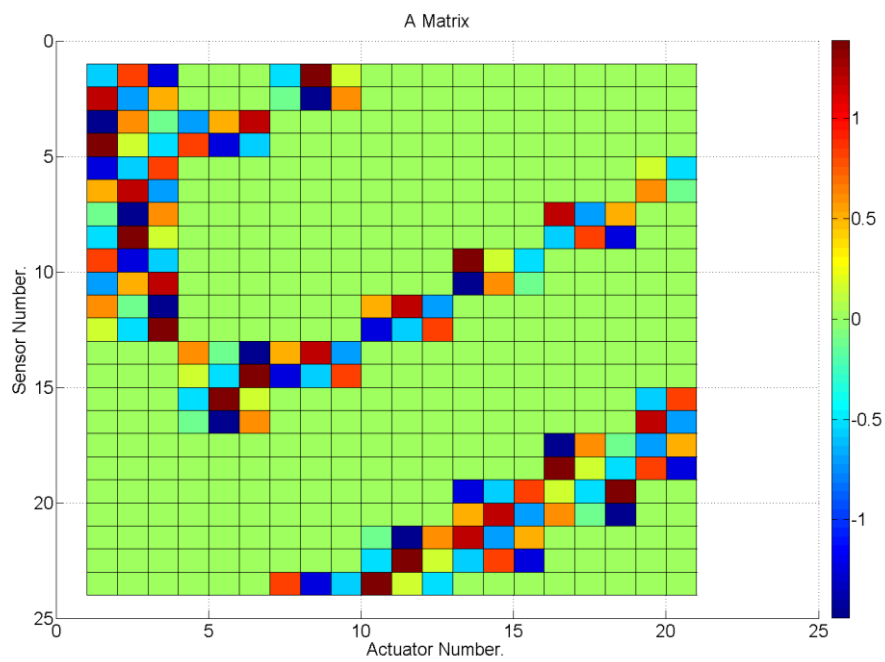
Figure 6-13 The A matrix of PSMT using parameters in Table 6-2.
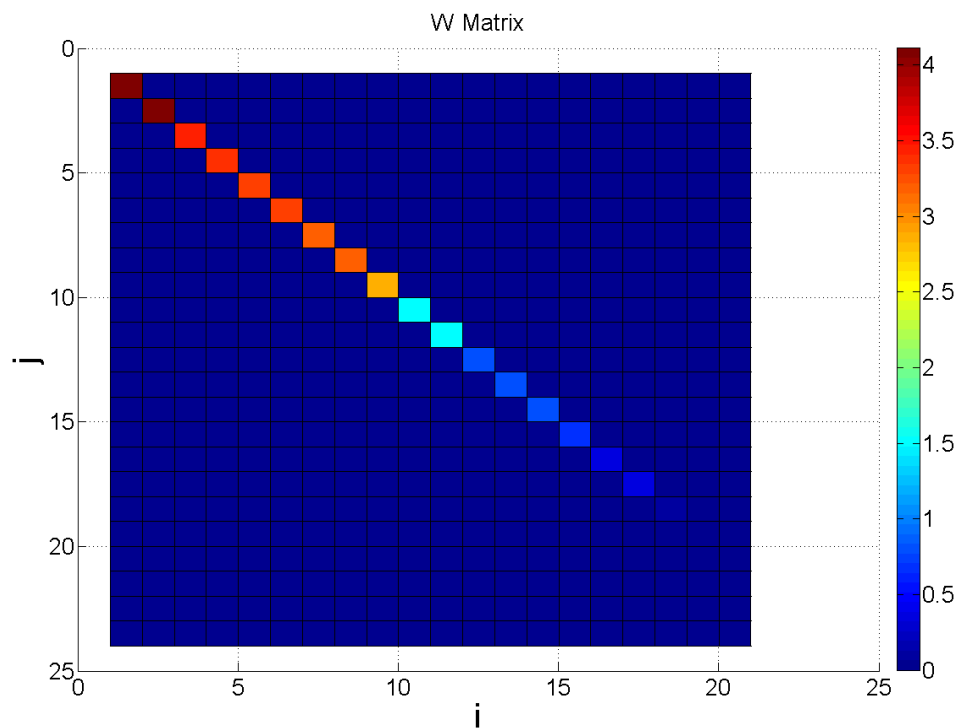
Figure 6-14 The graphical representation of the W matrix. Diagonal values of W are the singular values of matrix A. The diagonal matrix elements (σ_i) are singular values (Eigenvalues) of the A matrix.

For the control matrices considered here, three of the singular values are equal to zero, and the corresponding singular modes are the three actuator vectors corresponding to rigid body motion (piston, tip, and tilt) of the primary mirror as a whole. Because such motion has no effect on the edge sensor readings. If there are N segments, there are 3N actuators and 3N-3 modes of interest in the basis set. It is convenient to order the modes according to the size of their error multipliers, from largest to smallest. With this, we defined a residual error multiplier as the summation of error multiplier value for the indicated mode and for all higher order modes. Using Equation 6.20 and Equation 6.21 we calculated the Individual Error Multiplier and the Total Error Multiplier (with nominal parameters (Table 6-2) of PSMT). The Total Error Multiplier is 2.5806 for the PSMT.
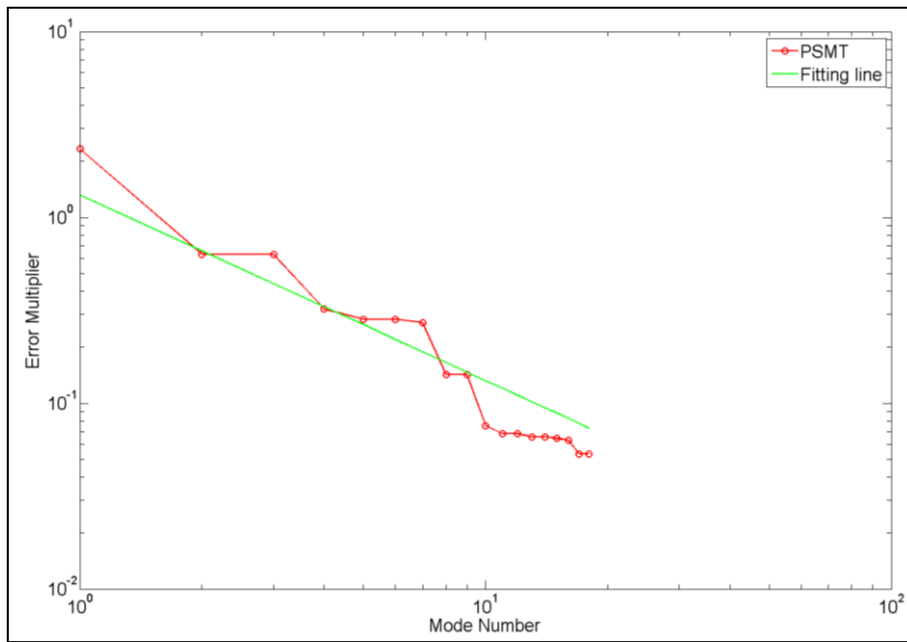
Figure 6-15. Individual Error Multiplier plot w.r.t., different surface modes of the PSMT. This plot is obtained from analytical calculations with nominal parameters. Most of the energy lies in the first few modes.
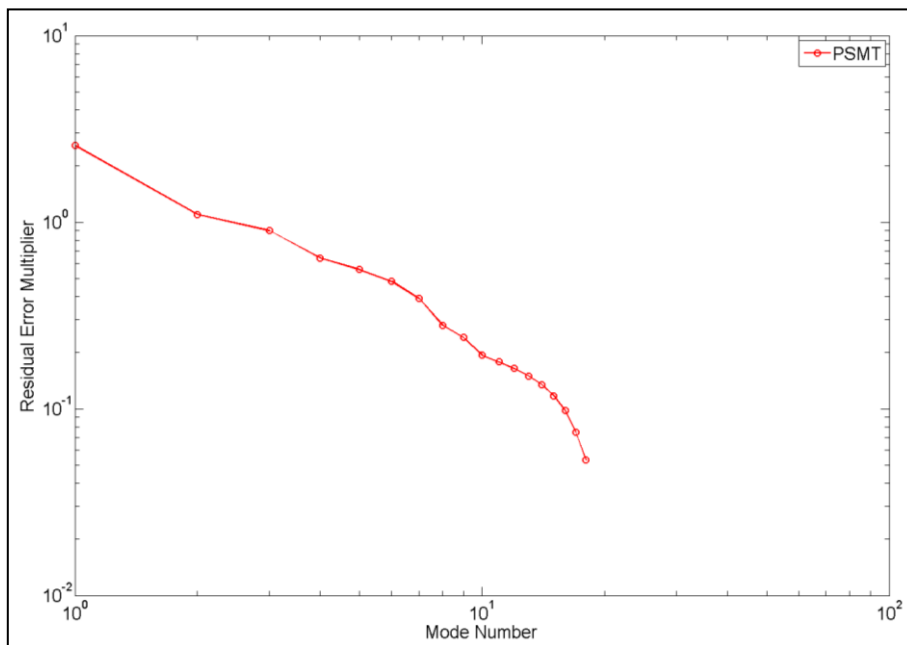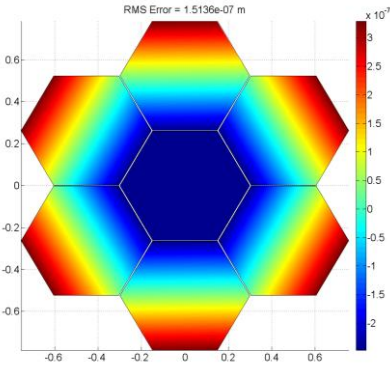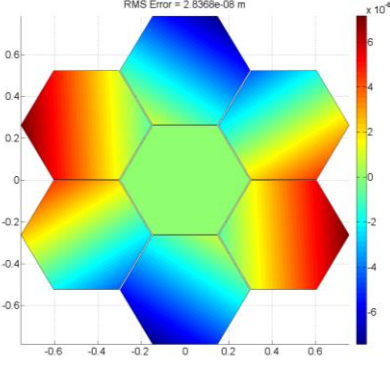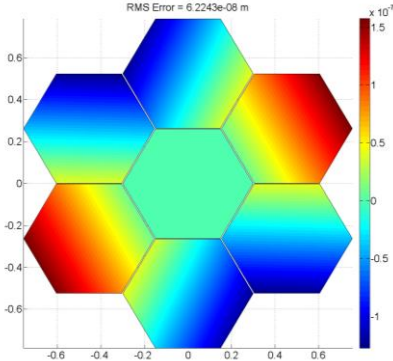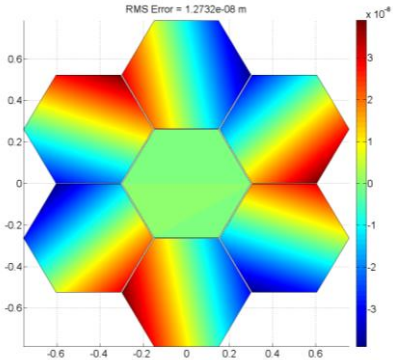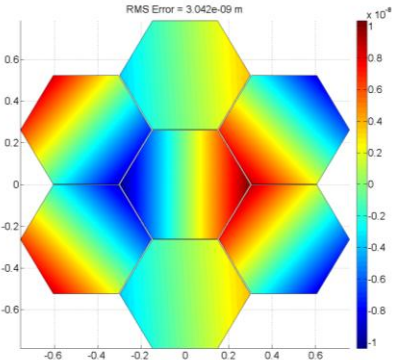
Figure 6-16. Residual Error Multiplier plot of PSMT. The residual error multipliers include the multipliers for the indicated mode and for all higher order modes. The first value in this plot gives the Total Error Multiplier and is 2.5806 for the PSMT.

For PSMT with its 7 segments, there are 18 (3x7-3) distinct shape modes corresponding to 18 different individual error multipliers. We plotted the PSMT primary mirror shapes corresponding to its first five singular modes Table 6-3. Detailed mirror shape plots of all the 18 modes of the PSMT are given in the Appendix E. The surface deformation (half of the wavefront error) of each of these plots is related to the individual error multipliers in Figure 6-15. In general, the energy in different modes decreases as mode number increases. As seen most of the RMS surface deformation is in the first Focus mode. Focus Mode (focus mismatch) is first non-singular control mode, with highest error multiplier and most of the energy is in the Focus mode.

Table 6-3 Mirror shape plot of the first five modes of PSMT Primary Mirror.

Mode No.	Individual Error Multiplier	Mirror Shape	RMS surface deformation (nm)
1	2.3332	Defocus	151.4
2	0.6326	Oblique Astigmatism	28.4

3	0.6326		62.2
		Astigmatism	
4	0.3212		12.7
		Oblique Trefoil	
5	0.2825		3
		Vertical Coma	

6.2.2 Error Multiplier from Numerical Calculation

In (Chanan, et al. 2004), it was suggested that the error multiplier is the response of actuators for sensor values, or rather; RMS sensor value multiplied by error multiplier gives us RMS of Actuator (Equation 6-20). So we derived equations and found that this is true only when we further take RMS of these error multipliers (see Appendix F for the derivation). In other words, if we generate lots of different error multiplier values numerically and take its RMS, then that value tends to the Total Error Multiplier value calculated analytically (see Figure 6-17). To validate this, we did Monte Carlo Numerical simulation using the codeSMT tool which has the facility to generate random edge sensor values and get corresponding actuator outputs. Also to speed up this computation process we used the High-Performance Computing facility (Fornax Computing Server 2017) at Indian Institute of Astrophysics, Bangalore. This is the first time someone has actually done the numerical calculation and shown that as simulation/iteration number tends to very large (10 million iterations in our case), the Total Error Multiplier tends to the Analytical value.

$$\alpha_k = \frac{\delta a_k}{\delta s_k} \Rightarrow Total\ Error\ Multiplier\ from\ k^{th}\ sumulation.$$

$$\delta a_k = rms\ of\ actuator\ values\ for\ k^{th}\ simulation\ run. \qquad \text{Equation 6-20}$$

$$\delta s_k = rms\ of\ sensor\ values\ for\ k^{th}\ simulation\ run.$$
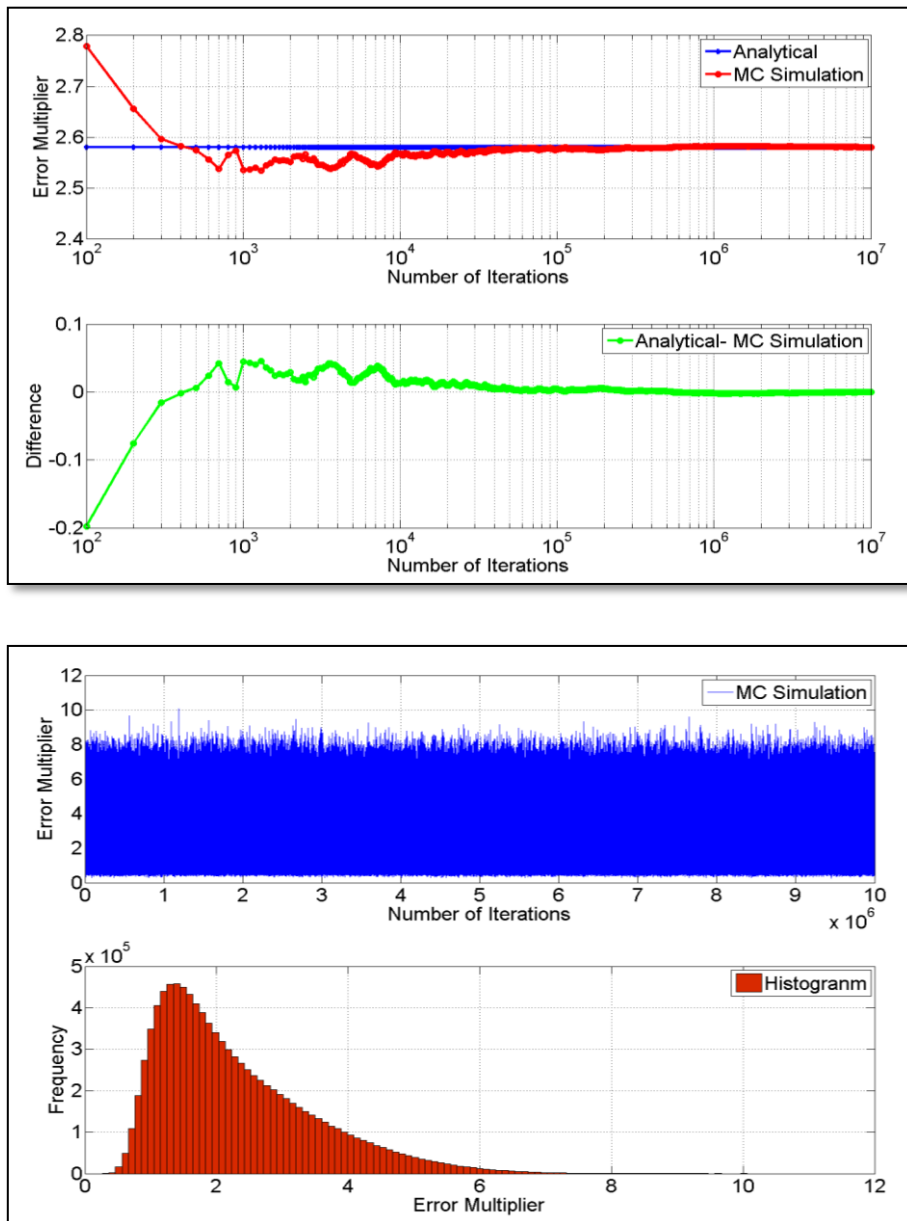
Figure 6-17. Total Error Multiplier estimation based on Analytical calculations and Monte Carlo Numerical simulations for PSMT. As the number of iterations increases the numerical simulation, value converges to the analytical value. The estimated value of Total Error Multiplier is 2.5806 for PSMT.

Table 6-4 Analytical and Numerical result of Total Error Multiplier for PSMT.

Method	Total Error multiplier
Analytical value	2.580649
Numerical value	2.580654

Figure 6-17 shows the Total Error Multiplier estimation based on Monte Carlo Numerical simulation in comparison with the Analytical calculation for the PSMT. The Monte Carlo simulation for 10 million iterations was conducted for the PSMT telescope configuration, and results were found to be accurate to 4th decimal places as compared to the analytical estimate (Table 6-4). As the number of iterations increases the numerical value converges to the analytical value. The estimated Total Error Multiplier value is 2.5806 from both the methods.

6.2.3 Error Multiplier parameter sensitivity

The PSMT parameters given in Table 6-2 are the baseline parameters for its M1CS. To understand the effect of change of any of these parameters on the error multiplier we did the parameter sensitivity analysis of these baseline parameters. Different M1CS parameters considered includes dihedral sensitivity (*eta*), mirror segment side (*a*), edge sensor location (*f*), actuator location (*h*), sensor vertical length (*l*), and sensor gap (*del*). All the parameters were varied ±25% and ±50% as compared to the PSMT baseline/nominal value. Here eta is again related to the *l*, *h*, and *del* as explained before in Equation 5-6. For PSMT, there are seven segments, so the number of segment rings (*Nr*) parameter is one.

6.2.3.1   Sensitivity with *eta*

The parameter *eta* is the dihedral sensitivity of the edge sensors and it arises due to the fact that the mirror moves in the curved path when it tilts causing the sensor also to move in the curved path. This parameter is dependent on the other parameters (i.e. *h, l* and *del)* and is selected by optimising them.

Table 6-5 Parameter Sensitivity w.r.t eta.

Parameters	Case 0 (Nominal Parameters)	Case 1 (+25%)	Case 2 (+50%)	Case 3 (-25%)	Case 4 (-50%)
Nr	1	1	1	1	1
a	0.30 m	0.30 m	0.30 m	0.30 m	0.30 m
f	0.057 m	0.057 m	0.057 m	0.057 m	0.057 m
h	0.235 m	-	-	-	-
l	0.02 m	-	-	-	-
del	0.004 m	-	-	-	-
eta	0.0531	0.0663	0.0796	0.0398	0.02655
Result	2.581	2.168	1.901	3.305	4.797
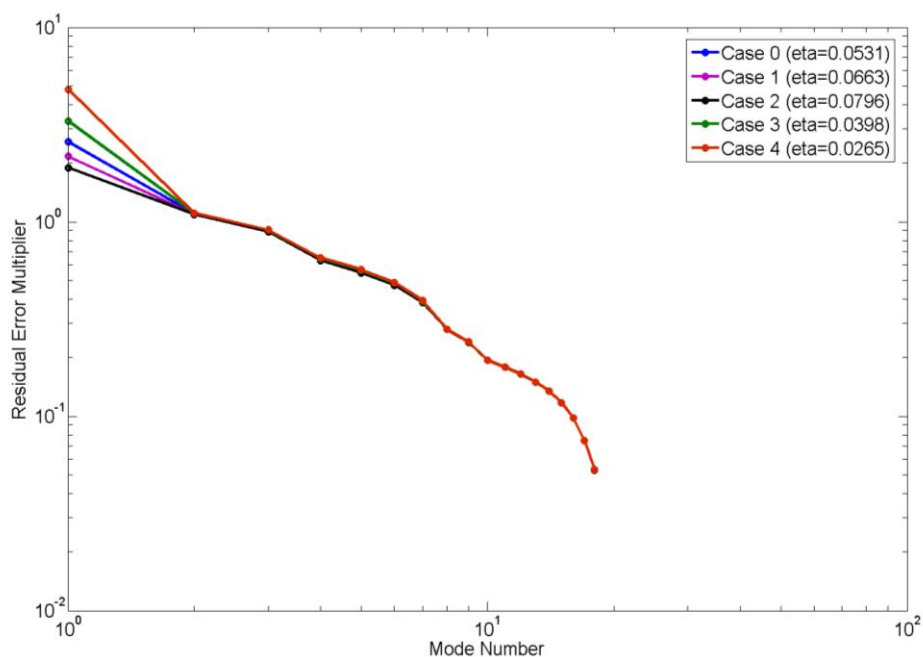
Figure 6-18. PSMT Error Multiplier Sensitivity w.r.t. eta.

6.2.3.2   Sensitivity with f

The parameter f is the distance of the edge sensor block from the nearest segment edge. Though it is not very sensitive parameter it needs selection based on available space and mass distribution requirements w.r.t the mirror segment.

Table 6-6 Parameter Sensitivity w.r.t f.

Parameters	Case 0 (Nominal Parameters)	Case 1 (+25%)	Case 2 (+50%)	Case 3 (-25%)	Case 4 (-50%)
Nr	1	1	1	1	1
a	0.30 m	0.30 m	0.30 m	0.30 m	0.30 m
f	0.057 m	0.07125	0.0855	0.04275	0.0285
h	0.235 m	0.235 m	0.235 m	0.235 m	0.235 m
l	0.02 m	0.02 m	0.02 m	0.02 m	0.02 m
del	0.004 m	0.004 m	0.004 m	0.004 m	0.004 m
eta	0.0531	0.0531	0.0531	0.0531	0.0531
Result	2.581	2.633	2.74	2.555	2.551
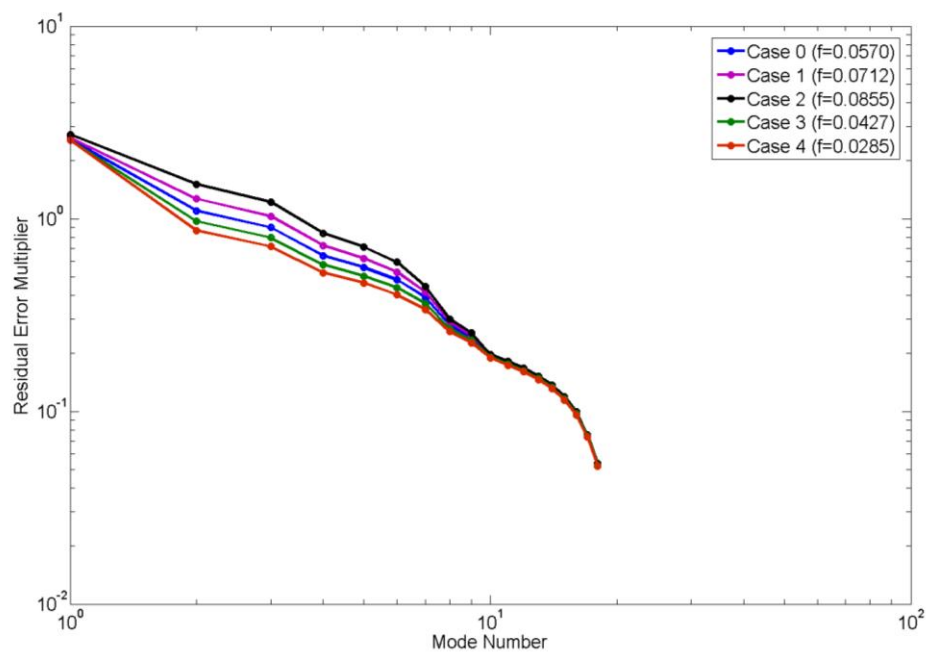
Figure 6-19. PSMT Error Multiplier Sensitivity w.r.t. f.

6.2.3.3   Sensitivity with *h*

The parameter *h* is the perpendicular distance of one actuator from the line joining the other two actuators of a given mirror segment, or in other words it defines the spacing of the actuators. This parameter is selected based on the actuator type, its footprint and available space below the mirror segment, etc.

Table 6-7 Parameter Sensitivity w.r.t h.

Parameters	Case 0 (Nominal Parameters)	Case 1 (+25%)	Case 2 (+50%)	Case 3 (-25%)	Case 4 (-50%)
Nr	1	1	1	1	1
a	0.30 m	0.30 m	0.30 m	0.30 m	0.30 m
f	0.057 m	0.057 m	0.057 m	0.057 m	0.057 m
h	0.235 m	0.29375	0.3525	0.17625	0.1175
l	0.02 m	0.02 m	0.02 m	0.02 m	0.02 m
del	0.004 m	0.004 m	0.004 m	0.004 m	0.004 m
eta	0.0531	-	-	-	-
Result	2.581	2.944	3.337	2.254	1.989
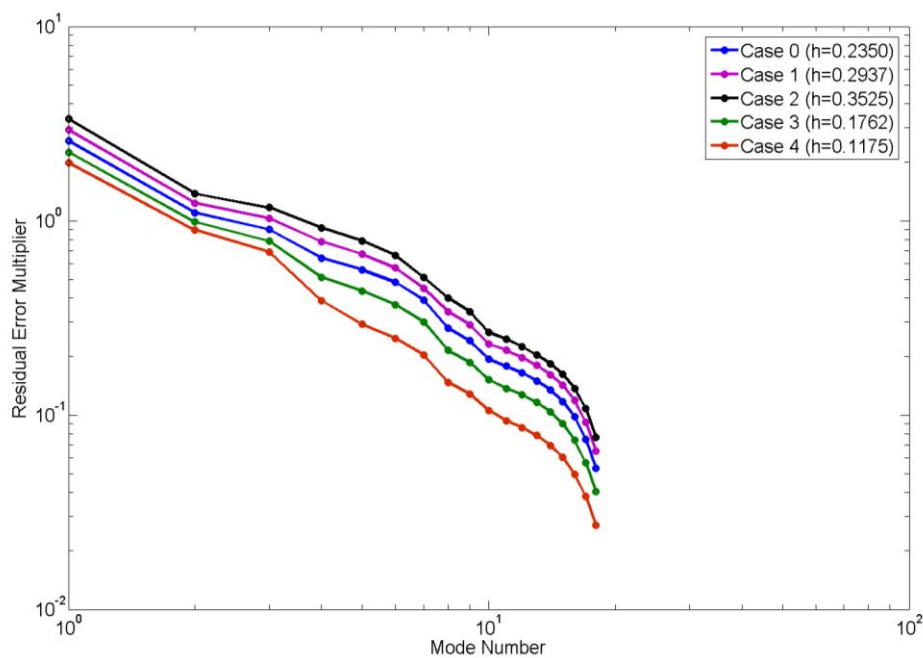
Figure 6-20. PSMT Error Multiplier Sensitivity w.r.t. h.

6.2.3.4 Sensitivity with *l*

The parameter *l* is the vertical length of the edge sensor. This parameter is one of the most sensitive to the error multiplier as well as mechanical design. It needs to be optimised considering both design feasibility and error multiplier contribution.

Table 6-8 Parameter Sensitivity w.r.t l.

''Parameters	Case 0 (Nominal Parameters)	Case 1 (+25%)	Case 2 (+50%)	Case 3 (-25%)	Case 4 (-50%)
Nr	1	1	1	1	1
a	0.30 m	0.30 m	0.30 m	0.30 m	0.30 m
f	0.057 m	0.057 m	0.057 m	0.057 m	0.057 m
h	0.235 m	0.235 m	0.235 m	0.235 m	0.235 m
l	0.02 m	0.025	0.03	0.015	0..01
del	0.004 m	0.004 m	0.004 m	0.004 m	0.004 m
eta	0.0531	-	-	-	-
Result	2.581	1.848	1.486	4.293	9.395
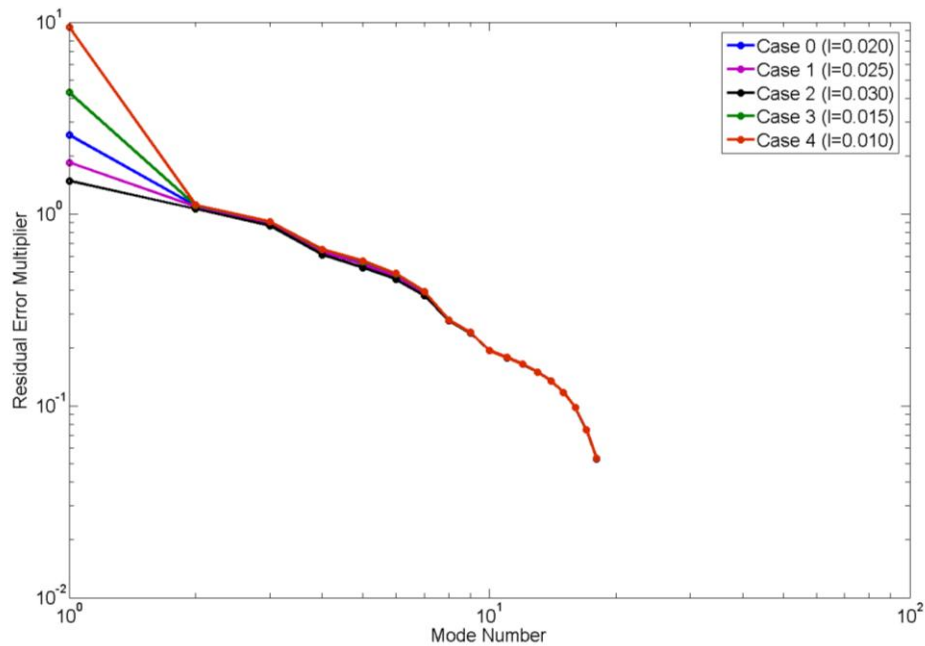
Figure 6-21. PSMT Error Multiplier Sensitivity w.r.t. l.

6.2.3.5   Sensitivity with *del*

The parameter *del* is the gap between edge sensor drive and sense plates. Practically for vertical edge sensors this gap need to be greater than or equal to the inter segment gap to avoid any interference while segment lifting and removal.

Table 6-9 Parameter Sensitivity w.r.t del.

Parameters	Case 0 (Nominal Parameters)	Case 1 (+25%)	Case 2 (+50%)	Case 3 (-25%)	Case 4 (-50%)
Nr	1	1	1	1	1
a	0.30 m	0.30 m	0.30 m	0.30 m	0.30 m
f	0.057 m	0.057 m	0.057 m	0.057 m	0.057 m
h	0.235 m	0.235 m	0.235 m	0.235 m	0.235 m
l	0.02 m	0.02 m	0.02 m	0.02 m	0.02 m
del	0.004 m	0.005 m	0.006 m	0.003 m	0.002 m
eta	0.0531	-	-	-	-
Result	2.581	3.119	3.67	2.064	1.586
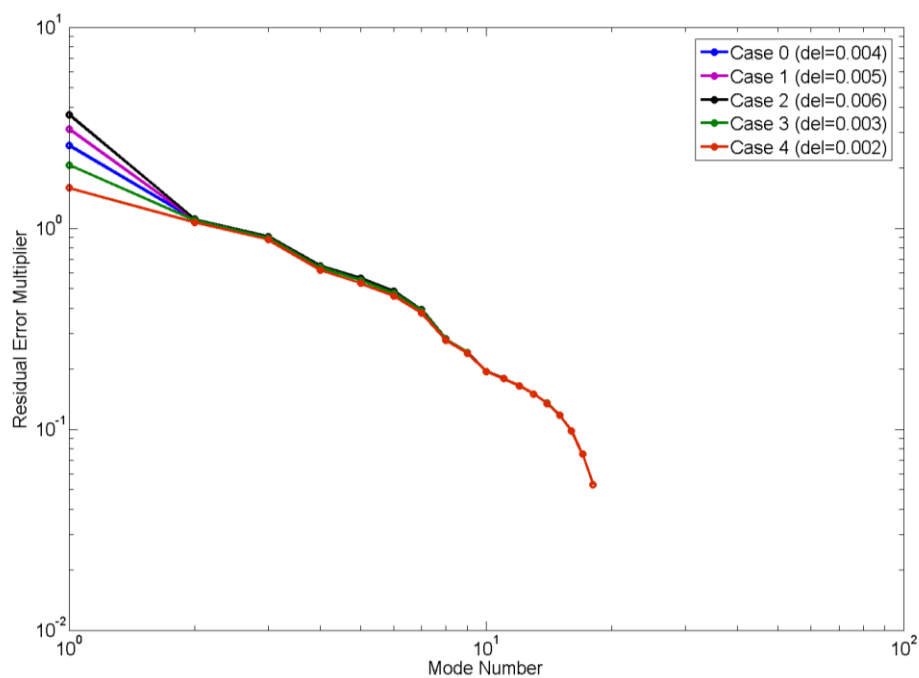
Figure 6-22. PSMT Error Multiplier Sensitivity w.r.t. del.

6.2.3.6   Comparison of parameter sensitivities

Based on the above sensitivity analysis, it can be seen (Table 6-10) that the most sensitive parameter is l which is basically the edge sensor vertical height. Though it can be seen that some parameters can be further changed to reduce the error multiplier whereas the baseline parameters are selected based on practical considerations such as space and volume availability behind the primary mirror. Such analysis is very helpful for parameter optimization of SMT primary mirror control system components.

Table 6-10 Summary of Sensitivity study of different PSMT parameters on error multiplier.

Parameters	Case 0 (Nominal Value)	Case 1 (+25%)	Case 2 (+50%)	Case 3 (-25%)	Case 4 (-50%)
1 *eta*	0.0531	0.0663	0.0796	0.0398	0.02655
error multiplier	2.581	2.168	1.901	3.305	4.797
2 *f*	0.057 m	0.07125	0.0855	0.04275	0.0285
error multiplier	2.581	2.633	2.74	2.555	2.551
3 *h*	0.235 m	0.29375	0.3525	0.17625	0.1175
error multiplier	2.581	2.944	3.337	2.254	1.989
4 *l*	0.02 m	0.025	0.03	0.015	0.01
error multiplier	2.581	1.848	1.486	4.293	9.395
5 *del*	0.004 m	0.005	0.006	0.003	0.002
error multiplier	2.581	3.119	3.67	2.064	1.586

6.3   Summary and Conclusion

In this case study, PSMT Error Multiplier analysis is presented. This study is entirely based on the codeSMT tool. The error multiplier was estimated based of two methods – Analytically and Numerically. Results obtained from both the methods are similar. Error multiplier sensitivity w.r.t. different M1CS parameters of the PSMT were also studied, and edge sensor vertical length was found to be the most sensitive parameter. As discussed in this chapter, the change in readings at Edge sensor lead to

the corrections at the actuator, and the RMS of actuator gives us the RMS of M1 surface. This property is used to estimate the wavefront error due to random noise at the Edge sensors, which reflect as the actuator corrections. These corrections lead to the common problem in SMT called the focus mode effect. The reason for the focus mode to build up is that it is the least observable mode by the ES and corresponds to the highest error multiplier. Other lower order modes namely Tip, Tilt, and Piston are not at all observable. The Error multipliers are very small for higher order modes because edge sensors are sensitive to such spatial deformation on the primary mirror. The sensitivity of error multiplier for varying dihedral angle (i.e., eta) suggests that the best way to reduce the problem of the focus mode is to design an edge sensor which can have very high dihedral sensitivity.

We decomposed the PSMT mirror in its different spatial mode shapes. It was observed that most of the RMS surface deformation (half the wavefront error) is in the first focus mode. The energy in different modes keeps on decreasing as modes increases. If we have a big segmented mirror telescope, this low order deformation effect becomes larger and larger and need to be detected and corrected with the aid of an on-axis wavefront sensor. As described in (Chanan, et al. 2004) & (MacMartin and Chanan. 2003), this effect is relatively small for seeing limited observations whereas it becomes a concern for the diffraction limited observation. Typically, large optical telescopes are usually equipped with Adaptive Optics system, which consists of a wavefront sensor. This wavefront sensor is capable of detecting the low order shape deformations and can offload it to the primary mirror through the global controller.

Chapter 7   PSMT M1CS Networked Control System Testbed

The global controller is responsible for the overall system control, calibration, configuration, diagnostics, and other executive functions as well provide an engineering interface. The primary role of the Global Controller is to run the Primary Mirror Control System (M1CS) algorithm in real-time. M1CS maintains the mirror shape in the presence of slow disturbances attributable to changing temperature and telescope elevation angle (gravity vector), as well as dynamic disturbances from wind and vibration sources. M1CS typically runs at 1Hz bandwidth. The reference set points of the M1CS are determined by the Alignment and Phasing System (APS). The global controller is also responsible for receiving calibration and offset data from the Telescope Control System (TCS) and uses it during the M1CS calculations.

7.1   PSMT M1CS Architecture

In this work, we have designed and implemented the entire global and local control system for the PSMT on the actual hardware. This hardware acts as a testbed for different experiments related to PSMT M1CS operation. It consists of the 21 actuator Local Controllers (LC) connected to the Global Controller (GC) via the Controller Area Network (CAN). Each LC is capable of handling actuators in different modes of operation (see Table 7-1). The Global Controller sends various commands to the LC via the CAN network in terms of the broadcast message or the direct messages. Presently Edge sensor data required for the GC operation is

simulated inside the GC with the noise characteristics corresponding to the Edge sensors. The GC converts this Edge sensors data into the necessary actuator commands, and send to the LC via the network as set point messages. Each LC can detect its serial number based on the hardware id number switches provided on the baseboard for each LC on the Networked Control System (NCS) testbed. This feature is handy to load a generic LC firmware, and then LC configures itself based on its id number. Also, any further settings can be updated from the GLC if required. The GLC does this in the mode called as parameter update mode where it reads the Configuration file provided by the user containing the list of parameters and their corresponding values for each local controller. At LC, precautionary measures are taken at the software level to avoid any repeated execution of the same mode due to delay in messages or any faulty situation.
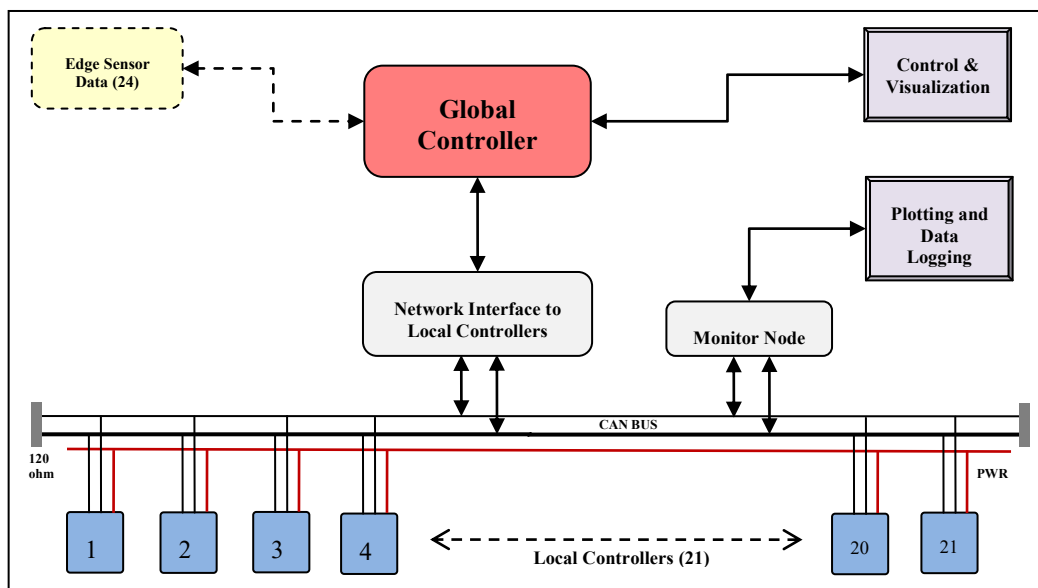
Figure 7-1. The System level block diagram of PSMT M1CS NCS experiment.

An additional monitor node connected to the network receives different information coming from GC and LC, and then sends it to the Personal Computer (PC) after decoding. On the PC this data is used by the serial plotting tool for real-time plotting and logging of individual actuator position and set points. The GC is

also connected to the PC from where it receives top-level commands from the user. A GUI is built in Matlab provides a front panel for controlling different modes of operation to the GC as shown in Figure 7-2. This GUI is also useful to monitor the Actuator and Edge sensor status along with the Visualisation of overall mirror shape. This Visualization tool will be further updated to provide the diagnostics feature.
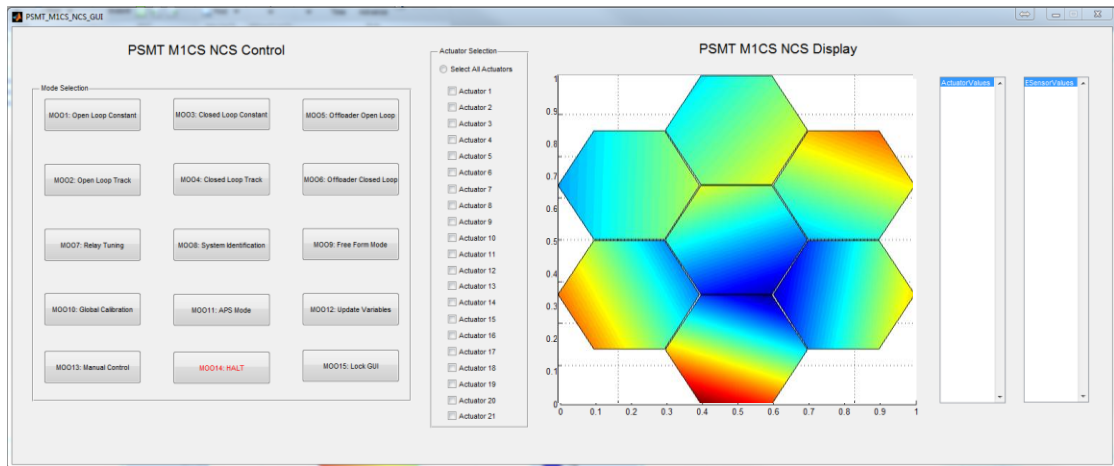
Figure 7-2. The GUI of PSMT M1CS NCS experiment. It is used for selecting different Modes of Operations (MOO), Actuator and Edge sensor values, and Visualizing the primary mirror shape.

The GUI runs the Mode Transition logic in the background for identifying which mode is allowed for transition and which one is forbidden, based on the user inputs and the present actuator mode. Any forbidden mode is detected and denied based on this logic and informed to the user with the possible transitions. Some modes can only be achieved through the sequence of few other modes, and this is identified by the GUI and indicated to the user.

Mode Transition Matrix	Next Mode Name	Open Loop - Constant	Open Loop - track	Close Loop - Constant	Close Loop -Track	Offloader mode - OL	Offloader mode - CL	Relay Tuning	Identification mode	Free Form Mode	Global Calibration	APS mode	Update Variables	Manual Control	Halt System	Lock GUI
Present Mode Name	Mode No.	MOO1	MOO2	MOO3	MOO4	MOO5	MOO6	MOO7	MOO8	MOO9	MOO10	MOO11	MOO12	MOO13	MOO14	MOO15
Open Loop - Constant	MOO1	1	1	1	1	1	1	1	1	1	0	0	0	1	1	NA
Open Loop - track	MOO2	1	1	1	1	1	1	0	0	1	0	0	0	1	1	NA
Close Loop - Constant	MOO3	1	1	1	1	1	1	0	0	1	1	1	0	1	1	NA
Close Loop -Track	MOO4	1	1	1	1	1	1	0	0	1	0	0	0	1	1	NA
Offloader mode - OL	MOO5	1	1	1	1	1	1	1	1	1	0	0	0	1	1	NA
Offloader mode - CL	MOO6	1	1	1	1	1	1	0	0	1	0	0	0	1	1	NA
Relay Tuning	MOO7	1	1	1	1	1	1	1	1	1	0	0	0	1	1	NA
Identification mode	MOO8	1	1	1	1	1	1	1	1	1	0	0	0	1	1	NA
Free Form Mode	MOO9	1	1	1	1	1	1	1	1	1	0	0	0	1	1	NA
Global Calibration	MOO10	1	1	1	1	1	1	0	0	1	1	1	0	1	1	NA
APS mode	MOO11	0	0	1	1	0	1	0	0	0	0	1	0	0	1	NA
Update Variables	MOO12	0	0	0	0	0	0	0	0	0	0	0	0	0	1	NA
Manual Control	MOO13	1	1	1	1	1	1	0	0	1	0	0	1	1	1	NA
Halt System	MOO14	1	1	1	1	1	1	1	1	1	0	0	1	1	1	NA
Lock GUI	MOO15	NA	NA	NA	NA	NA	NA	NA	NA	NA	NA	NA	NA	NA	NA	NA
NOTE:	0 = Forbiden / Allowed through intermidiate transitions.															
	1 = Direct Allowed transition.															

Figure 7-3. The Mode Transition Matrix implemented in the GUI for the NCS Mode selection and transition.

The mode transition from present to the next is only possible if the intersection has '1'. If it is '0' that mode is forbidden and user need to switch to other allowed mode before selecting the desired Mode of Operation (MOO). This method of mode selections ensures the next mode selected has favorable actuator and controller state.

7.2 PSMT M1CS Modes of Operation

In Table 7-1 different Modes of Operation of PSMT M1CS are listed along with their operational details. All these modes are implemented on the M1CS NCS testbed.

Table 7-1. Different Modes of Operations of the PSMT M1CS.

Mode No.	Mode Name	Description
MOO1	Open Loop - Constant	In this mode all the actuators run in open loop mode, the drive signal is proportional to the setpoint input. The Local Controllers (LC) keeps
MOO2	Open Loop - Track	reading the setpoints received from the network and executes it in open loop mode. The position of actuators is sent back on the network and is received by the monitor node for display and logging purpose. The open loop (OL) modes can work in two ways - one with a constant set point update and other with a track rate input in addition to the discrete set point updates.
MOO3	Close Loop - Constant	In this mode, all the actuators run in closed loop mode and try to attain the given set point. The drive value is calculated based on the PID law and
MOO4	Close Loop - Track	position error. The closed loop (CL) modes can work in two ways - one with constant setpoint update and other with an additional component of actuator track rate in addition to the setpoint update.
MOO5	Offloader mode- OL	In the offloading mode, actuators can be kept in either OL or CL mode. The user can send start offloader and stop offloader commands. When start
MOO6	Offloader mode -CL	offloader is received, the offloader will run at a constant rate in the specified direction.
MOO7	Relay Tuning	This mode is to find the optimum PID gains of the actuator controller. Here in the relay mode actuator goes in OL state and the setpoint is updated automatically inside the LC every time the threshold position is reached. The setpoint is switched between two predefined values. The actuator position response is continuously sent on the network for monitoring and analysis purpose. At a time only one controller will be active and rest all will be in the halt state.
MOO8	Identification mode	This mode is to identify the actuator plant model. Once this mode is selected actuator starts running in OL state and the set points are updated with the sine sweep signal inside the LC. Corresponding position response is continuously sent on the network for monitoring and analysis purpose along with the set point sine-sweep data. At a time only one controller will be active and rest all will be in the halt state.
MOO9	Freeform	In this mode, actuators are driven at a fixed input based on the previous set

	Mode	point in OL mode, and the position data is sent on the network continuously. The system remains in this mode until the next MOO command.
MOO10	Global Calibration Mode	This mode is to estimate the Interaction matrix of the telescope required in M1CS calculation. To do this GC commands one LC at a time to execute a sequence of square wave set point with a predefined amplitude and duty cycle. While this is happening LC will send back the Actuator position and GLC will forward the Edge Sensor readings on the network. Both actuator and Edge sensor data are collected by the monitor node for further analysis.
		This calibration needs to be done whenever there is a change in the hardware on the primary mirror (typically once in a month for PSMT). This procedure can be multiplexed to speed up the calibration process, but since PSMT is a relatively small system and involves only 21 actuators, we will do this calibration with one actuator at a time for simplicity.
MOO11	APS mode	In this mode, GLC gets offsets to be achieved for co-aligning/ co-phasing the primary mirror from the Alignment and Phasing System (APS) controller. All the actuators work in the closed loop mode and execute the set point change commands coming from the global controller. The global controller generates the set points to the LC based on the Tip, Tilt, and Piston (TTP) values received from the APS controller.
MOO12	Update Variables	In this mode, GLC sends all the settings provided by the user in the form of a controller configuration file which consists of different parameters like PID gains, Mapping relations, Track rate, Delay times, Relay amplitudes, System id frequencies, etc. In the configuration file, this information is provided for individual 21 controllers in a systematic format so that GLC can read it and send it to respective LCs one by one. The received parameters are used by the LC to update its current parameters.
		The LC also maintains the set of all the predefined default parameter values in its memory. So in the situation when the user wants to roll back to the default parameters, a flag is enabled by the user in the configuration file, and the GC passes this flag to the respective LCs for assigning default parameters to the current variables in the LC.
MOO13	Manual Control	In the manual control mode, the user can select the sub-mode of operation (i.e., OL/CL) and provides the displacement value through which actuator

		should move from its existing position. In this mode, offloader can also be controlled to offload the actuator in the required direction for user inputted distance/steps.
MOO14	Halt System	In this mode, all the actuator controllers will be halted and will be waiting for further MOO command. The user can halt a single actuator or all of them at a time. In this mode LC does the following operations:
		Resets the VCM drive board, resets the setpoint to zero, resets the drive value to zero, resets the Offloader drive board, resets the encoder position to 0 (if requested by the user).
MOO15	Lock GUI	As the name suggests, all the control buttons on the GUI software gets deactivated to avoid any unwanted command from the user. In this mode, LC and GC continue to run in their previous MOO. GUI gets activated again by pressing same Lock GUI button.

All the above modes of operation are implemented in the NCS testbed hardware (Figure 7-4), and they are tested thoroughly for the functionality. The main flowchart of NCS operation is also given in Appendix D.

7.3   NCS Testbed

In the NCS testbed hardware, we have used 21 Local Controllers based on the Programmable System on Chip (CY8CKIT-050 PSoC 5LP board). We are using a Single Board Computer (1.2GHz 64-bit quad-core ARMv8 Rpi3 board) as a Global Controller. We calculated the Global Controller Computational Requirements (see Appendix G for details) for the PSMT and found that we will not need very high processing capability in a small telescope like the PSMT.
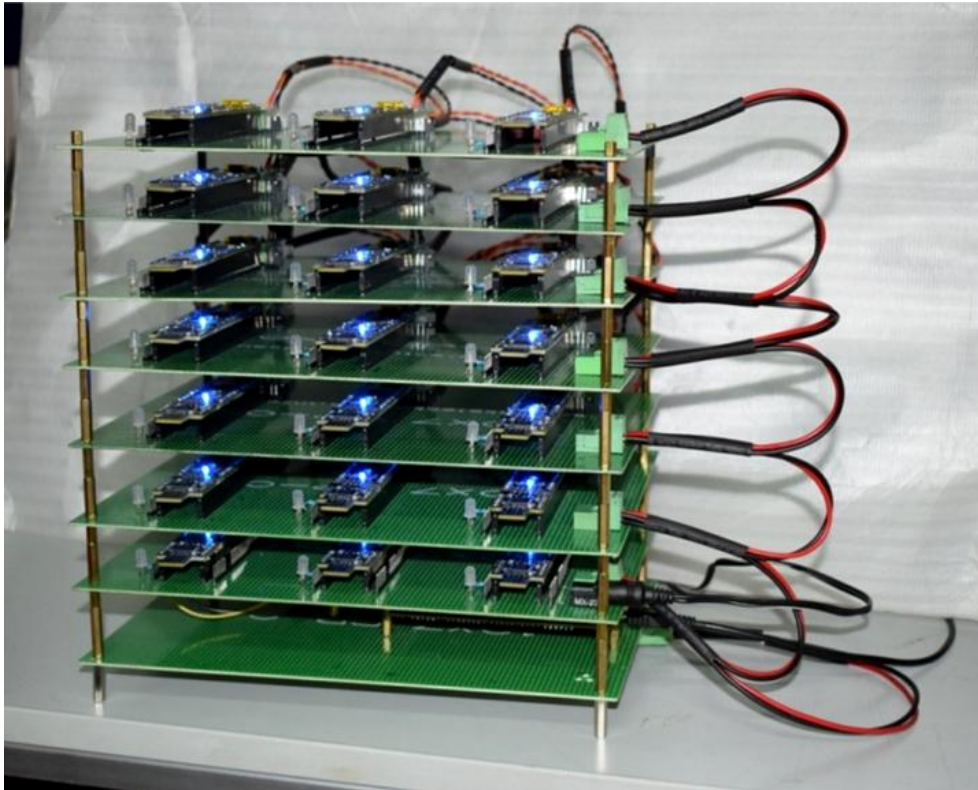
Figure 7-4. The PSMT M1CS NCS testbed hardware with 21 Local Controllers (CY8CKIT-050 PSoC 5LP board) connected on a CAN network with the Node box and the Global Controller board (1.2GHz 64-bit quad-core ARMv8 Rpi3 board).

The NCS hardware is designed in a modular fashion such that individual controllers can be plugged on the baseboard through which it gets connected to the CAN network and all its GPIO and special function pins are accessible to the user. The baseboard also provides the feature of connecting LC in different network topologies by using additional network tap points. A separate wiring harness is designed for powering all the controllers from a single power supply. Two sets of CAN network cable options are available, one with short twisted pair patch cables and other with actual length (1.22m long) shielded twisted pair cables. We conducted the network performance tests using the CAN bus analyzer feature on the Mixed Signal Oscilloscope (MSO) at different data rates and following is the result obtained. As can be seen, 8K CAN frame per second (64 KBps data) was transferred with around 98% network utilization and without any frame losses. This is more than sufficient

compared to the actual frame rate requirement for NCS experiment. At its most demanding data rate for the PSMT M1CS modes (i.e., Relay tuning and system identification), 5K frames per sec (40 KBps) are required to be transferred over the NCS network.
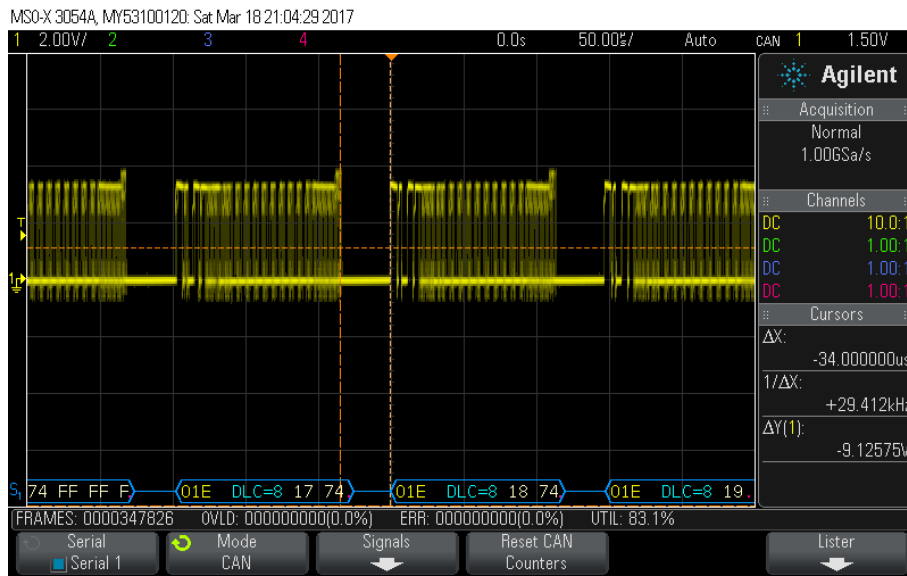
Figure 7-5. Sample screenshot of the network performance test using the CAN bus analyzer on the Mixed Signal Oscilloscope.
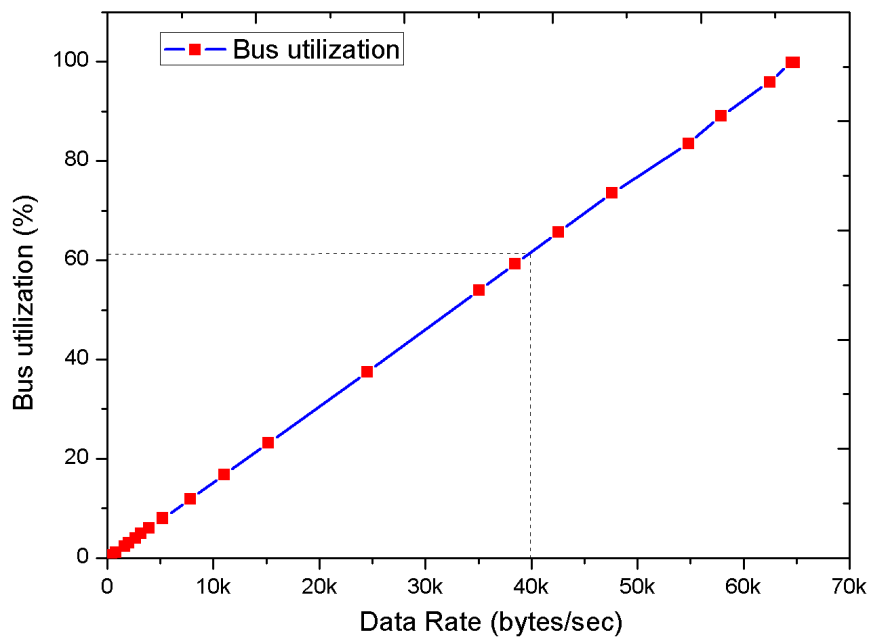
Figure 7-6. M1CS NCS CAN network bus utilization w.r.t. data rate. Satisfactory performance is achieved without any frame loss. The dotted line indicates the minimum required performance for the PSMT.

7.4   Test Results

The working of NCS hardware and software was verified, and test results are presented in this section. The GLC, monitor node and all 21 controllers were connected to a CAN bus. The GLC sends commands to the actuator, and all the actuators send back the setpoint information to the node controller. The monitor node controller plots the data sent by all the local controllers. Figure 7-7 shows the screenshot of data being received on the serial terminal which is logged as a text file for further analysis. There are hardware LEDs connected to each actuator controller to indicate its present modes of operation. Actuators go into a particular mode of operation as asked by GLC. All communication is done at a baud rate of 1 Mbps. The test results presented are to validate the functionality of NCS hardware and software, all 21 actuators were not connected physically, but their local controllers were connected and programmed to send the representative data. So the test results for open loop and closed loop are similar here. The functionality test is done for different modes of operations and results are found to be satisfactory.
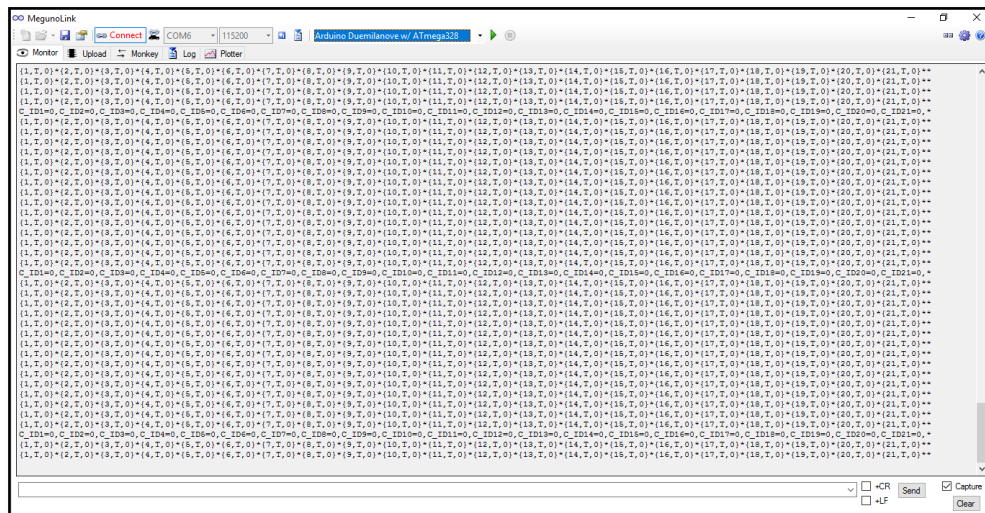
Figure 7-7. Screenshot of monitor node which receives data from all 21 controllers.

7.4.1 Step response

In this test, GLC commanded all actuators at a regular interval of 15sec to step to the new constant setpoint value (stepped by 500nm). As seen in Figure 7-8 all actuators respond to this command and send back the position data on the network at the rate 1Hz. Monitor node receives this data and logs it. This test was repeated by commanding only 5th and 10th actuator with some time gap and similar results were obtained as seen in Figure 7-9. This verifies that the step command and data sent by GLC are received by local controllers. Also, all of them go into freeform mode after updating its set point.
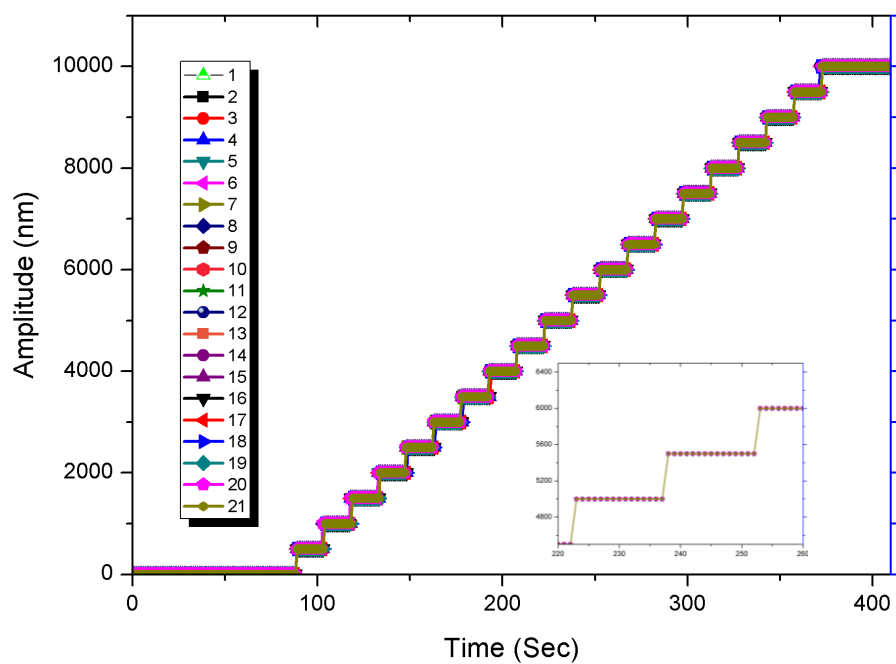
Figure 7-8. Step response (Open Loop and Closed Loop Constant mode) with all 21 local controllers active.
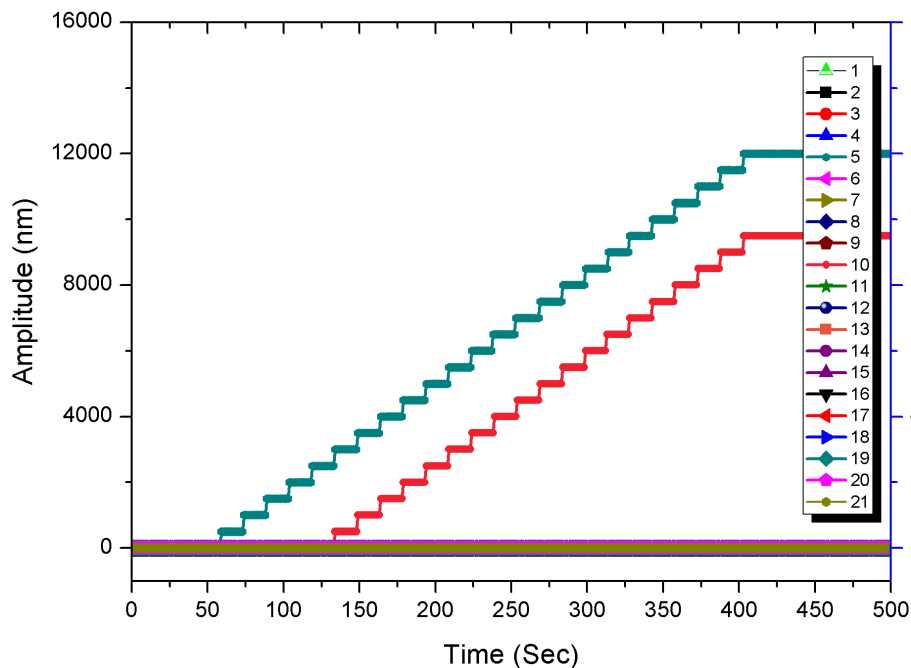
Figure 7-9. Step response (Open Loop and Closed Loop Constant mode) with only 5th and 10th local controllers active.

7.4.2 Track response

In this test, GLC commanded all actuators at a regular interval of 30 sec to follow a track rate input (at 800 nm/sec) for a 30-sec duration. As seen in Figure 7-10 all actuators respond to this command and send back the position track data on the network at the rate 1Hz. Monitor node receives this data and logs it. This test was also repeated by commanding only 5th and 10th actuator with some time gap and similar results were obtained as seen in Figure 7-11. This verifies that the track command and data sent by GLC are received by local controllers. Also, all of them go into the freeform mode after the tracking duration of 30sec is over.
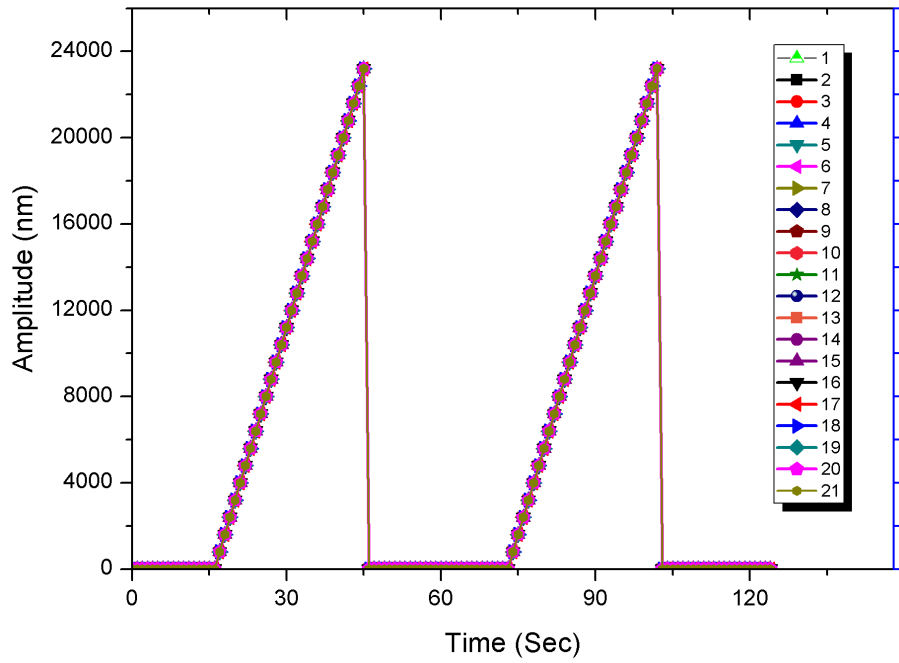
Figure 7-10. Track response (Open Loop and Closed Loop Track mode) with all 21 local controllers active.
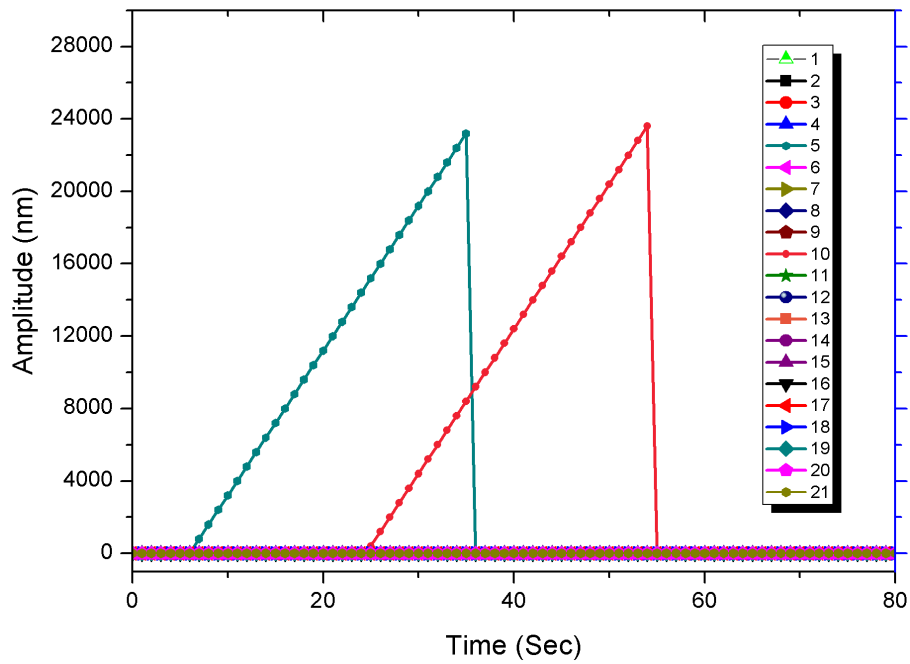
Figure 7-11. Track response (Open Loop and Closed Loop Track mode) with only 5th and 10th local controllers active.

7.4.3 System Identification

In this test, we command only one actuator at a time so as to get system identification (SID) data at the higher rate of 400Hz (400 samples per second). The GLC commanded only 6th actuator to start SID routine with default parameters and actuator local controller generates sine sweep signal (with the duration of 50sec, maximum frequency up to 50Hz, and amplitude of ±1000nm) internally to drive actuator with it. As seen in Figure 7-12 actuator position oscillates with this sine sweep input and this position data is sent back on the network at the rate of 400Hz (against 1Hz nominal data rate in other modes). Here Monitor node receives this data and logs it. This verifies the system Identification capability of global and local controllers along with the capability of handling the data rate of 400Hz. Once test duration is over, the local controller goes into the freeform mode by default.
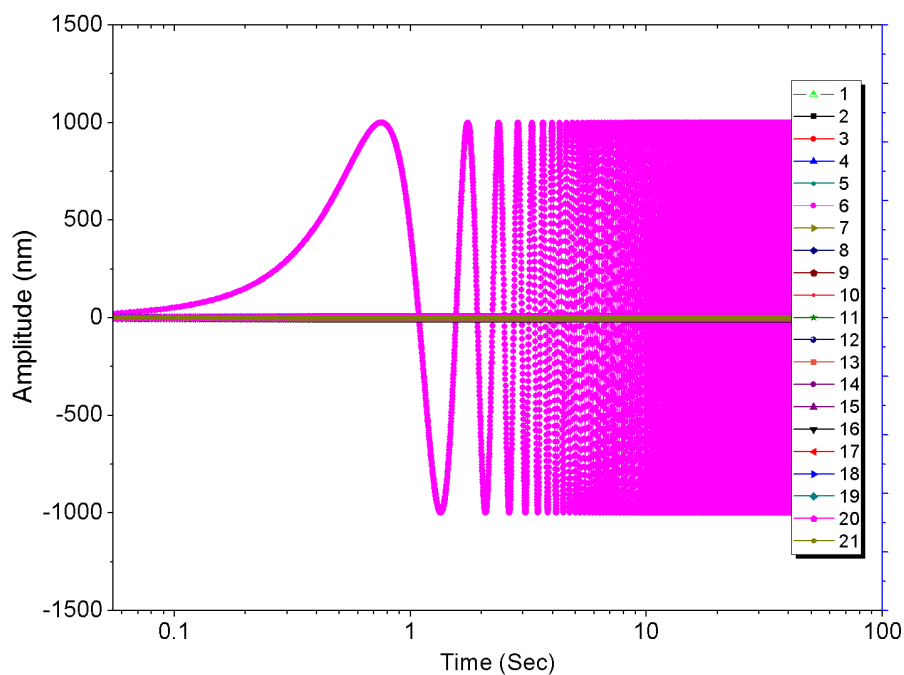
Figure 7-12. System Identification mode with only 6th local controllers active and with data rate (sampling) of 400Hz. This signal has the sweep duration of 50sec, the maximum frequency of 50Hz, and the amplitude of ±1000nm. (The x-axis is plotted in log scale to see lower frequencies in the sine sweep signal clearly).

7.4.4 Global calibration mode

This mode is designed to estimate the Interaction matrix of the telescope required in M1CS calculation. To do this GC commanded one Local Controller (LC) at a time to execute a sequence of two square waves set point with an amplitude of 2500nm. While this is happening LC sends back the Actuator position and GLC is supposed to forward the Edge Sensor readings on the network (presently hardware not connected). Both actuator and edge sensor data need to be collected by the monitor node for further analysis. This calibration needs to be done whenever there is a change in the hardware on the primary mirror (typically once in a month for the PSMT). This procedure can be multiplexed to speed up the calibration process but since the PSMT is relatively small system and involves only 21 actuators we did this test one actuator at a time as shown in Figure 7-13 for simplicity.
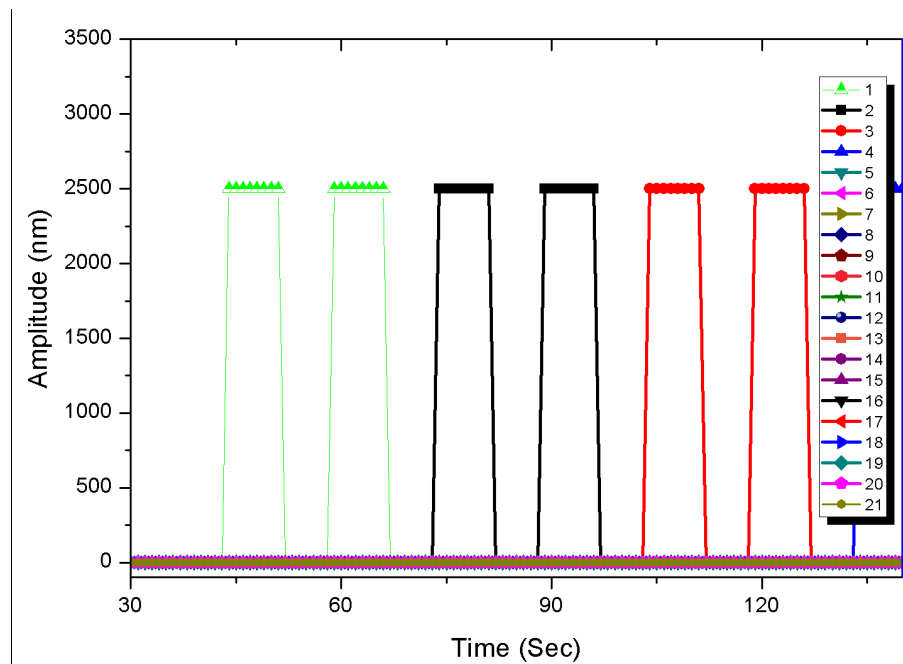
Figure 7-13. Global Calibration Mode with one local controller active at a time. Every local controller is activated sequentially for two square wave cycles from the global controller.

7.4.5 Freeform & Halt Modes

In this test we check the functionality of NCS testbed to execute two basic but very useful modes of operations – Freeform and Halt modes. In the Freeform mode, actuators are driven at a fixed input based on the previous set point in open loop mode, and the position data is sent on the network continuously. The system remains in this mode until the next MOO command. In the Halt mode, all the actuator controllers will be halted and will be waiting for further MOO command. Initially, global controller commanded all the actuators to enter in the track mode, and at 20th second, the freeform mode was commended for the duration of 15 seconds. After freeform mode, actuators are commanded again to enter in track mode which terminates with a Halt command where all the actuators get reset. Operation of both Freeform and Halt modes are confirmed as shown in Figure 7-14.
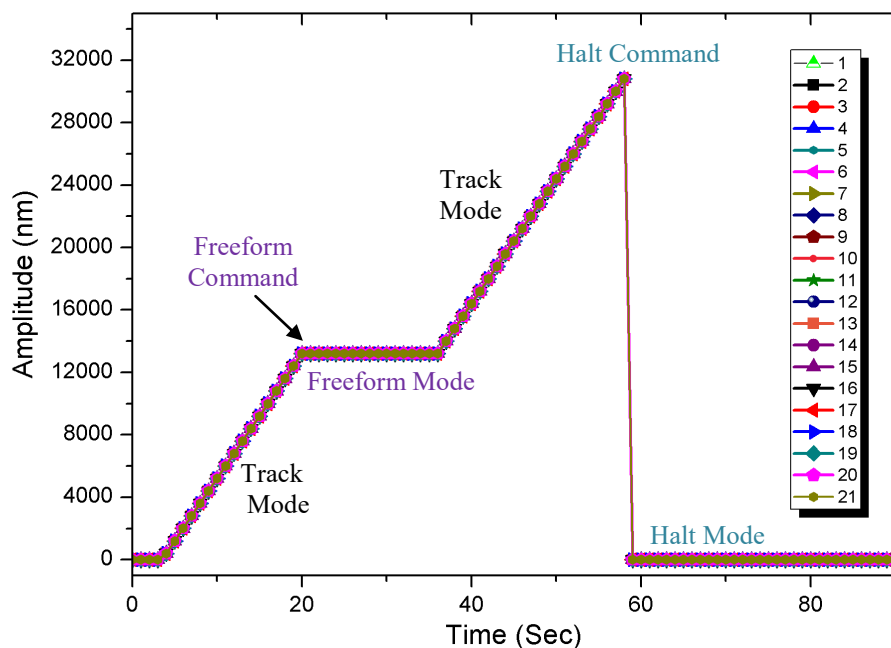
Figure 7-14. Freeform and Halt mode with all 21 local controllers active.

7.5   Summary and Conclusion

In this chapter, we presented the design and implementation aspects of the global and local control system for the PSMT on the actual hardware. This hardware acts as a testbed for different experiments related to PSMT M1CS operation. It consists of the 21 actuator Local Controllers (LC) connected to the Global Controller (GC) via the Controller Area Network (CAN). Each LC is capable of handling actuators in different modes of operation. Different modes were identified, and their functionality was defined in the context of PSMT M1CS. The Global Controller acts as the master node and sends various commands to the LC via the CAN network in terms of the broadcast message or the direct messages. A control GUI was implemented with mode transition matrix as a governing and is crucial while switching between the modes.

The complete NCS testbed hardware was implemented in a modular way, using 21 identical Local Controllers based on the Programmable System on Chip (CY8CKIT-050 PSoC 5LP board) and a Single Board Computer (1.2GHz 64-bit quad-core ARMv8 Rpi3 board) that acts as a Global Controller. Both local and global controllers communicate over the CAN network. Performance of CAN network was evaluated on the MSO CAN analyzer and found to be sufficient for our requirements. Further entire NCS testbed was tested for its Modes of Operations and results obtained were found to be meeting the functionality requirements. In future, this NCS hardware will be further tested and fine-tuned to act as the PSMT M1CS NCS hardware on the actual telescope.

Chapter 8   Conclusion and Future Work

In this thesis, I studied the Primary Mirror Control System aspects of the Prototype Segmented Mirror Telescope under design at the Indian Institute of Astrophysics, Bangalore. The primary aim of this thesis was to Model, Simulate and Implement the Primary Mirror Control System for the Prototype Segmented Mirror Telescope. The entire work carried under this thesis can be broadly divided into two parts. The first part deals with the design, development, and testing of a soft actuator for the PSMT telescope. Whereas, the second part primarily deals with creating a generic simulation tool and implementation of a global controller for the PSMT primary mirror.

In this chapter, I will summarize the content of this thesis along with a few directions in which I would like to continue my work in the future.

8.1   PSMT Actuator and Controller

For the PSMT we develop a soft actuator, which is not only lesser in cost but also simple in manufacturing. We had a choice of either opting a hard actuator like one used in Keck (Meng, et al. 1990), SALT (Swiegers and Hitesh 2004) and LAMOST (Xu, Xu and Jin 2003) telescopes or go with VCM based soft actuator to be used in TMT (Lorell, Aubrun, et al. 2006) and E-ELT (Jiménez, et al. 2010) telescopes. Looking at ease in realizing the soft actuator which also does a better job when it comes to rejecting the dynamic disturbance, we decided to follow the path chosen by TMT and E-ELT. First, we developed a parametric model of the actuator followed by conceptual mechanical design which was further fine-tuned to meet the

requirements. Then after detailed built to print drawing were generated and all the mechanical components were manufactured in IIA workshop. This actuator design led to the indigenous development of a subcomponent named Voice Coil Motor (VCM) and Disc Flexures.

In addition to electromechanical design, the performance of actuator also depends on the controller electronics as well as control algorithms. Therefore, we also developed a robust actuator controller and related driver electronics. The control algorithms are implemented on a Programmable System on Chip (PSoC) based hardware. The PSMT actuator has gone through a rigorous performance test and found to meet most of the design requirements. The closed-loop step response was achieved with the steady-state error of 5.73 nm RMS. We could successfully demonstrate that the closed loop position tracking error can be as small as 10.15 nm, which was better than the tracking accuracy required for the PSMT. The discrete offloading in closed loop mode was achieved at the rate of 500nm/sec. The tracking error during the offloading period was found to be no more than 40nm.

The PSMT actuator is a compact, lightweight and very low-cost solution in comparison to TMT and E-ELT actuators, for the relatively small and low budget project like the PSMT. The main limitation of the PSMT actuator is high power consumption due to the on-axis mechanism in comparison to the off-axis counterpart. Also due to the on-axis mechanism, it needs larger VCM with high force constant. Based on the experience of this first prototype (P1) actuator, we have modified the actuator design to the second prototype (P2). The main feature of P2 is to give similar performance as that of P1 but with the reduced size and footprint. In the near future, we intend to carry out few advanced tests like lifetime and survivability (to understand the vibration and earthquake effect). The life testing of a few crucial components will be useful to understand the component reliability. Based on all these test results (of P1 and P2 actuators), the final actuator design will be realized, and 21 such actuators will be implemented in the PSMT.

8.2   Dynamic Loading Assembly (DLA)

To test the performance of actuators when it is subjected to the variable force such as gravity and wind-induced forces, we have developed a novel laboratory device named Dynamic Loading Assembly (DLA). We modeled, designed, manufactured and tested a dynamic loading assembly which can be used to simulate the wind-induced disturbances in the laboratory. Before realizing the device, through a simple spring-mass-damper based mathematical model, we ensured that the concept would indeed work. The care was taken to keep the structural modes out of wind spectral range (< 10Hz) and minimize the loss of force due to the device itself. A voice coil motor (VCM) is used in DLA to generate dynamic disturbances, which provide high bandwidth and frictionless operation. We have also developed a dedicated control electronics for the DLA, which can also handle a couple of sensors used in the device. The drive electronics has provision to select either voltage or current mode of operation to drive VCM. The smoothing effect of back emf generated by the VCM can be avoided if we operate VCM in the current mode, which in turn generate more accurate wind force profile at higher frequencies. DLA have a static and a dynamic loading capability up to 250N and 18N respectively, with a bandwidth sufficient to generate wind disturbances. It can generate force profiles by making use of wind model or else there is a provision to input the real wind data from the telescope site.

In the beginning, different tests were conducted to check the performance of DLA device itself followed by the performance test of the PSMT prototype actuator. We could demonstrate that despite being soft, the PSMT actuators can effectively suppress the wind-induced disturbances when operated in the closed loop with the RMS tracking error of 12.43 nm. With the PSMT actuator and DLA, the closed loop force track rate of 22mN/sec was achieved with the RMS tracking error of 5.44nmRMS.

After conducting varieties of the tests over the period of about two years, we have identified few limitations in the present DLA system. One of the limitations of the system is that it cannot generate force slew rates (say 15N/s), may require to test

actuator performance when the telescope is slewing from one object to other during the pointing. Another limitation is that the DLA does not allow simulating gravity loading at different telescope elevations by means of actual tilting the DLA and Actuator system. Whereas, by using the VCM of the DLA we have tried to generate force track rate on the actuator, representing the variable gravity force. But present DLA can introduce maximum static load up to 250N. These limitations will be taken into account while developing the DLA2, which will be the next version of the DLA. The DLA2 will have special primary mirror related features (inspired from the (Witvoet, et al. 2015) test setup of E-ELTs PACT actuator) including tilting entire DLA & Actuator system.

8.3   The CodeSMT tool

The codeSMT is a generic design and simulation tool developed for conducting a variety of studies related to the Primary Mirror Control System of any SMT's. The codeSMT is fairly generic in the sense that it can be used for any size telescope made of one or more rings as well having a different sensor-actuator geometrical configuration. The basic computation module in the codeSMT is to transform the edge sensor readings into the corresponding actuator corrections so as to maintain the shape of the primary mirror w.r.t., the reference shape. The underlying mathematical formulation used in codeSMT has been derived from the pioneer works carried out by Jerry Nelson and his collaborators for the Keck and TMT telescopes (Nelson, Mast and Chanan 2013). The tool is capable of carrying out error analysis, more specifically it allows to study the effect of sensor noise on various modes of the primary mirror. Another notable feature of this tool is that it can incorporate the dynamic behavior of the actuators in the presence of wind disturbances, which helps to evaluate telescope performance.

The interaction matrix i.e. A matrix used in this tool required a scheme for the ordering and numbering of segments, actuators and sensors and we did not find any published literature addressing this requirement. The giant telescopes like TMT and E-ELT use a sophisticated methodology to generate their A matrix, which is very

telescope specific and just cannot be used to some other SMT project. After knowing that there is no generalized way for numbering the component and constructing influence matrix, we decided to take this challenge and come up with a relatively simple technique. To solve the numbering problem, we have introduced a new scheme which can be used to generate the interaction matrix database. Presently we have developed the database of 12 rings telescope and is of the size of 1407×7 elements. The advantage of this approach is that this database needs to be developed only once and is reusable for formulating any SMTs.

The codeSMT tool is equipped with different features such as formulating the SMT with various telescope parameters like mirror sizes, the number of segments, types of sensors and actuators, disturbances, control loops, etc. It not only generate results in the form of a data but also visualizes output in a variety of forms like deformations of the mirror surface, wavefront error, PSF, error multiplier plots, sensitivity plots, etc. A dedicated segment plotting tool is developed and integrated with codeSMT, so as to visualize overall primary mirror shape as well as the shape of the primary mirror in different spatial modes (defocus, astigmatism, coma, spherical, etc. See Appendix E). The sensitivity of various parameters linked with the primary mirror can be studied in terms of its effect on the mirror shape and on the error multipliers which is a very useful feature during the early design phase of the SMTs.

The codeSMT has been used to conduct two major studies for the PSMT, one of Active Control Simulation and other of Error Multiplier analysis.

8.3.1 Active Control Simulation of PSMT

The codeSMT tool, combined with realistic actuator and wind disturbance models, has been used to simulate the active primary mirror control of the PSMT. In this study we used 21 actuator modules to form a local control system which were interfaced with the global controller through the codeSMT. This simulation tool allows us to explore the performances of the entire primary mirror control system, which comprises the wind disturbance model, global controller, local controller, actuator, and sensors. It greatly helps to fine-tune some of the critical parameters

linked with the actuator and sensors. Another major advantage of our tool is that it is fully parametric and can be used for the design and analysis of any upcoming segmented mirror telescopes.

In one of the active control simulation case, the PSMT mirror surface was subjected to wind disturbances (4m/sec) without any correction. In this case, the RMS surface error was 53.9nm. Whereas, once both local and global controllers are switched on then the corrected mirror surface error become 12nm.

In the future, we plan to incorporate the Telescope Mount control model in the present active control model. Also, we plan to develop an actuator dynamic model based on Model-Based Design approach so as to include the vibration disturbance to the actuator. This will also be helpful to consider and study the Control-structure interaction (MacMartin, Thompson, et al. 2014) on the telescope.

8.3.2 Error Multiplier of PSMT

Irrespective of which type of edge sensor chosen, all of them will be subjected to random uncorrelated noise/error. The control of segmented primary mirror by use of noisy edge sensors leads to unavoidable deformation in the overall shape of the primary mirror. The sensor noise gets reflected as 3N-3 modes, where N is the number of segments. Use of SVD for inversion of control matrix allows us to determine the noise multipliers for each mode which also naturally get arranged in increasing special frequency (MacMartin and Chanan. 2003). The codeSMT tool is very useful for evaluating the overall error multiplier for a given telescope configuration. The codeSMT offers two ways to estimate this error multiplier value – Analytically by using Interaction matrix and Numerically using the Monte Carlo numerical simulation. We have used both the methods while doing error analysis for the PSMT which is a single ring telescope. This is the very first time in the literature that anyone has estimated the error multiplier numerically, despite the fact that concept has been already outlined in (Chanan, et al. 2004). The Monte Carlo simulation for 10 million iterations was conducted for PSMT, and results were found to be accurate to the 4th decimal places as compared to analytical estimates. The

estimated Total Error Multiplier value from both the methods (Analytically and Numerically) was 2.5806.

Further to understand the effect of change of any of M1CS parameters on the error multiplier we did the parameter sensitivity analysis w.r.t the PSMT nominal/baseline parameters. The sensitivity of error multiplier for varying dihedral angle suggests that the best way to reduce the focus mode problem is to design an edge sensor which can have very high dihedral sensitivity.

In the future, we plan to expand the features of the codeSMT tool as a generic Integrated Modeling tool for the SMTs. This integrated model will include the codeSMT as its main backbone along with other modules such as optical analysis tools, structural models, disturbances, etc. Also, we plan to develop an interface to the optical analysis software for direct performance estimation of the PSMT. This will enable us to study the correlation between wind disturbance, mirror shape and the image quality of the telescope.

8.4 PSMT M1CS NCS Testbed

Finally, we attempted to develop a customized PSMT primary mirror controller which can be used in real PSMT telescope. We have successfully demonstrated the implementation of the entire global and local control system for the PSMT on the actual hardware. This hardware also acts as a testbed for different experiments related to PSMT M1CS operation. It consists of 21 Local Actuator Controllers (LC) connected to the Global Controller (GC) via Controller Area Network (CAN) interface. All 21 LC has got unique hard-coded identification number provided on their respective baseboard. This feature is very useful to load a generic LC firmware, and then LC configures itself based on its id number. Also, any further settings can be updated from the GLC if required. There is a provision of a monitor node connected to the network to monitor and receive data from all the LCs. A GUI is built in Matlab to provide a front panel for controlling different modes of operation

and to monitor the Actuator and Edge sensor status along with the Visualisation of overall mirror shape.

Further entire NCS testbed was tested for its Modes of Operations and results obtained were found to be meeting the functionality requirements. In future this NCS testbed hardware will be installed on Industrial Control chassis, further tested and fine-tuned to act as the PSMT M1CS NCS hardware on the actual telescope. Also in the future, it is planned to update the Visualization tool of the NCS testbed GUI, to provide the diagnostics capabilities for the PSMT.

Appendix A: Supplementary material of PSMT Actuator and Controller

a. Local Controller Flowchart
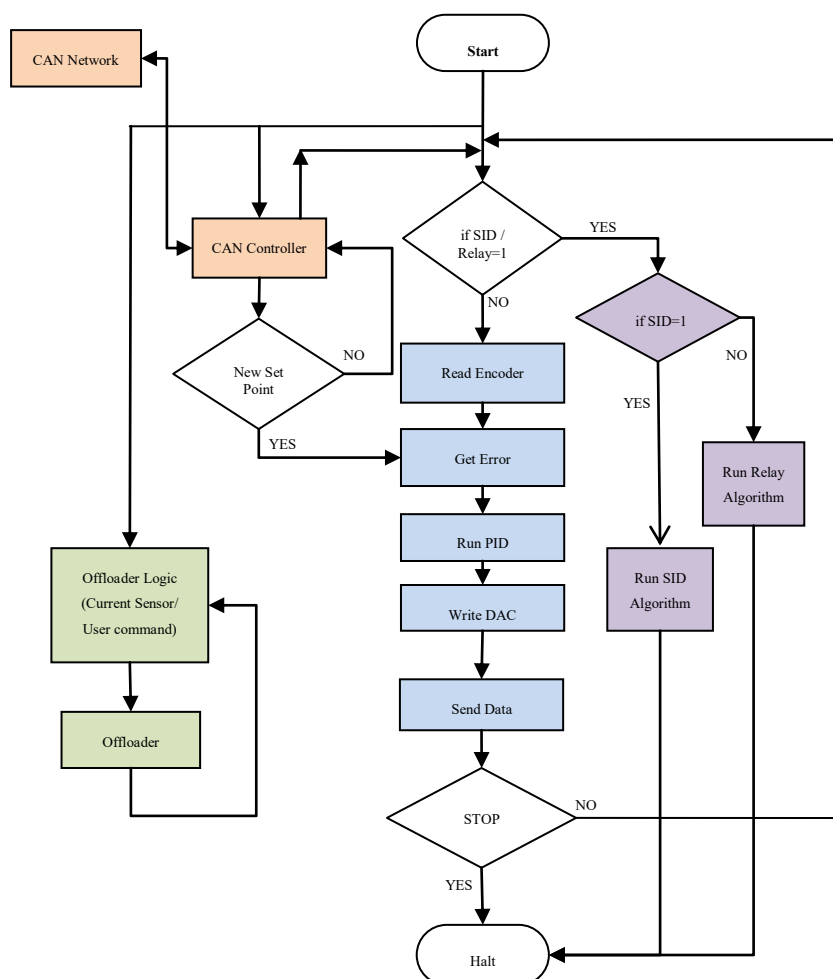
Figure A-1. Flowchart of the Actuator Local Controller.

The flowchart of the local actuator controller is shown above. Different tasks of the controller include:

1) Timers and Interrupt Service Routine (ISR) for synchronizing different tasks.

2) Communicating to the network to receive controller settings and the position set points.

3) Read encoder position information from the Quadrature Decoder.

4) Generate correction command using PID law.

5) Send and receive data from the PC / global controller using UART/CAN interface respectively.

6) Read current sensor information for the offloading.

7) Writing command to DAC via SPI interface.

 8) Run controller tuning and identification algorithms.

9) Monitor the actuator health status sensors and take appropriate actions.

Synchronization among the different controller tasks and modules is achieved by using timers and interrupts. Three timer interrupts of 2.5msec, 5msec and 1sec are implemented in the controller. The ISR of 2.5msec timer is to read position, filter the position data and send data to the UART/CAN. The function of 5msec interrupt service routine is to calculate error, then calculate PID command by using already stored PID gains and write the drive command to DAC via SPI interface. The function of 1sec ISR is to update setpoint based on the setpoint value received from the CAN network.

b. Controller Main loop
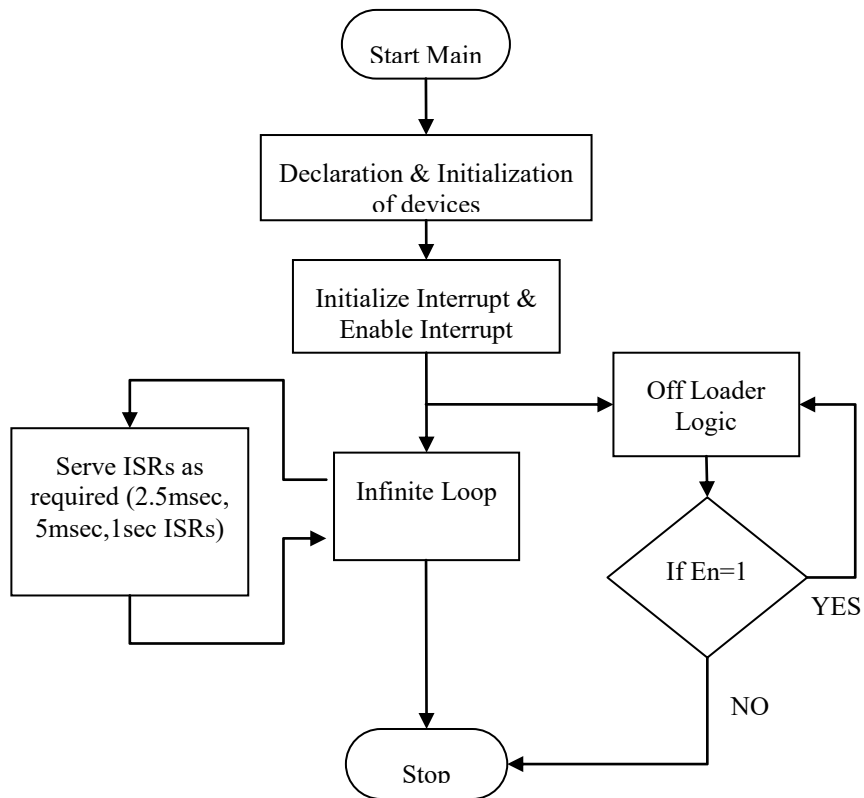
Figure A-2. Flowchart of Main Loop

c. ISR of 2.5msec

```
          ┌─────────────────────┐
         (   Start ISR 2.5msec   )
          └──────────┬──────────┘
                     ↓
          ┌─────────────────────┐
          │ Read Encoder Position│
          └──────────┬──────────┘
                     ↓
          ┌─────────────────────┐
          │ Running Average filter│
          └──────────┬──────────┘
                     ↓
          ┌─────────────────────┐
          │Send Filtered Data to UART│
          └──────────┬──────────┘
                     ↓
          ┌─────────────────────┐
          │Send Drive command Data to│
          │         UART         │
          └──────────┬──────────┘
                     ↓
          ┌─────────────────────┐
          │ Set Point Data to UART│
          └──────────┬──────────┘
                     ↓
          ┌─────────────────────┐
          │  Reset 2.5msec flag  │
          └──────────┬──────────┘
                     ↓
              (    RETI    )
```
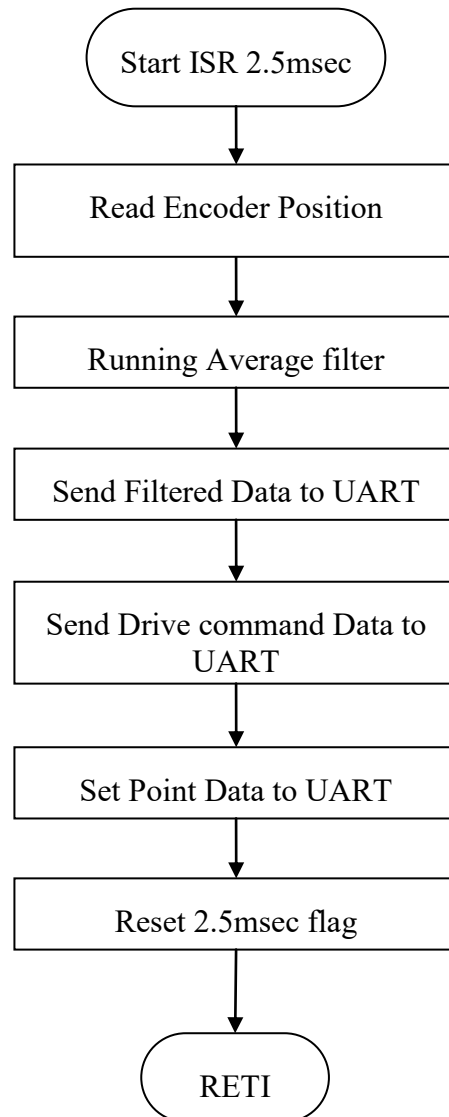
Figure A-3. Flowchart of 2.5msec ISR

d. ISR of 5msec
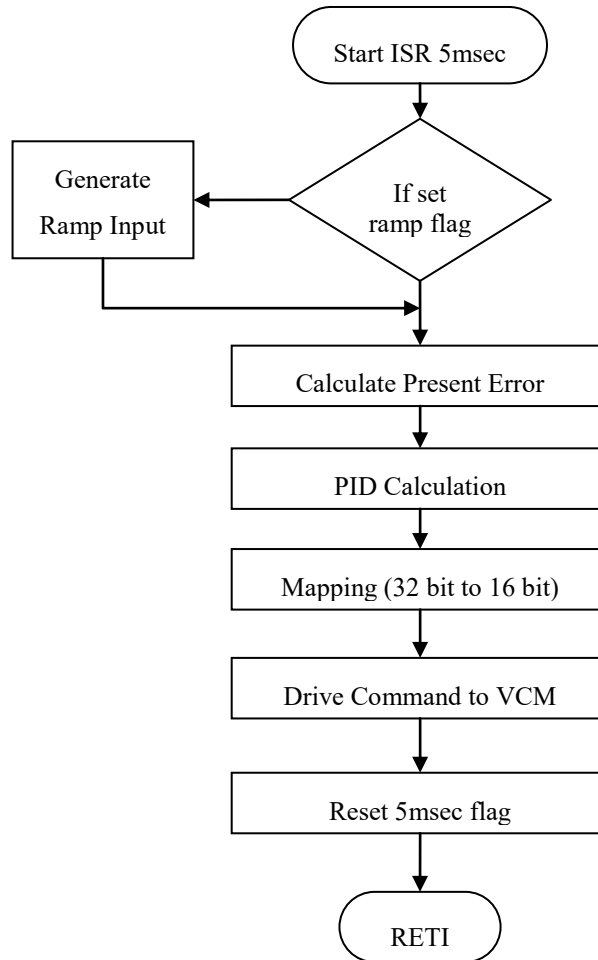
Figure A-4. Flowchart of 5msec ISR

e. ISR of 1sec
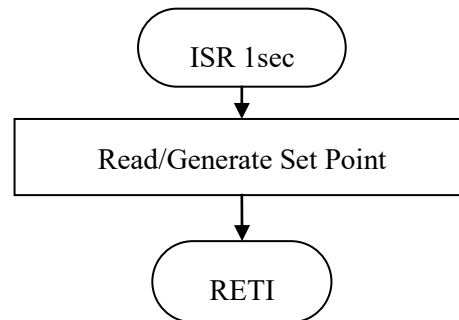
Figure A-5. Flowchart of 1sec ISR

f. Modules of PSOC library

Different modules of PSOC library which are used in the implementation of actuator local controller are listed below:

1. Clocks
2. Quadrature Decoder: Reading sensor data
3. SPI (Serial Peripheral Interface): Writing command to DAC
4. UART(Universal Asynchronous Receiver and Transmitter): Send diagnostic data over UART
5. CAN controller
6. Timer and Interrupts
7. Digital Logic blocks: Offloader Logic.
8. ARM Cortex M3 CPU: PID algorithm, Averaging Filter, Mapping Function, Number to digit conversion, Relay tuning, System Identification, IO Mapping.
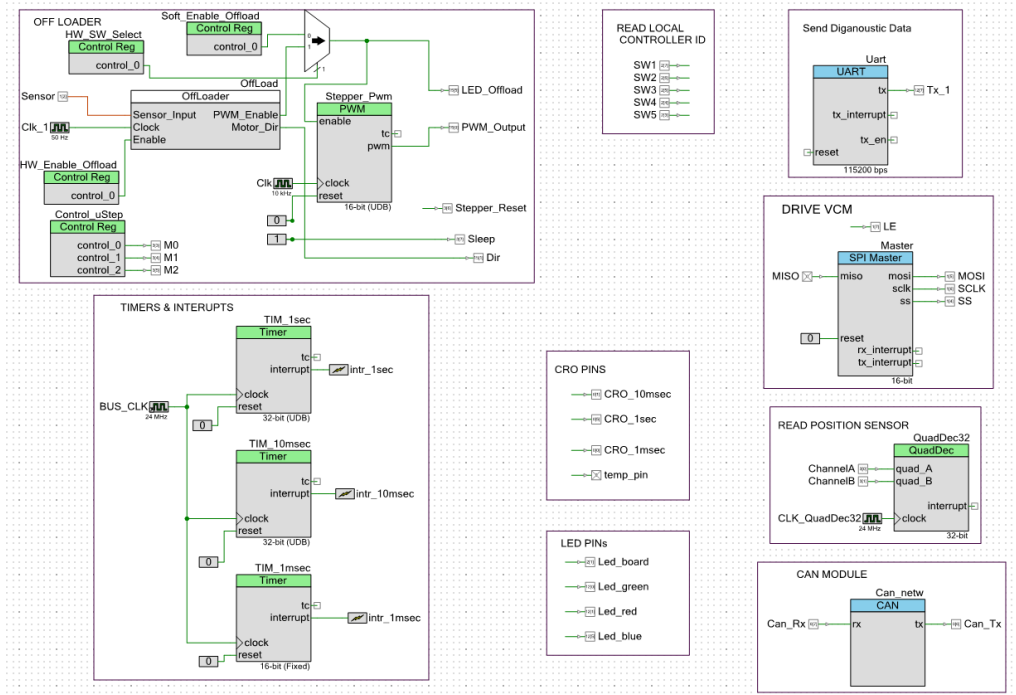
Figure A-6. Different modules of PSOC library incorporated in the actuator controller.

g. Hardware implementation of offloading logic
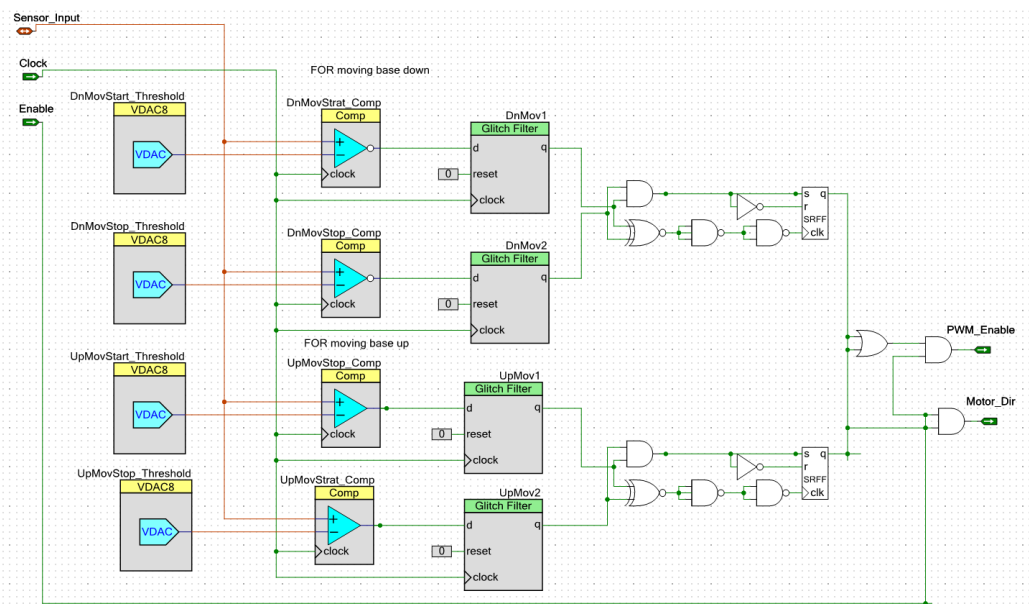
Figure A-7. The hardware implementation of automatic Offloader Logic on PSOC.

The offloading logic is a complete hardware-based logic implemented in parallel to the main position loop running on the soft processor. In Figure A-7, the upper part of the logic is responsible for moving the offloader down and the lower part to moves the offloader up. It consists of four voltage DACs which holds the four threshold values (e.g., 1 V, 1.5 V, 3 V, 3.5 V) as per the hysteresis diagram shown in the Figure 3-6. These four fixed voltages are compared with the input of the offloader block (current sensor output) with the help of four comparators. The output of the comparators is given to the glitch filters to suppress any noise being propagated further in the system. Further, the output of the glitch filter is given to a sequence detector which detects a sequence of digital values of 00, 01, 11 and produces a logic high output. The output of the sequence detector (i.e., PWM_En) is used to turn the stepper motor ON/OFF. As the motor turns ON, the current through VCM starts reducing since the compression or expansion of spring will provide the force to assist the load on the VCM. Similarly, the output of the sequence detector turns off the stepper motor when the current through VCM reduces within the dead band of hysteresis. The signal Motor_Dir decides the clockwise or counter-clockwise movement of the stepper motor. The En_Logic signal enables the overall offloader block operations.

Appendix B: DLA Modeling & Simulation

Analytical modeling conducted for DLA along with the simple actuator model is given here. The primary objective of this exercise is to ensure that the DLA concept is feasible to generate dynamic disturbances.

Let us consider the actuator equivalent model represented as spring mass and damper as shown in the figure below.
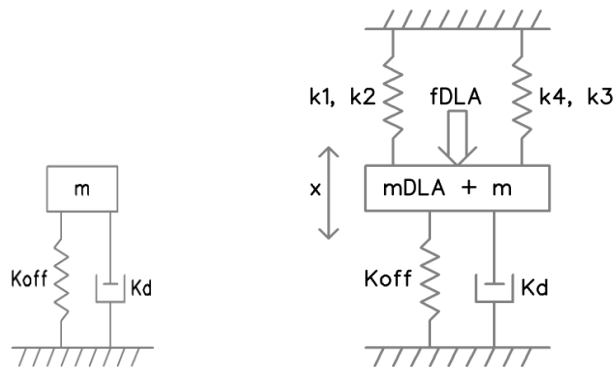
Figure B-1. (Left) Simple spring, mass, and damper based actuator model. (Right) An equivalent model of the DLA along with the actuator.

For the prototype actuator under test:

$$Actuator\ stiffness = K_{off} = 2 \times 10^5\ N/m, Damping = d = 6000\ Kg/s,\ Wind\ load = \pm 2\ N.$$

Let, M= (mDLA + m) = total moving mass of the system (Kg)

x = displacement of mass M

K_{sp} =effective spring constant (N/m) of side springs (k_1,k_2,k_3,k_4)

K_{off} =offloader spring constant (N/m)

K_d =damping force constant of the damper (N.sec/m)

$fDLA$ =force exerted on mass M (N)

The force F is due to the VCM of the DLA (not by the actuator). Here, we have considered the effect of the damper in the system. Also, we do not consider DLAs VCM dynamics as we will be driving the DLA in current mode. If we drive VCM in voltage mode, then additional damping due to back electromotive force (back emf) of VCM need to be considered.

As can be seen, when DLA exerts a force on the actuator, actuator spring gets compressed whereas DLA side springs get expanded. This leads to some loss of force already acting on actuator due to compressed DLA side springs. To keep this loss minimum, we make the following assumption:

Assumption 1: the contribution of DLAs side springs force loss should be less than 10% that of the VCM force.

$$For\ DLA:\ \text{Dynamic force} = 2N\ (wind)$$

$$\therefore \text{Maximum displacement of actuator} = \frac{2 \times 1}{2 \times 10^5} = 10um.$$

$$\therefore 10um\ \text{displacement of spring} \Rightarrow 0.2N$$

$$\therefore \text{Spring constant (side arm spring)} = K_{spring}$$

$$K_{sp} = \frac{0.2\,N}{10\,um} = 0.002 \times 10^6\ N/m$$

$$= 2000\,N/m$$

As seen in the figure below, four side springs are used are responsible for effective DLA spring constant. This is explained below:

$$\therefore K_{sp} = k_1 + k_2 + k_3 + k_4$$

$$\therefore K_{sp} = 4 \times k_{1-4} \quad (\because k_1 = k_2 = k_3 = k_4 = k_{1-4})$$

$$\therefore k_{1-4} = \frac{K_{sp}}{4} = 2000/4 = 500\ N/m$$
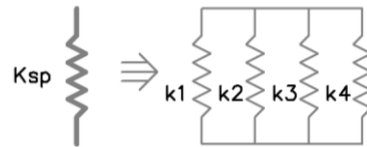
Figure B-2. Equivalent spring constant from four parallel springs

The actual springs designed have a spring constant of around 600 N/m. This value is used in further calculations. Further, to find the effective stiffness and natural frequency of our system, we approximate our system as a mass between two spring systems (Eric W. Weisstein) with Single-Degree-of-Freedom (SDOF). Using this, we obtain the equations for natural frequency and effective stiffness.
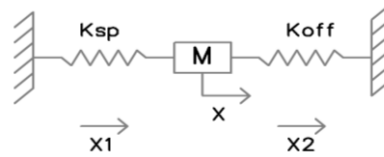
Figure B-3. Spring-mass model with two springs and mass between them.

The equation of motion for the above system can be written as

$$\therefore M\ddot{x} = (-k_{sp} \times x) + (-k_{off} \times x) = -(k_{sp} + k_{off}) \times x$$

$$\therefore \ddot{x} = -\left(\frac{k_{sp} + k_{off}}{M}\right) \times x$$

$$\therefore K_{eff} = k_{sp} + k_{off} \qquad \&$$

$$\omega_n = \sqrt{\frac{k_{sp} + k_{off}}{M}} \qquad ...rad / sec$$

Where, K_{eff} is the effective spring constant of the system and ω_n is the natural frequency. The effective spring constant in our case is:

$$\therefore K_{eff} = K_{off} + K_{sp}$$

$$= (2 \times 10^5 + 0.024 \times 10^5) \quad N/m$$

$$= 2.024 \times 10^5 \quad N/m$$

The natural frequency is an important parameter in the DLA design, and we have made the following assumption:

Assumption 2: the first natural frequency mode of the DLA+Actuator system should be outside the operating frequency band (0 to 10Hz).

In DLA we have provisions of inserting weight blocks of different values as a static load. Presently we have three weight blocks of 2.273Kg, 3.25Kg, and 4.92Kg. Also, the intermediate support plates of 5.339Kg which rest on actuator act as a static

weight in addition to weight blocks. This means we have three static loading options and respective natural frequencies are:

$$M = 5.339 + 2.273 = 7.612 \text{Kg} \quad \ggg \quad f_{osc} = 25.9 \quad ...Hz$$
$$M = 5.339 + 3.25 = 8.589 \text{Kg} \quad \ggg \quad f_{osc} = 24.4 \quad ...Hz$$
$$M = 5.339 + 4.92 = 10.259 \text{Kg} \quad \ggg \quad f_{osc} = 22.36 \quad ...Hz$$

This shows that natural frequency of DLA+Actuator system will be away from its required band of operation which is <10Hz. Whereas, due to finite damping in the system actual natural frequency will be the damped natural frequency and will be evaluated in this section. The damped natural frequency will be slightly lower than the natural frequency. In all the experiment results explained in this paper, we have used M= 7.612 Kg.

Further, to obtain the transfer function of the system, the free body diagram can be represented as follows:
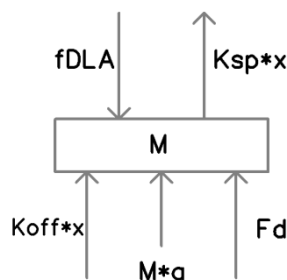
Figure B-4. Free body diagram of the DLA+Actuator system.

The equation of force equilibrium can be written as

$$fDLA = K_{sp}x + K_{off}x + Ma + K_d v$$

Where,

x =resultant displacement (in meter) due to the force $fDLA$.

a =acceleration of mass M

v =rate of change of displacement

$$fDLA = (K_{sp} + K_{off})x + Ma + K_d \frac{dx}{dt}$$

$$fDLA = K_{efff} x + M \frac{d^2x}{dt^2} + K_d \frac{dx}{dt}$$

Taking the Laplace Transform of the above equation with initial conditions as zero,

$$fDLA(s) = K_{eff} X(s) + Ms^2 X(s) + K_d sX(s)$$

The transfer function can be written as:

$$TF = \frac{X(s)}{fDLA(s)} = \frac{1}{K_{eff} + K_d s + Ms^2} \quad ....m/N$$

Since our system consists of a damper, we can obtain the damped natural frequency ω_d with ξ as the damping coefficients.

$$\omega_d = \omega_n \sqrt{1 - \xi^2} \qquad ...rad/sec$$

Different parameters used during the experiment are listed below:

$M = 7.6$kg, $K_d = 1000$N sec/m,

$K_{sp} = 2400$N/m, $K_{off} = 200000$N/m,

$K_{eff} = 202400$N/m.

$$\therefore TF = \frac{X(s)}{fDLA(s)} = \frac{1}{7.6\ s^2 + 1000\ s + 202400} \quad ....m/N$$

$\therefore$ *From this TF we get* :

$f_n = 25.9\ Hz, \quad \xi = 0.403, \quad f_d = 23.7Hz.$

Using the above transfer function, we obtained step response and frequency transform of the system as shown below:
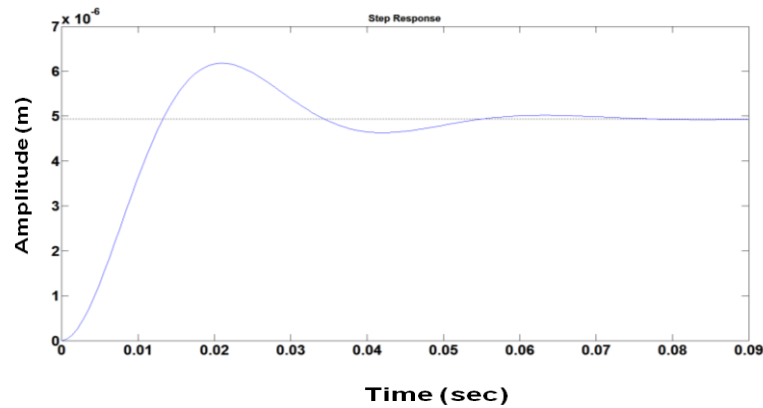
Figure B-5. Step response of DLA System. The damped resonant oscillation can be seen in the transient response.
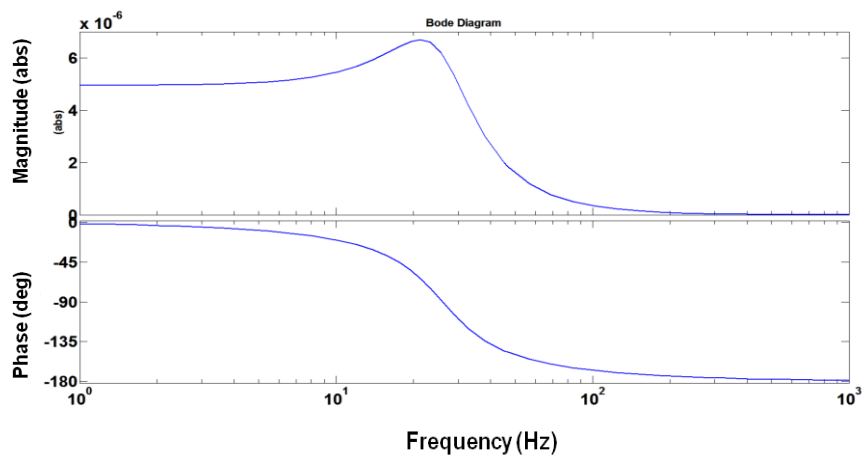
Figure B-6. Bode plot of the DLA system is indicating damped natural frequency mode at 23.7Hz.

As seen in the time response of the system is stable, and the initial damped oscillation around the steady state is due to the damped natural frequency of the system. This damped natural frequency mode can be clearly seen in the bode plot at 23.7Hz. So this system will pass the wind disturbance frequencies generated by DLA (<10Hz) without any problem.

Appendix C: Error due to matrix inversion method

We calculated the error in SVD based inversion technique and compared it with other methods. This calculation was done in Matlab which facilitates different matrix inversion functions such as QR, pinv, backslash along with the SVD method.

The formula used for calculating error:

$$If, \ \hat{z} = computed \ solution$$
$$z = actual \ solution$$
$$e = (z - \hat{z}) = computaion \ error$$

$$s - A\hat{z} = r \quad ....(residue \ with \ Error)$$
$$s - Az = 0 \quad ....(no \ Error)$$

$$\because \ r = s - A\hat{z}$$
$$\therefore \ r = Az - A\hat{z}$$
$$\therefore \ r = A(z - \hat{z})$$
$$\therefore \ r = Ae$$

$$\therefore \ e = A^{-1}r$$
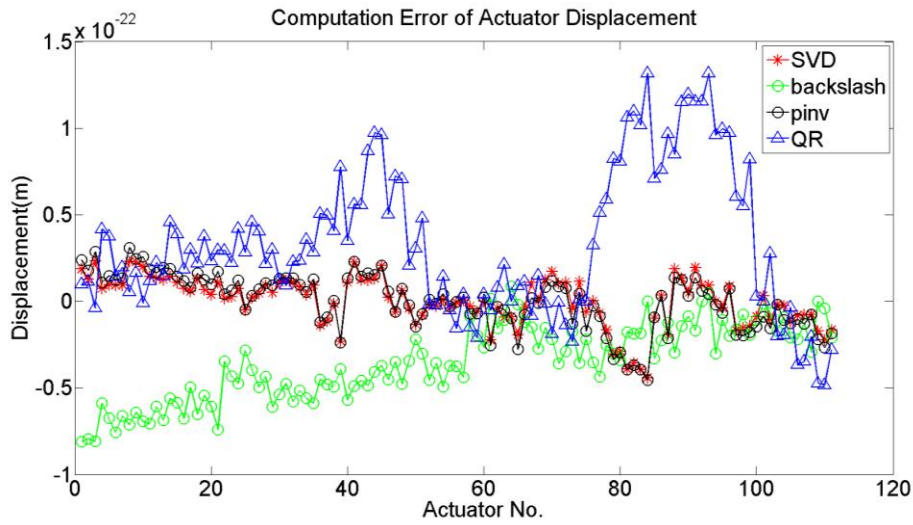
Figure C-1 Matrix inversion methods and associated error. As can be seen, all the errors are of the order of 10^{-22} which is negligible.

Comparison of Error	
RMS_Error_SVD	= 1.4106e-23
RMS_Error_backslash	= 4.1496e-23
RMS_Error_pinv	= 1.5893e-23
RMS_Error_QR	= 5.3231e-23

The contribution of computation error in the overall error in the system is extremely less and can be neglected.

Appendix D: Flowcharts of NCS MOO

Flow charts of M1CS NCS MOO implemented for the PSMT are given below.

```
                      ┌──────────────┐
                      │    Start     │
                      └──────┬───────┘
                             │
                             ▼
        ┌────────────────────────────────────────────────┐
        │ All global variable initialization and Function prototypes │
        └────────────────────────┬───────────────────────┘
                                 │
                                 ▼
        ┌────────────────────────────────────────────────┐
        │ Initialization of all components like timers, ISRs, PWM etc. │
        └────────────────────────┬───────────────────────┘
                                 │
                                 ▼
            ┌─────────────────┐        ┌──────────────┐
            │  Infinite Loop  │◄──────►│   1 Sec ISR  │
            └────────┬────────┘        └──────┬───────┘
                     │                         │
                     ▼                         ▼
              ┌──────────────┐              ╭──────╮
              │     Stop     │              │  A   │
              └──────────────┘              ╰──────╯
```
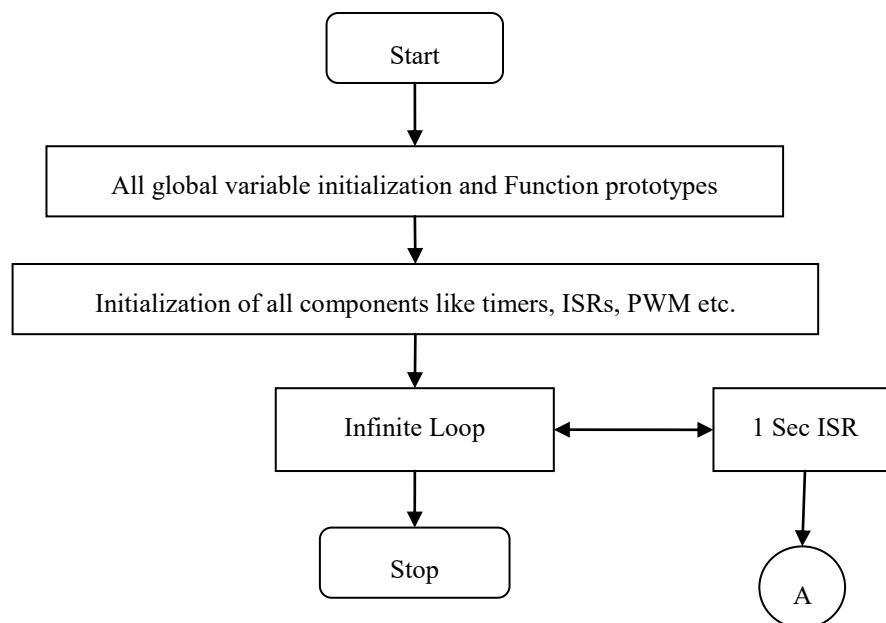
Note: Function Pointer is a pointer variable which holds the starting address of a function. This scheme is used to transfer the control to a particular function as per the corresponding mode ID. Every time we receive a new mode ID we change the Function pointer variable by the starting address of the function. This pointer variable is used at a rate of 1Hz to transfer control to the function.

A

Read CAN Message and Extract Message Serial
number, Controller ID and Mode ID

YES

ControllerID ==
Local ID

No

ControllerID ==
0x00

No

YES

YES

Local ID
mismatch Error

If 8ᵗʰ byte of received
data is 1

YES

Reset all flags

D

No

D

Write zero to the 8ᵗʰ byte of mode selection
message CAN buffer

Extract New Mode ID

Mode ID for
Switch Case

C

C

12	Open Loop Constant Mode	→	Update function Pointer	→	D
14	Open Loop Track Mode	→	Update function Pointer	→	D
13	Close loop Constant Mode	→	Update function Pointer	→	D
15	Close loop Track Mode	→	Update function Pointer	→	D
16	Free Form Mode	→	Update function Pointer	→	D
17	Offloader OL Mode	→	Update function Pointer	→	D
18	Offloader CL Mode	→	Update function Pointer	→	D
19	Identification Mode	→	Update function Pointer	→	D
20	Relay Mode	→	Update function Pointer	→	D
21	APS Mode	→	Update function Pointer	→	D
22	Global Calibration Mode	→	Update function Pointer	→	D
23	Halt Mode	→	Update function Pointer	→	D
24	Update Variable or constant	→	Update function Pointer	→	D
25	Manual Control	→	Update function Pointer	→	D
Default	Generate Mode error	→	Update function Pointer by free form mode	→	D

D → Call Function Pointer → Clear all 1sec pending interrupt → RETI

Appendix E: Plots showing different modes of surface fluctuations in the PSMT primary mirror control

In PSMT there are 7 segments. So in total, there are 18 modes of interest. For a telescope with N segments, there are 3N-3 shape modes. Modal plots of all 18 (3N-3) modes of PSMT are given in the table below. As discussed earlier most of the energy is in the Focus mode (Mode 1). Focus Mode (focus mismatch) is first non-singular control mode, with highest error multiplier.
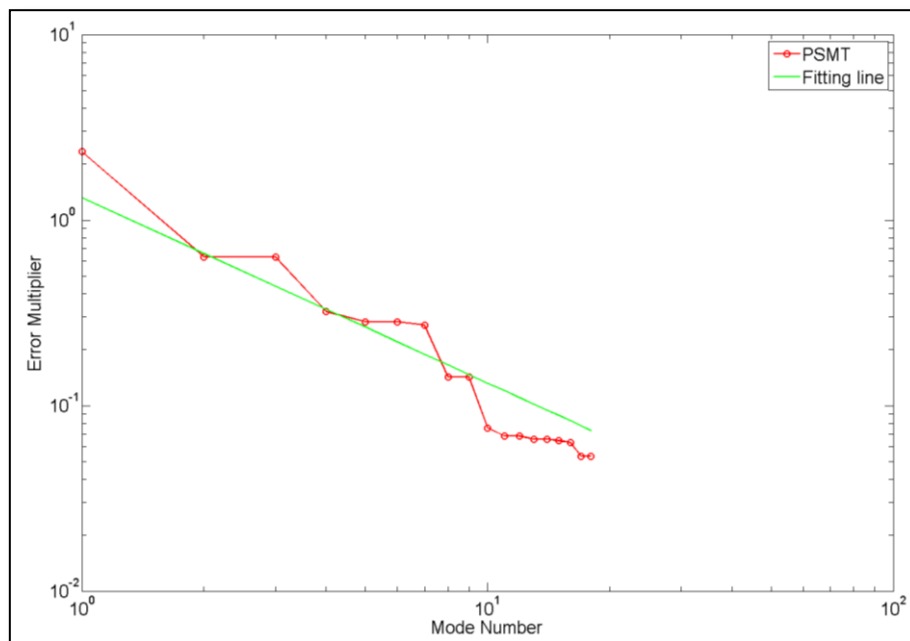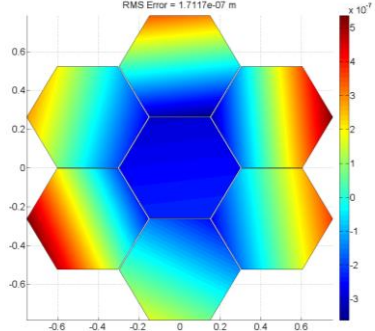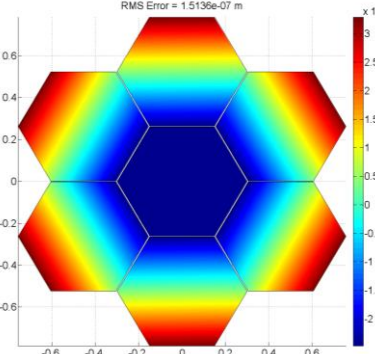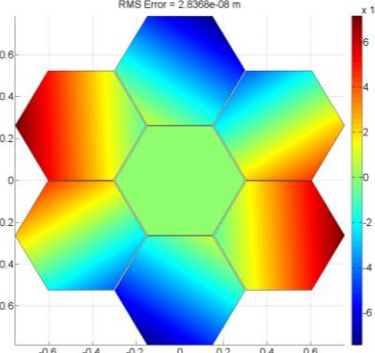

Figure E-1. Individual Error Multiplier plot w.r.t., different surface modes of the PSMT.
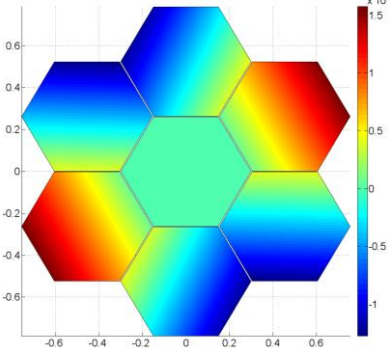
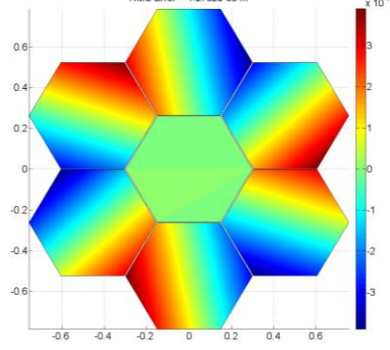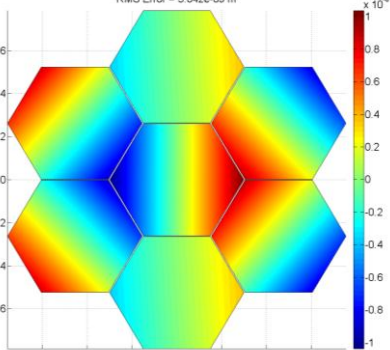Appendix E: Plots showing different modes of surface fluctuations in the PSMT 194 primary mirror control

Table E-1. Mirror shape plots of all 18 modes of the PSMT Primary Mirror.
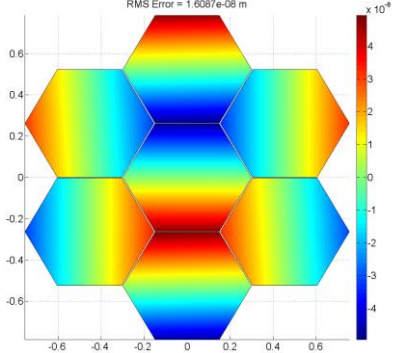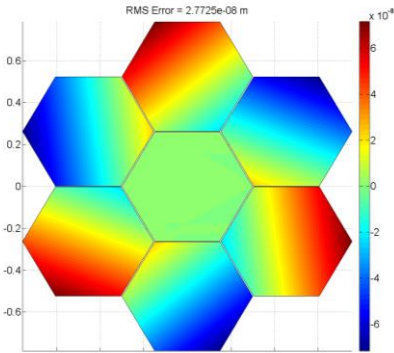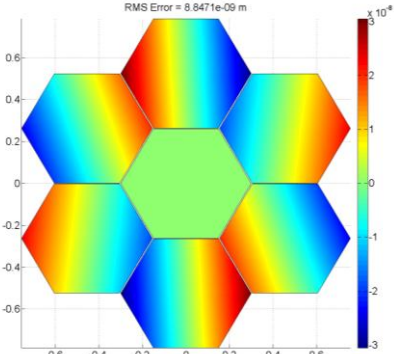
Mode No.	Individual Error Multiplier	Mirror Shape	RMS surface deformation (nm)
Overall shape (with all modes)	2.581		171 nm
1	2.3332	\nDefocus	151.4
2	0.6326	\nOblique Astigmatism	28.4
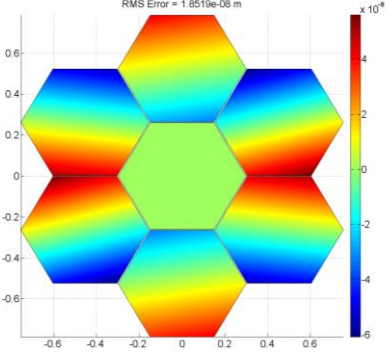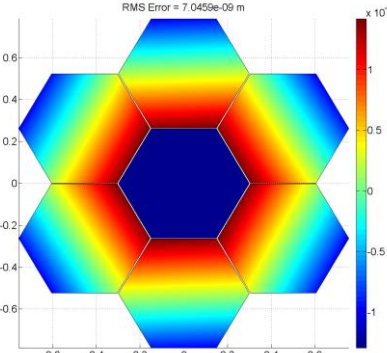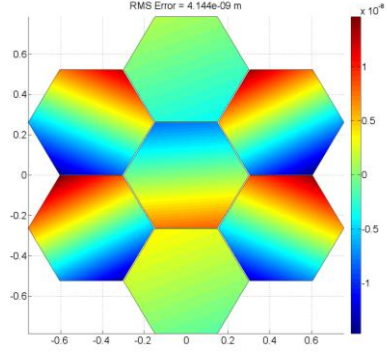
Appendix E: Plots showing different modes of surface fluctuations in the PSMT 195 primary mirror control

3	0.6326	RMS Error = 6.2243e-08 m Astigmatism	62.2
4	0.3212	RMS Error = 1.2732e-08 m Oblique Trefoil	12.7
5	0.2825	RMS Error = 3.042e-09 m Vertical Coma	3
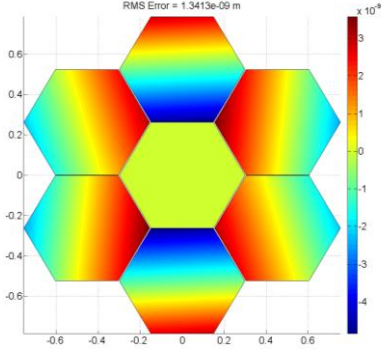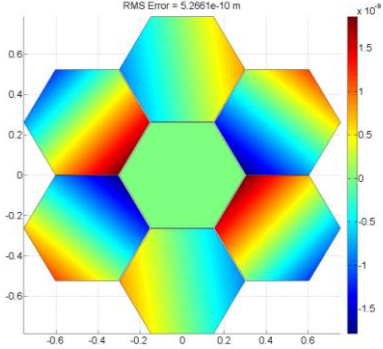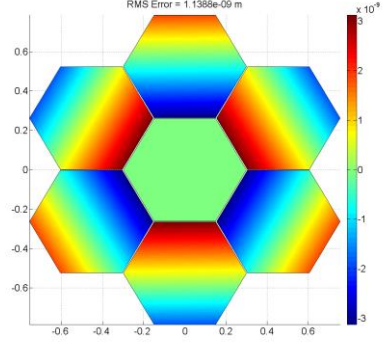
Appendix E: Plots showing different modes of surface fluctuations in the PSMT 196
primary mirror control

6	0.2825	RMS Error = 1.6087e-08 m	16
		Horizontal Coma	
7	0.2716	RMS Error = 2.7725e-08 m	27.7
		Horizontal Trefoil	
8	0.1430	RMS Error = 8.8471e-09 m	8.8
		Oblique Quatrefoil	
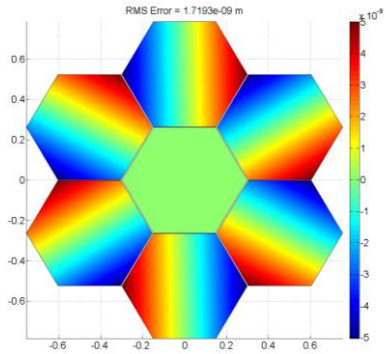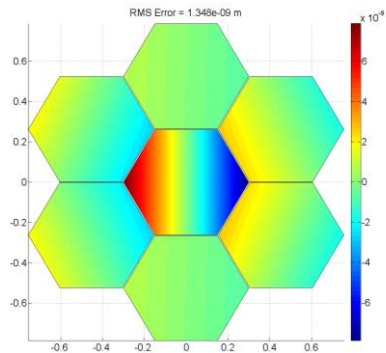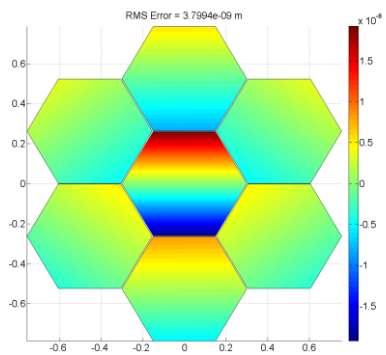
Appendix E: Plots showing different modes of surface fluctuations in the PSMT 197 primary mirror control

9	0.1430	Oblique Secondary Astigmatism	18.5
10	0.0756	Spherical Aberration	7
11	0.0684	Oblique Secondary Astigmatism	4.1

12	0.0684		0.8
		Quatrefoil	
13	0.0657		1.3
14	0.0657		0.5
15	0.0645		1.1

Appendix E: Plots showing different modes of surface fluctuations in the PSMT 199 primary mirror control

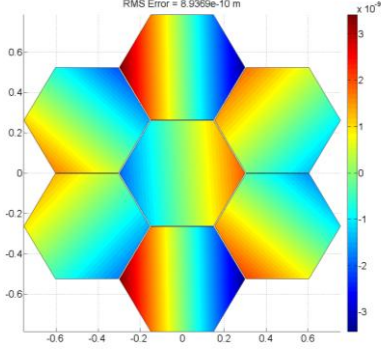| 16 | 0.0632 | | 1.7 |
| 17 | 0.0530 | | 1.3 |
| 18 | 0.0530 | | 3.8 |

Appendix E: Plots showing different modes of surface fluctuations in the PSMT 200 primary mirror control

Appendix F: Error Multiplier derivation

Here we have done the derivation of - Why Simulation RMS value is Numerical Error multiplier?

Assuming that the noise on different sensors is uncorrelated, the RMS error in the estimation of the deflection at the actuator locations is the product of the RMS sensor noise and an Error Multiplier.

Proof of RMS of Monte Carlo simulation is equal to N:

$$(RMS_{MCSimulation})^2 = \sum_{k=1}^{n} \frac{\alpha_k^2}{n} = \frac{1}{n}\sum_{k=1}^{n}\alpha_k^2$$

n = number of Simulation runs

$\alpha_k = \dfrac{\delta a_k}{\delta s_k} \Rightarrow$ overall error multiplier from k^{th} sumulation. $(Chanan, et\ al.\ 2004)$.

δa_k = rms of actuator values for k^{th} simulation run.

δs_k = rms of sensor values for k^{th} simulation run.

$Let,$

$\alpha_{jk} \Rightarrow$ error multiplier for j^{th} actuator from kth sumulation

$$\therefore (RMS_{MCSimulation})^2 = \frac{1}{n}\sum_{k=1}^{n}\sum_{i=1}^{N_{act}}\frac{\alpha_{jk}^2}{N_{act}}$$

$$= \frac{1}{N_{act}}\sum_{i=1}^{N_{act}}\left[\frac{1}{n}\sum_{k=1}^{n}\frac{\alpha_{ik}^2}{N_{act}}\right]$$

$$\therefore (RMS_{MCSimulation})^2 = \frac{1}{N_{act}}\sum_{i=1}^{N_{act}}\left[\alpha_i^2\right]$$

$\alpha_i \Rightarrow$ RMS of error multiplier for i^{th} actuator.

From $\big($MacMartin and Chanan 2004$\big)$, we have:

$$(ErrorMultiplier)^2 = \frac{1}{N_{act}} \sum_{i=1}^{N_{act}} \left[\sigma_i^{-2} \right]$$

$\sigma_i =$ singular values of A matrix corresponding to i^{th} mode.

Note:

If there are x segments, there will be $3x$ actuators and $3x-3$ modes of interest.

(Actual number of modes will be $3x$ out of which 3 modes corresponding to rigid body motion PTT, and there singilurvaluesareZero).

From $\big($Chanan, et al. 2004$\big)$, we have:

$$\alpha_j = \sum_i \left(\frac{V_{ij}}{\sigma_j} \right)^2 \quad ----(i = \text{actuator No., } j = \text{mode } No.)$$

$$\& \quad \sum_i V_{ij}^2 = 1$$

$$\therefore \alpha_j \approx \frac{1}{\sigma_j}$$

Here,

α_j is error multiplier for j^{th} mode.

σ_j is error multiplier for j^{th} mode (which also coincides with the ith actuator).

From above discussion we get;

$$(RMS_{MCSimulation}) \approx (ErrorMultiplier)$$

Appendix G: Global Controller computational requirement

The processing cost requirements for implementing the M1CS calculations for SMT of different sizes are estimated below. The parameter for comparison used here is the number of floating-point operations per sec (FLOPS). A Floating-point number is a real number that is, a number that can contain a fractional part. In computing, FLOPS is a measure of computer performance, useful in fields of scientific calculations that make heavy use of floating-point calculations. For such cases, it is a more accurate measure than the generic instructions per second.

The number of FLOPS can be calculated using the equation (Ideal) (Novatte 2014):

$$FLOOPS = sockets \times \frac{cores}{socket} \times clock \times \frac{FLOPs}{cycle}$$

Following table summarizes the computational requirements for the telescope of different sizes with nominal parameters as listed in the table.

Table G-1 Global controller computational requirement for telescopes of different sizes.

	PSMT	NLOT	KECK	TMT	EELT	OWL
Aperture size (m)	1.5	10	10	30	39.3	100
Segment Size (m)	0.5	1.44	1.8	1.44	1.45	1.6
No of Segments	7	61	36	492	798	3042
No of Actuators	18	183	108	1476	2394	9126
No. of Sensors	24	366	216	2952	4788	18252
No. of Subtractions	24	366	216	2952	4788	18252
No. of	432	66978	23328	4357152	11462472	166567752

Multiplications						
No. of Additions	414	66795	23220	4355676	11460078	166558626
Total (FLOPS)	**80**	**134139**	**46764**	**8715780**	**22927338**	**333144630**
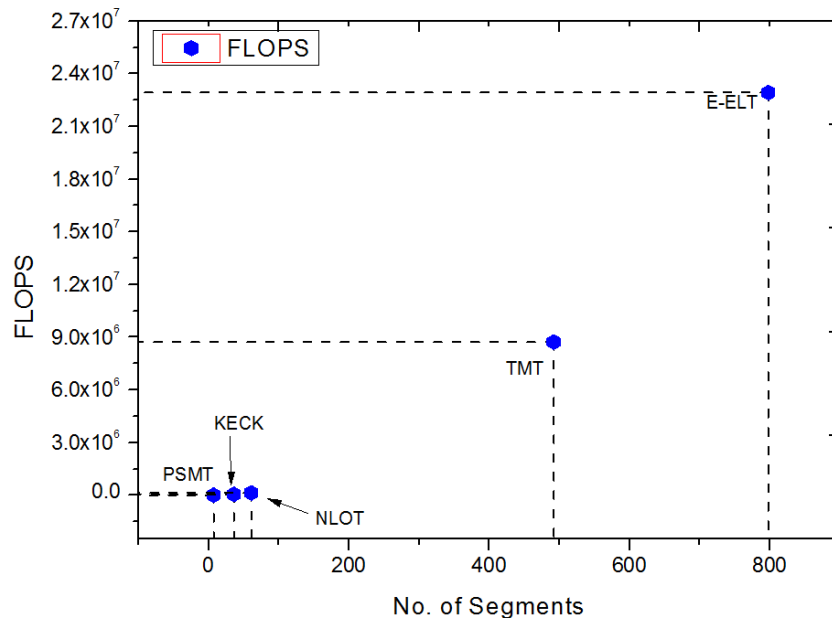
Figure G-1 M1CS Computational requirement for tzelescopes of different sizes.

As seen from the above discussion, we will not need very high processing capability in small telescope like the PSMT, but since in the larger SMTs the requirements for global controller calculations will be in terms of few milliseconds (and not per second) it will be worth of exploring the parallel processing application for applying for upcoming extremely large telescope like TMT & EELT. One such attempt can be seen by (Truchard 2009).

Bibliography

Andersen, Torben, and Anita Enmark. *Integrated modeling of Telescopes.* Vol. 377, 394-422. Springer Science & Business Media, 2011.

Anderson, E., et al. *LAPACK User's Guide.* User's Guide, Philadelphia: Society for Pure and Applied Mathematics, 1999.

Angeli, G.Z., M.K. Cho, and M.S. Whorton. "Active optics and control architecture for a Giant Segmented Mirror Telescope." *SPIE Astronomical Telescopes and Instrumentation.* International Society for Optics and Photonics, 2003. 129-139.

Angeli, G.Z., R.S. Upton, A. Segurson, and B.L. Ellerbroek. "Active optics challenges of a thirty-meter segmented mirror telescope." *Second Backaskog Workshop on Extremely Large Telescopes.* International Society for Optics and Photonics, 2004.

Åström, Karl Johan. *Control system design.* Lecture notes for ME 155A, Department of Mechanical and Environmental Engineering, University of California Santa Barbara, 2002.

Åström, KJ, and Hägglund Tore. *PID Controllers: Theory, Design, and Tuning, Second Edition.* International Society of Automation, 1995.

Barnes T. G., et al. "Commissioning experience with the 9.2-m Hobby-Eberly Telescope." *Telescope Structures, Enclosures, Controls, Assembly/Integration/Validation, and Commissioning.* International Society for Optics and Photonics, 2000.

Baronti, F., A. Lazzeri, F. Lenzi, R. Roncella, R. Saletti, and S. Saponara. "Voice coil actuators: From model and simulation to automotive application." *35th Annual Conference of IEEE Industrial Electronics.* IEEE, 2009. 1805.

Bastaits Renaud, André Preumont. "Extremely large segmented mirrors: dynamics, control and scale effects." PhD Thesis, 2010.

Beckers, J. M., Ulich, B. L., & Williams, J. T. "Performance of the Multiple Mirror Telescope (MMT) I. MMT-the first of the advanced technology telescopes." *In Advanced Technology Optical Telescopes I (Vol. 332, pp. 2-9).* International Society for Optics and Photonics, 1982.

Bely, Pierre. *The design and construction of large optical telescopes.* Springer Science & Business Media, 2006.

Chanan, G., D.G. MacMartin, J. Nelson, and T. Mast. "Control and alignment of segmented-mirror telescopes: matrices, modes, and error propagation." *Applied Optics* 43(6) (2004): 1223-1232.

Chevillard, J. P., Connes, P., Cuisenier, M., Friteau, J., & Marlot, C. "Near infrared astronomical light collector." *Applied optics*, 1977: 1817-1833.

Cho, M.K., L.M. Stepp, and S. Kim. "Wind buffeting effects on the Gemini 8-m primary mirrors." *International Symposium on Optical Science and Technology.* International Society for Optics and Photonics., 2001. 302-314.

Cohen, Richard, Teiry Mast, and Jeriy Nelson. "Performance of the WM Keck Telescope active mirror control system." *Advanced Technology Optical Telescopes V.* SPIE, 1994. 105-116.

D'Arturo Horn, G. "Pubblicazioni dell'Osservatorio Astronomico Universitario di Bologna, VI, 6." 1955.

Deshmukh, Prasanna, and Padmakar Parihar. "Precision controller for segmented mirror telescope actuator: Control and tuning." *Indian Control Conference (ICC).* IEEE, 2016. 245-252.

Deshmukh, Prasanna, Padmakar Parihar, Deepta Sundar Mishra, Ajin Prakash, and P. M. M. Kemkar. "A soft actuator for prototype segmented mirror telescope." *SPIE Astronomical Telescopes+ Instrumentation.* International Society for Optics and Photonics, 2016.

Dimmler, M., et al. "E-ELT primary mirror control system." *Ground-based and Airborne Telescopes II.* International Society for Optics and Photonics, 2008.

Donglin, Ma. "Recommended conceptual optical system design for China's Large Optical-infrared Telescope (LOT)." *Optics express* 26, no. 1 (2018): 108-119.

Eric W. Weisstein. *wolfram.com.* 1996-2007. http://scienceworld.wolfram.com/physics/SpringsTwoSpringsandaMass.

Espinosa, JM Rodríguez, P. Alvarez, and F. Sanchez. "The GTC: An advanced 10M telescope for the ORM." 1998. 355-360.

Feucht, Dennis. "Op-Amp Current Sources: The Howland Current Pump." 2014. http://www.edn.com/design/analog/4430167/Op-Amp-Current-Sources--The-Howland-Current-Pump.

Fornax Computing Server. 2017. https://www.iiap.res.in/facilities/computing/fornax (accessed June 22, 2017).

Fuertes, J.M., S. De Miguel, R. Villa, J.C. Gonzalez, and J. Castro. "Dynamic analysis of a segmented telescope testbed." *European Control Conference (ECC).* IEEE, 1997. 2898-2903.

Gajjar, H., Menzies, J., Swiegers, J., Rozière, D., Courteville, A., Buous, S., & Luong, B. "Results from the capacitive edge sensing system for the active alignment of the SALT primary mirror." *Ground-based and Airborne Telescopes.* International Society for Optics and Photonics., 2006.

Gemini, Wind Data. *Gemini South Wind Tests Data, Version 2.0.* 1 August 2001. http://www.gsmt.noao.edu/studies/wind_tests1/index.html.

Gerhard, Meiring Jacobus, and David AH Buckley. "Southern African Large Telescope (SALT) project progress and status after four years." *Ground based Telescopes.* International Society for Optics and Photonics., 2004. 592-603.

Golub, Gene H., and Charles F. Van Loan. *Matrix computations.* Baltimore, MD, USA: Johns Hopkins University, Press, 1996.

H2W Technologies, Inc. "Non-Comm DC Voice Coil Linear Actuator - NCC15-24-050-1R." *H2W Technologies, Inc.* 4 2010. https://www.h2wtech.com/product/voice-coil-actuators/NCC15-24-050-1R.

Hägglund, Tore. "Signal filtering in PID control." *2nd IFAC Conference on Advances in PID Control.* IFAC, 2012. 1-10.

Haugen, Finn. "Discretization of simulator, filter, and PID." May 2010. http://www.mic-journal.no/PDF/ref/Haugen2010.pdf.

Jiang, S., P.G. Voulgaris, L.E. Holloway, and L.A. Thompson. "Distributed control of large segmented telescopes." *American Control Conference.* IEEE, 2006. 6.

Jiménez, A., E. Morante, T. Viera, M. Núñez, and M. Reyes. "Design of a prototype position actuator for the primary mirror segments of the European Extremely Large Telescope." *SPIE Astronomical Telescopes+ Instrumentation.* International Society for Optics and Photonics, 2010. 773354-77335.

Khalore, A.G. "Relay Approach for tuning of PID controller." *Int J Computer Technology and Applications* 3 (3) (2012): 1237-42.

Krabbendam, V.L., T.A. Sebring, F.B. Ray, and J.R. Fowler. "Development and performance of Hobby-Eberly Telescope 11-m segmented mirror." *Astronomical Telescopes & Instrumentation.* International Society for Optics and Photonics, 1998.

Lefort, B., and J. Castro. "The GTC primary mirror control system." *SPIE Astronomical Telescopes+ Instrumentation.* International Society for Optics and Photonics, 2008.

Lorell, K.R., J.N. Aubrun, R.R. Clappier, B. Shelef, and G. Shelef. "Design and preliminary test of precision segment positioning actuator for the California Extremely Large Telescope primary mirror." *Proceedings of SPIE*. 2003. 471-484.

Lorell, K.R., J.N. Aubrun, R.R. Clappier, S.W. Miller, and M. Sirota. "Design of a prototype primary mirror segment positioning actuator for the Thirty Meter Telescope." *SPIE Astronomical Telescopes+ Instrumentation.* International Society for Optics and Photonics, 2006. 62672T-62672T.

MacMartin, D.G., and G. Chanan. "Measurement accuracy in control of segmented-mirror telescopes." *Applied Optics* 43(3) (2004): 608-615.

MacMartin, D.G., P.M. Thompson, M.M. Colavita, and M.J. Sirota. "Dynamic analysis of the actively-controlled segmented mirror of the thirty meter telescope." *IEEE Transactions on Control Systems Technology* (IEEE) 22(1) (2014): 58-68.

MacMartin, Douglas G. "Control challenges for extremely large telescopes." *Industrial and Commercial Applications of Smart Structures Technologies* (International Society for Optics and Photonics,), 2003: 275-287.

MacMartin, Douglas G., and Gary A. Chanan. "Control of the California extremely large telescope primary mirror." *Astronomical Telescopes and Instrumentation.* International Society for Optics and Photonics, 2003.

MacMynowski, Douglas G., Peter M. Thompson, and Mark J. Sirota. "Analysis of TMT primary mirror control-structure interaction." *SPIE Astronomical Telescopes+ Instrumentation.* International Society for Optics and Photonics, 2008.

MacMynowski, Douglas G., Peter M. Thompson, J. Chris Shelton, Lewis C. Roberts Jr, M. Mark Colavita, and Mark J. Sirota. "Control system modeling for the Thirty Meter Telescope primary mirror." *Integrated Modeling of Complex Optomechanical Systems.* SPIE, 2011.

Meeker, D. *Finite element method magnetics: magnetics tutorial.* 2013. http://www.femm.info/wiki/MagneticsTutorial.

Meng, J.D., J. Franck, G. Gabor, R.C. Jared, R.H. Minor, and B.A. Schaefer. "Position actuators for the primary mirror of the WM Keck telescope." *Astronomy'90.* Tucson AZ: International Society for Optics and, 1990. 1018-1022.

Nelson, J. E., T. S. Mast, and S. M. Faber. *The design of the Keck Observatory and Telescope.* Keck Observatory Report No. 90, Berkeley: Keck Observatory Science Office, 1985.

Nelson, Jerry. "Segmented mirror telescopes." *Optics in Astrophysics* (Springer Netherlands), 2006: 61-72.

Nelson, Jerry, Terry Mast, and Gary Chanan. *Segmented Mirror Telescopes.* Springer Netherlands, 2013.

Novatte. *How to calculate peak theoretical performance of a CPU-based HPC system.* 2014. http://www.novatte.com/our-blog/197-how-to-calculate-peak-theoretical-performance-of-a-cpu-based-hpc-system.

Observatory, Gemini. "Gemini South Wind Tests Data." 2001. http://www.gsmt.noao.edu/studies/wind_tests1/index.html.

Palunas, P., MacQueen, P. J., Booth, J. A., Calder, R., Fowler, J. R., Shetrone, M. D., ... & Martin, J. " Imaging Performance of the Hobby-Eberly Telescope. ." *Ground-based and Airborne Telescopes.* International Society for Optics and Photonics, 2006. 62673V.

Parihar, Padmakar, Prasanna Deshmukh, Annu Jacob, Varun Kumar, Abhishek Goudar, S. Sriram, S. Nagabhusan et al. ""Prototype segmented mirror telescope: a pathfinder of India's Large Optical-NIR telescope project." *Ground-based and Airborne Telescopes VI.* International Society for Optics and Photonics, 2018. 107001A.

Physik Instrumente (PI). "Fast Steering Mirrors / Active Optics." 2009. http://www.www.pi-usa.us/pdf/2009_PI_Fast_Steering_Mirror_Scanner_Catalog.pdf.

Press, W., B. Flannery, S. Teukolsky, and W. Vetterling. *Numerical recipes in Pascal: the art of scientific computing.* 1. New York: Cambridge University Press, 1989.

Preumont, A., R. Bastaits, and G. Rodrigues. "Active optics for large segmented mirrors: scale effects." *IV ECCOMAS Thematic Conference on Smart Structures and Materials.* 2009.

Redd, Nola Taylor. "Extremely Large Telescope: The Biggest Eye on the Sky." *Space.com.* 2018. https://www.space.com/40746-extremely-large-telescope.html.

Rowell, Derek. "State-Space Representation of LTI Systems." *Analysis and Design of Feedback Control Systems.* October 2002. http://web.mit.edu/2.14/www/Handouts/StateSpace.pdf.

Swiegers, Jian, and Gajjar Hitesh. "Completion of the Southern African Large Telescope (SALT) primary mirror system." *SPIE Astronomical Telescopes+ Instrumentation.* International Society for Optics and Photonics, 2004. 881-891.

System Identification Toolbox. 2014. http://www.mathworks.com/products/sysid.

Thompson, P. M., D. G. MacMynowski, M. W. Regehr, M. M. Colavita, and M. J. Sirota. "Servo design and analysis for the Thirty Meter Telescope primary mirror actuators." *Ground-based and Airborne Telescopes III.* International Society for Optics and Photonics, 2010.

TMT M1CS Design Requirement, TMT Report. 2012.

Tomas, B Co. "Ziegler-Nichols Method." 2004. http://www.chem.mtu.edu/~tbco/cm416/zn.html.

Truchard, James. *Applying a Graphical System Design Approach to Enable Real-Time HPC.* Presentation, National Instruments, 2009.

Viera, Teodora, Pablo Zuluaga, Marcos Reyes, Miguel Núñez, and Javier Castro. "Wind Evaluation Breadboard Control Architecture, Dynamic Model and Performance." *IFAC Proceedings.* 2008. 7705-7710.

Witvoet, G., R. den Breeje, J. Nijenhuis, R. Hazelebach, and N. & Doelman. "High performance control of mirror segment actuators for the European Extremely Large Telescope." *SPIE Astronomical Telescopes+ Instrumentation.* International Society for Optics and Photonics, 2014.

Witvoet, G., R. den Breeje, J. Nijenhuis, R. Hazelebach, and N. Doelman. "Dynamic analysis and control of mirror segment actuators for the European Extremely Large Telescope." *Journal of Astronomical Telescopes, Instruments, and Systems* (SPIE) 1(1) (2015): 019003-019003.

Xu, Xinqi, Lingzhe Xu, and Gangping Jin. "Overview of LAMOST control system." *Astronomical Telescopes and Instrumentation.* International Society for Optics and Photonics, 2003.